PolyPublie
Polytechnique Montréal

POLYTECHNIQUE MONTRÉAL
UNIVERSITÉ D'INGÉNIERIE

Titre: Title:	Integrated Guided-Wave Structures and Techniques for Millimeter-Wave and Terahertz Electronics and Photonics
Auteur: Author:	Faezeh Fesharaki
Date:	2016
Type:	Mémoire ou thèse / Dissertation or Thesis
Référence: Citation:	Fesharaki, F. (2016). Integrated Guided-Wave Structures and Techniques for Millimeter-Wave and Terahertz Electronics and Photonics [Ph.D. thesis, École Polytechnique de Montréal]. PolyPublie. https://publications.polymtl.ca/2218/

Document en libre accès dans PolyPublie
Open Access document in PolyPublie

URL de PolyPublie: PolyPublie URL:	https://publications.polymtl.ca/2218/
Directeurs de recherche: Advisors:	Ke Wu, & Mohamed Chaker
Programme: Program:	génie électrique

Ce fichier a été téléchargé à partir de PolyPublie, le dépôt institutionnel de Polytechnique Montréal
This file has been downloaded from PolyPublie, the institutional repository of Polytechnique Montréal

https://publications.polymtl.ca

UNIVERSITÉ DE MONTRÉAL

INTEGRATED GUIDED-WAVE STRUCTURES AND TECHNIQUES FOR MILLIMETER-WAVE AND TERAHERTZ ELECTRONICS AND PHOTONICS

FAEZEH FESHARAKI

DÉPARTEMENT DE GÉNIE ÉLECTRIQUE

ÉCOLE POLYTECHNIQUE DE MONTRÉAL

THÈSE PRÉSENTÈE EN VUE DE L'OBTENTION

DU DIPLÔME DE PHILOSOPIAE DOCTOR

(GÉNIE ÉLECTRIQUE)

AOÛT 2016

© Faezeh Fesharaki, 2016.

UNIVERSITÉ DE MONTRÉAL

ÉCOLE POLYTECHNIQUE DE MONTRÉAL

Cette thèse intitulée :

INTEGRATED GUIDED-WAVE STRUCTURES AND TECHNIQUES FOR MILLIMETER-WAVE AND TERAHERTZ ELECTRONICS AND PHOTONICS

présentèe par : FESHARAKI Faezeh

en vue de l'obtention du diplôme de : Philosophiae Doctor

a été dûment acceptée par le jury d'examen constitué de :

M. KASHYAP Raman, Ph. D., président

M. WU Ke, Ph.D., membre et directeur de recherche

M. CHAKER Mohamed, Ph. D., membre et codirecteur de recherche

M. CARDINAL Christian, Ph. D., membre

M. AZANA José, Ph. D., membre externe

DEDICATION

Dedicated with love and gratitude to:

My Mother

ACKNOWLEDGEMENTS

My deepest gratitude is to my thesis supervisor, Prof. Ke Wu, for his inspirational mentorship, constant encouragement, and constructive criticisms. Prof. Ke Wu offered his unreserved help and guidance throughout my graduate studies. He guided me through tough times and was always with me to check on my research progress. I am deeply grateful to him for the long discussions we had, for holding me to a high research standard and enforcing strict validations for each research result, and therefore teaching me how to do research.

I am deeply grateful to Prof. Mohamed Chaker, my co-supervisor, director of Laboratory of micro- and nanofabrication (LMN). He was always eager to help me and I am grateful to him, for being friendly, caring, supportive and helpful in numerous ways. I am indebted to him for his continuous encouragement and guidance.

I also thank Dr. Tarek Djerafi and Dr. Nadir Hossain with whom I had very educative interactions during my research. I am also very grateful to all the personnel at the Poly-Grames Research Center, especially all the technicians including Mr. Jules Gauthier, Mr. Traian Antonescu, Mr. Steve Dubé and Mr. Maxime Thibault. My gratitude extends to Mrs Rachel Lortie for her assistance with all the administrative works and also to Mr. Jean-Sébastien Décarie for his technical support for solving all the IT problems. I am also very grateful to all the personnel at LMN, especially Dr. Sébastien Delprat, Dr. Boris Le Drogoff and also Ms. Johanne Roy. I would like to thank all my friends and colleagues in the Poly-Grames Research Center and LMN.

I would also like to thank my family for the support they provided me through my entire life and in particular, I would like to express my heartfelt gratitude to my husband, Hadi Razavipour, without whose love and encouragement, I would not have finished this thesis.

RÉSUMÉ

Pour faire face à la demande croissante en bande passante, les prochaines générations des systèmes sans fil et filaires devront exploiter la large gamme spectrale 100 GHz-1 Térahertz (THz) et au-delà. Cependant, les éléments constitutifs intégrés qui définiront les architectures et les normes des systèmes à très haute fréquence ne sont pas claires et généralement pas du tout disponible. Cette thèse contribue à ce nouveau défi en explorant de nouveaux concepts et techniques de transmission d'onde pour le développement des circuits intégrés et les systèmes électroniques et photoniques en ondes millimétriques (MMW) et THz.

Les lignes de transmission sont les éléments constitutifs de tous les circuits électroniques et photoniques intégrés. En dépit d'une expansion substantielle des applications électroniques et photoniques vers les THz, la structure de base des lignes de transmission standard, mis au point dans les années 1950, n'a pas évolué. L'un des problèmes fondamentaux dans le développement de systèmes électroniques et photoniques intégré THz est les limites intrinsèques de ces lignes de transmission classiques. Les dispositifs à ondes progressives électro-optiques et optoélectroniques ont été conçus sur la base de ces lignes de transmission, et sont donc limités en débit en raison de la limitation des performances au spectre RF. Plusieurs tentatives ont été faites pour améliorer ces lignes de transmission. Cependant, la configuration structurelle inhérente du métal est toujours l'obstacle dominant qui impose un mode de fonctionnement particulier qui est sujette à l'atténuation et la dispersion à une fréquence plus élevée. Pour faire face aux problèmes mentionnés et pour répondre à ces défis technologiques contraignants, trois orientations sont traités dans cette thèse: électro-optique, micro-ondes et optique.

Pour la première orientation, la ligne SIW est utilisée en tant que structure à onde progressive alternative d'un Modulateur EO sur polymère. Dans ce cas, la fréquence porteuse est déterminée par la fréquence de fonctionnement de la ligne SIW. Dans ce travail, la conception est faite pour un modulateur EO atteignant plus de 22% de la bande passante optique avec la fréquence centrale de 160 GHz.

En ce qui concerne la deuxième orientation, une ligne de transmission entièrement intégré avec une topologie simple est réalisée pour surmonter les problèmes persistants de forte atténuation, forte dispersion et faible confinement de mode dans la transmission du signal guidé du DC au THz. En conséquence, le concept et la conception d'une ligne de transmission "intelligente" à faible perte

et à faible dispersion de propagation du signal sur toute gamme de fréquences DC - Térahertz (THz) sont introduites, et démontrés. La ligne que l'on appelle la ligne de transmission a mode sélectif ou simplement "MSTL" fonctionne avec un comportement de commutation de mode dépendamment de la fréquence; la conception est réalisée de telle sorte qu'avec la croissance de la fréquence, un phénomène de "conversion" mode a lieu et le mode de fonctionnement est automatiquement reconfiguré intentionnellement et sans aucune intervention extérieure afin d'assurer une faible perte et une faible dispersion. Une approche théorique combinée avec des simulations avec un logiciel (3D) à ondes complètes et des mesures expérimentales est utilisée pour vérifier le concept et la structure proposée. Comme l'une des applications fondamentales, des interconnexions, y compris via une ligne et un coude, sont étudiées et conçues. MSTL est fabriqué en deux plates-formes de substrat différentes (quartz et du PCB) et caractérisé de DC à 500 GHz. La caractérisation est effectuée dans les domaines spectral et temporel pour examiner et vérifier la propagation des impulsions d'une durée de picosecondes, des impulsions rectangulaires numériques à haute débit et aussi pour obtenir et analysé un diagramme de l'œil. La diaphonie des lignes placé côte à côté est également mesurée pour confirmer les performances pour les interconnexions à haute densité. Cette technologie a permis, pour la première fois, la transmission d'impulsions avec débit ultra-rapide le long des lignes de transmission avec une dispersion et des pertes beaucoup plus faible que les technologies actuelles. Une méthode uniformisée destinée à extraire le modèle circuit et à calculé l'impédance caractéristique d'une ligne de transmission ou d'un guide d'onde avec profile ou mode arbitraire a également été mise en place, cette technique peut être appliquée pour obtenir l'impédance caractéristique de la ligne MSTL sur toute la bande de fréquence d'intérêt.

Dans la dernière orientation, un guide d'onde optique à faible perte et un coupleur optique à réseau de diffraction à haute efficacité ont été conçus et optimisés. Le guide d'onde optique est conçu sur la base de baryum et de calcium niobate (CBN), qui est un nouveau matériau électro-optique à haute performance et qui est disponible en film mince ainsi que en vrac. Une analyse Trois dimensionnels (3D) a onde complète d'un coupleur à réseau de diffraction hors-plan est réalisé pour la première fois et le diagramme de rayonnement ainsi que les caractéristiques sont dérivées. La conception et l'optimisation des deux structures ont été validées par la fabrication et la caractérisation.

Enfin, le dernier chapitre présente les conclusions de la thèse et propose les potentiel futurs travaux dans le domaine de mmW / THz électronique et photonique

ABSTRACT

In order to keep up with rising global demand for bandwidth, future generations of both wireless and wireline technology will need to exploit the spectral range over 100 GHz - 1 terahertz (THz) and beyond. However, the integrated building blocks that will well define such an ultra-high frequency system technology architecture and protocol are unclear and mostly unavailable. This dissertation set the stage in responding to this emerging challenge by exploring new guided wave structures, concepts and techniques for the development of millimeter-wave (mmW) and THz electronic and photonic integrated circuits and systems.

Radiofrequency integrated circuits are the backbone of all modern computing and communication electronic and photonic networks and systems. Likewise, transmission lines are the most fundamental building blocks of all the electronic and photonics integrated circuits. In spite of a substantial expansion of electronic and photonic applications towards THz, the basic structure of traditional transmission lines, developed in the 1950s, has not been modified or evolved. One of the fundamental bottlenecks in the development of THz integrated electronic and photonic systems has been the inherent limitations of those conventional transmission lines. The traveling-wave electro-optic and opto-electronic devices have been made based on those transmission lines, and are therefore limited in speed because of the RF spectrum performance limitations. Several attempts have been made to improve those transmission lines. However, the inherent structural configuration is still the dominant obstacle that dictates a particular operating mode that is prone to attenuation and dispersion at higher frequencies. To tackle those mentioned problems and to respond to those constraining technological challenges, three research orientations are considered in this PhD thesis: electro-optic, microwave, and optics.

For the first orientation, SIW (substrate integrated waveguide) is used as an alternative traveling-wave structure of a polymer EO modulator. In this case, the carrier frequency is determined by the SIW frequency of operation. The design in this work is completed for an EO modulator with the center frequency of 160 GHz achieving more than 22% optical bandwidth.

With respect to the second orientation, a fully integrated transmission line with simple topology is realized to overcome the long-standing bottleneck problems of high attenuation, high dispersion, and low mode confinement in the guided signal transmission from DC to THz. Accordingly, the concept and design of a “smart” transmission line for low-loss and low-dispersion signal

propagation over the entire DC-to-THz frequency range is introduced and demonstrated. The so-called mode-selective transmission line or simply “MSTL” operates with frequency-dependent mode-switching behavior; the conception is accomplished in such a way that with increasing frequency, a “mode-conversion” phenomenon takes place and the operating mode is reconfigured intentionally and automatically without any external intervention to ensure a desired low-loss and low-dispersion performance. A theoretical approach together with full-wave three-dimensional simulations and experimental measurements is developed to verify the concept and the proposed structure. As one of the fundamental applications, MSTL interconnects, including lines and bends, are studied and designed. MSTL is fabricated in two different platforms of quartz substrate and PCB and characterized from DC to 500 GHz. The characterization is carried out in both frequency domain and time domain to examine and verify the propagation behaviors of picosecond pulses, high frequency digital rectangular pulses, and to obtain the eye-diagram. The crosstalk of the side-by-side placed lines is also measured to confirm the performance for high-density interconnects. This technology allows, for the first time, the transmission of fast pulses along the transmission lines with much lower dispersion and loss than the today’s technologies. A unified method for extracting the circuit model and calculating the characteristic impedance of arbitrary transmission line and waveguide in connection with any type of mode is also introduced, and may be applied to obtain the MSTL characteristic impedance over all frequencies of interest.

In the last orientation, low-loss optical waveguide and high-efficiency optical grating coupler have been designed and optimized. The optical waveguide is designed based on calcium barium niobate (CBN), which is a high performance novel electro-optic material and is available in thin-film as well as bulk form. Three-dimensional (3D) full-wave analysis of an out-of-plane grating coupler is achieved for the first time, and the radiation pattern and characteristics are derived. The design and optimizations of both structures have been validated through fabrication and characterization. Finally, the last chapter provides the conclusions of the thesis and outlines some of the future works planned in the field of mmW/THz electronics and photonics.

TABLE OF CONTENTS

DEDICATION III

ACKNOWLEDGEMENTS IV

RÉSUMÉ V

ABSTRACT VII

TABLE OF CONTENTS IX

LIST OF TABLES XIV

LIST OF FIGURES XV

LIST OF SYMBOLS AND ABBREVIATIONS XXIII

CHAPTER 1 INTRODUCTION 1

1.1 Overview 1

1.2 Motivation 3

1.2.1 Millimeter-wave photonics 5

1.2.2 Terahertz electronic 6

1.2.3 Objective 7

1.3 Methodology and contributions 7

1.3.1 Non-TEM mode electro-optical modulator for mmW and THz applications 7

1.3.2 Devising and demonstrating low-loss and low-dispersion transmission lines 9

1.3.3 Design and demonstration of the optical waveguide and modulator based on CBN 11

1.4 Thesis roadmap 13

CHAPTER 2 ARTICLE 1 : BAND-PASS NON-TEM MODE TRAVELING-WAVE ELECTRO-OPTICAL POLYMER MODULATOR FOR MILLIMETER-WAVE AND TERAHERTZ APPLICATION 15

2.1 Introduction 16

2.1.1 General 16

2.1.2 Polymer electro-optic material and modulator 18
2.1.3 Substrate integrated waveguide 19
2.1.4 Contribution of this work 20
2.2 Device structure 21
2.3 Theory 24
2.3.1 Millimeter-wave driving power 24
2.3.2 Modulation frequency response 26
2.4 Results and parametric discussion 29
2.5 Optimization 33
2.6 Conclusion 38
2.7 Appendix 39
2.8 References 40
CHAPTER 3 ARTICLE 2 : LOW-LOSS AND LOW-DISPERSION TRANSMISSION LINE OVER DC-TO-THZ SPECTRUM 46
3.1 Introduction 47
3.2 MSTL concept and design parameters 50
3.3 Fabrication and measurement 56
3.3.1 Fabrication 58
3.3.2 Device measurements 58
3.3.3 Time domain characterization 59
3.3.4 Results 59
3.4 Conclusion 61
3.5 References 61
CHAPTER 4 ARTICLE 3 : GUIDED-WAVE PROPERTIES OF MODE-SELECTIVE TRANSMISSION LINE 66

4.1 Introduction 68
4.1.1 General 68
4.1.2 Theoretical background 69
4.1.3 Contribution of this work 71
4.1.4 MSTL structure and operation principle 71
4.2 Theoretical description 73
4.2.1 Background 73
4.2.2 Mode coupling and mode conversion in MSTL 73
4.2.3 Discussion 75
4.3 Design considerations and MSTL simulation 76
4.4 MSTL waveguiding characterization 80
4.5 Modal analysis 80
4.5.1 Loss Derivation 81
4.5.2 Parametric Study 83
4.6 Experimental verifications 89
4.6.1 Fabrication 89
4.7 Measurements 90
4.8 Conclusions 94
4.9 References 95
CHAPTER 5 ARTICLE 4 : MODE-SELECTIVE TRANSMISSION LINE FOR TERABIT-PER-SECOND ON-CHIP INTERCONNECTS 100
5.1 Introduction 102
5.1.1 Design and optimization 105
5.2 Fabrication and measurement 108
5.3 Characterization 110

5.3.1 Attenuation 110
5.3.2 Dispersion 113
5.3.3 Signal reflection and ringing 114
5.3.4 Signal delay and distortion 115
5.3.5 Crosstalk 116
5.3.6 Conclusion 117
5.4 References 118
CHAPTER 6 ARTICLE 5 : S-PARAMETER DE-EMBEDDING ALGORITHM AND ITS APPLICATION TO SUBSTRATE INTEGRATED WAVEGUIDE LUMPED CIRCUIT MODEL EXTRACTION 122
6.1 Introduction 123
6.1.1 Circuit modeling 123
6.1.2 Numerical calibration 124
6.1.3 Contribution of this work 126
6.2 Description of method 127
6.3 Derivation of equations 129
6.4 Characteristic impedance calculation from de-embedded s-parameters 135
6.5 Results 137
6.5.1 Method validation 139
6.5.2 Application example: SIW 140
6.6 Conclusion 145
6.7 Appendix A 147
6.8 Appendix B 149
6.9 References 151

CHAPTER 7 ARTICLE 6 : THEORETICAL ANALYSIS AND EXPERIMENTAL EVALUATION OF SIO2-CBN-MGO RIB WAVEGUIDE STRUCTURE 154

7.1 Introduction 155

7.2 Design and simulation 157

7.3 Fabrication 160

7.4 Characterization and experimental evaluation 161

7.5 Conclusions 163

7.6 References 164

CHAPTER 8 ARTICLE 7 : ACCURATE THEORETICAL AND EXPERIMENTAL CHARACTERIZATION OF OPTICAL GRATING COUPLER 166

8.1 Introduction 167

8.2 Method of Analysis 169

8.3 Simulations and Calculations 172

8.4 Fabrication and Measurement 179

8.5 Conclusion 180

8.6 References 181

CHAPTER 9 GENERAL DISCUSSION 183

CHAPTER 10 CONCLUSIONS AND FUTURE WORK 186

10.1 Conclusions 186

10.2 Future work 187

BIBLIOGRAPHY 190

LIST OF TABLES

Table 2.1: Calculated driving power, driving voltage, and attenuation for 160 GHz SIW modulator with different height and length, r=30 pm/v 35

Table 2.2: Calculated driving power, driving voltage, and attenuation for 160 GHz SIW modulator with different height and length, r=90 pm/v 35

Table 2.3: Calculated bandwidth, maximum modulation efficiency, and FOM for different designs of 160 GHz SIW modulator 38

Table 2.4: Calculated bandwidth, maximum modulation efficiency, and FOM for different designs of 160 GHz SIW modulator 38

Table 4.1: Electric and Magnetic Field Distribution in the proposed MSTL on Fused Silica Substrate at Different Frequencies: Propagating Modes Change from TEM to TE_{10} Mode .81

Table 4.2: Electric and Magnetic Field Distribution in the Proposed MSTL made on Rogers Substrate for Different Frequency points: Propagating Modes Change from TEM Mode to TE_{10} Mode 88

Table 5.1: Electric and Magnetic Field Distribution in the Proposed MSTL made on Rogers Substrate at Different Frequency points: Propagating Mode Changes from TEM Mode to TE_{10} Mode.....107

Table 5.2: TL attenuation summary 111

Table 5.3: Rectangular Pulse (50 ps width, 1ps rise time) Propagation through Microstrip line and MSTL 113

Table 6.1: Comparison among numerical de-embedding techniques 125

Table 6.2: Comparison between wave ports and lumped ports.....128

Table 6.3: Circuit parameters for SIW circuit model.....144

LIST OF FIGURES

Figure 1.1: Schematic representation of electronic revolution and its driving technologies. 2

Figure 1.2: History of transmission line: with increasing edge speeds, wires have been replaced with TEM transmission lines.....3

Figure 1.3: Terahertz electronics and millimeter-wave photonics overlap and contribution of this thesis.....12

Figure 2.1: Schematic representation of polymeric substrate integrated waveguide (SIW) modulator. 22

Figure 2.2: Cross-sectional view of the first proposed device showing the push-pull operation in a polymer EO MZM. Black and gray arrows represent poling and modulation field directions, respectively.....22

Figure 2.3: Cross-sectional view of the second proposed device showing the push-pull operation in a polymer EO MZM. Black and gray arrows represent poling and modulation field directions, respectively.....22

Figure 2.4: a) SIW structure b) TE_{10} Electric field propagation along the waveguide c) TE_{10} Electric field distribution in the waveguide cross section. 23

Figure 2.5: Calculated attenuation as a function of frequency for polymer SIW modulator and polymer MSL modulator. SIW width $w_{eff}=20\ \mu m$, MSL width m, Height is changing 10 μm to 50 μm. The adopted approach for calculations has already been examined and validated for thick film SIW [44] and for MSL in [42].....30

Figure 2.6: Calculated millimeter-wave effective index as a function of frequency for polymer SIW modulator and polymer MSL modulator compared to the optical refractive index. SIW width "w" changes from 800 μm to 1000 μm. 30

Figure 2.7: MZI branch is optimized to achieve the highest output optical power.....31

Figure 2.8: Schematic of the buried rib waveguide and simulated mode shape using beam propagation method (BPM).....31

Figure 2.9: Calculated modulation index as a function of frequency for polymer SIW modulator; SIW width w_{eff} changes from 800 μm to 1200 μm, and height changes 10 μm to 50 μm. 32

Figure 2.10: Calculated effective driving power as a function of SIW height “h” for polymer SIW modulator. SIW width w_{eff} = 700 μm, f_c=160 GHz, L=10 mm. 32

Figure 2.11: Calculated maximum length as a function of frequency for polymer SIW modulator. SIW width w_{eff} = 800 μm, height H changes from 10 μm to 50 μm. 33

Figure 2.12: Calculated maximum length as a function of frequency for polymer SIW modulator. SIW width w_{eff} = 800 μm , height H changes from 10 μm to 50 μm. 34

Figure 2.13: Calculated effective driving power as a function of active length for polymer SIW modulator; SIW width w_{eff} = 800 μm, NLO coefficient r=90 pm/V, and Height is changing 10 μm to 50 μm.....34

Figure 2.14: Overlap integral improvement factor as a function of cladding permittivity for polymer SIW modulator. 37

Figure 3.1: A cross section view of mode-selective transmission line (MSTL). 51

Figure 3.2: Fields and current distributions in a typical MSTL. In frequency region I, MSTL works under a mode with characteristic similar to TEM mode. In region II, MSTL operates under a mode with characteristic similar to TE_{10} mode. 52

Figure 3.3: A schematic of MSTL and its principle of operation: the conductor configuration leads the structure to operate under the TEM mode in lower frequency range and changing gradually to TE_{10} mode in higher frequency range. 53

Figure 3.4: a) Effective dielectric constant of MSTL (h = 50 μm, d = 12h, s = 0.8h, w = 3h), and comparison with effective dielectric constant of microstrip line TEM (h = 50 μm, d >>h, s>>h, w = 3h), and rectangular waveguide TE_{10} mode (h = 50 μm, d = 12h, s = 0, w = d/2) on fused silica substrate (ε_r = 4.27). b) Group velocity of MSTL (h = 50 μm, d = 12h, s = 0.8h, w = 3h), and comparison with effective dielectric constant of microstrip line TEM (h = 50 μm, d>> h, s>> h, w = 3h), and rectangular waveguide TE_{10} mode (h = 50 μm, d = 12h, s = 0, w = d/2) on fused silica substrate (ε_r = 4.27). 54

Figure 3.5: Computed effective dielectric constant as a function of frequency: a) Slot width s as parameter, and ε_r = 4.27, h = 50 μm, d = 12h, w = 3h. b) Substrate thickness h as parameter, and ε_r = 4.27, h = 50 μm, d = 12h, s = 0.8h. c) Computed effective dielectric constant as a function of frequency, waveguide width d as parameter, and ε_r = 4.27, h = 50 μm, s = 0.8h, w

= 3*h*. d) Computed propagation loss as a function of frequency, waveguide width d as parameter, and ε_r = 4.27, *h* = 50 μm, *s* = 0.8*h*, *w* = 3*h*. 55

Figure 3.6: a) A fabricated sample line of MSTL on fused Silica substrate with a transition to picoprobe. b) A fabricated sample line of PCB prototype of MSTL with a transition to picoprobe. 57

Figure 3.7: Measurement setup. 57

Figure 3.8: a) Comparison of theoretical and experimental propagation phase constants (β) of MSTL fabricated on fused silica (*h* = 50 μm, *d* = 12*h*, *s* = 0.8*h*, *w* = 3*h*). b) Comparison of theoretical and experimental propagation loss characteristics of MSTL fabricated on fused silica (*h* = 50 μm, d = 12*h*, *s* = 0.8*h*, *w* = 3*h*) and thin-film microstrip line from [45]. c) Gaussian pulse (Ref: 1ps FWHM) propagation on PCB prototype pf MSTL line and bend as well as comparison with that of microstrip line- I: MSTL line (10mm long) from theoretical calculation, II: MSTL line from experimental results, III: MSTL bend from experimental results, IV: microstrip line (10mm long, the same substrate as that of MSTL, and 50 Ω characteristic impedance) from ADS MoM simulation. 60

Figure 4.1: A cross section view of mode-selective transmission line. 71

Figure 4.2: Intended modes in MSTL with the dominance of vertical electric field components: a) microstrip line mode, b) waveguide TE_{10} mode. 72

Figure 4.3: Equivalent transverse circuit network for MSTL in Fig. 1 with the reference plane in the middle of the slot s. 78

Figure 4.4: Propagation constant of guided-wave modes in MSTL using transverse resonance method and comparison with the results of FEM method and theoretical calculation [36]... 78

Figure 4.5: a) Fields and current distributions in MSTL designed on quartz (h=50μm, d=12h, w=3h, s=0.8h) from DC up to 0.5 THz range; f_{cutoff} =120GHz, f_{max}=500GHz. In region I of frequency range, MSTL works under a mode with characteristics very similar to that of TEM mode. In region II, MSTL operates with a mode with characteristics very similar to TE_{10} mode. b) Effective dielectric constant of MSTL on quartz (h=50μm, d=12h, w=3h, s=0.8h) and comparison with effective dielectric constant of microstrip line TEM mode and rectangular waveguide TE_{10} mode. c) Group velocity of MSTL on quartz (h=50μm, d=12h, w=3h, s=0.8h)

and comparison with group velocity of microstrip line TEM mode and rectangular waveguide TE_{10} mode. 79

Figure 4.6: Calculated mode coupling characteristics of MSTL 80

Figure 4.7: MSTL cross section with MOL discretization for hybrid-mode analysis. 82

Figure 4.8: Calculated different sources of loss using the MoL, including radiation loss using the HFSS package (MSTL with parameters ε_r=4.27, h=50μm, d=12h, w=3h, s=0.8h).....83

Figure 4.9: Comparison of calculated effective dielectric constant as a function of frequency using the MoL method and HFSS package; MSTL with geometrical parameters ε_r =4.27, h=50μm, d=10h, w=3h, s=0.8h.....83

Figure 4.10: Computed effective dielectric constant as a function of frequency: a) Strip width w as a parameter, and ε_r =4.27, h=50μm, d=12h, s=0.8h; b) Slot width s as parameter, and ε_r =4.27, h=50μm, d=12h, w=3h; and c) Substrate width d as a parameter, and ε_r =4.27, h=50μm, w=3h, s=0.8h. 84

Figure 4.11: Magnetic field and current distribution at 250GHz: a) MSTL, Magnetic field b) SIW, Magnetic field c) MSTL, Surface current d) SIW, Surface current.....85

Figure 4.12: Comparison of calculated propagation loss of MSTL and SIW as a function of frequency for different waveguide width d, ε_r =4.27, h=50μm, s=0.8h, w=3h.....86

Figure 4.13: MSTL guiding design curves in w/h-d/h plane showing the useful design region of interest. 87

Figure 4.14: Ey distribution (along the x-direction) for the fundamental propagating mode in MSTL (ε_r=4.27, h=50μm, d=12h, w=3h, s=0.8h).....87

Figure 4.15: a) Calculated effective dielectric constant as a function of frequency with substrate permittivity ε_r as a changing parameter, and h=50μm, d=12h, w=3h, s=0.8h; b) Computed loss as a function of frequency with substrate permittivity ε_r as a changing parameter, and h=50μm, d=12h, w=3h, s=0.8h.....90

Figure 4.16: a) Comparison of theoretical and experimental propagation phase constant (β) of MSTL prototype fabricated on RT/duroid® 6002 laminates from Rogers Corp. (h=127um, d=20h, s=1.6h, w=2.4h), b) Comparison of theoretical and experimental propagation loss

characteristics of MSTL prototype fabricated on RT/duroid® 6002 laminates from Rogers Corp. (h=127um, d=20h, s=1.6h, w=2.4h) and thin film microstrip line from ref [37].....91

Figure 4.17: a) Comparison of theoretical and experimental propagation phase constant (β) of MSTL prototype fabricated on quartz (h=50um, d=12h, s=0.8h, w=3h); b) Comparison of theoretical and experimental propagation loss characteristic of MSTL prototype fabricated on quartz (h=50um, d=12h, s=0.8h, w=3h) and thin film microstrip line from ref [39].....92

Figure 5.1: a) Mode-selective transmission line (MSTL) on a dielectric substrate. b) MSTL with TEM regime at lower frequency range (d>λg/2): electric and magnetic field distribution over the cross section and top view of magnetic field along the length of MSTL. c) MSTL with TE_{10} regime at higher frequency range (d<λg/2): electric and magnetic field distribution over the cross section and top view of magnetic field along the length of MSTL.....103

Figure 5.2: MSTL interconnect design curves (the mode-conversion frequency cutoff) for different values of substrate dielectric constants (ε_r =3, 4, 6, 9, 11).....104

Figure 5.3: Parametric study to optimize GVD over DC to 1 THz: thickness (h), strip width (w), slot width (s).....106

Figure 5.4: a) Fabricated MSTL line; b) Fabricated MSTL bend.....109

Figure 5.5: a) Comparison of theoretical and experimental propagation loss obtained from frequency domain characteristics of the MSTL prototype fabricated on RT/duroid® 6002 laminates from Rogers (h=127um, d=20h, s=1.6h, w=2.4h) and its corresponding microstrip line from ref [27]. b) Frequency domain characterization of MSTL 90° bend.....109

Figure 5.6: Comparison of signal overshoot vs rise time between microstrip line and MSTL. ..111

Figure 5.7: Gaussian pulse (Ref: 1ps FWHM) propagation on MSTL line and bend and comparison with microstrip line. I: MSTL line (10mm long) from theoretical calculation, II: MSTL line from experimental result, III: MSTL bend from experimental result, IV: microstrip line (10mm long, the same substrate as MSTL, and 50 ohm characteristic impedance) from ADS simulation.....112

Figure 5.8: a) Rectangular pulse (50 ps width, 1ps rise time) after propagating 10mm through microstrip line and MSTL. I: microstrip line—5 ps rise time and prepulse distortion, 20% overshoot, 18% backswing. II: MSTL, following the same rise time as the reference pulse,

6% overshoot, 8% backswing. b) Time domain characterization of RF/microwave signals: 2ps width, 0.1ps rise time via 1-cm-long MSTL, and comparison with the simulation of conventional 1-cm-long MTL. 112

Figure 5.9: Eye diagram fed from a pseudo random bit sequence NRZ signal source generator with a 100-Gb/s data rate and 0.5ps rise time: a) MSTL and b) Microstrip line. 114

Figure 5.10:.Fabricated circuit for crosstalk measurement. 116

Figure 5.11:.Crosstalk measurement between side by side MSTLs. 116

Figure 6.1: A schematic of computational electromagnetic (CEM) simulation involved with numerical calibration techniques. 127

Figure 6.2:. A transmission schematic representing a THRU simulation in a generalized calibration procedure. 128

Figure 6.3:. a) Network flow graph of a generalized TT calibration. b) Network flow graph of a THRU simulation in the proposed TT calibration. 130

Figure 6.4: Two-port network equivalence: a) Z-Network and b) Y-Network. 135

Figure 6.5: TEM/quasi-TEM mode transmission lines: a) CPW, b) Microstrip line; non-TEM mode transmission line, c) SIW, and d) fin-line. 137

Figure 6.6: Comparison of the calculated TEM transmission line characteristic impedance using the proposed TT numerical calibration technique, direct calculation from HFSS S-parameter, with experimental results from the literature: a) Amplitude or real part of Z0; b) phase of Z0 - I: CPW transmission line w=73 μm, s= 49 μm, wg= 250 μm on a fused silica substrate [23], II: Microstrip transmission line of 1.3 mil copper, w=0.1-in on an h=0.25-in alumina substrate [13], III: CPW transmission line of 0.5683 μm gold, w=71 μm, s= 49 μm, wg= 250 μm wide ground planes on an h=500 μm gallium-arsenide substrate [24], IV: CPW transmission line of 0.7 μm gold, w=73 μm, s= 49 μm, wg= 350 μm wide ground planes on a 500 μm gallium-arsenide substrate [25], V, VI: Microstrip transmission line of 1.3 mil copper, w=0.25-in, 0.5-in on an h=0.25-in alumina substrate [13].....138

Figure 6.7: Comparison of the calculated non-TEM transmission line propagation characteristics using the proposed TT numerical calibration technique with direct calculation from HFSS S-

parameter, and experimental and numerical results from the literature a) fin-line w=18mil, h=10mil in WR28, b) SIW a=4.8 mm on a h=1.5mm 2.2 permittivity substrate. 139

Figure 6.8: The distributed equivalent-circuit model (all elements are defined per length). 140

Figure 6.9: Calculated SIW characteristic of the first three modes (substrate ε_r=2.33 and 0.254 mm thickness, width=0.711 mm) using the proposed TT method: a) characteristic impedance, b) effective dielectric constant. 141

Figure 6.10: Calculated characteristic impedance for SIW of Fig. 5(c) (substrate ε_r=2.33, a = 6.096 mm) for different substrate thicknesses using the proposed TT method including and excluding loss in the calculations a) real part of characteristic impedance b) imaginary part of characteristic impedance, c) The phase constant, d) attenuation constant 142

Figure 6.11: Calculated SIW interconnect parameter (substrate ε_r=2.33, width = 6.096 mm) for different substrate thicknesses using the proposed TT method including and excluding loss in the calculations a) L (mH.s^{-1}/m) b) R (Ω) b) C (mF.s^{-1}/m) d) G (S) 143

Figure 6.12: A schematic of two types of ports and their principles of operation a) lumped port and b) wave port. 146

Figure 6.13: Wave port de-embedding in Ansoft HFSS. 147

Figure 6.14: Basic definitions of different impedance in a transmission line: a) input Impedance b) characteristic Impedance 149

Figure 7.1: Cross-sectional view of CBN rib waveguide 157

Figure 7.2: Cross section of a rib waveguide 157

Figure 7.3: Simulated critical W/H ratio as function of the CBN thin film thickness H for various values of r at λ = 1.55 μm in an SiO2-CBN-MgO rib waveguide structure. 159

Figure 7.4: SEM image of a 10% etched 2um epitaxial CBN thin film with 1μm SiO2 deposited by PECVD. 161

Figure 7.5: Characterization setup with lensed fiber input (~2um spot size and ~50um working distance), 10x objective output (5.6mm working distance). 161

Figure 7.6: Simulated (in color) and experimentally (in grey) measured mode profiles of SiO2-CBN-MgO rib waveguide structure with 2 μm CBN thickness, etch depth ~10% of CBN thickness and various rib widths. 163

Figure 8.1: Complete three-dimensional model of the SOI grating-waveguide device is considered in this paper in both simulation and fabrication. In the simulation, half of the structure with shorter taper and waveguide length is simulated. 173

Figure 8.2: 3D Simulated structure. Half of the device is simulated using the wave port excitation of the waveguide and the radiated beam is monitored. 174

Figure 8.3**:** The simulated radiation pattern of the proposed SOI grating coupler optimized to work at 1550nm wavelength for the different grating periods. SOI wafer (260nm silicon layer and 2μm buried oxide), waveguide width 500nm, grating width 12.5μm, etching depth 70nm, and taper length 650μm. Coupling angle is changed with the grating period.....175

Figure 8.4**:** Simulated efficiency versus incident angles for the proposed SOI grating coupler at 1550nm wavelength for the different grating period. SOI wafer (260nm silicon layer and 2μm buried oxide), waveguide width 500nm, grating width 12.5μm, taper length 650μm, and etching depth 70nm. 176

Figure 8.5**:** Simulated efficiency versus incident angle for the proposed SOI grating coupler at 1550nm wavelength for different grating etching depth. SOI wafer (260nm silicon layer and 2 μm buried oxide), waveguide width 500nm, grating width 12.5μm, taper length 650μm. a) grating period = 580nm, b) grating period = 600nm. 177

Figure 8.6**:** Simulated efficiency versus incident angle for the proposed SOI grating coupler for different wavelengths. SOI wafer (260nm silicon layer and 2 μm buried oxide), waveguide width 500nm, grating width 12.5 μm, taper length 650 μm, grating period 580nm, etching depth 70nm. 178

Figure 8.7: AFM scan of a grating coupler. 178

Figure 8.8**:** Measured efficiency of SOI grating coupler (260nm silicon layer and 2 μm buried oxide, 580nm grating period and 70nm etching depth) at 1550nm wavelength and comparison with the simulation 179

Figure 10.1: A schematic of the proposed MSTL photoconductive switch. 188

LIST OF SYMBOLS AND ABBREVIATIONS

2D	Two-Dimensional
3D	Three-Dimensional
5G	Fifth Generation
ADI	Alternating Direction Implicit
BW	Bandwidth
BPM	Beam Propagation Method
CBN	Calcium Barium Niobate
CEM	Computational Electromagnetic
CPW	Coplanar Waveguide
DUT	Device-Under-Test
EM	Electromagnetic
EBL	Electron-Beam Lithography
EO	Electro-Optical
FEM	Finite Element Method
FIT	Finite Integration Technique
FWHM	Full Width at Half Maximum
GSG	Ground-Signal-Ground
ICP	Inductively Coupled Plasma –
ICT	Information and Communications Technology
I/O	Input/Output
IC	Integrated Circuit
MZI	Mach-Zehnder Interferometer
MoL	Method of Lines

MoM	Method of Moments
MSL	Microstrip Line
mmW	Millimeter-Wave
MSTL	Mode-Selective Transmission Line
NC	Numerical Calibration
OE	Opto-Electronic
OE	Optoelectronics
PMPW	Parallel Metal Plate Waveguide
PCB	Printed Circuit Board
RF	Radiofrequency
RW	Rectangular Waveguide
RIE	Reactive Ion Etching
SOC	Short-Open Calibration
SOI	Silicon-on-Insulator
SUS	Structure-Under-Simulation
SIC	Substrate Integrated Circuit
SIW	Substrate Integrated Waveguide
SoC	System-on-a-Chip
SoP	System-on-a-Package
THz	Terahertz
TTB	Tetragonal Tungsten Bronze
TRL	Thru-Reflect-Line
TE/TM	Transverse Electric/Magnetic
TEM	Transverse Electromagnetic

TR	Transverse Resonance
ULSI	Ultra Large-Scale Integration
VNA	Vector Network Analyzer
VLSI	Very Large Scale Integration

CHAPTER 1 INTRODUCTION

1.1 Overview

Two well-established key technologies, namely semiconductor materials and integrated circuit design, have inspired the electronics revolution in the 20th century and beyond (Figure 1.1). Utilizing semiconductor material, the transistor was invented at Bell Telephone Laboratories in 1948 in the context of a long distance communication [1]. After developing the first integrated transistor, Jack Kilby's idea of the integrated circuit (IC) was born and the first working IC was demonstrated in 1958 [2]. From then on, applications of electronics have expanded dramatically thanks to a possible mass manufacturing of low-cost integrated circuits. Integrated circuits are used in almost all electronic equipment today. Computers, cell phones, smartphones, and other similar devices that are now inseparable parts of the structure of modern societies have been made possible through the development of low cost ICs.

With ever-increasing demands for global communication systems, the field of photonics came into a common use in the 1980s. Playing a complementary role to electronics, the applications of photonics have continued to emerge alongside. Thereupon, the revolutionary transition from old-fashioned teletype machines to the personal computer, computer networking, cell phones, and the World Wide Web all happened in less than four decades. All these technologies have been focused on communicating information at ever-increasing speeds, which are expected to continue to get improved and accelerated [3].

Recently, IEEE committees have declared that the bandwidth demand is growing faster than the current capacity to deliver it [4]. More than 44% of the world's population is estimated to be online at this time and this percentage will grow up [5]. More users and more devices generate more bandwidth demand. In addition, terahertz (THz) and millimeter-wave (mmW) bands have attracted huge interest in recent years, from both the research and industrial communities, due to their wide and unique applications in many areas, such as security, scientific imaging, radars, space communications, medical diagnosis, and wireless systems [6]–[8]. THz applications in the information and communications technology (ICT) sector hold plenty of potentials to enhance the speed and capacity of communication and sensing networks. Currently, this fundamental and urgent need depends on how far innovative ICT devices are developed over such bands [9].

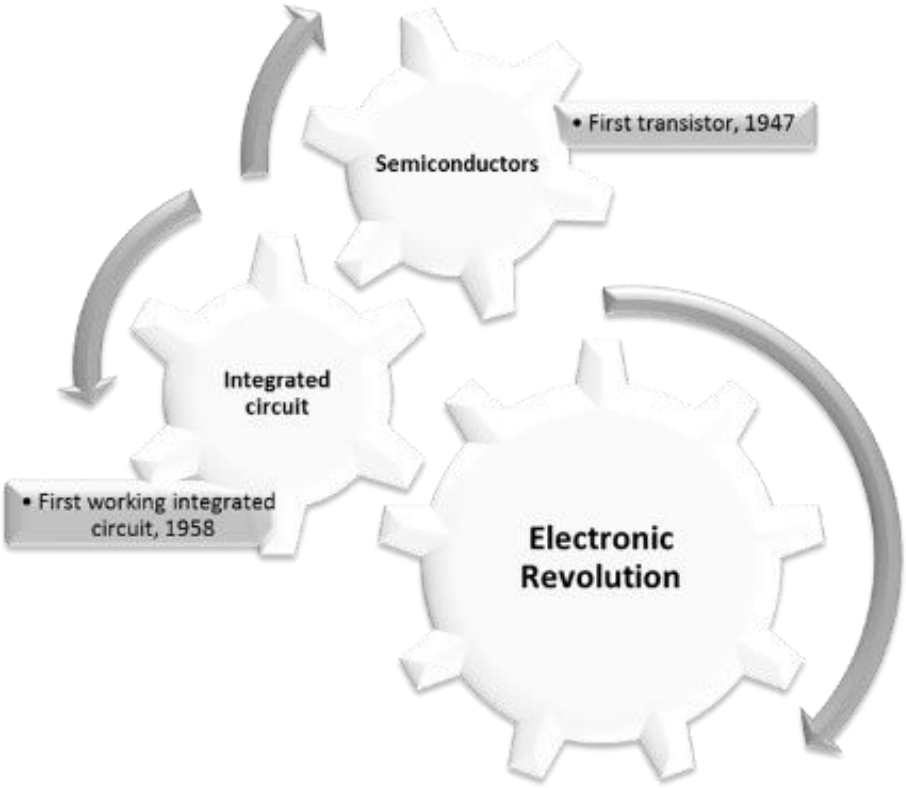

Figure 1.1: Schematic representation of electronic revolution and its driving technologies.

There is a strong virtuous circle encompassing advanced computing tools and better quality networking and information, subject to transmission speed or electrical signal frequency. As frequency increases, signals can carry more information resulting in improved computation speed and communication bandwidth. Nevertheless, there are some crucial bottlenecks, thereby restricting the development of both computing and telecommunication systems toward higher frequency as signal propagation and switching speeds in the electronic domain are inherently limited. Drawing an analogy to the electronic revolution and its fundamental elements, it is perceived that the first key to the success of electronic-photonic technology was the progress achieved in finding and fabricating high-performance and cost-effective optical and electro-optical materials. However, low cost and high performance design of THz and mmW integrated circuits is still a critical challenge.

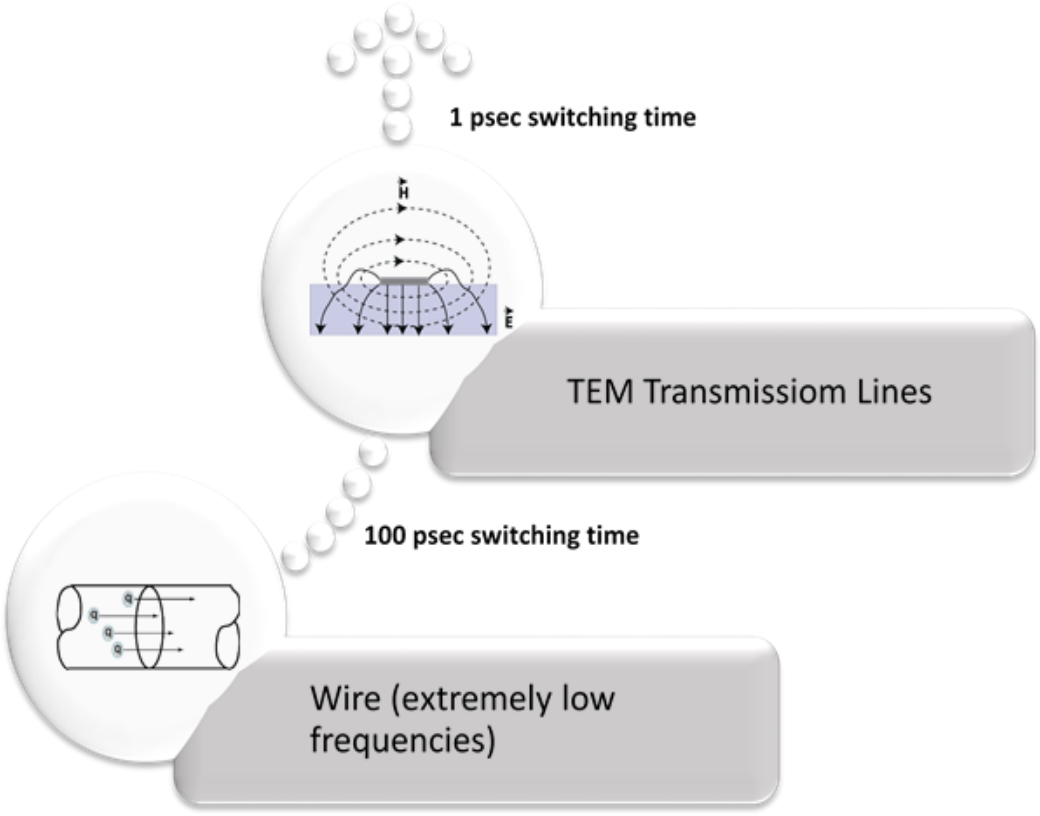

Figure 1.2: History of transmission line: with increasing edge speeds, wires have been replaced with TEM transmission lines.

1.2 Motivation

In 2010, the booming volume of data transmitted around the globe rendered the standardization of the 100 Gb/s Ethernet and 100G optical transport network, and still now higher rate interfaces are pushing research and industry toward exploring 400G as well as Terabit Ethernet [10]. On the other hand, increasing data rate in wireless communications pushes the transformation of radiofrequency (RF) technology toward a high mmW and THz frequency region as the fifth generation (5G) wireless communications technology is just on the horizon.

With rise and fall times around 100 psec, wire interconnects were transformed to transmission lines [11]. Integrated transmission lines in the form of microstrip line, coplanar waveguide (CPW), and their derivatives have been the backbone of modern electronic and photonic integrated circuits and systems. Following the evolution of IC technologies and processing techniques in the field, those fundamental structures have been continuously studied and improved to meet the constantly

updated bandwidth and capability requirements. The planar transmission lines are the foundation of any high frequency ICs such as RFICs and MMICs, whose performance factors and cost indices are first limited by the transmission line building elements. Countless electromagnetic applications from DC to THz [9], and also growing needs for faster data communication rates have raised the question of whether traditional transmission lines can satisfy the demand of sophisticated applications for high performance [12]–[14] (Figure 1.2). Currently, the increase in bandwidth related to ultra-high-speed wireline digital computing systems, such as memory chips, CPUs, GPUs, backplanes, and wired LANs, are enabled by increasing the number of input/output (I/O) channel interconnects on chips [15]. To keep up with bandwidth demand and to avoid prohibitive cost and complexity, fast time-domain pulse signals would require the bus lines or interconnects design to support low-loss and low-dispersion signal transmission from DC to the mmW spectrum, and even up to THz bands if pico-pulsed signals are used. On the other hand, in wireless applications, although radio-over-fiber techniques are applied and high-density modulation schemes are used, available radiofrequency bandwidth is still relatively low [15]. In this case, the challenges are in pushing the use of radiofrequency signals toward the frequency range of mmW and higher [16], necessitating the development of ultra-high-speed electro-optical devices such as modulators and photodetectors, for which high performance DC-to-mmW/THz “electronic” transmission lines and interconnects are needed for integrated “electrodes” [17], [18].

With regard to the explosive Moore’s law and beyond [19] and the increasing trend in test cost for each new generation of chip manufacturing, new concept devices and circuits should be introduced to translate the recent achievements in finding and fabricating new high performance materials [20] and to enable the next generation of mmW and THz photonics applications in computing and telecommunications. Efforts have been made to evolve and improve the existing transmission line structures through the modification of current waveguiding structures, but the ultimate scientific and technological challenge necessitates the emergence of a revolutionary or disruptive concept in doing so. It is of great importance for us to establish a robust transmission line structure that enables the development of all-frequency integrated circuits from DC to THz, based on a single design and development platform.

1.2.1 Millimeter-wave photonics

In the late 1970s, experiments were initiated in order to take advantages of photonic technologies in microwave systems to accomplish the tasks that were deemed very complex or even impossible to perform entirely in the RF domain. Following that thread, the field of microwave photonics has been built up as an interdisciplinary field connecting radiofrequency (RF) and optoelectronics engineering worlds, and expanded in a way that microwave engineering techniques are also used to improve the performance of photonic communication networks and systems [21], [22].

Implementing mmW radio in backhaul networks and taking the desired advantages of THz-band wireless systems have encouraged the development of high performance mmW and THz photonic links. Wireless expansion of the next generation broadband access fiber optic networks, Gigabit Ethernet, and multigigabit communication systems is very promising and attractive in the form of a radio-over-fiber approach, enabling the easy transmission and delivery of mmW and THz signals over a long distance via low-loss optical fibers. However, their performance in terms of speed and capacity is closely linked to that of the devices on which they are based, as they should be supported by ultra-broadband devices and circuits on both the electronic and photonic sides.

To date, conventional available microwave structures are associated with advanced modulation schemes and signal-processing technologies to accommodate the required bandwidth, but available bandwidth is still relatively narrow in wireless applications. The fact is that the rate at which microwave integrated circuits have been improved has been unparalleled in the current countless applications of mmW and THz, and the key to accelerating the use of microwave photonics techniques in up-to-date real world systems is to improve the RF performance of microwave photonics devices. In other words, a particular challenge in this connection is to improve the RF spectral region of operation in these devices and to push the use of RF signals toward the frequency range of mmW and higher, while at the same time reducing cost [21]. High performance transmission lines are essential for improving microwave photonic applications, since traveling-wave-based structures are the key elements of guided-wave electro-optical and optoelectronic devices and circuits [20], [21]. As conventional TEM-mode structures are applied as the driving traveling-wave structure in EO devices, they suffer from extremely high loss at higher frequencies, and pose a limitation on high frequency performance. In addition, millimeter-wave and THz modulators with conventional TEM-mode electrodes introduce a great challenge in the packaging

of the modulator structures, which has also limited the use of those structures over such a frequency range. This is because of their unbounded signal transmission. Similarly, the most common method for producing THz bandwidth electrical signals in integrated circuits and devices is through optoelectronics. However, current conventional transmission lines fail to accommodate the picosecond electrical pulses generated by OE switches, and these pulses with several hundred gigahertz bandwidth fade and disperse within a few millimeters of propagation [23]. Moreover, in optical network communications, global RF interconnects are used ubiquitously in almost all chip-to-chip and module-to-module interfaces.

1.2.2 Terahertz electronic

Realizing THz electronics or establishing compact, high-performance electronic circuits that operate at THz frequencies, necessitates the conception and development of electrical and electronic devices as well as integration technologies that can operate at frequencies above 1 THz. Currently, limitations in transistor performance have been addressed to a great extent, making it possible to drive solid-state electronics directly at these frequencies. Whereas the first high-frequency transistor, developed in 1953, was capable of operating up to 60 MHz, with the advances in transistor technology, f_{max} above 1 THz has already been demonstrated [24], [25] and a single device switching time has been reduced to 2 picoseconds or less [26]. By increasing the transistor speed, on-chip interconnects, although keeping the same structure, become even denser. In 1995, Intel declared, “on-chip interconnect scaling has become the real limiter of high-performance integrated circuits” [27]. In 1992, personal computers were equipped with Intel 486, clocking 66 MHz; CPU clock speed increased and soon passed 500 MHz, and continued upward. However, in 2005, the top speed of the high-end processors resided around 4 GHz and since then, improving the speed has been accomplished through applying multi-core processors. The well-known bottlenecks related to high-speed digital and/or broadband analog signal interconnects, for example, have been the primary limitations to various integrated circuits and systems with respect to their loss- and dispersion-limited performance. This creates a strong motivation to search for super wideband transmission lines and make related discoveries and innovations [9], [12]–[14]. On-chip interconnects in such a high frequency are increasingly becoming the major bottlenecks and greater performance limiters of system-on-a-chip (SoC) and system-on-a-package (SoP) than transistors [29]–[31]. Ultrahigh-speed pulse transmission (covering the DC-THz range) requires

transmission lines with low dispersion and low loss, which can be readily integrated into optoelectronic circuits and other devices [32].

1.2.3 Objective

The overall objective of this thesis is to establish a new platform in integrated electronic and photonic circuits and systems to bridge the gap between electronics and photonics. From this overall goal, three detailed objectives are identified as follows:

1)To propose novel EO and opto-electronic (OE) devices based on non-TEM mode integrated transmission lines for mmW and THz applications as well as the design and full study of an SIW EO modulator as an example;

2)To design, devise and demonstrate a low-loss low-dispersion transmission line for DC to THz frequency spectrum, and to demonstrate an interconnect prototype for THz electronic applications; and

3)To design and demonstrate optical waveguides and optical grating couplers based on novel high-performance EO material applicable to mmW and THz.

In the long term, this work is intended to establish a groundwork for the interdisciplinary field of terahertz electronics and photonics and a breakthrough offering the promise of greater computation speed and communication bandwidth (Figure 1.3).

1.3 Methodology and contributions

1.3.1 Non-TEM mode electro-optical modulator for mmW and THz applications

A fundamental challenge in optical telecommunication is to modulate mmW or THz bandwidth, or simply carrier signals, onto an optical wave carrier in phase and/or amplitude, depending on broadband communication services. This is usually accomplished with an external EO modulator, varying either the intensity or the phase of a light emitted by a laser diode. EO modulators are utilised in a variety of ways. At millimetric scale, they can be employed to adapt an optical channel to carry information such as telephone calls and digital data for network transmissions. At micrometric scale, they can be used to interconnect chip microprocessors in multi-core systems. In

either case, these devices modulate a light beam carrier through an RF modulating signal, inserting data to be sent to the receiver side. A high-frequency EO modulator is critical in enabling signal processing and distribution in next generation cloud computing, telemedicine, and telecommunications.

To achieve this, a great deal of research has been conducted on molecular engineering of electro-optically active materials and cladding material properties to improve overall device performances. Novel organic EO materials enhance the EO modulator response to the point that high bandwidth polymer modulator designed for the 100G optical communications channel is now commercially available [33]. Thanks to an excellent velocity match between the modulating signal and lightwave in polymers, this device must be able to operate within an ultra-broad bandwidth. However, in the conventional device structure of EO modulators, the driving power is applied through the microstrip line, which plays the role of metal electrodes. This kind of transmission line is significantly lossy for high-frequency operations.

The modulator structure can be modified so that the electrical driving power is controlled by an appropriate transmission line, which is applicable in high frequency operation. The purpose of this work is to design, develop, and realize a novel EO modulator structure based on substrate integrated circuit (SIC) technology. In this project, substrate integrated waveguide (SIW) is exploited as an alternative fundamental transmission line structure in support of electrical signal for the design and development of mmW and THz traveling-wave polymeric EO modulators. Supporting theoretical development and modeling results are established to validate the concept. The proposed theoretical model for traveling-wave operation together with optical simulation provides an efficient approach that will specify the values of various parameters in order to obtain the optimized EO modulator design. This technology may lead to a whole new generation of ultra-high-speed EO modulators with more than 100 GHz modulation speed. Such SIW-based EO modulators may play important roles in enabling RF photonics and next generation higher-bit-rate optical fiber communication systems [17].

1.3.2 Devising and demonstrating low-loss and low-dispersion transmission lines

Transmission lines are the building blocks of all electronic and photonic integrated circuits and systems. In spite of a substantial expansion of electronic and photonic applications toward THz, the basic structure of traditional transmission lines, developed in the 1950s, has yet to be modified. One of the fundamental bottlenecks in the development of THz integrated electronic and photonic systems has been the intrinsic limitations of those conventional transmission lines. Incremental efforts have been made to evolve and improve existing transmission line structures to meet the increasingly stringent demands for signal transmission bandwidth and performance. However, the inherent structural metal configuration is still the dominant obstacle dictating a particular operating mode that is prone to attenuation and dispersion at higher frequencies. A potentially revolutionary scheme or disruptive concept is required in support of future technological needs and bridging the gap between electronics and photonics.

There are two categories of waveguiding structure, namely, the transverse electromagnetic (TEM)-mode type, such as microstrip lines, and transverse electric/magnetic (TE/TM)-mode type such as SIW. TEM structures support the transmission of signal from zero frequency (DC), but they experience increasing signal attenuation and dispersion at mmW and THz frequencies. The current transmission lines used in electronic integrated circuits operate under the fundamental TEM mode. They suffer from inherent drawbacks such as strong signal attenuation and pronounced modal dispersion at room temperature, and they cannot be useful over a broad frequency range from DC to THz or ultra-high-speed pulse transmission. TE/TM structures, on the other hand, support the transmission of those high frequency signals but cannot cover DC and low frequency signals, and they are dispersive because of cut-off frequency.

In this work, a class of transformative transmission lines and waveguides are devised and demonstrated. The so-called “mode-selective transmission line” or simply MSTL, supports a dominant mode very similar to the microstrip line scenario in lower frequency range covering DC, while it is automatically reconfigured to support the fundamental mode of rectangular waveguide at higher frequency [34], [35]. This “smart” transmission line, effectively covering the desired operation from DC to THz frequency range, is suitable for full DC-THz electromagnetic propagation and ultra-high-speed THz pulsed signal transmission. It can be made to support a

single-mode transmission over a super-wide range of frequency. This MSTL, in a fully integrated form, exhibits a disparate modal characteristic of traditional planar microwave transmission lines and non-planar metallic waveguides. Whereas at low frequency MSTL operates under the TEM regime, the operating mode is gradually converted to low-loss TE_{10} mode for operation at high frequencies, such as millimeter-wave and THz. This approach allows for the possibility of developing densely integrated interconnects and planar guided wave structures for DC-THz bandwidth [28], [29].

During the course of this PhD project, a unified method will also be introduced and formulated for deriving the equivalent circuit model of a two-port network and the characteristic impedance of a transmission line or waveguide for any mode [40]. This method is devised through the combination of a multimode calibration and a commercial numerical simulator. It is based on a generalized calibration technique, which is applicable to the case of TEM mode as well as non-TEM and higher-order propagating modes. The method is simple and straightforward, without any complication in the calculations or limitation in the operating frequency.

1.3.2.1 **Application in mmW/THz photonics**

MSTL can be exploited as an alternative fundamental transmission line structure in support of RF electrical signal for the design and development of mmW and THz photonics devices. Two central applications are in an optoelectronic photoconductive switch for THz pulse generation and an electro-optic Mach-Zehnder modulator.

Photoconductive switching has been the most common method for producing THz bandwidth electrical signals in transmission lines throughout integrated circuits and devices. Ultrafast electrical pulses (DC-THz range) require transmission lines with low dispersion and loss, which can be readily interconnected to optoelectronic and other devices. A major problem in transmission lines for ultrafast electrical pulses is dispersion, since it causes pulse broadening and loss of speed [23]. Several theoretical analyses of this dispersive broadening of pulses on microstrip line and coplanar waveguide show that a strong dispersion exists in these transmission lines, especially when the pulse rise time is short (*e.g.*, tens of picoseconds). To solve this problem, conventional transmission lines are replaced with MSTL to insure low-loss and low-dispersion THz bandwidth pulse propagation. On the other hand, for EO modulator, finding an appropriate scheme for applying mmW/THz waves to the lightwave channel has been a particular problematic issue. To

address this problem, applying MSTL serves as the traveling wave structure, providing low loss and low dispersion characteristics. This work proposes using organic nonlinear EO polymer material, due to its intrinsic material bandwidths, high EO coefficients, easy processability, and integrability with semiconductor VLSI electronics and silica fiber optics, and potential for low cost. In this structure, the velocity mismatch is minimized and can easily be controlled. Therefore, in wireless communications, carrier frequency will increase to the point that bandwidth is wide enough to achieve a large data capacity even with a simple modulation technique. Furthermore, this EO modulator is a key element for improving the performance of opto-electronic oscillators. Such THz photonic integrated circuits would help to close the THz technology gap between microwave electronics and infrared photonics. This research would result in the development of next generation high-frequency performance-demanding mmW/THz photonic integrated circuits and systems.

1.3.2.2 **Application in THz electronics and on-chip interconnect**

MSTL allows for the possibility of developing densely integrated interconnects and planar guided-wave structures for DC-THz bandwidth applications. To increase bandwidth related to ultra-high-speed wireline digital domains or computing systems, each set of existing input/output (I/O) channels would be replaced by a single ultra-wideband MSTL interconnect. This low-loss, low-dispersion broadband integrated transmission line is a key enabling disruptive technology towards the development of the next generation of DC-to-THz integrated electronic circuits and systems. Additionally, this concept points out a self-packaging solution that is necessarily required for THz and mmW integrated circuits, as it is anticipated that unavoidable dielectric loss and insufficient patterning accuracy may limit the use of current packaging techniques for mmW and THz-wave applications.

1.3.3 **Design and demonstration of the optical waveguide and modulator based on CBN**

Calcium barium niobate (CBN) is a new EO material in the form of thin films [41], [42]. These films exhibit a high Curie temperature (>50 °C) that ensures thermal stability. It was also shown that the CBN film EO coefficient (r_{33} as high as 130 pm/V) is more than 4 times higher than that of $LiNbO_3$ [42], which enables a significant reduction of $V\pi$. This film has also the potential of

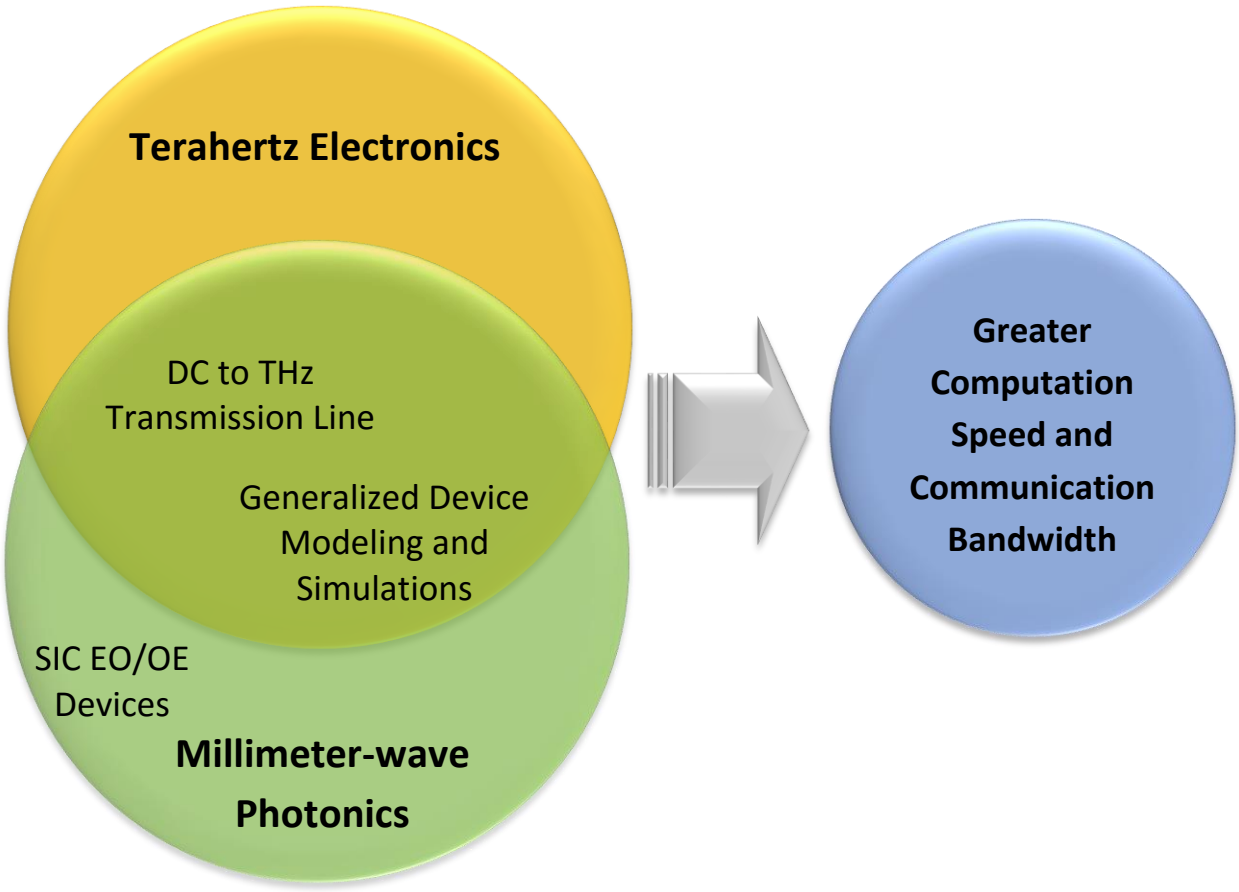

Figure 1.3: Terahertz electronics and millimeter-wave photonics overlap and contribution of this thesis.

being integrated in a silicon platform. The deposition, structural characterization, and fabrication of this material stack can be found in [44]–[46].

Although the operation of waveguide devices is well studied and understood, their particular performance relies on many parameters, such as geometry, wavelength, initial field distribution, material data, and electro-optic driving conditions. These parameters must be optimized before fabricating a device. In this work, a CBN-based low-loss optical waveguide is designed and demonstrated as the first step to realizing a CBN-based EO modulator [46]. The optical design of a static CBN electro-optic is also prepared. Simulation parameters are based on the corresponding achievements in the fabrication process of growing and etching CBN, which is a completely novel unexplored electro-optic material. Simulations are carried out based on Beam Propagation Method

(BPM), applying commercially available software. BPM is a systematic method for simulating the passage of light through a waveguide medium in which the optical field can be tracked at any point as it propagates along the guiding structure. BPM is based on a numerical solution for an approximation of the Helmholtz equation, which governs light propagation in dielectric media. Refractive index distribution and starting propagation field (i.e., a waveguide mode in our case) are required for three-dimensional (3D) modeling. 3D BPM simulator is based on Alternating Direction Implicit (ADI) mode solver, in which the semi-vector algorithm provides a choice between quasi-TE and quasi-TM polarization.

Since end-fire coupling presents some difficulties in characterizing the CBN optical waveguide, a new approach for the design of an out-of-plane grating coupler is also established during the course of this PhD project [47]. A three-dimensional simulation of the grating coupler is performed for the first time, which enables a rigorous investigation of this periodic structure. Using the vector formulation of the Maxwell's electromagnetic equations with a commercial software package in the context of a full-wave finite-element method, the power distribution diffracted by a grating (radiation pattern) is resolved and the grating efficiency is examined. A parametric study is performed to determine the dependence of the wave leakage on structural geometry, operating wavelength, and polarization as well as incident angle of the light. In addition, since the complex propagation constant ($\gamma=\alpha+j\beta$) cannot be obtained directly from the simulation, we have determined it through a numerical calibration method. A grating design involving Silicon-on-Insulator (SOI) wafer is optimized. Test structures with grating couplers and tapered strip waveguides are fabricated using a two-step electron-beam lithography and high-density plasma etching processes, and characterized showing an excellent agreement among theory, simulation, and experiment, fully validating the design method.

1.4 Thesis roadmap

This thesis is organized as follows:

Chapter 2: The concept of SIC EO modulator is introduced and SIW EO modulator is studied in detail [17], [18].

Chapter 3: The concept of MSTL is introduced and its principle of operation is discussed. The device is fabricated and characterized in both time and frequency domains [34], [36].

Chapter 4: Complete theoretical study is performed on MSTL and guided-wave properties are derived. A detailed semi-analytical hybrid-mode analysis is developed through the application of method of lines (MOL) and propagation characteristics in terms of dispersion, modal, and loss properties are examined, which leads to the establishment of some basic MSTL design guidelines and also an optimization approach [35], [37].

Chapter 5: MSTL is exploited as an alternative approach to accommodating the growing requirements of ultra-large-scale integration (ULSI) for density, performance, and bandwidth. A detailed parametric study is performed to optimize the MSTL structure for high-speed global interconnects and high-performance signal integrity [38], [39].

Chapter 6: A unified method is introduced and formulated for deriving the equivalent circuit model of a 2-port network and the characteristic impedance of a transmission line or waveguide for any mode. The method is verified for both TEM and non-TEM propagating mode and is applied to extract the characteristic impedance and circuit model of non-TEM guided wave structures [40].

Chapter 7: An electro-optical SiO_2-CBN-MgO rib waveguide structure is designed. The simulation, optimizations, and optical characterizations are included [46]–[48].

Chapter 8: A three-dimensional simulation of grating coupler is conducted, guided wave and leakage characteristics of an out-of-plane grating coupler are studied in detail, and the coupling efficiency is derived. The simulations are verified through characterization [49], [50].

Chapter 9: Details on the general discussion are given.

Chapter 10: Conclusions and future work are discussed.

CHAPTER 2 ARTICLE 1 : BAND-PASS NON-TEM MODE TRAVELING-WAVE ELECTRO-OPTICAL POLYMER MODULATOR FOR MILLIMETER-WAVE AND TERAHERTZ APPLICATION

Overview: electro-optic modulator is one of the key components in optical communication systems. In an optical transmitter, the first step after light generation through a semiconductor light source is modulating the light to carry information. Because direct modulation of semiconductor lasers leads to frequency chirp, external modulation is used and Mach-Zehnder modulator is the most common one. To transform microwave photonics to mmW/THz photonics effectively, developing mmW/THz electro-optic modulator plays a critical role. Nonlinear organic optical material has the fastest electro-optic response rate and can be used in mmW/THz. This work presents an electro-optic polymer modulator in which the traveling-wave structure is substrate integrated waveguide (SIW). The operating frequency or data rate of such EO modulator is determined by the operating frequency of the utilized SIW structure.

(Journal of Lightwave Technology, publication date: December 2012)

Band-Pass Non-TEM Mode Traveling-Wave Electro-Optical Polymer Modulator for Millimeter-Wave and Terahertz Application

Faezeh Fesharaki[1] and Ke Wu[1]

[1]Poly-Grames Research Center, École Polytechnique de Montréal, QC H3T 1J4, Canada

Abstract — High-frequency electro-optical modulator is critical for enabling signal processing and distribution in the next generation cloud computing, tele-medicine, and telecommunications. In this paper, substrate integrated waveguide (SIW) is exploited as an alternative fundamental transmission line structure in support of electrical signal for the design and development of millimeter-wave and terahertz (THz) traveling-wave polymeric electro-optic (EO) modulator. Optical and full-wave electromagnetic analyses are conducted and structure optimization is made based on such analyses in order to obtain millimeter-wave transmission characteristics and optical response. Compared to its conventional TEM-mode transmission lines, this bandpass non-TEM mode SIW-based EO modulator presents numerous advantages, namely compact structure, low transmission loss, low driving power, simple packaging and flat optical response over a wide frequency range.

IndexTerms — Electro-optic modulators, millimeter wave integrated circuits, millimeter wave technology, optical polymers.

2.1 Introduction

2.1.1 General

As demand for information bandwidth increases, information photonics are becoming more and more instrumental and photonic-based communication systems are playing a crucial role to overcome the inherently limited-speed barriers of electronics. To meet the increasing needs for

higher data rates in optical communications and next generation backhaul connectivity of Gbit/s wireless picocell base stations, ultra-high-speed optical transmission systems have been under intensive development towards the speed of 160 Gbit/s and beyond [1]. Since the data rate depends on the carrier frequency, the most promising way is to exploit intact frequencies above 100 GHz. Alongside, THz and millimeter-wave frequency region from 100 GHz to 10 THz has captured significant attention [2]–[5] for ultra-fast wireless communication links. THz techniques can find applications in many areas such as security enhancement, medical diagnosis, scientific imaging, and material identification. High-altitude THz telecommunications is being considered or a possible use for future wireless system providing data rate of more than 10 Gbit/s [6]. Wireless expansion of the next generation broadband access fiber optic networks, Gigabit Ethernet, and multi-gigabit communication systems are very promising [7] which should be supported by ultra-broadband devices and circuits on both electronic and photonic sides. The possibility of minimizing the size of wireless equipment and improving the antenna directivity is other appealing features of THz and millimeter waves, which would lead to a more compact and cost-effective system because the antenna can be integrated with other devices on the same chip. To implement the wireless system operating at such a high frequency, photonic technologies are advantageous against electronic approaches because of its inherent broadband nature, and allow us to deliver photonic THz and millimeter-waves over long distance using optical fibers. To date, this demand has been accommodated with advanced modulation schemes and signal processing technologies at microwave frequencies. However, without increasing the carrier frequencies for more spectral resources, it may be quite difficult to keep up with the needs of users.

A fundamental challenge in optical telecommunication is to modulate millimeter-wave or THz bandwidth or just carrier signals onto an optical wave carrier in phase or amplitude, depending on broadband communications services. This is usually done with an external EO modulator to vary either the intensity or phase of the light emitted by a laser diode. Unlike direct laser-bias modulation, external EO modulator such as the Mach-Zehnder Modulator (MZM) can support the transmission of very-high frequency RF signals or ultra-wide bandwidth over optical carrier [8]. MZM, which is based on push-pull interferometric operation, results in chirp-free modulation and provides an effective approach to reducing the driving power of the modulator and improving the gain and performance [9]. However, two fundamental hurdles prevent the ultra-broadband high-speed operation such as millimeter-wave or THz. First, THz and millimeter-wave signal attenuation

is extremely high for conventional TEM-mode traveling-wave structures. The other restriction is related to the frequency dispersive characteristics of the modulation index, which causes the driving power to increase as modulation frequency increases. This response degradation arises from two distinct physical origins, namely the limited modulation length due to the velocity mismatch between signal and carrier waves and power dissipation due to high-frequency loss, which is mainly related to the conductor loss [9]. In addition, millimeter-wave and THz modulators with conventional TEM-mode electrodes present a great challenge in the packaging of the modulator structures, which has also limited the use of those structures over such a frequency range because of their unbounded signal transmission.

2.1.2 **Polymer electro-optic material and modulator**

Generally speaking, organic electro-optical (EO) polymers have attracted much attention thanks to special properties afforded by these materials including the potential for low driving power, ease of manufacture, and compatibility with very large scale integration (VLSI) oriented semiconductor processing technology. Polymer EO material has the essential properties to operate in very high-frequency photonic devices. The bandwidth of a polymer modulator is not limited intrinsically by the influence of velocity mismatch. Likewise, tremendous efforts have invested into the development and optimization of those materials. Nonlinear EO coefficient of r=100pm/V or even higher has been reported as the state-of-the-art results [10]. In addition, the dielectric properties of many polymers are suitable for high-frequency applications as millimeter-wave measurements on numerous polymers suggest very low loss tangent values and low material dispersion. However, the traveling-wave design of the active electro-optical interaction region affects the performance of modulator in terms of both modulation bandwidth and driving power. This is why it is still a proven difficulty to design and develop very broadband polymer modulators. Therefore, finding an appropriate scheme for applying millimeter-wave electrical fields to the light-wave channel is one of the particular issues that have to be addressed [10].

To date, microstrip line (MSL) has been applied as a driving traveling-wave structure. Whereas, contrary to $LiNbO_3$, NLO polymer does not limit the EO modulation frequency by its nature, these conventional TEM-mode structures, suffering from an extremely high loss at higher frequencies, pose the limit on high-frequency performances. In addition, the manufacturing of MSL devices at such high frequencies requires very tight geometrical tolerance due to small wavelength.

Concerning the explosive Moore's law [11] and increasing trend in test cost for each new generation of chip manufacturing, new-concept devices and circuits should be introduced to enable a large-scale use of organic EO materials for next generation of millimeter-wave and THz photonics applicable to computing and telecommunications. Translating recent achievements into finding and fabricating new high-performance materials through the structural modification is the core ingredient in the progress and success of developing a new technology.

2.1.3 **Substrate integrated waveguide**

Achieving TE_{10} single-mode THz coupling and propagation in a metallic rectangular waveguide was first demonstrated by [12]. A recent investigation on the propagation characteristics of the TEM-mode and TE-mode of the parallel-plate waveguide has demonstrated an extraordinary low ohmic loss characterization of TE_1 mode [13]. Particularly, TE_1 is introduced as an efficient viable alternative operating mode for THz/millimeter-wave applications. The extension of this plane-wave description to the dominant TE_{10} mode of the hollow metallic rectangular waveguide, results in the well-known steady frequency response behavior over the working bandwidth [14].

Recently, substrate integrated waveguide (SIW) techniques, which belong to the family of substrate integrated circuits (SICs), have been proposed as non-TEM mode integrated rectangular waveguides in planar form [15]. Since the field distributions are free from singularities and generally spread over the entire structure, lower-loss transmission properties at higher frequencies are anticipated [16]. Thanks to its broadband characteristics, low-loss, and excellent tolerances, SIW is extremely useful for the design of high-speed millimeter-wave and THz signal interconnects up to 1000 GHz [16]. Efforts have been made to broaden the frequency response by shortening the length of TEM-mode modulator. However, the response of the device is essentially required to be flattening out at higher frequencies.

With the concept of substrate integrated circuits (SICs) [15], the recently proposed and developed integration technologies of planar and non-planar structures, an integrated circuit technology for high-speed wireless link systems using photonic techniques can be realized [17]. In this case, carrier frequency will increase to the point where bandwidth is wide enough to get large data capacity even with a simple technique and configuration. Moreover, this concept will develop a self-packaging solution that is necessarily required for THz integrated circuits as it is simply predicted that unavoidable dielectric loss and insufficient patterning accuracy may limit the use of

current packaging techniques for THz-wave applications. Combining the advantages of planar technology of low fabrication cost with the low-loss intrinsic to the waveguide, SIW technology is a most promising candidate for the current development of communication and sensor applications towards millimeter-wave and THz. Having non-TEM traveling-wave structure, synthesized in planar substrate with arrays of metallic vias, SIW provides a vacuum-packaged solution, free from unwanted external electromagnetic interactions.

2.1.4 **Contribution of this work**

In this paper, a novel structure for the millimeter-wave and THz EO polymer modulator based on SIW structure is introduced and investigated. Supporting theoretical development and modeling results are established to validate the concept. The proposed theoretical model for traveling-wave operation together with the optical simulation provides an efficient approach that will specify the values of various parameters in order to obtain the optimized EO modulator design. A method for obtaining the lowest possible driving power for given center frequency and designated bandwidth is presented. The operation of the proposed push-pull polymer EO modulator is achieved by poling the MZM arms in reverse direction and driving both arms in phase through the SIW structure. Such push-pull poled polymer configuration for MZM was typically realized with a single MSL; demonstrations beyond 100 GHz have been reported previously [18]. It has been shown that in such a structure, bandwidth is determined by conductor resistance while the effects of dielectric loss and velocity mismatch are negligible [9]. The proposed SIW modulator exhibits roughly uniform frequency response that is not limited by substantial millimetre-wave or THz attenuation at high frequency. In this case, broad bandwidth as well as improved efficiency and high-RF power capability are expected. Furthermore, high-pass characteristics of the SIW structure impart low-frequency noise nullification and thermal noise reduction, thereby improving the noise figure [19]. In addition, SIW as an enclosed self-shielded structure can remove potential crosstalk and unintentional radiation loss. Additionally, the difficulty in fabricating an optical push-pull structure with single MSL [18], which is imposed by the minuscule script of MSL width, will be overcome as well.

2.2 Device structure

Figure 2.1 shows the structural schematic of the proposed EO modulator, which consists of modulating region, optical input and output, and RF input and output. SIW generally consists of two vertical walls, a top conductive layer, a bottom conductive layer, and a dielectric material in between. Because there are via arrays along the sidewalls, TM modes cannot be guided while the vertically directed currents of TE_{n0} waveguide modes are fully supported in which TE_{10} mode is the fundamental mode (see Figure 2.4). SIW supports the traveling-wave propagation of millimeter-wave and THz signals. As the millimeter-wave/THz fields interact with the polymeric optical waveguide, the optical refractive index is modified through the EO effect. The basic design of the modulator is a push-pull Mach-Zehnder interferometer (MZI) whose cross-sectional view is described in Figure 2.2 and Figure 2.3.The optical waveguide is a vertically stacked optical ridge channel. Due to the DC-bias drift and other associated problems especially at higher frequencies, several bias-free modulators with highly linear response have been introduced [20], [21]. The push-pull mode operation is achievable with no DC bias and this bias-free push-pull MZM modulator is introduced as the best choice in several optical communication systems [24]–[26]. Our device is also designed with zero bias.

The initial design for the optical waveguide is based on a structure proposed by [27], which consists of an active poled chromophore bonded in a host as the active core sandwiched between lower and upper cladding layers. Two different prototypes arrive at the necessity of larger thickness of the cladding. In the first one (Figure 2.2) buffer layer is proposed from the same material as cladding while in the second design (Figure 2.3), lower cladding is replaced with a thick SiO_2 layer.

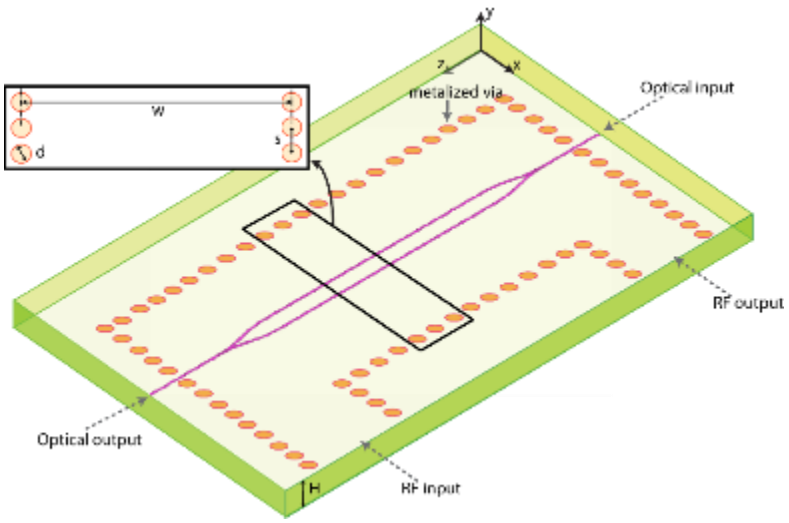

Figure 2.1: Schematic representation of polymeric substrate integrated waveguide (SIW) modulator.

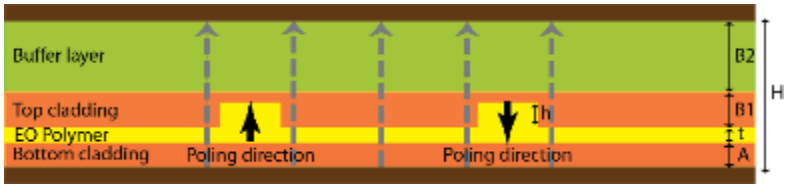

Figure 2.2: Cross-sectional view of the first proposed device showing the push-pull operation in a polymer EO MZM. Black and gray arrows represent poling and modulation field directions, respectively.

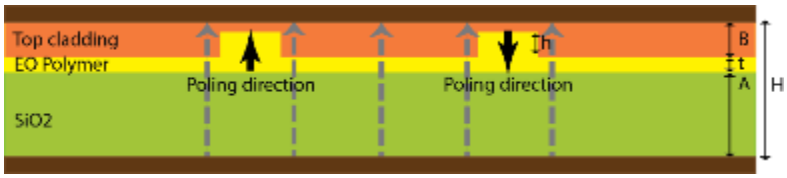

Figure 2.3: Cross-sectional view of the second proposed device showing the push-pull operation in a polymer EO MZM. Black and gray arrows represent poling and modulation field directions, respectively.

The rib optical waveguide configuration is chosen due to its advantages of optimizing the operation of EO polymeric modulator [28]. Generally, keeping the single mode operation of the optical waveguide requires a sufficiently thin thickness of the core layer; in the case of a three-dimensional rib waveguide, this is not a very crucial factor [29]. It has been shown that even if the core layer is not so thin that it could support several modes in its slab waveguide, it is still possible to design the rib waveguide to confine only one mode by radiating the higher order modes horizontally into the slab modes [30]. In this case, while a high coupling loss between the optical fiber and waveguide does not take place, the oversized rib waveguide will support only the single mode without additional radiation loss [31]. On the other hand, more confined optical field will be obtained by increasing the rib height and the overlap integral will be improved in turn (see Section 2.4). Dimensions of the optical waveguide are determined and optimized with respect to these considerations. The arms of the MZM are poled in opposite directions, resulting in a push-pull design. After poling, the temporary electrodes are removed and buffer layer and SIW are then fabricated as the final supporting traveling wave structure. This process is similar to the dual-cladding process, which was applied by [32]. Amplitude modulation is achieved by interfering two optical phase modulated beams after passing through the domain-inverted polymer.

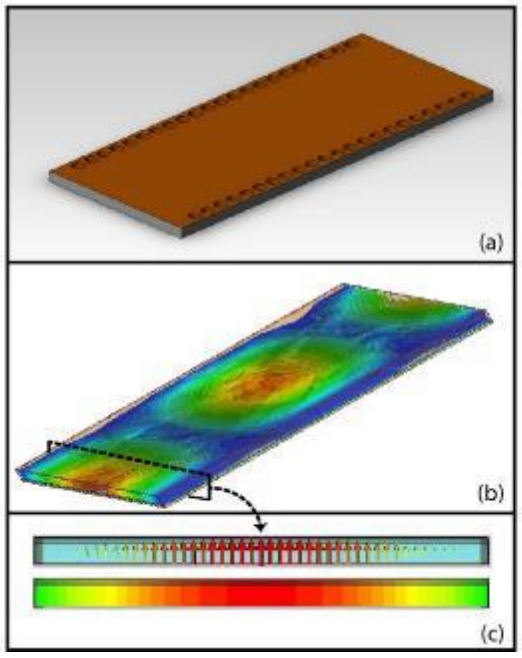

Figure 2.4: a) SIW structure b) TE_{10} Electric field propagation along the waveguide c) TE_{10} Electric field distribution in the waveguide cross section.

In selecting the material, apart from the compatibility in the fabrication process and poling [10], some basic physical characteristics are considered for efficient operation. While the core optical refractive index is higher than the cladding in order to confine the light, its relative permittivity is lower than other layers, cladding and buffer layers, to improve overlap integral [9]. Secondly, in traveling-wave devices, the optical radiation and millimeter-wave are required to propagate at similar (ideally the same) speeds within the interaction region of the modulator.

2.3 Theory

2.3.1 Millimeter-wave driving power

In the push-pull version of MZM, electrical field creates opposite phase shift in the arms because of reverse polarity. Accordingly, the output optical intensity may be represented as [36]

$$I = I_0 \cos^2(\frac{\Phi_0}{2} + \Delta\Phi) \tag{1}$$

where I_0 is the maximum output intensity, $\Phi_0 / 2$ represents any static phase imbalance between the interferometer's arms, and is the electro-optically induced phase shift (see Appendix) which is proportional to the applied voltage or square root of applied power P :

$$\Delta\Phi = \frac{\pi}{2}\frac{V}{V_\pi} = \frac{\pi}{2}\sqrt{\frac{P}{P_\pi}}M(f) \tag{2}$$

The factor *M(f)* specifies the frequency dependence of the modulator and includes the effect of electro-optical velocity mismatch as well as millimeter-wave or THz attenuation [37]. The power P_π is defined as the required power for achieving a π-phase shift between the two arms of the interferometer. The required $\Delta\Phi$ in each arm of MZM for zero output power is $n\pi/2$. Since in our structure E_{RF} is constant over the core region, using (27) and (2)

$$\sqrt{\frac{P}{P_\pi}} = \frac{V_\pi}{V} = \frac{rn^3\Gamma L}{2\lambda_0} \simeq \frac{rn^3 E_{RF} L}{2\lambda_0} \tag{3}$$

P_π is related also to the millimeter-wave characteristic of traveling-wave design. The propagation characteristic of SIW is the same as those of its equivalent rectangular waveguide. Equivalent width w_{eff} is determined by three parameters *w*, *s*, and *d* (see Figure 2.1) through an empirical equation [15]:

$$\omega_{eff} = \omega - 1.08\frac{d^2}{s} + 0.1\frac{d^2}{\omega} \tag{4}$$

which is accurate as long as s/d is smaller than 3 and w/d is smaller than 1/5. Applying Poynting's theorem, the power flow along the guide for the TE_{10} mode is calculated by [40]:

$$P = \frac{{E_{RF}}^2 w_{eff} H \sqrt{1-(\frac{f_c}{f})^2}}{4\eta} \tag{5}$$

where $f_c = 1/(2w_{eff}\sqrt{\mu_0\varepsilon_0\varepsilon_r})$ is the cutoff frequency for TE_{10} mode, and $\eta = \sqrt{\mu_0/(\varepsilon_0\varepsilon_r)}$ is the TEM wave impedance.

From (3) and (5), the millimeter-wave driving power is calculated by

$$P_\pi = (\frac{V_\pi}{V})^2 P = \frac{{\lambda_0}^2 w_{eff} H \sqrt{1-(\frac{f_c}{f})^2}}{16\eta(\mathrm{rn}^3\mathrm{L})^2\Gamma^2} \tag{6}$$

However, this value is regarded as the minimum. In the traveling-wave configuration of the modulator, a millimeter-wave signal that starts out with power $P_{RF}(0)$ is attenuated as it propagates along the modulator and the attenuation is frequency dependent. Therefore, power as a function of distance and frequency can be expressed as

$$P_{RF}(\mathrm{d},\mathrm{f}) = P_{RF}(0, f)\exp(-\alpha(\mathrm{f})\mathrm{d}) \tag{7}$$

In order to assess the value of the applied power needed to produce an effective P_π, the integrated effect of the power over the modulator length is considered. From a simple integration, it can be shown that the applied voltage at the input of the modulator to produce an effective P_π is given by:

$$P_{\pi,eff}(\mathrm{f}) = \frac{\alpha(f) P_\pi L}{1-\exp(-\alpha(\mathrm{f})L)} \tag{8}$$

$\alpha(f)$ is the overall millimeter-wave attenuation, which can also be calculated in the next section.

Eventually, drive voltage V_π is evaluated as the standard measure of modulator sensitivity. For our modulator from applying the line integral of the maximum electrical field along the SIW layer

$$V = \int_0^H E_{RF}.dy \tag{9}$$

in which electric field E_{RF} is resolved from driving power P_π (see (6) and (28)). The value of V_π is used to compare the results with other EO modulators.

2.3.2 **Modulation frequency response**

The EO modulation index calculation is subject to two main analyses over both the optical and millimeter-wave frequency ranges. Millimeter-wave analysis is carried out to determine the device effective index and to evaluate the transmission-line loss. The overall attenuation constant for SIW is determined by the attenuation coefficient because of dielectric loss α_d and conductor loss α_c. This linear superposition is valid as the losses are small:

$$\alpha = \alpha_\mathrm{d} + \alpha_c \tag{10}$$

It may not be necessary to introduce leakage loss α_r in SIW as it can almost be ignored by proper design of vias and their spacing [15]. Knowing loss tangent $\tan\delta$ of the core and cladding materials, the attenuation constant caused by dielectric loss is derived from the propagation constant and is given by [39]:

$$\alpha_\mathrm{d} = \frac{\mathrm{k}^2 \tan\delta}{2\beta} Np/m \tag{11}$$

where β, the millimeter-wave propagation constant for the dominant TE_{10} mode, is given by

$$\beta = \sqrt{(\frac{\pi}{w_{eff}})^2 - k^2} \tag{12}$$

and *k* is the wavenumber

$$k = \omega\sqrt{\mu_0 \varepsilon_0 \varepsilon_r} \tag{13}$$

On the other hand, the attenuation caused by conductor loss α_c is calculated by using a well-established perturbation method [39]. Value depends α_c on the field distribution, and for the fundamental TE_{10} mode is given by

$$\alpha_c = \frac{2R_s}{b\eta\sqrt{1-(\frac{f_c}{f})^2}}\frac{1}{2} + \frac{b}{a}(\frac{f_c}{f})^2 \tag{14}$$

$R_s = 1/(\sigma_c \delta_f)$ is the surface resistance of the waveguide walls, and $\delta_f = \delta(1-\mathrm{e}^{-t/\delta})$ is a modified skin depth proposed by Hiraoka [40], where $\delta = 1/\sqrt{\pi f \mu_0 \sigma_c}$, and *t* is the conductor thickness. δ_f extends the skin depth to the frequency range where t/δ is not large.

The millimeter-wave effective index N_m for the SIW as a special form of dielectric-filled waveguide, is derived analytically. For the dominant mode TE_{10}, the propagation constant is only related to the width and is calculated from

$$N_m = \sqrt{\varepsilon_r}\frac{\beta}{k} \tag{15}$$

Following these calculations, the modulation frequency response under the impedance matching condition can be obtained from [28]

$$M(f) = \left|\exp(-ju)\frac{\sin(u)}{u}\right| \tag{16}$$

where

$$u = \frac{1}{c}\pi f L(\mathrm{N}_m - \mathrm{N}_{eff}) - \mathrm{j}\frac{1}{2}\alpha L \tag{17}$$

$\alpha = \alpha_\mathrm{d} + \alpha_c$ is the total millimeter-wave signal attenuation, and N_{eff} is the optical effective index, determined through optical analysis. Providing the impedance and velocity matching ($N_m - N_{eff} \approx 0$), the bandwidth is limited only by the conductor and dielectric losses. For the modulator operated near a point of maximum or minimum output intensity (i.e., bias at null point

or $\Phi_0 = 0$), under small signal operation ($\delta V \ll V_\pi$), an AC optical intensity $\delta I(\mathrm{f})$ is produced such that

$$\delta I(\mathrm{f}) \propto (\delta V M(f))^2 \tag{18}$$

Our proposed modulator is designed to minimize the driving power at center frequency, f_0. Therefore, the 3-dB frequency point occurs when [36]

$$\frac{\delta I(f_{3dB})}{\delta I(f_0)} = (\frac{\delta M(f_{3dB})}{\delta M(f_0)})^2 = \frac{1}{2} \tag{19}$$

$$10Log(\frac{\delta I(f_{3dB})}{\delta I(f_0)}) = -3dB \tag{20}$$

Before moving on to the next section, a notation should be made concerning the modulator's length. Although increasing the modulator's active length will decrease the required driving power (see (6)), it does not necessarily yield better performance and higher efficiency. Therefore, two factors should be examined together to determine the maximum tolerable length:

• Insertion loss ($S_{21} > -6\ dB$)

• 3-dB bandwidth of modulation frequency response (M > 0.5).

Millimeter-wave attenuation α resolves the first one. For the second, the calculation is simplified by dealing the polymeric EO modulator as a near velocity-matched device. In this case, the millimeter-wave–optical walk-off is zero and the modulation frequency response can be written as

$$M_v(f) = \frac{(1-\exp(-\alpha \mathrm{L}/2))^2}{(\alpha \mathrm{L}/2)^2} \tag{21}$$

At the -3dB point, $M_v(f) = 0.5$, the maximum tolerable active length is derived from the solution to the transcendental equation

$$M_v(f) = 0.5 \Rightarrow \alpha \mathrm{L}/2 = 0.742 \Rightarrow L_{\max} = \frac{1.484}{\alpha} \tag{22}$$

As the variation over the whole frequency band of interest for the SIW modulator is negligible, the maximum supportable length is not very much frequency dependent. This feature is a remarkable advantage in the device's general quality compared to the conventional ones. For example, in MSL

$\alpha \propto \sqrt{f}$ and therefore maximum length $L_{\max} \propto 1/\sqrt{f}$, which dictates another significant restriction on high-frequency performance [41].

2.4 Results and parametric discussion

To maximize the bandwidth of a high-speed traveling-wave EO modulator, it is necessary to match the millimeter-wave effective index N_m with the optical refractive index N_{eff}. Once the phase velocity matching is achieved, the next limiting factor is the total millimeter-wave propagation loss. Typical variations of millimeter-wave effective indices N_m and N_{eff} for polymeric material are illustrated in Figure 2.6. It is observed that N_m of SIW modulator in TE_{10} mode operation (curves group C and D) is a function of SIW width and dielectric permittivity. Therefore, knowing dielectric permittivity ε_r and determining N_{eff}, a little adjustment in the SIW width may be used to realize the velocity matching. It is observed that the frequency dispersion is negligible in the frequency range of interest.

The millimeter-wave attenuation of SIW and MSL for different substrate thicknesses is shown in Figure 2.5. in which both conductor and dielectric loss are included. Low thickness substrate results in a significant increase in conductor loss and, therefore, a buffer layer is planned in our structure to reduce the loss. Although higher thicknesses of MSL may also reduce conductor loss, this leads to a substantial increase in radiation loss. The millimeter-wave attenuation for the proposed structure for 2 μm thick conductor with 10 mm length is less than 3.5 dB having 10 μm buffer layer and less than 0.5 dB having 40 m buffer layer. On the contrary, the attenuation for such a structure with 10 mm length in thin-film MSL is more than 7 dB at 110 GHz [42] and the loss increases in proportion to the square root of frequency. The derived formula and calculations were formerly validated by measurement results presented in [44] for MSL, ε_r=3 and tanδ = 0.01, and in [44] for SIW, ε_r=8 and tanδ = 0.006.

3D beam propagation method (BPM [45]) is used to simulate the optical propagation, N_{eff} derivation, and to optimize the dimensions of the rib waveguide and Y-branch power splitter geometry (Figure 2.8, Figure 2.7). The waveguide ridge height is set at 0.35 m to assure single mode operation. The waveguide width is selected to be 7 μm, large enough to avoid as much fiber coupling loss as possible, and A=B=3.9 μm, t=1 μm. Considering a good separation between the MZI arms, 50 μm in this case, the output optical field is examined. The lowest optical loss is

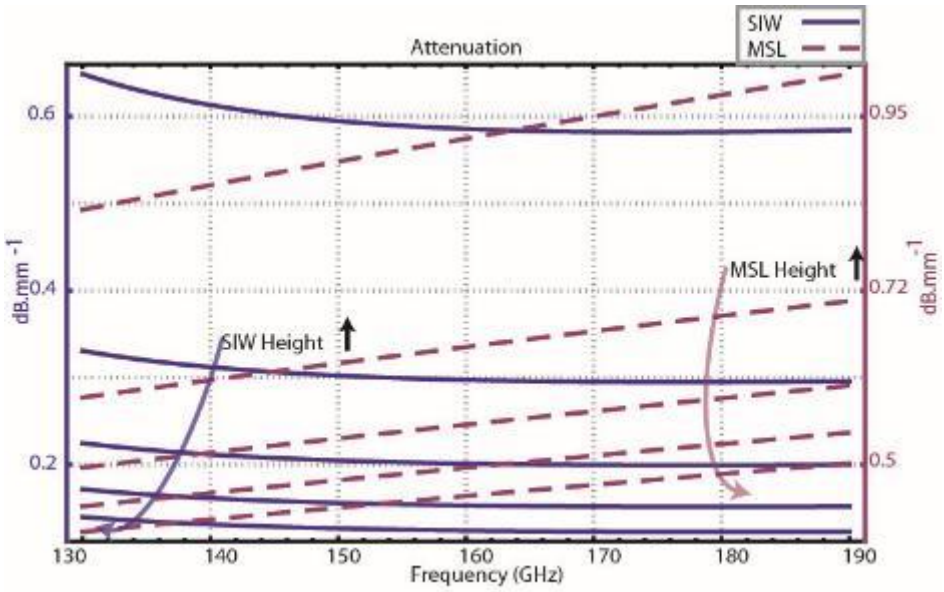

Figure 2.5: Calculated attenuation as a function of frequency for polymer SIW modulator and polymer MSL modulator. SIW width $w_{eff}=20\ \mu m$, MSL width m, Height is changing 10 μm to 50 μm. The adopted approach for calculations has already been examined and validated for thick film SIW [44] and for MSL in [42].

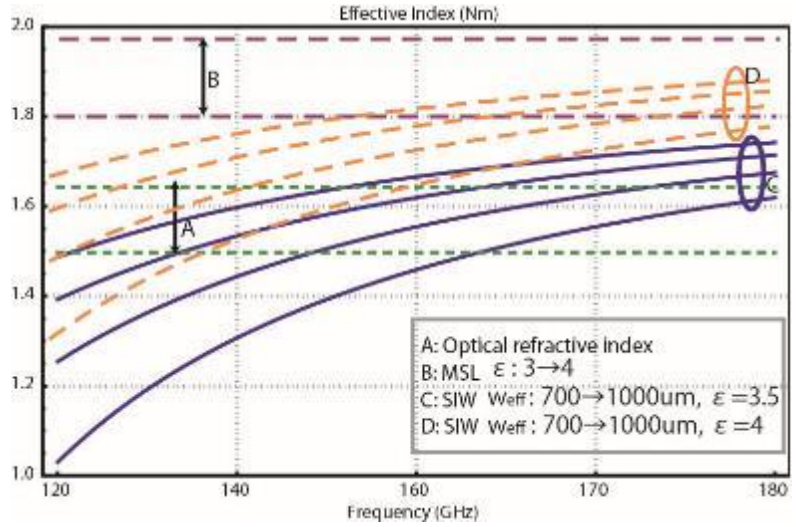

Figure 2.6: Calculated millimeter-wave effective index as a function of frequency for polymer SIW modulator and polymer MSL modulator compared to the optical refractive index. SIW width "w" changes from 800 μm to 1000 μm.

obtained for a Y-branch composed of a parabolic taper and an arc sine branch, 100 μm and 600 μm

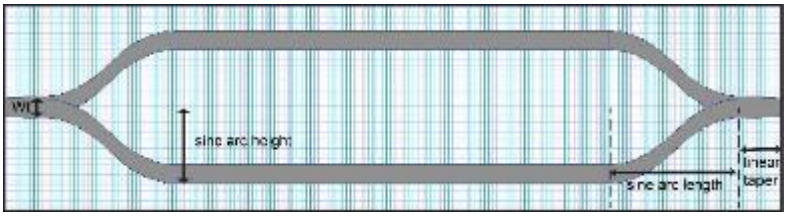

Figure 2.7: MZI branch is optimized to achieve the highest output optical power.

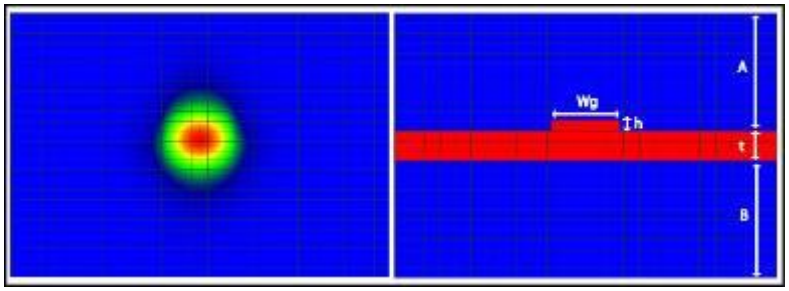

Figure 2.8: Schematic of the buried rib waveguide and simulated mode shape using beam propagation method (BPM).

long, respectively. In the proposed structure, the ridge optical waveguide etched into the core has a guided mode optical index N_{opt}=1.59. This value for such a polymeric waveguide is typically between 1.5 to 1.63 [10].

Figure 2.9 demonstrates the calculated modulation frequency response for 10 mm active length, different widths, and different heights. Exhibiting band-pass characteristic, the SIW width "w" is selected to comply with the intended center frequency, f_c. f_c is the middle point of the useful operating frequency band, from 1.25 f_{cutoff} to 1.95 f_{cutoff}, in which $f_{cutoff} = 1/(2a\sqrt{\mu_0\varepsilon_0\varepsilon_r})$ is the cut off frequency for TE_{10} mode [39]. The maximum of the electric field is at the center of the SIW where the MZM is placed (Figure 2.4). Therefore, the performance of the modulator is not sensitive to the SIW width. However, lower width, which corresponds to the higher frequency operation, results in lower driving power (6). Polymer permittivity ε_r is usually a value between 2.5 to 4.

The height of the SIW, on the other hand, is optimized by changing H to decrease the loss and increase the modulation efficiency. It is also illustrated that the modulation frequency response of the proposed modulator is modified for different buffer layer thicknesses, while the SIW width is fixed for the band-pass modulation with center frequency f_c = 160 GHz.

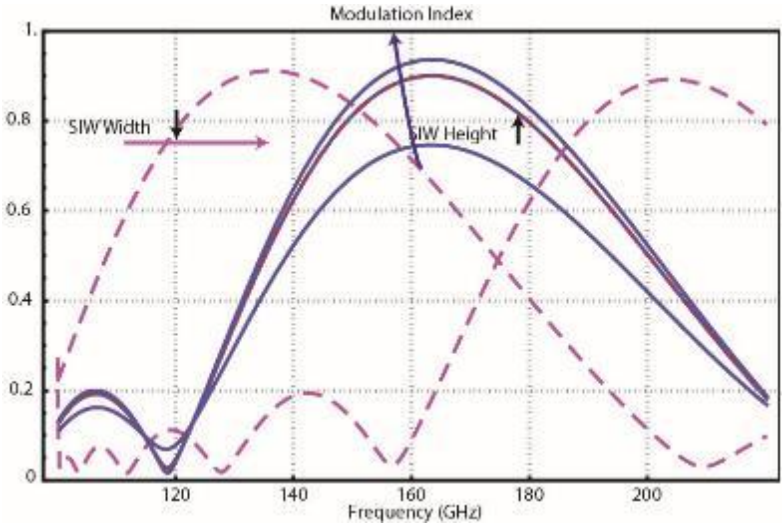

Figure 2.9: Calculated modulation index as a function of frequency for polymer SIW modulator; SIW width w_{eff} changes from 800 μm to 1200 μm, and height changes 10 μm to 50 μm.

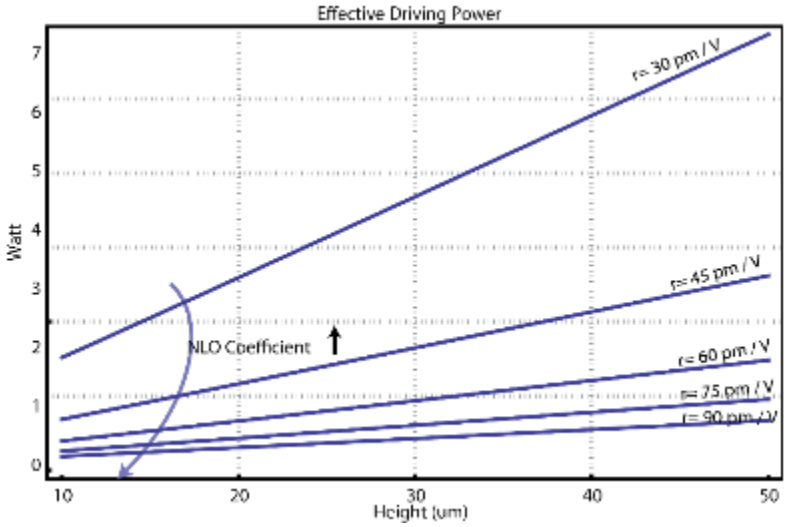

Figure 2.10: Calculated effective driving power as a function of SIW height "h" for polymer SIW modulator. SIW width w_{eff} = 700 μm, f_c=160 GHz, L=10 mm.

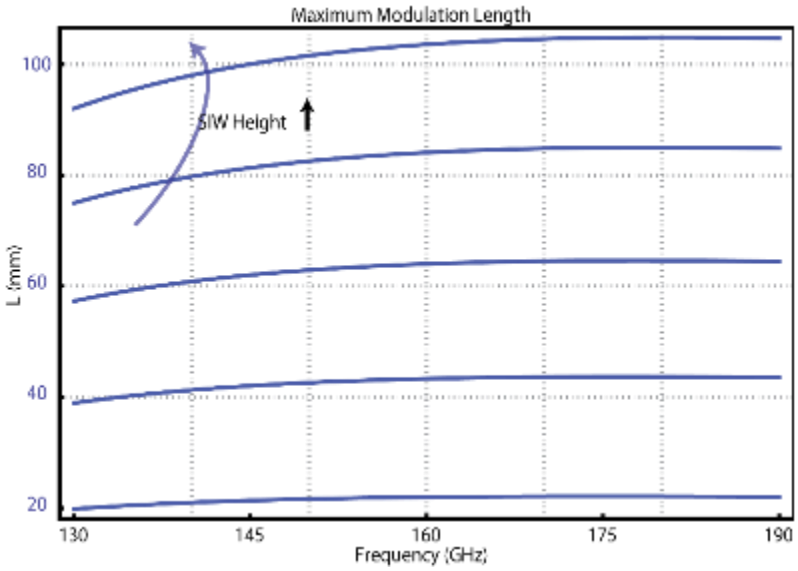

Figure 2.11: Calculated maximum length as a function of frequency for polymer SIW modulator. SIW width w_{eff} = 800 μm, height H changes from 10 μm to 50 μm.

The required driving power [38] for the proposed modulator is derived by applying the Poynting vector calculation for the TE_{10} mode. Since in the traveling-wave configuration the millimeter-wave signal is attenuated as it propagates, the effective driving power is assessed considering the modulator length (8). Figure 2.10 illustrates the variation of the calculated driving power versus *H* for 10 mm active length and different electro-optic coefficients at 160 GHz. Clearly, for an exact active length, a higher EO coefficient results in lower driving power. Whereas thickening the SIW height *H* decreases the millimeter-wave attenuation, it simultaneously increases the driving power. Therefore, while *r* is known, an optimization is required to find the best adjustment of L and H (see Section 2.6). Before optimization, the limit on the maximum length (22) to assure 3 dB modulation index bandwidth ($M > 0.5$) is investigated. Thicker configuration allows for longer length to the point at which changing height from 10 m to 50 m corresponds to 22 mm to 102 mm acceptable active length (Figure 2.11).

2.5 Optimization

In order to optimize performance, two distinctive issues are considered: the selection of appropriate dimensions, and the choice of an appropriate set of polymer material to construct the device stack.

This section deals with design trade-offs that can be made with polymer devices for different applications in practical systems. As the first step, a typical value for material permittivity is assumed to optimize the dimensions. The effect of selecting appropriate material to improve the efficiency is discussed subsequently.

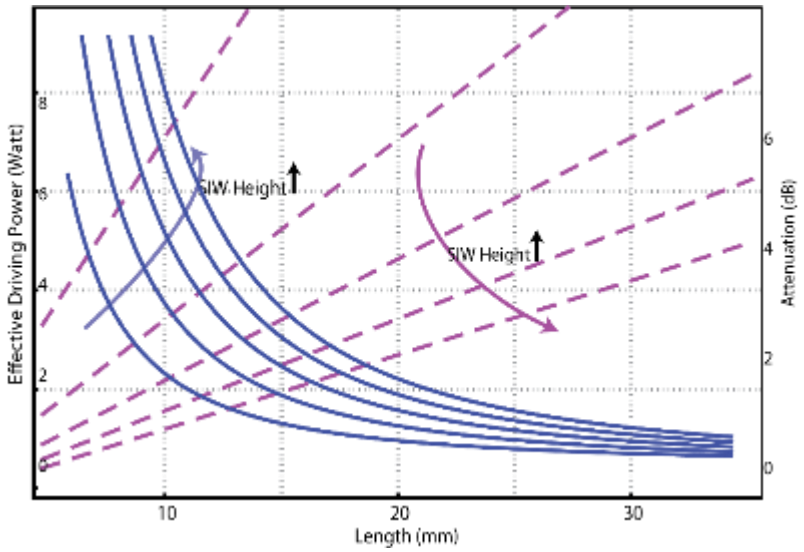

Figure 2.12: Calculated maximum length as a function of frequency for polymer SIW modulator. SIW width w_{eff} = 800 μm , height H changes from 10 μm to 50 μm.

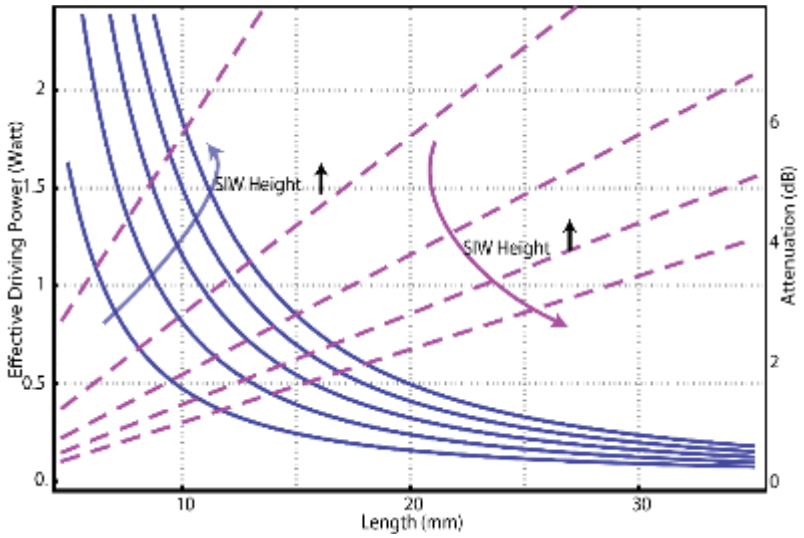

Figure 2.13: Calculated effective driving power as a function of active length for polymer SIW modulator; SIW width w_{eff} = 800 μm, NLO coefficient r=90 pm/V, and Height is changing 10 μm to 50 μm.

In order to determine the optimum H to obtain minimum driving power, attenuation α and effective driving power $P_{\pi,eff}$ must be examined together. Figure 2.13 and Figure 2.12 illustrate two groups of curves, representing effective driving power and attenuation vs. length, for the different heights of proposed SIW modulator with center frequency f_c = 160 GHz. The former is established considering the EO coefficient r=30 pm/V (e.g., DR1-PMMA [9]), and the latter is based on r=90 pm/V (e.g., B10-APC [32]). Accordingly, two sets of device parameters and associated characteristics are presented in Tables 2.2 and 2.3.

It should be noted that the reported V_π in the literature is usually DC-referenced and also without effective value calculation. Nevertheless, the TEM-mode modulators radically suffer from 1-dB drop-off in response at low frequency. The DC-referenced V_π is reported around 4 V for LiNbO and 1.6 V for polymer-based commercial modulators [32], while the measured frequency response does not overtake 110 GHz. With these considerations, the expected value for V_π in our calculation is very appropriate.

Table 2.1: Calculated driving power, driving voltage, and attenuation for 160 GHz SIW modulator with different height and length, r=30 pm/v

No.	**H (μm)**	**L (mm)**	**V_π (V)**	**P_π (mW)**	**$P_{\pi,eff}$ (W)**	**S_{21} (dB)**
1-1	50	35	9	620	$\simeq 1$	-4
1-2	40	35	7.1	500	< 1	-5
1-3	30	28	6.7	580	$\simeq 1$	-6
1-4	20	19	6.6	850	$\simeq 1.4$	-6

Table 2.2: Calculated driving power, driving voltage, and attenuation for 160 GHz SIW modulator with different height and length, r=90 pm/v

No.	**H (μm)**	**L (mm)**	**V_π (V)**	**P_π (mW)**	**$P_{\pi,eff}$ (W)**	**S_{21} (dB)**
2-1	50	35	3	69.8	88.2	-4
2-2	40	35	2.4	55.8	74.4	-5
2-3	30	30	2.1	57	78.7	-6
2-4	20	20	2.1	85.5	117.7	-6

In order to improve the fill factor, enough care should be taken in choosing the material. The introduction of a high-permittivity cladding material creates more electrical field confinement in the core and improves the fill-factor, and so overlap integral as well [47].

To calculate the overlap integral (28), the spectral index method [48] is used to figure out the optical field distribution; for the polymer modulator with rib height h=0.35 μm, overlap integral is about 0.94 (also shown by [46]) and even more improved by h=0.7 μm. The reason is that increasing the rib height will confine the optical field mostly in the lateral direction and increase overlap with the modulating electrical field. Considering the multilayer structure of the polymer modulator (Figure 2.2) as basically a parallel-plate capacitor, overlap integral improvement factor is resolved.

$$F = \frac{H\varepsilon_A\varepsilon_B}{\varepsilon_A\varepsilon_B t + \varepsilon_t\varepsilon_B A + \varepsilon_t\varepsilon_A(B1 + B2)} \tag{23}$$

While overlap integral is enhanced by factor F, driving power is reduced by the factor $1/F^2$. F is calculated for a variety of core and cladding permittivity (Figure 2.14). According to Figure 2.14, it is predicted that provided $\varepsilon_{r,\,core} = 2.5$ and $\varepsilon_{r,\,cladding} = 4$, driving power will be reduced by 60%. Therefore, the general design strategy is decreasing the core permittivity relative to the cladding and creating the greatest possible contrast between the millimeter-wave dielectric constant of the core and cladding layers. The effect of increasing the buffer-layer thickness is also evaluated. While the buffer-layer permittivity is high (as the cladding layer), no significant effect on F is observed.

The last tread is looking into figure of merit (FOM) and modulation efficiency together and finalizing the design parameters. A useful FOM is the drive power per unit bandwidth, $P/\Delta f$ [49]. The advantage of this FOM definition is that it is more compelling for comparing high-frequency performance. As presented in Table 2.3, the best FOM and modulation efficiency are expected from design No. 2–3. More than 25 GHz bandwidth at 160 GHz is predicted.

As mentioned earlier, modulation length has an inverse effect on driving power and loss, which in turn affects modulation efficiency and bandwidth. Although lower length for the modulator increases the driving power, it increases the bandwidth as well. In the last table, design Nos. 2–2, 2–3, and 2–4 are reconsidered with reduced length and better FOM is obtained. With regard to the operation frequency, the estimated FOM is commendable compared to previous works (e.g., FOM = 3.9 by [50]).

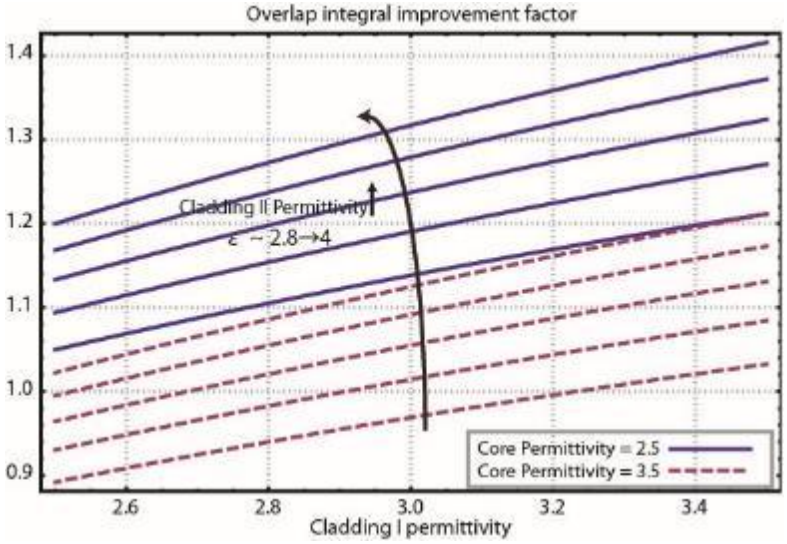

Figure 2.14: Overlap integral improvement factor as a function of cladding permittivity for polymer SIW modulator.

The last point that should be mentioned here is that the required power for the modulator is indeed much less than the driving power, which is calculated for complete switching (π-phase shift). Driving power is merely a standard value to estimate device performance. Eventually, according to the goal modulation efficiency and desired bandwidth (i.e., depends on application), the design is concluded.

It is worth noting that for the traditional TEM-mode structure, the computed optical response suggests a maximum 3 dB bandwidth up to 80 GHz [51]. However, experimentally speaking, 3 dB bandwidth at 34 GHz, starting from a few MHz, has been achieved in such a structure, as it is limited by the RF loss of the MSL [30]. For the higher frequency, finline transition structure has been used to adapt from non-TEM millimeter-wave waveguide to MSL, and operation from 74 to 113 GHz has been demonstrated [52].

Table 2.3: Calculated bandwidth, maximum modulation efficiency, and FOM for different designs of 160 GHz SIW modulator

No.	**BW (GHz)**	**Modulation Efficiency (%)**	**FOM (mW/GHz)**
1-1	20	82	34.72
1-2	20	82	6.94
1-3	20	75	32.98
1-4	20	75	6.25
1-5	25	85	5.55

Table 2.4: Calculated bandwidth, maximum modulation efficiency, and FOM for different designs of 160 GHz SIW modulator

No.	**L(mm)**	**F**	**BW (GHz)**	**$P_{\pi,eff}$ (mW)**	**Modulation Efficiency (%)**	**FOM (mW/GHz)**
2-2	20	1.2	36	202	85	4.08
2-3	20	1.2	36	159	52	3.24
2-4	20	1.2	36	117	75	2.38

2.6 Conclusion

A fundamentally novel structure for the development of push-pull electro-optical MZM is proposed, in which the modulating electrical field is guided by SIW as the driving traveling-wave structure instead of conventional TEM mode “electrodes” for millimeter-wave and THz applications. Performing theoretical millimeter-wave analysis together with optical simulation, the optical response is derived. At operation frequency of 160 GHz, more than 22% optical bandwidth is expected. Buffer layer thickness is optimized to increase the efficiency. SIW guided-wave structures together with the polymer optical waveguides and EO materials not only provide an excellent material system to support high-frequency low-voltage operation, but can also be

integrated into multifunctional devices, which are crucial for future millimeter-wave and THz photonic applications and next generation optical communication systems. To achieve ultra-broadband operation from DC to millimeter-wave and THz frequency ranges, SIW techniques can be combined with the conventional MSL or coplanar waveguide TEM mode techniques in designing hybrid electro-optical modulator systems. This research work presents a unique solution for millimeter-wave and THz modulator design platforms, which can be made at low loss, low voltage, and low cost.

2.7 Appendix

Electro-optical effect

The relationship between electrical flux density *D* and linearly polarized electrical field *E* in an isotropic EO medium is characterized by second-order nonlinear polarization density as

$$D = \varepsilon_0 E + P \tag{24}$$

where

$$P = \varepsilon_0[\chi^{(1)}\,\mathrm{E} + \chi^{(2)}\,\mathrm{E}.E] \tag{25}$$

$\chi^{(1)}$, linear susceptibility, is related to the medium refractive index by $n^2 = 1 + \chi^{(1)}$ and $\chi^{(2)}$ is second order susceptibility [33]. Therefore, the harmonic polarization density in response to the externally applied electric field $E_t = E_{opt}(\nu) + E_{RF}(f)$ (ν, optical frequency and *f*, millimeter-wave or THz frequency) is

$$\mathrm{P}_{NL}(\nu) = \varepsilon_0 E_{opt}(\nu)[\chi^{(1)} + \delta\chi]. \tag{26}$$

It follows that change in susceptibility is proportional to RF electric field ($\delta\chi \propto E_{RF}$) and it is converted into a refractive index change. In other words, the propagation of the guided-wave mode is affected by a change in susceptibility of the material. Therefore, a beam of light traversing an EO cell of length L to which an electrical field E_t is applied undergoes a phase shift $\Delta\Phi$ in any arm created by electric field E_t. From the perturbation analysis [34]:

$$\Delta\Phi = \pi \frac{r n^3 L \Gamma}{\lambda_0} \tag{27}$$

where Γ, overlap integral factor, is defined as [35]

$$\Gamma = \frac{\int_{EOcore} E_{RF}(x) E_{opt}{}^{2}(x,y)dxdy}{\int E_{opt}{}^{2}(x,y)dxdy} \tag{28}$$

In (27) and (28), is EO coefficient, λ_0 is the free-space wavelength, E_{opt} is the optical field, and E_{RF} is the modulating millimeter- wave or THz electrical field.

2.8 References

[1] K. Igarashi and K. Kikuchi, "Optical signal processing by phase modulation and subsequent spectral filtering aiming at applications to ultrafast optical communication systems," IEEE J. Sel. Topics Quantum Electron., vol. 14, no. 3, pp. 551–565, 2008.

[2] R.W. McGowan, G. Gallot, and D. Grischkowsky, "Propagation of ultrawideband short pulses of terahertz radiation through submillimeter diameter circular waveguides," Opt. Lett., vol. 24, no. 20, pp. 1431–1433, 1999.

[3] K. Kawase, Y. Ogawa, Y. Watanabe, and H. Inoue, "Non-destructive terahertz imaging of illicit drugs using spectral fingerprints," Opt. Express, vol. 11, no. 20, pp. 2549–2554, 2003.

[4] H. Han, H. Park, M. Cho, and J. Kim, "Terahertz pulse propagation in a plastic photonic crystal fiber," Appl. Phys. Lett., vol. 80, no. 15, p. 2634–2636, 2002.

[5] K. Wang and D. M. Mittleman, "Metal wires for terahertz wave guiding," Nature, vol. 432, no. 7015, pp. 376–379, 2004.

[6] J. Federici and L. Moeller, "Review of terahertz and subterahertz wireless communications," J. Appl. Phys., vol. 107, no. 11, pp. 111101(1)–111101(22), 2010.

[7] R. Piesiewicz et al., "Short-range ultra broadband terahertz communications: Concepts and perspectives," IEEE Antennas Propag. Mag., vol. 49, no. 6, pp. 24–39, 2007.

[8] E. L. Wooten et al., "A review of lithium niobate modulators for fiber-optic communications systems," IEEE J. Sel. Topics Quantum Electron., vol. 6, no. 1, pp. 69–82, Jan./Feb. 2000.

[9] M. Lee et al., “Broadband modulation of light by using an electro-optic polymer,” Science, vol. 298, no. 5597, pp. 1401–1403, 2002.

[10] L. R. Dalton, P. A. Sullivan, and D. H. Bale, “Electric field poled organic electro-optic materials: State of the art and future prospects,” Chem. Rev., vol. 110, no. 1, pp. 25–55, 2010.

[11] S. E. Thompson and S. Parthasarathy, “Moore’s law: the future of Si microelectronics,” Materials Today, vol. 9, no. 6, pp. 20–25, 2006.

[12] G. Gallot, S. P. Jamison, R. W. McGowan, and D. Grischkowsky, “Terahertz waveguides,” J. Opt. Soc. Amer. B, vol. 17, no. 5, pp. 851–863, 2000.

[13] R. Mendis and D. M. Mittleman, “Comparison of the lowest-order transverse-electric (TE1) and transverse-magnetic (TEM) modes of the parallel-plate waveguide for terahertz pulse applications,” Opt. Express, vol. 17, no. 17, pp. 14839–50, 2009.

[14] R. Mendis and D. M. Mittleman, “An investigation of the lowest order transverse-electric (TE1) mode of the parallel-plate waveguide for THz pulse propagation,” J. Opt. Soc. Amer. B, vol. 26, no. 9, pp. A6–A13, 2009.

[15] K. Wu, D. Deslandes, and Y. Cassivi, “The substrate integrated circuits - a new concept for high-frequency electronics and optoelectronics,” in 6th Int. Conf. Telecommun. Modern Satellite, Cable, Broadcasting Service (TELSIKS 2003), vol. 1, pp. P-III–P-X, 2003.

[16] K. Wu, “Towards the development of terahertz substrate integrated circuit technology” (invited paper), in IEEE Silicon Monolithic Integrated Circuits in RF Systems (SiRF), 2010 Topical Meeting on, pp. 116–119, New Orleans, LA, 2010,

[17] K. Wu, E. Mortazy, and M. Bozzi, “Development of microwave and millimeter-wave traveling-wave electro-optical devices using substrate integrated circuit concept,” Proc. Microw. Photon., 2007 IEEE International Topical Meeting on, pp. 62–65, 2007.

[18] W. Wang, Y. Shi, D. J. Olson, W. Lin, and J. H. Bechtel, “Push-pull poled polymer Mach-Zehnder modulators with a single microstrip line electrode,” IEEE Photon. Technol. Lett., vol. 11, no. 1, pp. 51–53, Jan. 1999.

[19] C. H. Cox, E. I. Ackerman, G. E. Betts, and J. L. Prince, “Limits on the performance of RF-over-fiber links and their impact on device design,” IEEE Trans. Microw. Theory Tech., vol. 54, no. 2, pp. 906–920, 2006.

[20] S. Tang, Z. Shi, D. An, L. Sun, and R. T. Chen, “Highly efficient linear waveguide modulator based on domain-inverted electro-optic polymers,” Opt. Eng., vol. 39, no. 3, pp. 680–688, 2000.

[21] P. L. Liu, B. J. Li, and Y. S. Trisno, “In search of a linear electrooptic amplitude modulator,” IEEE Photon. Tech. Lett., vol. 3, no. 2, pp. 144–146, 1991.

[22] T. Baehr-Jones, B. Penkov, J. Huang, P. Sullivan, J. Davies, J. Takayesu, J. Luo, T. D. Kim, L. Dalton, A. Jen, M. Hochberg, and A. Scherer, “Nonlinear polymer-clad silicon slot waveguide modulator with a half wave voltage of 0.25 V,” Appl. Phys. Lett., vol. 92, no. 16, p. 163303, 2008.

[23] J. J. O’Reilly, P. M. Lane, R. Heidemann, R. Hofstetter, “Optical generation of very narrow linewidth millimetre wave signals,” Electronics Lett., vol. 28, no. 25, pp. 2309–2311, 1992.

[24] T. Sakamoto, T. Kawanishi, and M. Izutsu, “Optoelectronic oscillator using push-pull Mach-Zehnder modulator biased at point for optical two-tone signal generation,” in Proc. Conf. Lasers Electro-Opt., CLEO, vol. 2, pp. 877–879, 2005

[25] T. Tokle, C. Peucheret, and P. Jeppesen, “Advanced modulation formats in 40 Gbit/s optical communication systems with 80 km fibre spans,” Opt. Commun., vol. 225, no. 1–3, pp. 79–87, 2003.

[26] T. Sakamoto, A. Chiba, and T. Kawanishi, “Electro-optic synthesis of 8PSK by quad-parallel Mach-Zehnder modulator,” in Proc. OFC/NFOEC, San-Diego, CA, 2009

[27] H. Zhang, M. C. Oh, A. Szep, W. H. Steier, C. Zhang, L. R. Dalton, H. Erlig, Y. Chang, D. H. Chang, and H. R. Fetterman, “Push-pull electro-optic polymer modulators with low half-wave voltage and low loss at both 1310 nm and 1550 nm,” Appl. Phys. Lett., vol. 78, no. 20, pp. 3136–3138, Sep./Oct. 2001.

[28] B. M. A. Rahman, V. Haxha, S. Haxha, and K. T. V. Grattan, “Design optimization of polymer electrooptic modulators,” J. Lightw. Technol., vol. 24, no. 9, pp. 3506–3513, Sept. 2006.

[29] R. A. Soref, J. Schmidtchen, and K. Petermann, “Large single-mode rib waveguides in GeSi-Si and Si-on-SiO2,” IEEE J. Quantum Electron., vol. 27, no. 8, pp. 1971–1974, Aug. 1991.

[30] M.-C. Oh et al., “Recent advances in electrooptic polymer modulators incorporating highly nonlinear chromophore,” IEEE J. Sel. Topics Quantum Electron., vol. 7, no. 5, pp. 826–835, Sep./Oct. 2001.

[31] U. Fischer, T. Zinke, J.-R. Kropp, F. Arndt, and K. Petermann, “0.1 dB/cm waveguide losses in single-mode SOI rib waveguides,” IEEE Photon. Technol. Lett., vol. 8, no. 5, pp. 647–648, 1996.

[32] B. Li, R. Dinu, D. Jin, D. Huang, B. Chen, A. Barklund, E. Miller, M. Moolayil, G. Yu, Y. Fang, L. Zheng, H. Chen, and J. Vemagiri, “Recent advances in commercial electro-optic polymer modulator,” in Proc. OFC/OC, pp. 115–117, 2007.

[33] B. E. A. Saleh and M. C. Teich, Fundamentals of Photonics, New York: Wiley, 1991.

[34] W. S. C. Chang, Fundamentals of Guided-Wave Optoelectronic Devices, Cambridge, U.K.: Cambridge University Press, 2010.

[35] C. M. Kim and R. V. Ramaswamy, “Overlap integral factors in integrated optic modulators and switches,” J. Lightw. Technol., vol. 7, no. 7, pp. 1063–1070, 1989.

[36] R. A. Becker, “Traveling-wave electro-optic modulator with maximum bandwidth-length product,” Appl. Phys. Lett., vol. 45, pp. 1168–1170, 1984.

[37] K. Kubota, J. Noda, and O. Mikami, “Traveling wave optical modulator using a directional coupler LiNbO3 waveguide,” IEEE J. Quantum Electron., vol. 16, no. 7, pp. 754–760, 1980.

[38] H. Chung, W. S. C. Chang, and E. L. Adler, “Modeling and optimization of traveling-wave LiNbO3 interferometric modulators,” IEEE J. Quantum Electron., vol. 27, no. 3, pp. 608–617, 1991.

[39] D. M. Pozar, Microwave Engineering, 4th ed., New York: Wiley, 2012.

[40] T. Hiraoka, T. Tokumitsu, and M. Aikawa, “Very small wide band MMIC magic T’s using microstrip on a thin dielectric film,” IEEE Trans. Microw. Theory Tech., vol. 37, no. 10, pp. 1569–1575, 1989.

[41] A. Chowdhury and L. McCaughan, “Figure of merit for near-velocity-matched traveling-wave modulators,” Opt. Lett., vol. 26, no. 17, pp. 1317–9, 2001.

[42] G. E. Ponchak and A. N. Downey, “Characterization of thin film microstrip lines on polyimide,” IEEE Trans. Compon., Packag. Manufac. Tech., vol. 21, no. 2, pp. 171–176, 1998.

[43] M. Konno, “Conductor loss in thin-film transmission lines,” Electron. Commun. Japan, pt. 2, vol. 82, no. 10, pp. 83–91, 1999.

[44] D. Stephens, P.R. Young, and I. D. Robertson, “Millimeter-wave substrate integrated waveguides and filters in photoimageable thick-film technology,” IEEE Trans. Microw. Theory Tech., vol. 53, no. 12, pp. 3832–3838, 2005.

[45] OptiBPM© ver. 11.0, by OptiWave Systems, Inc., Nepean, ON, Canada.

[46] D. M. Gill and A. Chowdhury, “Electro-optic polymer-based modulator design and performance for 40 Gb/s system applications,” J. Lightw. Technol., vol. 20, no. 12, pp. 2145–2153, 2002.

[47] D. M. Gill, D. Jacobson, and R. Wolfe, “Electro-Optic Modulators,” U.S. Patent 6 172 791, 2001.

[48] S. V. Burke, “The spectral index method for semiconductor rib and ridge waveguides,” J. Progr. Electromagn. Res., vol. 10, pp. 41–74, 1995.

[49] R. G. Hunsperger, Integrated Optics: Theory and Technology, 6th ed. New York: Springer-Verlag, 2009.

[50] Y. Zhou, M. Izutsu, S. Member, and T. Sueta, “Low-drive-power asymmetric Mach-Zehnder modulator with band-limited operation,” J. Lightw. Technol., vol. 9, no. 6, pp. 750–753, 1991.

[51] W. S. C. Chang, RF Photonic Technology in Optical Fiber Links, W. S. C. Chang, Ed. Cambridge, U.K.: Cambridge Univ. Press, 2002.

[52] D. Chen, H. R. Fetterman, A. Chen, W. H. Steier, L. R. Dalton, W. Wang, Y. Shi, “Demonstration of 110 GHz electro-optic polymer modulators,” Appl. Phys. Lett., vol. 70, pp. 3335–3337, 1997.

CHAPTER 3 ARTICLE 2 : LOW-LOSS AND LOW-DISPERSION TRANSMISSION LINE OVER DC-TO-THZ SPECTRUM

Overview: As pointed out in the previous chapter, to achieve an ultra-broadband operation from DC to millimeter-wave and THz frequency ranges, the non-TEM SIW techniques needs to be combined with the conventional TEM mode transmission lines. Therefore, in this following work, a new type of transmission line is devised and demonstrated that functions as a conventional microstrip line over lower frequency range and SIW at higher frequency range.

(IEEE Transactions on Terahertz Science and Technology, publication date: July 2016)

Low-Loss and Low-Dispersion Transmission Line Over DC-to-THz Spectrum

Faezeh Fesharaki[1], Tarek Djerafi[1], Mohamed Chaker[2], and Ke Wu[1]

[1]Poly-Grames Research Center, École Polytechnique de Montréal, QC H3T 1J4, Canada

[2]Centre Énergie Matériaux Télécommunications, Varennes, QC J3X 1S2, Canada

Abstract — Transmission lines or waveguides are the most fundamental building blocks of all electronic and photonic circuits and systems. Efforts have been made to incrementally evolve and improve existing transmission line structures to meet the increasingly stringent demands for signal transmission bandwidth and performance. However, a potentially revolutionary scheme or disruptive concept is required in support of future technological needs and bridging the gap between electronics and photonics. In this paper, we report on a fully integrated transmission line with simple structure that overcomes the long-standing bottleneck problems of high attenuation, strong dispersion, and low mode confinement in the guided-wave signal transmission from DC to terahertz (THz). This so-called mode-selective transmission line (MSTL) supports super-broadband and/or ultra-fast pulse signal propagation, making it a disruptive solution for building future high-performance analog and digital integrated electronics and photonics. To demonstrate this scheme, an MSTL on fused silica substrate is designed, fabricated, and experimentally measured from near-DC to 0.5 THz, showing less than 0.35 dB/mm attenuation and low dispersion characteristics over the entire frequency range.

IndexTerms — Dispersion, integrated circuits (ICs), loss, mode-selective transmission line (MSTL), terahertz (THz), transmission line, waveguide.

3.1 Introduction

Transmission lines and waveguides are the foundation for building analog and digital electronic and photonic circuits and systems, regardless of their operating wavelength, frequency or speed,

whose transmission quality and features are fundamentally characterized by two basic parameters of signal, namely loss (or attenuation) and dispersion. They are responsible for signal integrity of ultra-fast signal transmissions and interconnects such as picosecond pulse transmission and for broadband response ranging from DC to terahertz (THz).

Countless electromagnetic applications from DC to THz [1], and the growing needs for faster data communication rates have raised the question of whether traditional transmission lines can satisfy the demand of sophisticated applications for high performances [2]–[4]. The well-known bottlenecks related to high-speed digital and/or broadband analog signal interconnects, for example, have been the primary limitations to various integrated circuits (ICs) and systems with respect to their loss and dispersion-limited performance. This creates a strong motivation of searching for super wideband transmission lines and making related discoveries and innovations [1]–[4]. Likewise, high-performance transmission lines are essential for improving microwave photonic applications since traveling-wave-based structures are the key elements of guided-wave electro-optical or optoelectronic devices and circuits [5], [6]. In fact, if future high-speed digital or super-wideband analog circuits are to take advantage of the already-demonstrated switching speed of 2.0 ps to explore several potential applications for THz integrated circuits [1]–[4], inherent fundamental and physical limitations and issues must be addressed [6]. This is because all the existing transmission lines fail to yield a high-quality low-loss and low-dispersion DC-THz signal propagation on a chip or in an integrated transmission line [7], [8].

Ultra-high-speed pulse transmission (covering the DC-THz range) requires transmission lines with low dispersion and low loss, which can be readily integrated into optoelectronic cicuits and other devices [9]. However, current transmission lines used in electronic integrated circuits operate under the fundamental transverse electromagnetic (TEM) mode. They suffer from inherent drawbacks such as strong signal attenuation and pronounced modal dispersion at room temperature, and they are not useful over a broad frequency range from DC to THz [10]–[13].

To accommodate the required signal bandwidth, photonic technologies have been used and sophisticated modulation schemes have been applied. Still, wireless data rates remain relatively low [14], [15]. On the other hand, the bandwidth broadening in wireline applications and/or in computing systems has been enabled by expanding the number of input/output (I/O) port interconnects on a chip, thereby resulting in much greater cost and complexity [16]. However, a

viable approach for providing a truly large bandwidth with potentially minimum cost and complexity is to increase carrier frequency while deploying transmission lines operating up to up-mmW band and THz frequency range [16], [17]. Efforts have been made to evolve and improve the existing transmission line structures through the modification of the current waveguiding structures, but the ultimate scientific and technological challenge necessitates the emergence of a revolutionary or disruptive concept in doing so. It is of great importance for us to establish a robust transmission line structure that enables the development of all-frequency integrated circuits from DC to THz based on a single design and development platform.

Several waveguides were demonstrated within the last few years to meet the growing design needs for useful DC-THz applications. Among them, metal-wire THz waveguide is an attractive candidate but suffers from poor mode confinement as well as difficulty of mode excitation, and it cannot be integrated and used in chip interconnects [18], [19]. On the other hand, those studied high-frequency metallic, dielectric or metallo-dielectric waveguides proposed for low-loss THz applications cannot be useful because of their high-dispersion at low frequency due to their inherent frequency-cutoff [20]–[22], as they cannot operate over a frequency range starting from DC.

Waveguide mode profile is known to directly affect its transmission loss characteristics. The TEM mode of conventional planar transmission lines such as microstrip or coplanar waveguide (CPW) presents a longitudinal current density distribution that changes from a minimum at the center to an over-shoot (singularity) at the edges of the line. Therefore, TEM mode losses generally increase with frequency and/or narrowing linewidth as far as the conductor losses are concerned [23]. On the other hand, tangential electric field components of the transverse electric (TE) mode are vanishing on metallic surfaces, and losses of the TE mode decrease with frequency [24]. In 1970 at Bell Laboratories, it was demonstrated that the loss of TE_{01} mode can be made significantly small in a hollow metallic circular waveguide [25]. Subsequently, achieving a TE_{10} single-mode THz coupling and also a low-loss propagation up to 1 THz in a metallic rectangular waveguide was demonstrated [26]. However, the TE_{10} mode, like all other TE and TM modes, is dispersive because of its cutoff frequency. Therefore, it is not amenable to the guiding of broadband DC-THz signals or the transmission of pico-second pulses with all frequency components extending from DC to THz. This type of structure presents a prohibitive group velocity dispersion near the cutoff point. Such dispersive structures would result in non-recoverable distortion of ultra-fast pulse waveforms or DC-THz broadband signal transmissions. A promising study has been reported in

support of a dispersionless propagation of THz-bandwidth pulses through an ultra-low ohmic loss TE_{10} mode in a parallel metal plate waveguide (PMPW) [27], [28]. In addition, a plasmonic mode in PMPW has been observed in which the field distribution of TEM mode is abruptly changed [29]. However in PMPW, the diffraction loss is the dominant loss mechanism, and mitigating this diffraction loss is an important design consideration towards the practical realization of an ultra-low loss THz waveguide.

In this work, we devise and demonstrate a concept of transmission line that supports a dominant mode very similar to the microstrip line scenario in lower frequency range covering DC while it is automatically reconfigured to support the fundamental mode of rectangular waveguide at higher frequency. This mode-selective-transmission-line (MSTL), effectively covering the desired operation from DC to THz frequency range, is suitable for full DC-THz electromagnetic propagation and ultra-high-speed THz pulsed signal transmission. It is made to support a single-mode transmission over a super-wide range of frequency. MSTL, in a fully integrated form, exhibits a disparate modal characteristic of traditional planar microwave transmission lines and non-planar metallic waveguides. In fact, this solution is inspired from the development of substrate integrated waveguide (SIW) in which any non-planar waveguide structure can be synthetized in planar form [30]–[32]. Whereas, at low frequency in this case, MSTL operates under TEM-mode regime, the operating mode is gradually converted to a low-loss TE_{10} mode for operation at high frequency such as mmW and THz. This approach allows for the possibility of developing densely integrated interconnects and planar guided-wave structures for DC-THz bandwidth. This low-loss, low-dispersion and broadband integrated transmission line is a key enabling technology towards the development of a new generation of DC-to-THz electronic and photonic circuits and systems.

3.2 MSTL concept and design parameters

It is known that the planarization of non-planar waveguides such as rectangular waveguide allows a complete integration of any non-TEM-mode structures with any TEM-mode planar structures such as microstrip or coplanar waveguide, thanks to the recent development of SIW and substrate integrated circuits (SICs) [33], [34]. This suggests that two dissimilar structures can be made in the same substrate geometries with single processing techniques. Inspired by the concept of SIW and SICs, dissimilar propagation modes should be able to be allocated over a super-wide frequency range to take advantage of each mode while its disadvantages can be avoided. To be more specific,

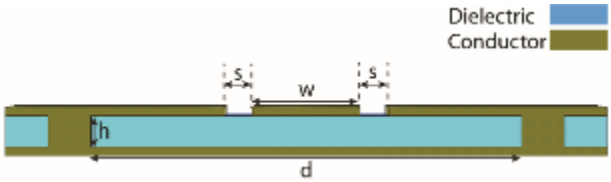

Figure 3.1: A cross section view of mode-selective transmission line (MSTL).

each frequency range can operate with one particular mode, for example, low-frequency operation is supported by TEM mode whereas high-frequency operation can be enabled by non-TEM mode, depending on the requirement of performances. Therefore, a special physical mechanism of autonomous mode selection or conversion is needed over frequency range. This is the foundation for the development of a MSTL in which mode selection is made possible over the use of a dispersion in connection with the MSTL's geometry.

Figure 3.2 shows the cross-sectional view of a typical MSTL and its associated coordinate system for our analysis. The structure is similar to a dielectric-filled rectangular waveguide or SIW but with two parallel slots on the top conductor forming a metal strip in the center. The substrate has dielectric constant ε_r, thickness h, and width d. The metallic layer has a large but finite conductivity, and the center metallic strip has width w and the slots are of size s. From DC up to cutoff frequency of TE_{10} mode, the mode characteristic is very similar to the TEM mode of a microstrip line. The cutoff frequency f_{cutoff} of the TE_{10} mode is determined by $f_{cutoff} = (2d\sqrt{\mu_0\varepsilon_0\varepsilon_r})^{-1}$. At this frequency, the attenuation constant of TE_{10} is very large, which causes a mode transition from the propagating TEM mode to TE_{10} mode [35], and the electromagnetic power is transferred from one mode to another with the following interaction term:

$$P_{TE_{10},TEM} = \frac{1}{2}\oint_s E_{TE_{10}} \times H^*_{TEM} . a_z ds \qquad (1)$$

Since $E_{TE} = E_y.a_y$, $H_{TEM} = H_x.a_x$, according to equation (1), the total coupling from one mode to the other is attained ($E_y.\, a_y \times H_x.\, a_x.\, a_z = E_y.\, H_x.\, a_y \times a_x.\, a_z = E_y.\, H_x.\, a_z.\, a_z = E_y.\, H_x\ (a_z.\, a_z=1)$).

The dimensions of the MSTL are purposely selected to ensure the expected behavior over the desired frequency range. First, thickness h is chosen thin enough to avoid the appearance of unwanted surface modes at higher frequency [36], and width d is chosen as $d > 8h$. Therefore, according to the theory of potential for microstrip lines [37], in the lower frequency range, two conducting side walls have no influence on the characteristics of the microstrip line, and field and

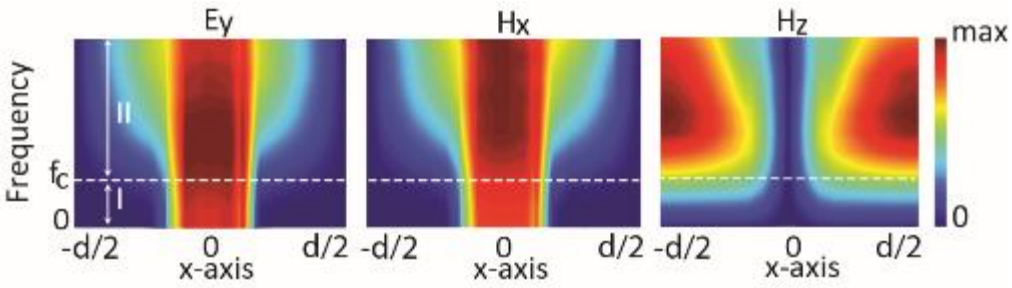

Figure 3.2: Fields and current distributions in a typical MSTL. In frequency region I, MSTL works under a mode with characteristic similar to TEM mode. In region II, MSTL operates under a mode with characteristic similar to TE_{10} mode.

current distributions are very similar to the cases of a microstrip line. It is also important to avoid a potential stimulation of the CPW mode which is undesired in MSTL. In CPW operation, the effective dielectric constant is close to the average of the dielectric constant of substrate (50% filling factor) and that of free space. While the effective dielectric constants of the microstrip TEM mode and waveguide TE_{10} mode converge to the substrate's relative permittivity, providing a smooth transition from one to the other. Moreover, in CPW mode of propagation, horizontal electric field is large, which is not suitable for some applications, e.g., in certain types of electro-optical device. To stay away from the CPW mode, dimensions w and s are chosen with regard to the thickness to ensure $w/2 + s > h$ [38].

In our demonstration, single crystal fused silica wafer is considered as the substrate for MSTL to minimize its dielectric loss. Our available thinnest fused silica wafer has the thickness of h = 50 μm with dielectric constant ε_r = 4.27. Width d is selected equal to 600 μm to have the frequency cutoff of TE_{10} mode at 120 GHz, and dimensions w and s are selected equal to 3h and 0.8h, respectively. Two numerical methods, finite integration technique (FIT) of CST Microwave Studio, and finite element method (FEM) [39] of HFSS, are used to simulate the proposed MSTL. Figure 3.2 shows the field and current distributions computed with the FEM. In the lower frequency range (I: DC to f_{cutoff}), fields are confined to the proximity of the metallic strip. Both electric and magnetic fields, E_y and H_x having a uniform distribution, are lying in a perpendicular plane to the axis of propagation as one would expect for the TEM mode [37]. As frequency approaches the cutoff of the TE_{10} mode, an evolution in the field distribution is observed where the field spreads out to the lateral boundaries, and therefore, the power is converted to TE_{10} mode. Magnetic field

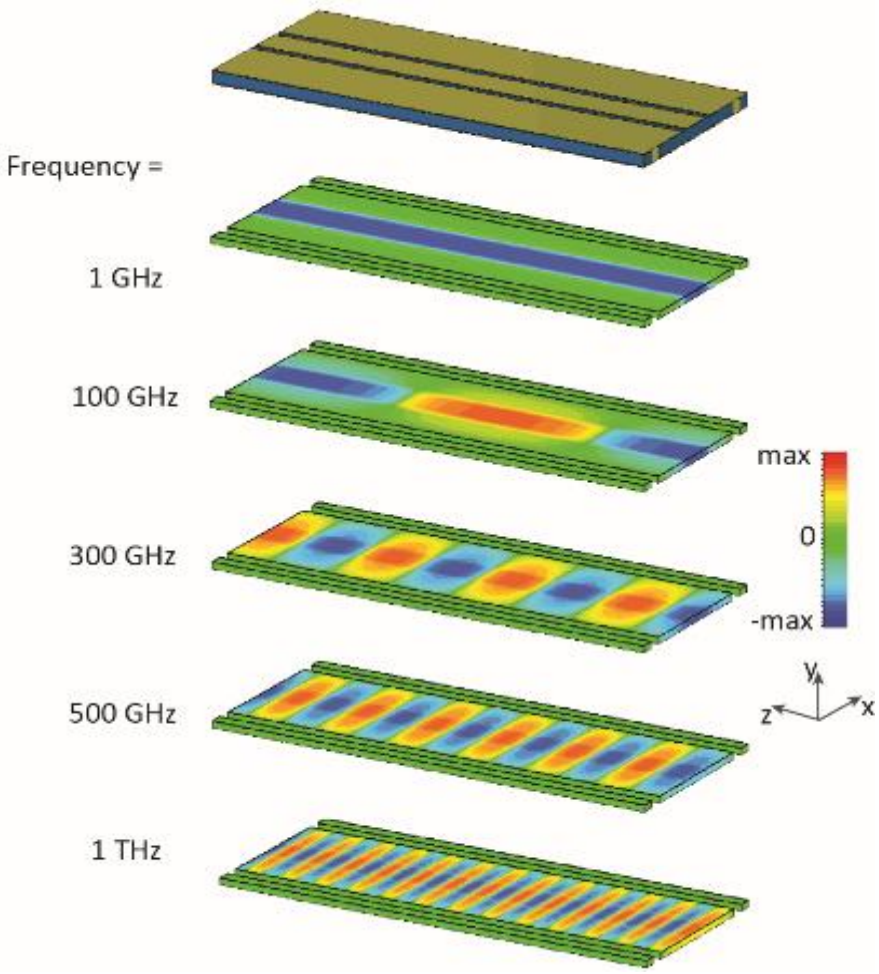

Figure 3.3: A schematic of MSTL and its principle of operation: the conductor configuration leads the structure to operate under the TEM mode in lower frequency range and changing gradually to TE_{10} mode in higher frequency range.

H_z appears and bouncing propagating plane waves emerge. The current distribution is spreading over the whole waveguide width. Figure 3.3 illustrates the electric field distribution in the MSTL calculated with FIT. As is shown, a unique propagation phenomenon occurs: as frequency increases, a transition in the mode configuration occurs, and energy distribution extends from the center to the edges of the waveguide. Figure 3.4 shows the propagation characteristics of the fundamental mode supported by an MSTL. In the same figure, the dispersion relation for the first mode supported by the microstrip line (line width w) and the rectangular waveguide (width d) on the same substrate are also demonstrated. In the lower frequency range (I: DC to 120 GHz), fields are confined to the proximity of the strip and effective permittivity ε_{eff} and group velocity V_g of

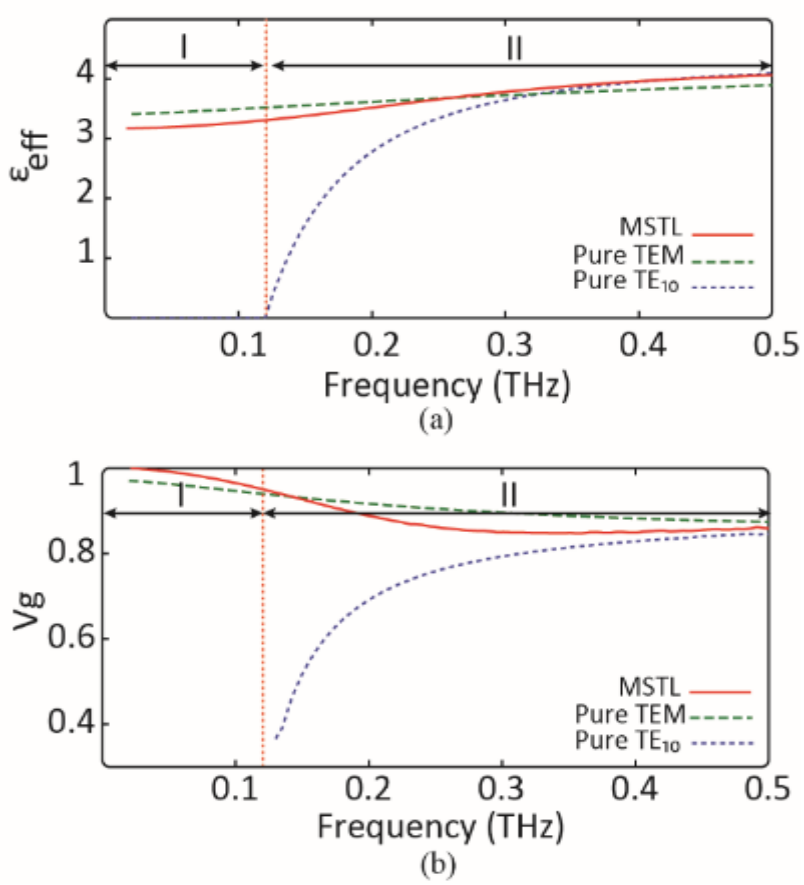

Figure 3.4: a) Effective dielectric constant of MSTL (h = 50 µm, d = 12h, s = 0.8h, w = 3h), and comparison with effective dielectric constant of microstrip line TEM (h = 50 µm, d >>h, s>>h, w = 3h), and rectangular waveguide TE_{10} mode (h = 50 µm, d = 12h, s = 0, w = d/2) on fused silica substrate (ε_r = 4.27). b) Group velocity of MSTL (h = 50 µm, d = 12h, s = 0.8h, w = 3h), and comparison with effective dielectric constant of microstrip line TEM (h = 50 µm, d>> h, s>> h, w = 3h), and rectangular waveguide TE_{10} mode (h = 50 µm, d = 12h, s = 0, w = d/2) on fused silica substrate (ε_r = 4.27).

the dominant mode are almost coincident with the TEM mode of microstrip line. As frequency approaches the cutoff of the TE_{10} mode, since the electric lines are more confined to the substrate dielectric, effective dielectric constant of the propagating mode is slightly increased. The propagating mode is gradually converted to TE_{10} mode from TEM mode; although a pure TE_{10} propagation mode of rectangular waveguide is very dispersive near its cutoff frequency point,

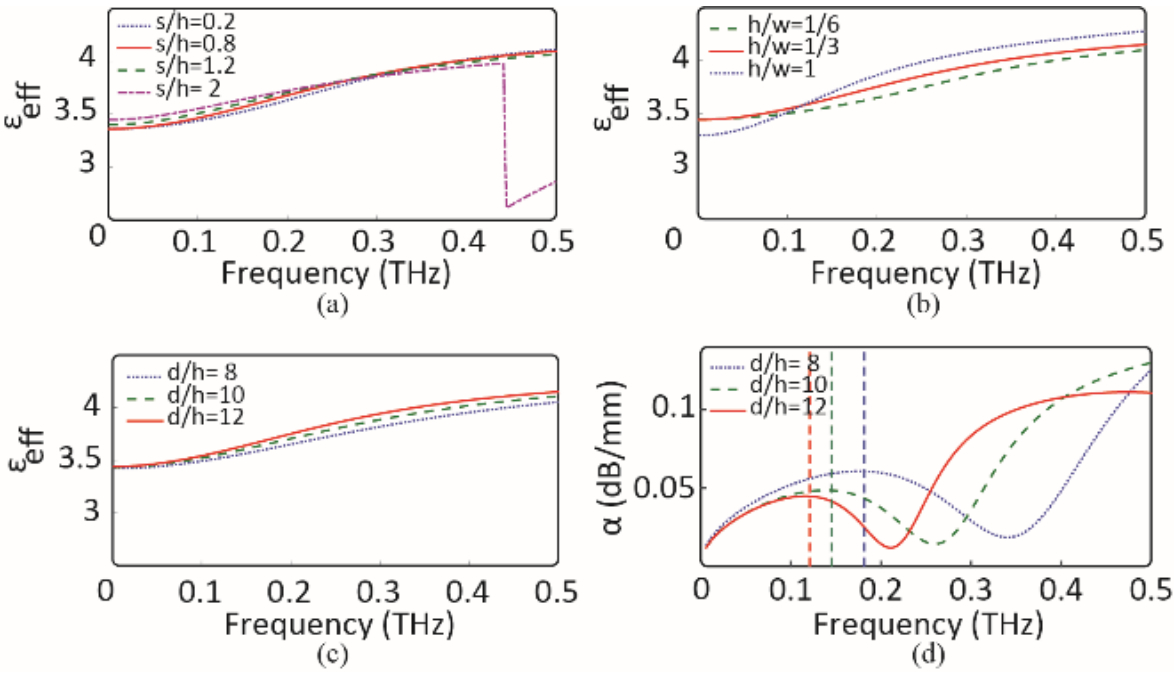

Figure 3.5: Computed effective dielectric constant as a function of frequency: a) Slot width s as parameter, and ε_r = 4.27, h = 50 µm, d = 12h, w = 3h. b) Substrate thickness h as parameter, and ε_r = 4.27, h = 50 µm, d = 12h, s = 0.8h. c) Computed effective dielectric constant as a function of frequency, waveguide width d as parameter, and ε_r = 4.27, h = 50 µm, s = 0.8h, w = 3h. d) Computed propagation loss as a function of frequency, waveguide width d as parameter, and ε_r = 4.27, h = 50 µm, s = 0.8h, w = 3h.

MSTL shows a smooth effective dielectric constant and group velocity insuring dispersionless characteristics, since around that region, a hybrid combination of TEM and TE_{10} modes takes place. In order to understand the physical and electrical behaviors of the structure, and also to identify the underlying design limitations, parametric study is performed using a semi-analytical approach derived from the method of lines (MoL) [40]. Figure 3.5(a) presents the effective dielectric constant ε_{eff} of MSTL for a variation of slot width s. As is shown, for a given constant thickness h with increasing s above 2h, the occurrence of CPW mode at higher frequency is observed. On the other hand, as illustrated in Figure 3.5(b), for a given constant width of center conductor w and with increasing h above w, the CPW mode in lower frequency range appears. The effect of waveguide over the cutoff frequency of TE10 mode and the occurrence of higher-order modes. For a given constant thickness (h = cte), with an increasing value of d, the cutoff frequency of TE_{10} shifts to a lower frequency range. This can be observed from both ε_{eff} curves in Figure 3.5 (c) and loss curves

in Figure 3.5 (d). When width *d* is greater than a half-wavelength, mode conversion happens and power is width d on the performance is illustrated in Figure 3.5 (c), (d). The line width provides a direct control over the cutoff frequency of TE_{10} mode and also the occurrence of higher-order modes. For a given constant thickness (h = cte), with an increasing value of d, the cutoff frequency of TE_{10} shifts to a lower frequency range. This can be observed from both ε_{eff} curves in Fig.5c and loss curves in Fig.5d. When width d is greater than a half-wavelength, mode conversion happens and power is handed over from semi-TEM to semi-TE_{10} mode. The transverse resonance method [41] is used to study the TE_{10} mode propagation, and it is seen that the slits shift down the cutoff of the TE_{10} mode by just about 0.5%. A smooth change in the curve of effective dielectric constant ensures a low-dispersion behavior. The total loss is increased up to the cutoff frequency of TE_{10} mode. The attenuation of TE_{10} mode is high at this frequency; therefore, the total loss follows a decreasing trend until reaching a minimum and then rises again following an almost rigid trend after around 200 GHz. The TE_{10} propagating mode can be synthesized by two plane waves that bounce between the long sides of the waveguide and undergo a power loss at each bounce because of the imperfectly conducting surfaces [6]. In rectangular waveguide, the top and bottom conductor surfaces as well as side walls lead to this power loss. However in MSTL, the mode is more confined and metallic side walls do not contribute to the conductor loss. Therefore, the metallic loss is lower compared to that of a rectangular waveguide.

3.3 Fabrication and measurement

To validate the concept, MSTL structure was fabricated and measured up to 0.5 THz. The fabrication of MSTL samples were done in two different substrate platforms. The fabrication on a fused silica substrate was done on a wafer with 50 μm thickness. From the previous section, the optimized dimensions were selected as d=600 μm, s=40 μm, and w=150um. In addition to the fabrication of MSTL on the fused silica substrate, a PCB prototype was also designed and optimized using RT/Duroid® 6002 laminates substrate from Rogers Corporation with low dielectric constant ε_r = 2.94 and low loss substrate tanδ=0.0012, which is a proper choice for high frequency applications. In this case, substrate thickness is chosen to be 127 μm, which is the minimum available thickness of this substrate. Width *d* is selected equal to 1500 μm. To minimize loss and dispesion of the structure, *w* and *s* are selected equal to 305 and 203 μm, respectively. Samples of the fabricated circuit on quartz and PCB are respectively shown in Figure 3.6(a) and

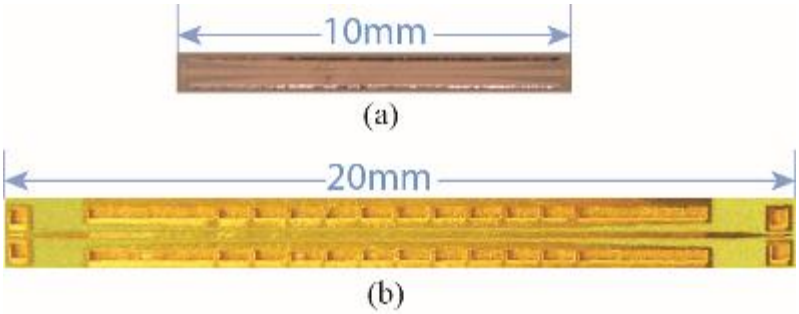

Figure 3.6: a) A fabricated sample line of MSTL on fused Silica substrate with a transition to picoprobe. b) A fabricated sample line of PCB prototype of MSTL with a transition to picoprobe.

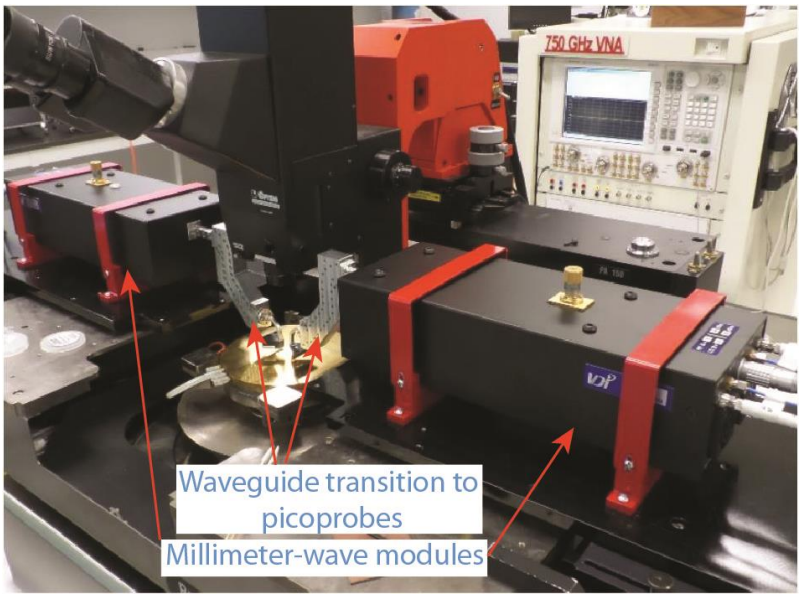

Figure 3.7: Measurement setup.

Figure 3.6(b). The fabrication of MSTL can also be performed using a microshiledling technology that would decrease the propagation loss even further [42], [43].

The coupling/decoupling could be simply achieved within an integrated platform on the same substrate. Since our available measurement equipment are limited, the only choice we had was to use GSG wafer probes that drive a GCPW head. The position between the middle point of the center strip and the edges of the launch transition pads is calculated and designed to avoid a potential excitation of CPW mode at the input. This method also avoids slot modes, preventing possible pad parasitic capacitive effects, and improving the placement accuracy of the probe tips.

Via-hole is used for our PCB prototype. As operating frequency increases, the via-hole input impedance becomes inductive because its electrical length to the ground plane increases. The reactance of the grounding via hole becomes noticeable and then prejudicial to calibrations and measurements. The used large grounding via-hole dimensions ensure the limitation of via-hole inductance and allow its use in grounding and building a launch transition for on-wafer measurements. For the fused-silica prototype, an RF short-circuit designed with one quarter wavelength open sector was used in the launch transition. The use of an open stub overcomes the undesirable reactive effects and avoids some fabrication uncertainties at higher frequency.

3.3.1 **Fabrication**

For the fabrication of MSTL on fused silica (quartz) substrate, first the back coating metalization of the substrate was done with sputtering and the thin 50 μm quartz substrate were stuck to a thick 500 μm quartz substrate. Because quartz is optically transparent, it presents a major difficulty for laser drilling. We used abrasive waterjet for drilling the side holes as this tool is capable of cutting a wide variety of materials using the waterjet stream to accelerate abrasive particles to erode the material. After filling up the holes and final top sputtering, the patterning was made using lithography with less than 1 μm precision.

For the PCB prototype, fabrication was done on RT/duroid® 6002 laminates from Rogers Corporation with our standard printed circuit board (PCB) process with 1 mil precision and minimum 3 mil trace/gap width combining with laser cutting to define the lateral walls.

3.3.2 **Device measurements**

Picoprobes with ground-signal-ground (GSG) head were used in the measurement. To perform wafer measurement, a launch structure was required to interface between the GSG coplanar probe head and the MSTLs. The required distance between the middle of the center strip and the edges of the launch transition pads was designed precisely to minimize the mismatch and reflection. A radial open stub circuit was used to form the launch transition, and a thru-reflect-line (TRL) calibration method was used to avoid calibration errors and to define the measurement reference planes. TRL kits were designed for each 1:8 frequency band. To test the MSTL, a PNA-X with millimeter-wave modules was used. The PNA-X that we had used was limited to 0.75 THz but our available millimeter-wave modules were limited to 0.5 THz at the present time. Therefore, S-

parameter measurement was done up to 0.5 THz (Figure 3.7). The on-wafer measurements using high-frequency probes provided accurate and repeatable results up to THz band.

3.3.3 Time domain characterization

Knowing the physical characteristics of MSTL, finite-size causal passive component, accurate time-domain model was obtained from band-limited S-parameter data with the use of Kramers-Kronig relation [44] which is provided by ADS Transient Convolution Element.

3.3.4 Results

The transmission characteristics are presented in Figure 3.8. Figure 3.8(a) shows the theoretical and experimental propagation phase constants over the whole frequency range of interest. Figure 3.8(b) shows the theoretical and experimental attenuations of the MSTL compared to the experimental results of a low dispersion thin-film microstrip line fabricated on a low-resistivity Si substrate with polymerized cyclotene as a high-quality dielectric from [45]. As expected, the MSTL grants a continuous low attenuation over the entire measured frequency range. The measured attenuation displays a frequency dependency; close to the TE_{10} cutoff frequency of 0.12 THz, the attenuation falls off and goes up again up to 0.2 THz from where it remains constant. Up to 0.15 THz the attenuation is less than 0.1 dB/mm and it continues in a range of 0.3 to 0.35 dB/mm up to 0.5THz. In case of the microstrop line, however, the attenuation increases with frequency up to 3 dB/mm at 0.5 THz.

In order to provide more accurate and detailed information on dispersion, the MSTL time domain characteristic is illustrated. Figure 3.8(c) shows the propagation of a Gaussian pulse on the line derived from PCB prototype continuous measurement results. A Gaussian pulse with 1ps full width at half maximum (FWHM) is used as the reference to observe the evolution of Gaussian-shaped picosecond pulse on MSTL. In the same figure, a Gaussian pulse propagation derived from the theoretical study using an inverse Fourier transform is also presented for the same line. A 50 Ω microstrip line is also designed on the same substrate and simulated in a Method of Moments of Advanced Design System (MoM ADS) and the same Gaussian pulse is observed after passing through the same length of this line as well. The figure clearly shows the difference in the dispersion characteristics of these transmission lines.

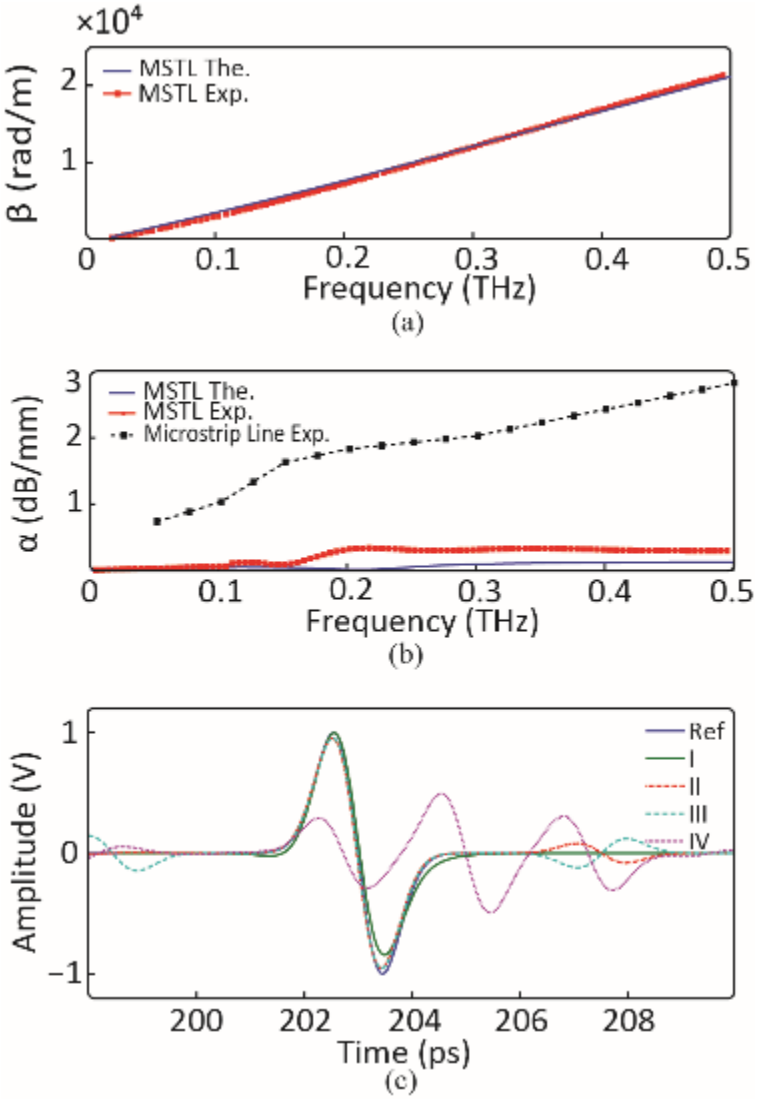

Figure 3.8: a) Comparison of theoretical and experimental propagation phase constants (β) of MSTL fabricated on fused silica (h = 50 µm, d = 12h, s = 0.8h, w = 3h). b) Comparison of theoretical and experimental propagation loss characteristics of MSTL fabricated on fused silica (h = 50 µm, d = 12h, s = 0.8h, w = 3h) and thin-film microstrip line from [45]. c) Gaussian pulse (Ref: 1ps FWHM) propagation on PCB prototype pf MSTL line and bend as well as comparison with that of microstrip line- I: MSTL line (10mm long) from theoretical calculation, II: MSTL line from experimental results, III: MSTL bend from experimental results, IV: microstrip line (10mm long, the same substrate as that of MSTL, and 50 Ω characteristic impedance) from ADS MoM simulation.

In addition to our fabrication tolerances, other factors may cause the discrepancy of results

between the theoretical models versus the fabricated counterparts for measurement. The copper surface roughness of substrates affects the conductor losses as well as the propagation constant of the transmission line [46]. The MSTL is subject to such copper surface roughness effects, and the field and current move more toward the bottom of the metals where the roughness lies. The conductor trapezoidal effect or "edge profile," where the conductors are supposed to be rectangular, can increase the influence of the copper surface roughness on the losses and the propagation constant. Additionally, radiation loss, although very negligible, is not considered in the MoL theoretical calculations.

3.4 Conclusion

In this work, a DC-to-THz low-loss and low-dispersion signal waveguiding structure is introduced. This transmission line is designed to be an automatic mode-selective and operates with TEM mode over low frequency range and TE mode over high frequency range. Experimental results and numerical simulations are found in a good agreement over DC to 0.5 THz frequency range and they show the mode conversion effects. The loss is less than 0.35dB/mm which is more than 20 times less than the microstrip counterpart from 0.1 THz to 0.5 THz. Dispersion-less characteristic is verified by applying the measurement results to estimate the propagation of a typical Gaussian pulse along straight and curved MSTL. The comparison with microstrip line shows clearly the improvement and advantages of using MSTL in high date rate applications. The proposed waveguide also provides a self-packaging solution for integrated electronic and photonic circuits which is essential for developing the DC-THz integrated platforms, as it is predicted that unavoidable dielectric loss and insufficient patterning accuracy may limit the use of current packaging techniques for THz electronics and photonics applications. Combining the benefits of a low-cost planar processing technology with the low-loss intrinsic to the operation mode, MSTL seems to present a most promising candidate that enables current and future ICs developments and applications towards high-performance, high-density and broadband DC-THz modules and high-speed interconnects.

3.5 References

[1] M. Tonouchi, "Cutting-edge terahertz technology," Nat. Photon, vol. 1, no. 2, pp.97–105, 2007.

[2] R. Kirchain, L. Kimerling L, “roadmap for nanophotonics,” Nat. Photon, vol. 1, no. 6, pp.303–305, 2007.

[3] M. Bohr, “Interconnect scaling - The real limiter to high performance,” Proc. IEDM, pp. 241 –244, 1995.

[4] D. Loke D et al, “Ultrafast phase-change logic device driven by melting processes,” Proc. Natl. Acad. Sci. USA, vol. 111, no. 37, pp. 13272–13277, 2014.

[5] J. Capmany, D. Novak, “Microwave Photonics combines two worlds,” Nat. Photon, vol. 1, pp. 319–330, 2007.

[6] L. Dalton, P. Sullivan, D. Bale, “Electric field poled organic electro-optic materials: state of the art and future prospects,” J. Chemical reviews, vol. 110, no. 1, pp. 25-55, 2009.

[7] P. Peercy, “The drive to miniaturization,” Nat., vol. 406, pp.1023–1026, 2000.

[8] R. Chau, B. Doyle, S. Datta, J. Kavalieros, K, Zhang, “Integrated nanoelectronics for the future,” Nat. Mater., vol. 6, pp. 810–812, 2007.

[9] T. Spencer, T. Osborn, P. Kohl P, “High-Frequency Chip Connections,” Science, vol. 320, pp.756–757, 2008.

[10] R. Willardson, Semiconductors and semimetals, Academic Press. 1977

[11] D. H. Auston, “Ultrafast Optoelectronics,” in Ultrashort Laser Pulses and Applications, 2nd ed., vol. 60 in Topics in Applied Physics, W. Kaiser, Ed., Berlin, Springer-Verlag, 1988.

[12] G. Hasnain, A. Dienes, J. Winnery, “Dispersion of picosecond pulses in coplanar transmission lines,” IEEE Trans. Microwave Theory Tech., vol. 34, pp.738–741, 1989.

[13] D. Phatak, A. Defonzo, “Dispersion characteristic of optically excited coplanar striplines,” IEEE Trans. Microwave Theory Tech. vol. 38, pp.654–661, 1990.

[14] D. Hillerkuss et al, “26 Tbit s-1 line-rate super-channel transmission utilizing all-optical fast Fourier transform processing,” Nat. Photon, vol. 5, no. 6, pp.364–371, 2011.

[15] S. Narenda, L. Fujino, K. Smith, “Through the Looking Glass Continued (III): Update to Trends in Solid-State Circuits and Systems from ISSCC 2014 [ISSCC Trends],” IEEE Solid-State Circuits Magazine, vol. 6, no. 1, pp. 49–53, 2014.

[16] K. Feher, Digital Communications, Englewood Cliffs (NJ: Prentice-Hall), 1981.

[17] Wooten E et al, “A review of lithium niobate modulators for fiber-optic communications systems,” IEEE J. Select Topics Quantum Electron, vol. 6, no. 1, pp.69–82, 2000.

[18] K. Wang, D. Mittleman, “Guided propagation of terahertz pulses on metal wires,” J. OSA B, vol. 22, pp. 2001-2008, 2005.

[19] K. Wang, D. Mittleman, “Metal wires for terahertz wave guiding,” Nat., vol. 432, pp. 376-379, 2004.

[20] R. Mendis, D. Grischkowsky, “Plastic ribbon THz waveguides,” J. Appl Phys, vol. 88, pp. 4449, 2000.

[21] C. Yeh et al, “Communication at millimetre-submillimetre wavelengths using a ceramic ribbon,” Nat., vol. 404, pp. 584-588, 2000.

[22] G. Gallot, S. Jamison, R, McGowan, D. Grischkowsky, “Terahertz waveguides,” J. OSA B, vol. 17, no. 5, pp. 851-863, 2000.

[23] H. Casimir, J. Ubbink, The skin effect. I. Introduction the current distribution for various configurations, Philips Research Labs., Eindhoven, Netherlands, 1967.

[24] R. Mendis, D. Mittleman, “An investigation of the lowest-order transverse- electric (TE1) mode of the parallel-plate waveguide for THz pulse propagation,” J. Opt. Soc. Am. B, vol. 26, no. 9, pp. A6–A13, 2009.

[25] T. Abele, D. Alsberg, P. Hutchison, “A high-capacity digital communication system using TE01 transmission in circular waveguide,” IEEE Trans. on Microwave Theory and Tech., vol. 23, no. 4, pp. 326–333, 1975.

[26] D. Alsberg, J. Bankert, P. Hutchison, “WT4 millimeter waveguide system: The WT4/WT4a millimeter-wave transmission system,” Bell System Tech. J., vol. 56, pp. 1829–1848, 1977.

[27] R. Mendis, D. Grischkowsky, “THz interconnect with low-loss and low-group velocity dispersion,” IEEE Microwave and Wireless Compon Lett., vol. 11, no. 11, pp. 444–446, 2001.

[28] R. Mendis, D. Grischkowsky, “Undistorted guided-wave propagation of subpicosecond terahertz pulses,” Optics lett., no. 11, vol. 26, pp. 846–848, 2001.

[29] J. Liu, R. Mendis, D. Mittleman, “The transition from a TEM-like mode to a plasmonic mode in parallel-plate waveguides,” Appl Phys Lett, vol. 98, pp. 231113, 2011.

[30] D. Deslandes, K. Wu, “Integrated microstrip and rectangular waveguide in planar form,” IEEE Microwave and Wireless Components Lett., vol. 11, pp. 68–70, Feb 2001.

[31] K. Wu, “Substrate integrated circuits (SICs) for terahertz electronics and photonics: current status and future outlook,” FREQUENZ, vol. 65, pp. 255–259, 2011.

[32] D. Deslandes, K. Wu, “Accurate modeling, wave mechanisms, and design considerations of substrate integrated waveguide,” IEEE Trans. Microwave Theory Tech., vol. 54, pp. 2516–2526, June 2006.

[33] A. Patrovsky, M. Daigle, and K. Wu, “Coupling mechanism in hybrid SIW-CPW forward couplers for millimeter wave substrate integrated circuits,” IEEE Trans. Microwave Theory Tech., vol. 56, no. 11, pp. 2594–2601, November 2008.

[34] K. Wu, D. Deslandes, and Y. Cassivi, “The substrate integrated circuits - a new concept for high-frequency electronics and optoelectronics,” in 6th Int. Conf. Telecommun. Modern Satellite, Cable, Broadcasting Service (TELSIKS 2003), vol. 1, pp. P-III–P-X, Oct. 2003.

[35] R. Collin, Field Theory of Guided Waves, ch. 4, 5, McGrow-Hill Book Company INC. NY, 1960.

[36] D. Pozar, Microwave Engineering, ch3, Wiley, ed.4, NY, 2009.

[37] B. Kretch, R. Collin, “Microstrip dispersion including anisotropic substrates,” IEEE Trans. Microwave Theo and Tech, vol. 35, pp.710–718, 1987.

[38] G. Ghione, C. Naldi, “Coplanar waveguides for MMIC applications: Effect of upper shielding, conductor backing, finite-extent ground planes, and line-to-line coupling,” IEEE Trans on Microwave Theo and Tech, vol. 35, pp. 260–267, 1987.

[39] J. Deibel, L. Berndsen, K, Wang, D. Mittleman, “Finite-element method simulations of guided wave phenomena at terahertz frequencies,” Proc. IEEE, vol. 95, pp.1624–1640, 2007.

[40] U. Schulz and R. Pregla, “A new technique for the analysis of the dispersion characteristics of planar waveguides and its application to microstrips with tuning septums,” Radio Sci., vol. 16, pp. 1173–1178, 1981.

[41] N. Marcuvitz, Waveguide Handbook, vol. 10, 1951: McGraw-Hill.

[42] T. M. Weller, L. P. B. Katehi, and G. M. Rebeiz, “High-performance microshield line components,” IEEE Trans. Microwave Theory and Tech., vol. 43, pp. 534–543, 1995.

[43] M. Moallem, J. East and K. Sarabandi, “Optimally designed membrane-supported grounded CPW structure for submillimeter-wave applications,” 2009 IEEE Antennas and Propagation Society International Symposium, Charleston, SC, pp. 1–4, 2009.

[44] C. Warwick, “Understanding the Kramers-Kronig relation using a pictorial proof,” J. Physi Rev, vol.104, pp.1760–1770, 1956.

[45] H. Heiliger, M. Nagel, H.G. Roskos, H. Kurz, F.Schnieder, W.Heinrich, R.Hey, and K. Ploog, “Low-dispersion thin-film microstrip lines with cyclotene (benzocyclobutene) as dielectric medium,” Appl. Phys. Lett., vol. 70, no. 17, pp. 2233–2235, 1977.

[46] S.P Morgan, “Effect of surface roughness on eddy current losses at microwave frequencies,” J. of Applied Physics, vol. 20, no. 4, pp. 352–362, 1949.

CHAPTER 4 ARTICLE 3 : GUIDED-WAVE PROPERTIES OF MODE-SELECTIVE TRANSMISSION LINE

Overview: MSTL was devised and demonstrated in chapter 3. This chapter presents a detailed study on MSTL guided-wave characteristic. This includes a theoretical study, full-wave analysis through numerical simulations, parametric study, and optimization as well as design guidelines.

(IEEE Transactions on Microwave Theory and Techniques, submission date: June 2016)

Guided-Wave Properties of Mode-Selective Transmission Line

Faezeh Fesharaki[1], Tarek Djerafi[1], Mohamed Chaker[2], and Ke Wu[1]

[1]Poly-Grames Research Center, École Polytechnique de Montréal, QC H3T 1J4, Canada

[2]Centre Énergie Matériaux Télécommunications, Varennes, QC J3X 1S2, Canada

Abstract — A "smart" transmission line for low-loss and low-dispersion signal propagation over the entire DC-to-terahertz (THz) frequency range is studied theoretically and experimentally. This so-called mode-selective transmission line or simply "MSTL" operates with a frequency-dependent mode-switching behavior. This self-adaptive mode-selective guided-wave structure begins with the propagation of electromagnetic waves over the lower frequency range in the form of a quasi-TEM fundamental mode similar to the microstrip line case, then followed by a fundamental quasi-TE_{10} mode with reference to rectangular waveguide over the higher frequency region. To gain insight into the physical mechanism and fundamental features of this mode-selective transmission line, a detailed semi-analytical hybrid-mode analysis is developed through the application of a method of lines (MoL). This method allows accurate and effective modeling of MSTL guided-wave properties. Propagation characteristics of this proposed mode-agile structure in terms of dispersion, modal, and loss properties are examined, which leads to the establishment of some basic MSTL design guidelines. Numerical results confirm the expected mode conversion and low-loss behavior through the observation of field evolutions along the structure. For experimental verification, a set of MSTL prototypes are fabricated on two different substrates through dissimilar fabrication processes. Measurements are carried out from DC-to-500 GHz using a vector network analyzer. Excellent agreement between theoretical and experimental results is observed. It is confirmed that the low-dispersion and low-loss behavior of MSTL makes it an outstanding integrated waveguide in support of high-performance super-broadband signal transmission and/or ultra-fast pulse propagation in a fully-integrated platform.

Index Terms — Mode-selective transmission lines (MSTL), hybrid mode analysis, method of lines (MoL), super-broadband signal, ultra-fast pulse.

4.1 Introduction

4.1.1 General

Electromagnetic (EM) waveguiding techniques have been established as one of the earliest milestone developments in radiofrequency (RF), wireless, and microwave engineering. They have been truly instrumental as any successful and practical design and application of high-frequency electromagnetic devices, circuits, and systems, are closely related to the deployment of their distinctive guided-wave properties. Although rectangular waveguide (RW) has been in use since the 1930s, the intensive development of microstrip line and coplanar waveguide (CPW), which started, respectively, in the 1950s and 1960s, has been considered as the most critical driving force for the design of RF and microwave integrated circuits and systems. Integrated transmission lines in the form of microstrip, CPW, and their derivatives of geometry have been the backbone of the modern electronic and photonic integrated circuits and systems. Following the evolution of ICs technologies and processing techniques in the field, those fundamental structures have been continuously studied and improved to meet the constantly updated bandwidth and expanded capabilities requirements. However, the ever-increasing demands for bandwidth and performance as well as the highly anticipated applications of millimeter-wave (mmW) and terahertz (THz), have raised the fundamental question of whether those classical transmission lines are able to cope with the demands for low-loss and low-dispersion guided-wave propagation [1]. Indeed, planar transmission lines are the foundation of any high-frequency ICs, such as RFICs and MMICs, whose performance factors and cost indices are first limited by the transmission line building elements.

Currently, the increase in bandwidth related to ultra-high-speed wireline digital domains or computing systems such as memory chips, CPUs, GPUs, backplanes, and wired LANs, are enabled by increasing the number of input/output (I/O) channel interconnects on chips [1]. To keep up with bandwidth demand and to avoid prohibitive cost and complexity, fast time-domain pulse signals would require bus lines or interconnects design to support low-loss and low-dispersion signal transmission from DC to mmW spectrum, and even up to THz bands if pico-pulsed signals are used. In this case, each set of existing I/O channels would be replaced by a single ultra-wideband

interconnect. On the other hand, in wireless application, although radio-over-fiber techniques are applied and complicated modulation schemes are used, available RF bandwidth is still relatively low [2]. In this case, the challenges are in pushing the use of RF signals toward the frequency range of mmW and higher, which necessitates the development of ultra-high-speed electro-optical devices such as modulators and photodetectors for which high-performance DC-to-mmW/THz "electronic" transmission lines are needed for integrated "electrodes" [3].

Efficient guiding of electromagnetic waves through analog interconnects with minimized dispersion and loss effects over an extended bandwidth on a chip is of paramount importance for future broadband front-ends in wireless systems [4], [5]. The fact is that using transmission lines operating up to mmW/THz frequency range is a long-term solution to providing outstanding large bandwidth with minimum cost and complexity in both wireline/wireless and digital/analog applications. The system-on-chip concept [6], [7], which is being extended from RF and microwave applications to mmW and THz integrated platforms, critically depends on the use of transmission line and chip-interconnect properties. Obviously, worldwide efforts have been made for a long time to evolve and improve the existing transmission line structures through numerous incremental manners, but it still remains an ultimate scientific and technological challenge, which necessitates the emergence of a revolutionary concept.

4.1.2 **Theoretical background**

Depending on waveguide structure, guided waves exhibit different operating modes in the frequency domain, featuring different loss and dispersion behaviors. The microstrip line supports a fundamental quasi-TEM mode in which longitudinal field components along the propagating direction are negligible compared to their transverse counterparts. Its signal line presents a longitudinal current distribution changing from a minimum in the middle to an over-shoot (singularity) at the two line edges. As frequency goes higher and higher, the current becomes more and more confined to the surface, resulting in increased resistance and, therefore, skin effects are much more pronounced. Note that the substrate thickness and line width are generally reduced as frequency increases to comply with the impedance design. As a result, TEM mode-related conductor or ohmic losses increase with frequency. TEM mode has no cut-off frequency but at higher frequency, other modes begin to propagate on a microstrip line, resulting in excessive dispersion effects beyond a certain frequency point. Therefore, this transmission line is not

amenable to the mmW/THz frequency range because of some prohibitive signal attenuation coupled with modal dispersion.

An emerging planar technology called substrate integrated circuits (SICs) has recently been studied and developed for various microwave and millimeter-wave applications [8], [9]. This scheme allows for the making of any non-planar structures in planar form, which renders possible the synthesis and integration of RW, dielectric waveguides, and coaxial lines at low cost with high performance. Among the proposed SICs topologies, easy-to-make planar synthesized RW or SIW has been the most popular, which supports the fundamental quasi-TE mode [10]. Having a longitudinal component of magnetic field along the propagating direction, the TE mode (mainly TE_{10} mode) can be decomposed into two plane waves according to the waveguide theory, which bounce back and forth between the waveguide sidewalls with s-polarized incidence while propagating. The electric field fades on the metallic surfaces, and losses of the TE mode follow a steady unchanging trend with increasing frequency [11], [12].

In 1970 at Bell Laboratories, it was demonstrated that the loss of TE_{01} propagating mode in a hollow metallic circular waveguide can be made significantly small [13]. Following that work, achieving a TE_{10} single-mode THz coupling and propagation up to 500 GHz in a metallic rectangular waveguide was accomplished [14], [15]. However, the TE_{10} operating mode, like all other TE and TM modes, is dispersive and presents a fundamental nature of cutoff frequency. This type of structure suffers from group velocity dispersion close to cutoff frequency, resulting in a non-recoverable distortion of ultra-fast pulse waveforms and DC-THz broadband signal transmission [16], [17]. Therefore, it has never been considered for the guiding of DC-to-high-frequency broadband signals or the transmission of pico-second digital pulses with all frequency components extending from DC to THz.

In 2001, promising studies reported and suggested a non-dispersive propagation of THz pulses through ultra-low ohmic loss TE_{10} mode in a parallel metal plate waveguide (PMPW) [18]. Additionally, a plasmonic mode in PMPW was observed in which the field distribution of TEM mode is abruptly changed [19]. However, the diffraction loss in PMPW is the dominant loss mechanism, and mitigating this diffraction loss is an impeding concern that must be addressed for any practical realization of such an ultra-low-loss THz waveguide [11], [12].

4.1.3 Contribution of this work

In this work, our recently proposed mode-selective transmission line (MSTL) [20] is studied and characterized in detail. Its physical characteristics, operation principle, and super-wideband propagation are further examined and discussed here. As its name implies, MSTL supports a dominant mode very similar to the case of the microstrip line quasi-TEM in the lower frequency range covering DC. It is then automatically reconfigured with the phenomenon of a mode conversion at higher-frequency (mmW in this case), and the fundamental mode becomes TE_{10} similar to the RW case, as explained in [20]. In this work, the mode coupling and mode conversion along MSTL are theoretically studied and mathematically formulated. A semi-analytical method of lines (MoL) [21], [22] is used to model and investigate the guided-wave properties of MSTL, including loss and dispersion characteristics, and to establish a systematic design approach for its applications. The structure is also simulated with numerical methods based on two different commercial software packages, namely finite element method (FEM) of HFSS and finite integration technique (FIT) of CST Microwave Studio, which are used to double-check the field distribution obtained by the MoL and to investigate the radiation loss. The structure is fabricated on two different substrates using two different fabrication processes. Design techniques, theoretical results, and simulated results are all verified by measurements.

4.1.4 MSTL structure and operation principle

The cross-sectional view of a typical MSTL and its associated coordinate system for our analysis are shown in Figure 4.1. The structure at first glance is similar to a dielectric-filled rectangular waveguide with two parallel slots etched on the top conductor layer, with a metal strip in the center.

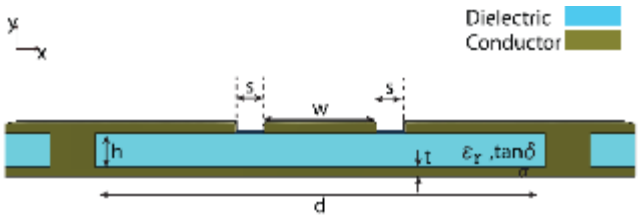

Figure 4.1: A cross section view of mode-selective transmission line.

For the following modeling and analysis, the dielectric substrate of choice is characterized by

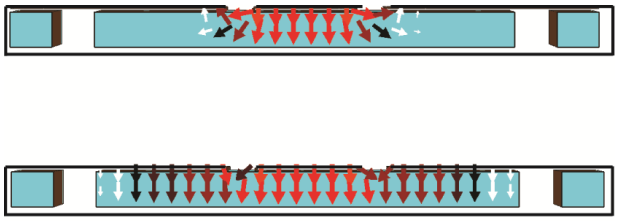

Figure 4.2: Intended modes in MSTL with the dominance of vertical electric field components: a) microstrip line mode, b) waveguide TE_{10} mode.

dielectric constant ε_r, thickness h, and width d. The metallic layer has a large but finite conductivity σ, and the center metallic strip has width w and the slots of size *s*.

Figure 4.2 shows the desired electric field distributions generated by numerical simulations in the cross section of MSTL. The two modes, supported by MSTL, have the electric field component aligned along the y-axis. Figure 4.2(a) shows MSTL electric field at lower frequency and Figure 4.2(b) shows MSTL electric field at higher frequency range. From DC up to cutoff frequency f_{cutoff} of TE_{10} mode of a RW of width *d*, the dimensions of MSTL are chosen in a way that the mode characteristic is very similar to the TEM mode of a microstrip line of strip width w. Cutoff frequency f_{cutoff} of TE_{10} mode is determined by:

$$f_{cutoff} = \frac{1}{2d\sqrt{\mu_0 \varepsilon_0 \varepsilon_r}} \tag{1}$$

At this frequency, attenuation constant of TE_{10} is large, and a strong mode coupling from the propagating TEM mode to TE_{10} mode takes place [23], and the electromagnetic power is transferred from one mode to another with the following interaction term:

$$P_{TE_{10},TEM} = \frac{1}{2}\oiint_S \overline{E}_{TE_{10}} \times \overline{H}^*_{TEM} . a_z ds \tag{2}$$

Since $\overline{E}_{TE} = E_y a_y$ and $\overline{H}_{TEM} = H_x a_x$, according to (2), the total coupling from TEM mode toTE_{10} mode is realized ($E_y a_y \times H_x a_x . a_z = E_y H_x a_y \times a_x . a_z = E_y H_x a_z . a_z$ $E_y H_x (a_z . a_z = 1)$).

Therefore, as frequency goes beyond the point of f_{cutoff}, mode characteristic becomes similar to the TE_{10} mode of RW or SIW. Through this unique propagation phenomenon in MSTL, a field

transition or transformation in mode pattern occurs with increasing frequency, and energy distribution extends from the waveguide center area to its edges.

4.2 Theoretical description

4.2.1 Background

The common knowledge in our community is that mode conversion and coupling generally happen when there is a geometrical discontinuity or field disruption along the propagation direction [24]. This is absolutely true because the boundary condition is disrupted by the discontinuity. Interestingly, such mode conversion and coupling can also take place for a longitudinally uniform waveguide or transmission line as long as there is a presence of physical irregularities or field singularities within the cross section of the waveguide or transmission line in question. In this case, the formed mode is no longer a pure TEM mode or TE/TM mode, which cannot be describable by a closed-form analytical formulation. Indeed, such non-pure TEM or TE/TM modes can be regarded as a "coupled body" of pure mode (e.g., TEM mode) and the other modes. This mode coupling or energy conversion between the pure mode and other modes is enabled by dispersion as frequency changes (usually increases). This is because the guided mode is subject to the incremental adjustment of boundary condition in which frequency definitely plays a role. Regarding the mathematical analysis, the mode conversion in an inhomogeneous cross section can be considered a problem of solving the Maxwell's equations with frequency-dependent boundary condition. The implication of dispersion effects in the formulation is implicit. Physically, single-waveguide mode coupling occurs [25] for which local modes are derived through wave optics or physical optics approximation [26].

4.2.2 Mode coupling and mode conversion in MSTL

MSTL is a longitudinally uniform guided-wave structure with an asymmetric inhomogeneous cross section. As frequency increases, the conversion of the zero-frequency propagation mode into an appropriate fundamental mode is necessary to satisfy the boundary condition. For the mathematical analysis, MSTL may be well considered as a multiconductor transmission line [27], namely a system of two coupled transmission lines:

1) Microstrip line of width w, and propagation constant β_1

2) SIW of width d, propagation constant β_2.

Both lines are made on the same substrate (ε_r, thickness h). Coupling characteristics between these two isolated transmission lines are expressed as a function of frequency. Below the cutoff frequency of SIW TE_{10} mode, f_{cutoff}, MSTL works as the microstrip line. Beyond frequency point f_{cutoff}, electromagnetic fields of the microstrip TEM mode and the SIW TE_{10} mode become overlapped and a mode coupling occurs between theses dissimilar integrated waveguides, which was briefly examined in one of our early works [30] but under different context. The key equations governing the mode coupling are reflected in overlap integral and coupling coefficient, which are obtained from the reciprocity theorem and defined for two coupled lines 1 and 2 by (3) and (4) [27]:

$$N_{12} = \frac{1}{2}\oint_S [\mathrm{E}_1 \times H_2].\mathrm{a}_z ds \tag{3}$$

$$Q_{12} = -\frac{j}{4}\int_{c_n} [\mathrm{E}_{1,t}.J_{2,t} - \mathrm{E}_{1,z}.J_{2,z}]dxdy \tag{4}$$

N_{12} determines the overlap between the two modes and Q_{12} resolves the coupling coefficient from the first mode to the other.

In this formulation, the eigenmode fields and currents of isolated microstrip line and isolated SIW are used (1: TEM and 2: TE_{10},). The field amplitudes are normalized so that $N_{11}=N_{22}=1$ over all the frequency bands of interest and the coupling characteristics are derived:

$$N_{12} = \frac{2\sqrt{2}}{\pi}\sqrt{\frac{\Gamma}{\mu}}\sqrt{\frac{a}{w}}\sqrt{\frac{\beta_2}{\omega}}\sin(\frac{\pi w}{2a}) \tag{5}$$

$$N_{21} = \frac{2\sqrt{2}}{\pi}\sqrt{\frac{\mu}{\Gamma}}\sqrt{\frac{a}{w}}\sqrt{\frac{\omega}{\beta_2}}\sin(\frac{\pi w}{2a}) \tag{6}$$

$$Q_{12} = \sqrt{2\pi}\sqrt{\frac{\Gamma}{\mu}}\sqrt{\frac{1}{a^3 w}}\sqrt{\frac{1}{\omega\beta_2}} \tag{7}$$

(5) and (6) are the mode overlap integrals and (7) is the coupling coefficient from mode 1 to mode 2. The coupling coefficient from mode 2 to 1 $Q_{21}=0$ because the current component of TEM mode is oriented only in the longitudinal z direction, whereas the longitudinal electric field of TE_{10} mode does not exist ($E_{z,\,TE10} = 0$). In the above equations, Γ is the free-space impedance, and $\omega = 2\pi f$. At

the frequency at which the TE_{10} mode appears, ($\beta_2>0$), the coupling from TEM to TE_{10} is induced. Physically speaking, a mode conversion occurs where the propagation vector in the direction of inhomogeneity (K_x along the x-axis in this case) deviates [28]. Whereas for the TEM mode, the x-direction wavenumber is zero ($K_{x,TEM}=0$), with the appearance of TE_{10} mode at f_{cutoff}, the value is changed to $K_{x,TE10}=\pi/a$. The mode conversion becomes strongest when their respective propagation constants are quite close to each other or equal [30].

As a result, for an input signal in this structure with frequency $f<f_{cutoff}$, a quasi-TEM mode dominates and for $f>f_{cutoff}$, a quasi-TE_{10} mode presides over, and therefore it is a mode-selective guided wave structure, enabled by a frequency change.

4.2.3 **Discussion**

An assumption has always been made in the conventional modal analysis of a transmission line for which the modes are orthogonal to each other. This statement may be true if the modes belong to the same reference structure. However, in MSTL, the mode coupling takes place between two electrically different structures exhibiting different boundary conditions for those modes, which are no longer orthogonal in space. For the TEM mode, most of its electric field is confined under the center conductor, whereas for the TE_{10} mode, the electric fields are extended to the edges. With the electric fields of both modes being primarily vertical, none of the field components for the modes are orthogonal to each other. Therefore, the orthogonal coupled mode theory is no longer valid for the physical description of a mode-coupling process in this case.

Other forms of transmission lines, such as microstrip lines and CPW, also support the frequency-dependent mode conversion and coupling phenomena caused by asymmetrical cross sections. However, in those structures, mode coupling and conversion result in strong dispersion and radiation. Such coupling effects are frequency-dependent and this is why some visible coupling effects can well be pronounced at high frequencies [29], [31]. Leaky-mode structures are a well-known example, as well as other examples in mutually-coupled hybrid mode structures, including complex mode issues [32], which are based on a uniform transmission line with an asymmetrical cross section; such an asymmetry does not need to be realized physically and it can even be managed electrically.

4.3 Design considerations and MSTL simulation

Dimensions of MSTL should be adequately selected to ensure the expected mode conversion behavior over a desired frequency range. After choosing a substrate, width *d* is selected as:

$$d > 8h \tag{8}$$

According to the potential theory for microstrip lines [33], the two conducting sidewalls have no influence on the characteristics of the microstrip line modal configuration in MSTL at low frequency operation, and fields and current distributions are very similar to the case of a quasi-TEM mode of standard microstrip line. Looking into (1), one can determine that width *d* also provides a direct control on the mode conversion frequency.

The possible presence of surface wave modes may deteriorate mstl performance, especially along discontinuities. As such, considering the maximum operating frequency, thickness *h* must be thin enough to avoid the emergence of surface waves with the proposed design condition as follows [36]:

$$\frac{h}{\lambda_{\max}} < \frac{1}{2\sqrt{\varepsilon_r - 1}} \tag{9}$$

It is also imperative to avoid a potential excitation of the CPW mode, which is undesirable in the case of MSTL. It is known that effective dielectric constant of CPW mode is close to the averaged value of the dielectric constant of dielectric substrate (50% filling factor) and that of the free space. Neverthless, the effective dielectric constant of microstrip TEM mode and waveguide TE_{10} mode is more prone to the dielectric constant of substrate, providing a smooth transition from one mode to another. Moreover, for the propagating CPW mode, the horizontal electric field is large, which is not suitable for some applications, e.g., in the design of certain electro-optical devices. Therefore, to stay away from the CPW mode [34], dimensions *w* and *s* must be chosen with regard to the thickness in order to satisfy the following simple condition,

$$w/2+s>h \tag{10}$$

In this work, single crystal fused silica (quartz) wafer (dielectric constant ε_r=4.27 and $tan\delta$=0.0002) with thickness h=50 μm is selected as the prototype substrate to minimize the dielectric loss in the experiments. Width *d* is selected equal to 600 μm to have the frequency cutoff

of TE_{10} mode around 120 GHz, and performing a parametric study (details will be given in the next section), the dimensions *w* and *s* are selected equal to 3*h* and 0.8*h*, respectively. FIT numerical simulation of CST MWS is used for modeling MSTL through the calculation of its field distributions and mode conversion behavior. The results are shown in Table 4.1, from which the unique mode conversion propagation phenomenon is observed as anticipated. At relatively low frequencies, only transverse field components E_y and H_x exist, which are well confined to the center conductor, as expected for a TEM mode operation. By increasing frequency, the longitudinal magnetic field component H_z emerges, bouncing plane waves appear, and field distribution begins to extend toward the conductor sidewalls that makes up the quasi-TE_{10} mode.

To be more accurate and also physically convincing, a possible effect of top metallic layer slits on $f_{cutoff\ of}$ TE_{10} mode in MSTL, compared to SIW, as investigated in this work. Since $s/d<<1$ and substrate thickness *h* are less than the guided-wave wavelength, transverse resonance (TR) method [35] is deployed in this work to find the cutoff frequency of TE_{10} mode in MSTL. The equivalent transverse circuit network for the dominant operating mode consists of an inductance, representing non-radiating slits, shunted by two TE mode transmission lines with open- and short-circuit terminations. Figure 4.3 shows the equivalent network modeling of the structure with the TR method in the TE-mode regime. The propagation constant is thus calculated from the following resonance condition:

$$\tan(\beta_x a/2) + \beta_x/Y_0 + \cot(\beta_x(d/2 - a/2)) = 0 \tag{11}$$

where

$$\beta_z = \sqrt{K^2 - \beta_x^2} \tag{12}$$

β_x is the transverse component of propagation constant, $Y_0=1/Z_0$ is the admittance of each part as shown in Figure 4.3, and *K* is the wave number. The value of β_x/Y_0 is given by Marcuvitz in [35]. This equation leads to two solutions for the propagation constant, described in Figure 4.4. To verify the results, the package of HFSS [36] is also used to simulate the proposed MSTL and calculate the propagation constant. As is seen, one of the TR method solutions, solution No. 1 in Figure 4.4, shows a propagating mode with no cut-off frequency that has almost the same propagation constant as calculated by HFSS. The other solution, solution No. 2 in Figure 4.4, shows a propagation

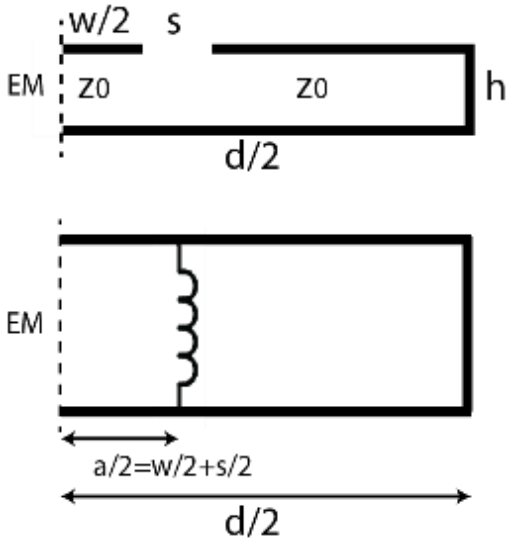

Figure 4.3: Equivalent transverse circuit network for MSTL in Fig. 1 with the reference plane in the middle of the slot s.

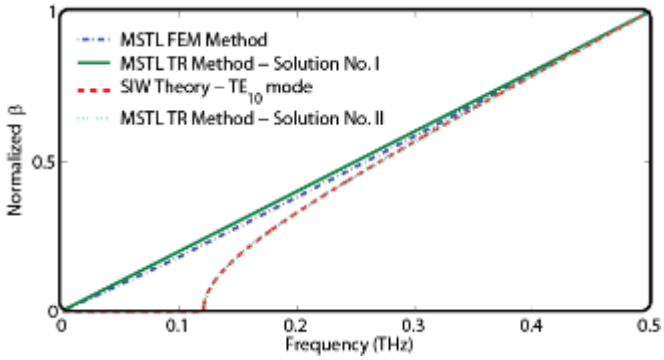

Figure 4.4: Propagation constant of guided-wave modes in MSTL using transverse resonance method and comparison with the results of FEM method and theoretical calculation [36].

constant almost the same as the TE_{10} mode of an SIW structure with the width *d*, having only 0.5% frequency shift toward the lower frequency side.

The HFSS simulated results are illustrated in Figure 4.5. Figure 4.5(a) shows the electric and magnetic field distributions of the proposed MSTL, and Figure 4.5(b) and Figure 4.5(c) present the propagation characteristics of the fundamental mode supported by MSTL. In the same figure, the

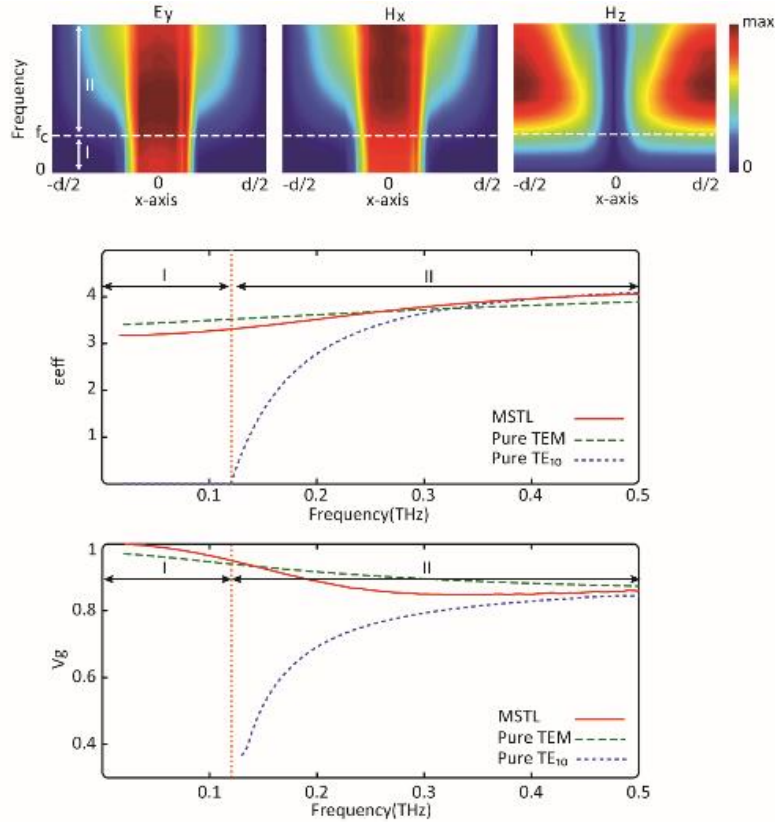

Figure 4.5: a) Fields and current distributions in MSTL designed on quartz (h=50μm, d=12h, w=3h, s=0.8h) from DC up to 0.5 THz range; f_{cutoff} =120GHz, f_{max}=500GHz. In region I of frequency range, MSTL works under a mode with characteristics very similar to that of TEM mode. In region II, MSTL operates with a mode with characteristics very similar to TE_{10} mode. b) Effective dielectric constant of MSTL on quartz (h=50μm, d=12h, w=3h, s=0.8h) and comparison with effective dielectric constant of microstrip line TEM mode and rectangular waveguide TE_{10} mode. c) Group velocity of MSTL on quartz (h=50μm, d=12h, w=3h, s=0.8h) and comparison with group velocity of microstrip line TEM mode and rectangular waveguide TE_{10} mode.

dispersion curve of the fundamental mode supported by microstrip line of width *w*, and rectangular waveguide of width *d*, on the same substrate are also demonstrated.

a

strip; both elec and magnetic fields, E_y and H_x with uniform distribution, lie in a perpendicular plane to the axis of propagation as one would expect for the TEM mode [35]. Over this frequency range, according to Figure 4.5(b), and Figure 4.5(c), phase constant and group velocity of the dominant mode are much the same as the TEM mode of microstrip line. As frequency approaches

b

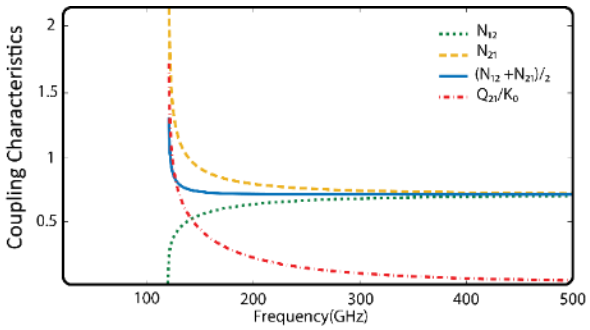

Figure 4.6: Calculated mode coupling characteristics of MSTL

the cutoff of the TE_{10} mode, as seen in Figure 4.5(a), an evolution in the field distribution is observed where the electric field is spread out up to the lateral boundaries. The magnetic field H_z appears and the bouncing propagating plane waves emerge, so the power is converted from the quasi-TEM mode to a quasi-TE_{10} mode. The magnetic field distribution is spread over the entire waveguide section. Since the electric lines are more confined to the dielectric of substrate, the effective dielectric constant of the propagating mode is slightly increased. Figure 4.7 shows the calculated mode coupling characteristics using (10), (11), and (12). As it can be seen at the cutoff frequency f_{cutoff}, the overlap integral $(N_{12} + N_{21})/2$ and normalized coupling coefficient Q_{12}/K_0 are at their maximum values. Although a pure TE_{10} propagation mode of rectangular waveguide is very dispersive near its cutoff frequency point, while MSTL shows a smooth effective dielectric constant transition over frequency, thus ensuring dispersion-less characteristics. This is because around that frequency range, hybrid TEM and TE_{10} modes exist.

4.4 MSTL waveguiding characterization

The proposed MSTL is a planar waveguide that consists of regions that are homogenious in one direction. Therefore, a semi-analytical method of lines (MoL) is used in this work for hybrid-mode analysis and evaluation of MSTL complex propagation constant $\gamma = j\beta + \alpha$, in which β is the phase constant and α is the attenuation constant [37]–[38].

4.5 Modal analysis

In the full-wave formulation of MoL, electric and magnetic potential functions are discretized along the x-direction (Figure 4.9). Applying boundary conditions at the dielectric interface, the resulting

Table 4.1: Electric and Magnetic Field Distribution in the proposed MSTL on Fused Silica Substrate at Different Frequencies: Propagating Modes Change from TEM to TE_{10} Mode

Frequency	Field Distribution			
	E_y	H_x	H_z	
1GHz	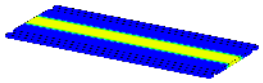	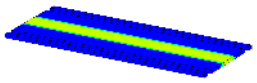	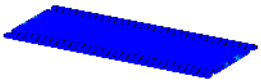	0dB - 40dB
100GHz	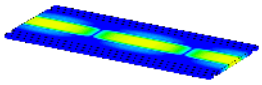	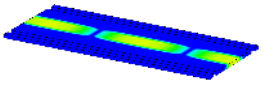	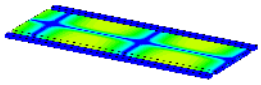	
300GHz	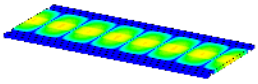	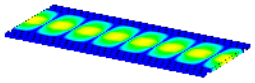	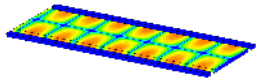	
500GHz	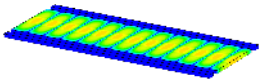	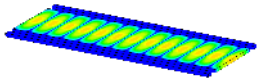	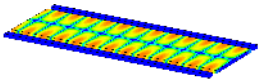	

Helmholtz equation in the discrete form is solved analytically after matrix transformation. Following a series of mathematical manipulations, a non-linear transcendental equation is obtained whose solutions lead to the eigenvalues associated with guided-wave characteristics. Therefore, effective dielectric constant is extracted over the whole frequency range from DC to 0.5 THz; electric field distribution is also derived and plotted on the cross section. To verify the accuracy and convergence of the discretization, the calculated effective dielectric constants are compared with the simulated FEM results. Figure 4.6 shows that the effective dielectric constant calculated with both methods demonstrates an excellent agreement in the high frequency range, and less than 3% difference in the low frequency region that may be caused by difference in discretization schemes.

4.5.1 **Loss Derivation**

To determine exact sources of loss, the attenuation constant α is divided into metallic loss (α_c) stemming from the finite conductivity σ, and dielectric loss (α_d) related to the substrate loss, tangent

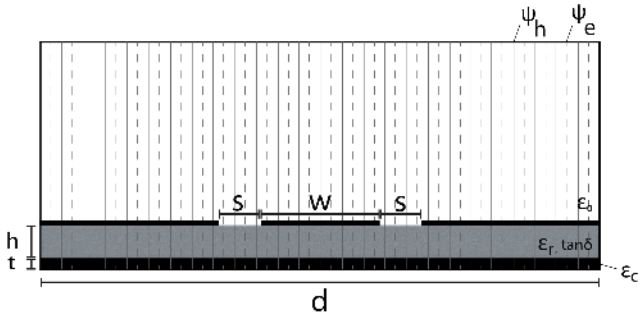

Figure 4.7: MSTL cross section with MOL discretization for hybrid-mode analysis.

tanδ. Metallic loss includes the loss of both the bottom conductive layer (α_{c1}) and top metallic layer (α_{c2}). Therefore, attenuation constant is calculated from the total value with a linear superposition $\alpha = \alpha_d + \alpha_{c1} + \alpha_{c2}$ with reference to the principal of pertubation. The bottom electrode layer or groundplane is usually thicker than the strips on the substrate surface, and is regarded as a dielectric layer with a thickness t equal to skin effect [40]:

$$t = \sqrt{\frac{2}{\omega\mu\sigma}} \tag{13}$$

where $\omega=2\pi f$ determines the angular frequency, and μ is the conductor permeability. This layer is modeled as a purely imaginary value with the permittivity ($\varepsilon_c=-j\frac{\sigma}{\omega}$) [41]. In the first step, a two-layer structure of dielectric substrate (ε_r , *tanδ*) on the groundplane (ε_c) is modeled, and complex propagation constant $\gamma_1 = j\beta_1 + \alpha_1$ is obtained, in which the real part β_1 is the transmission line phase constant and the imaginary part includes the contribution of dielectric and lossy ground plane in the attenuation constant ($\alpha_d + \alpha_{c1}$). Subsequent to the calculation of β_1, field and current components are then calculated along the cross section of mstl. In the second step, a perturbation method is used [36] to attenuation (α_{c2}), and finally the total loss (α) is derived. Radiation loss is not included in the above-mentioned MoL calculations, and it is estimated with the HFSS package. Figure 4.8 shows the calculated loss from the specified different sources of loss and also the total loss in the MSTL. As it is seen from the MoL calculation, loss is mostly due to the top conductor layer. The mode conversion is perceptible from the curve trend; the guided-wave mode is changed from a semi-TEM mode to a semi-TE_{10} mode. The total loss is increased up to around 120 GHz, the TE_{10} mode cutoff frequency, and then decreased. After reaching a frequency point with

minimum loss around 220 GHz, the loss rises again and continues steadily from around 400 GHz. The calculated radiation loss from the HFSS package is also added to Figure 4.6, interestingly showing that the radiation loss vanishes after the mode conversion. It appears again at higher frequency that may be caused by slight slits radiation over that frequency range.

4.5.2 **Parametric Study**

In order to understand better the physical behavior of mstl structure, and identify its limitations and design scheme, a comprehensive parametric study is performed in this section. Figure 4.10(a) presents the effective dielectric constant ε_{eff} of MSTL for a variation of the center conductor width *w*. As is shown for constant thickness (*h*=*cte*) with decreasing *w* below 2*h*, the occurrence of CPW mode at higher frequency is observed. For example, when *w*=1.5*h*, the CPW mode begins to appear

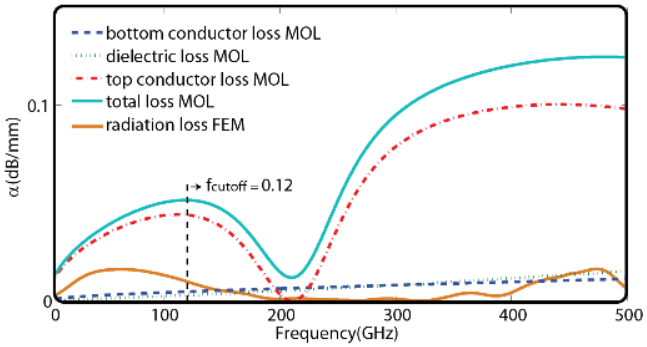

Figure 4.8: Calculated different sources of loss using the MoL, including radiation loss using the HFSS package (MSTL with parameters ε_r=4.27, h=50μm, d=12h, w=3h, s=0.8h).

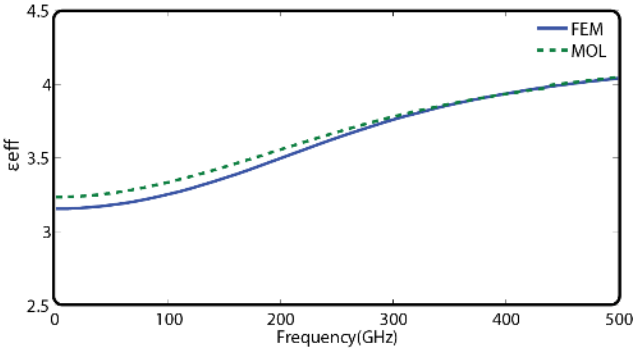

Figure 4.9: Comparison of calculated effective dielectric constant as a function of frequency using the MoL method and HFSS package; MSTL with geometrical parameters ε_r =4.27, h=50μm, d=10h, w=3h, s=0.8h.

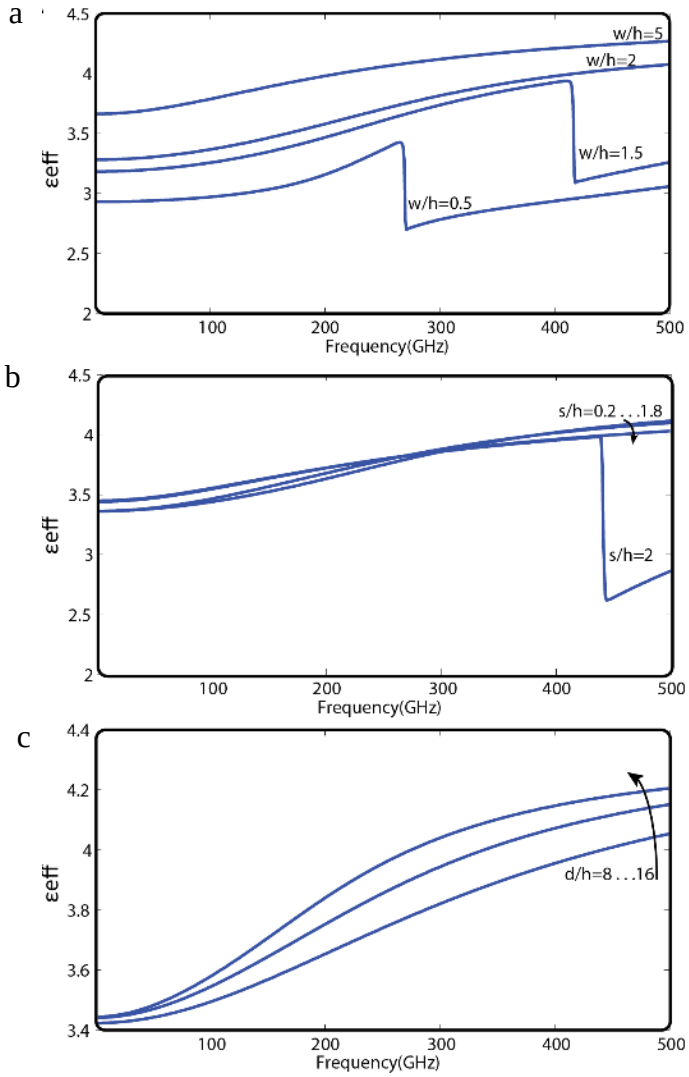

Figure 4.10: Computed effective dielectric constant as a function of frequency: a) Strip width w as a parameter, and ε_r =4.27, h=50μm, d=12h, s=0.8h; b) Slot width s as parameter, and ε_r =4.27, h=50μm, d=12h, w=3h; and c) Substrate width d as a parameter, and ε_r =4.27, h=50μm, w=3h, s=0.8h.

around 420 GHz, and if *w*=0.5*h*, it appears around 270 GHz. Figure 4.10(b) plots the effective dielectric constant ε_{eff} of MSTL for a variation of slot width *s*. Again for constant thickness (*h=cte*) with increasing *s* above *h*, the occurrence of CPW mode at higher frequency is observed. In this case, the upper limit for the parameter *s* is:

$$s<1.8h \tag{14}$$

It is seen that if $s=2h$, the CPW mode starts to appear around 340 GHz. The lower limit of s is determined by the fabrication process. Figure 4.10(c) shows the effect of width d on dispersion, and it can be seen that for constant h, a smaller d would result in a frequency-dependent response with lower dispersion.

The effect of waveguide width d on the loss is illustrated in Figure 4.12. As it is clearly seen, at the cutoff frequency of TE_{10}, where the width d is greater than a half-wavelength, the mode conversion

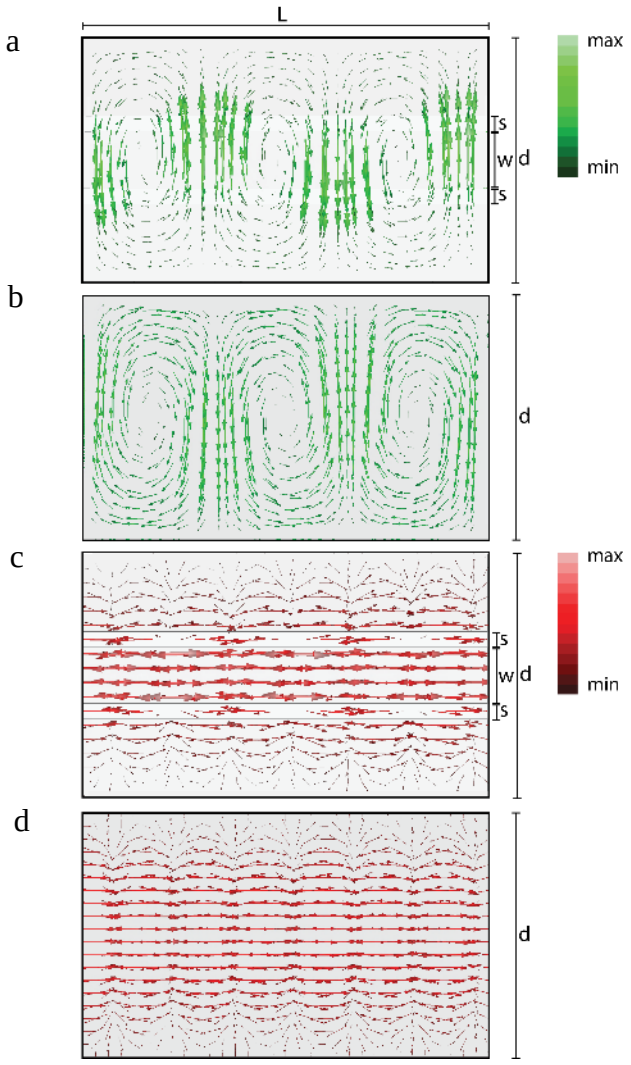

Figure 4.11: Magnetic field and current distribution at 250GHz: a) MSTL, Magnetic field b) SIW, Magnetic field c) MSTL, Surface current d) SIW, Surface current

occurs, guided-wave power is transferred from semi-TEM mode to semi-TE_{10} mode, and loss is

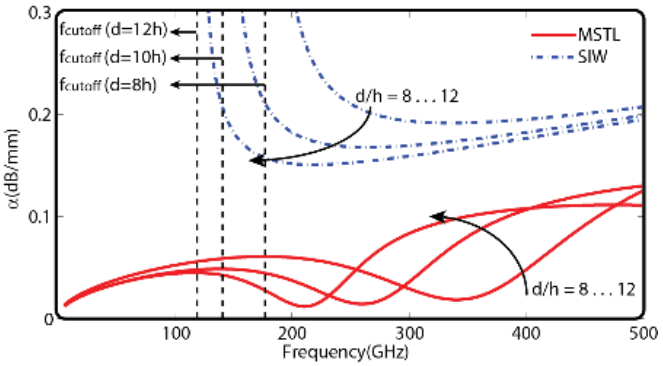

Figure 4.12: Comparison of calculated propagation loss of MSTL and SIW as a function of frequency for different waveguide width d, ε_r =4.27, h=50μm, s=0.8h, w=3h.

decreased. For constant thickness (*h=cte*) with increasing the value of *d*, the occurrence frequency of TE_{10} mode shifts to the lower frequency range.

In Figure 4.12, the calculated conductor loss of MSTL is also compared to the calculated conductor loss of a dielectric-filled rectangular waveguide (SIW), with the same waveguide width, *d*, showing less attenuation in the case of MSTL. Conductor loss is in direct association with current distribution. Therefore, to clarify this observation, magnetic field and surface current vectors in SIW and MSTL are calculated and compared using HFSS full-wave analysis. Figure 4.11 shows an example of this calculation at 250GHz in a waveguide of length L=1mm. The wave propagates along the waveguide where the bouncing plane waves of TE_{10} undergo a power loss at each bounce due to the imperfectly conducting surfaces [3]. In MSTL and SIW, the current distributions are similar, but MSTL presents a "compressed TE_{10}" mode due to the designed non-radiating slots on the top conductor. This compressed mode grants a lower conductor loss compared to a typical TE_{10} mode. The reason is that in MSTL compared to SIW, not only does the placement of the non-radiating slots not contribute to conductor loss, but also thanks to the TE_{10} compressed feature, the metallic sidewalls do not contribute to conductor loss and the structure dispersion becomes lower. This explains why the proposed MSTL structure has a superior low-loss and low-dispersion performance. The region of interest for MSTL design is defined by a set of values adapted to achieve a low-loss and low-dispersion characteristic in a desired bandwidth. The region of interest in the *d/h*-*w/h* plane is bounded by inequalities defined by (3) and (9), which define the minimum width of the waveguide and strip.

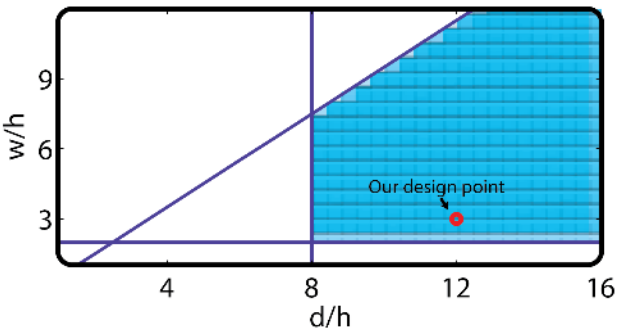

Figure 4.13: MSTL guiding design curves in w/h-d/h plane showing the useful design region of interest.

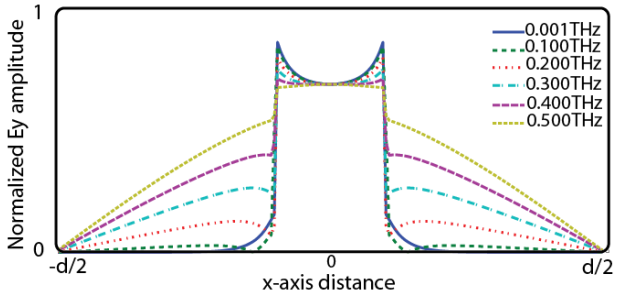

Figure 4.14: Ey distribution (along the x-direction) for the fundamental propagating mode in MSTL (ε_r=4.27, h=50μm, d=12h, w=3h, s=0.8h).

In addition, the cutoff of waveguide mode should be lower than the transverse resonance (TR) mode of microstrip line, which dictates [36]:

$$\frac{c}{2d\sqrt{\varepsilon_r}} < \frac{c}{\sqrt{\varepsilon_r}(2w+h)} \tag{15}$$

The defined design region is described in Figure 4.13. Figure 4.14 shows some typical field distributions from 1 to 500 GHz along the air-substrate interface ($y = h$), calculated through MoL. The field components are normalized to their amplitude at the strip center. Once again, the mode conversion is observed. As expected, the field is confined to the proximity of the strip over the low-frequency range. As frequency approaches the cut-off point of the first higher mode, the field

Table 4.2: Electric and Magnetic Field Distribution in the Proposed MSTL made on Rogers Substrate for Different Frequency points: Propagating Modes Change from TEM Mode to TE_{10} Mode

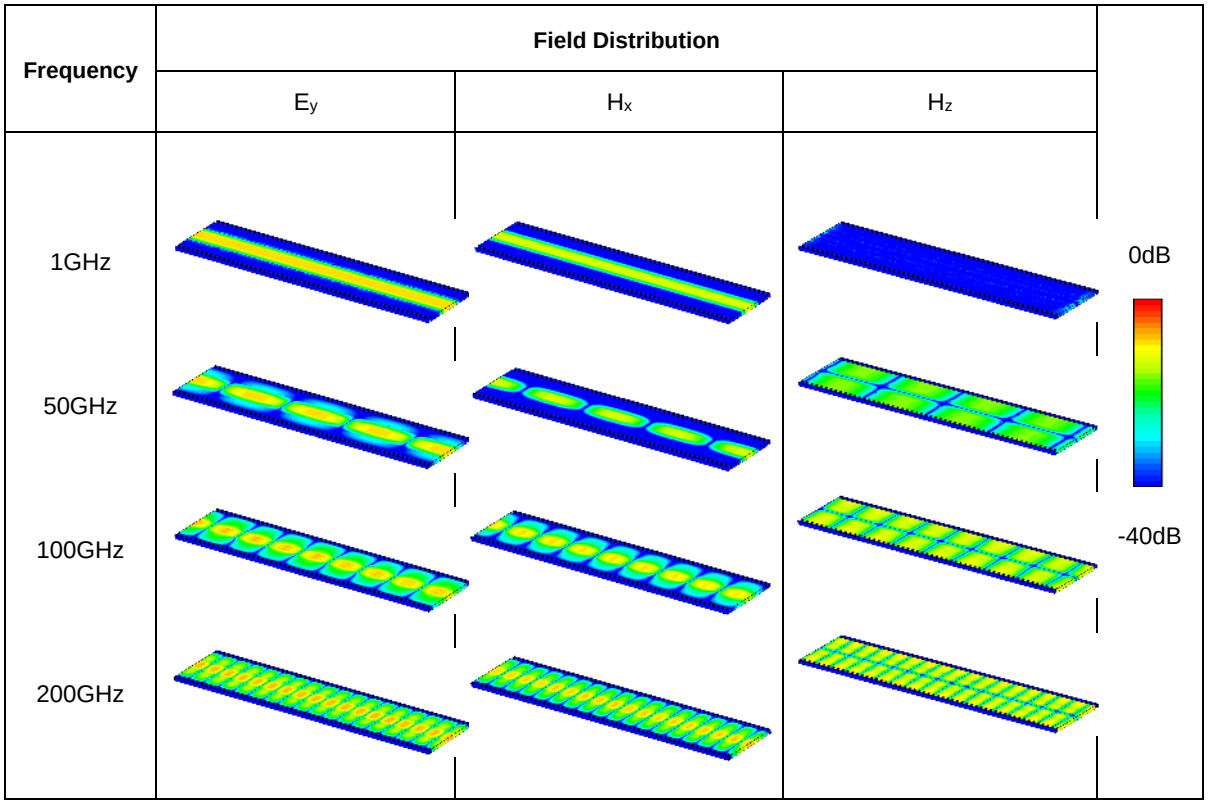

is spread out up to the lateral boundaries. As frequency is raised from 1 GHz to 500 GHz, the field distributions are much changed from a pure microstrip mode to a quasi-sinusoidal distribution (waveguide mode). Therefore, it is empirically deduced that in the design process, the strip width *w* must also be smaller than half of the waveguide width *d*.

Figure 4.15 depicts the effect of increasing dielectric substrate permittivity ε_r on the effective dielectric constant and attenuation constant. ε_{eff} variation (dispersion) from low to high frequency increases with increasing ε_r, which can be expected as higher ε_r would contribute to a larger dispersion. The variation from 1 to 500 GHz is about 5% with ε_r=4 and 20% with ε_r=10. The effect of increasing the permittivity on dielectric loss tangent, and therefore the total loss, is negligible since the conductor losses are much larger than those from the dielectric substrate. The mode conversion frequency is decreased with increasing ε_r, where the curves are similar to the propagation loss variation as a function of waveguide width *d*, as shown in Figure 4.10.

4.6 Experimental verifications

Our experimental prototypes of MSTL are fabricated through two different technological platforms. In addition to the fabrication of MSTL on a fused silica substrate, a PCB prototype is also designed based on the proposed design procedure using RT/duroid® 6002 laminates substrate from Rogers Corporation, with low dielectric constant ε_r=2.94 and low loss substrate $tan\delta$=0.0012, which is a proper choice for high frequency applications. Substrate thickness is chosen to be 127μm, which is the minimum available thickness of this substrate. Width d is selected equal to 1.5 mm (≈12h) making the conversion frequency around 60GHz. After a parametric study, w and s are selected equal to 2.4h and 1.6h for achieving minimum loss and dispersion. The CST package is used to calculate the field distribution and examine the mode conversion. Table 4.2 shows the simulation results in which the unique propagation phenomenon and the TEM-TE_{10} mode conversion are clearly spelled out. In the lower frequency range, transverse fields E_y and H_x are the only field components, and then longitudinal H_z emerges in the higher operating frequency. This evidence again confirms the mode selectivity over the frequency range.

4.6.1 Fabrication

The fabrication of MSTL samples in our Poly-Grames Research Center on the fused silica wafer with 50 μm thickness presents some technical difficulties and challenges that have been addressed and briefed as follows. Since the substrate is very thin, a back coating metallization of the substrate with sputtering was done as the first step and the thin 50 μm quartz substrate was affixed to a thick 500 μm quartz substrate. Another major difficulty in the processing is related to its laser drilling, because quartz is optically transparent. Abrasive waterjet machining was used with a modified and refined head for drilling the side holes, as this tool is capable of cutting a wide variety of materials using a very high-pressure mixture of water and an abrasive substance. After filling up the holes and the final top sputtering, the patterning was made using a lithograph with less than 1 μm precision. For the printed circuit board (PCB) prototype, the fabrication was done with an in-house standard PCB process with 1 mil precision and minimum 3 mil gap/trace combined with laser cutting to define the lateral walls.

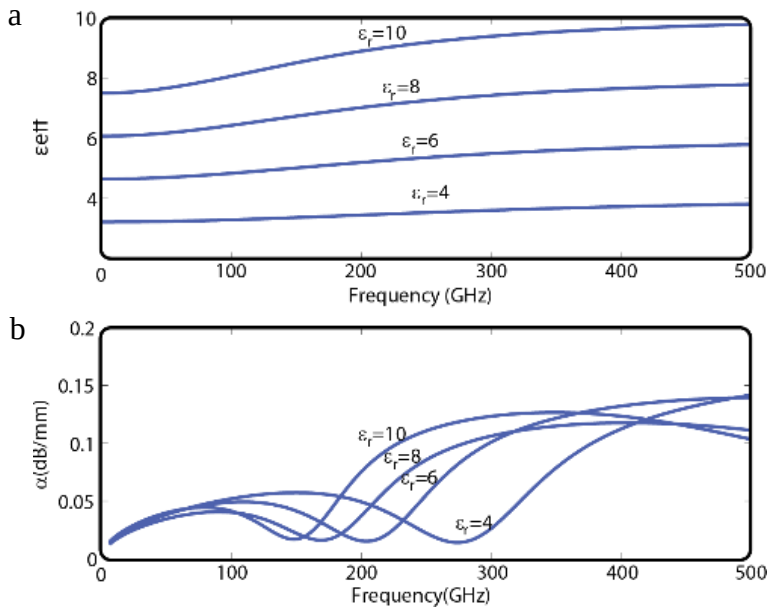

Figure 4.15: a) Calculated effective dielectric constant as a function of frequency with substrate permittivity ε_r as a changing parameter, and h=50μm, d=12h, w=3h, s=0.8h; b) Computed loss as a function of frequency with substrate permittivity ε_r as a changing parameter, and h=50μm, d=12h, w=3h, s=0.8h.

4.7 Measurements

On-wafer characterization was done with thru-reflect-line (TRL) calibration techniques to remove errors occurring during the measurements, and also to define the measurement reference planes. Picoprobes with ground-signal-ground (GSG) head were used in the measurements. To avoid forcing or exciting the unwanted CPW mode in MSTL, the position between the middle of the center strip and the edges of the launch transition pads is calculated precisely. This avoids the propagation of CPW mode and slot modes, prevents possible pad parasitic capacitive effects, improves the placement accuracy of probe tips, and also minimizes mismatch. For the transition, slots are tapered out exponentially to the lateral boundaries and the center metal strip is tapered to the 50 Ω-impedance width. To guarantee a smooth transition between mstl section and the microstrip line over a very wide frequency range, their characteristic impedance and field distributions are both matched. The transition provides a gradual transformation of electric fields from the microstrip mode to mstl propagation mode. A quarter-wavelength multi-step profile of

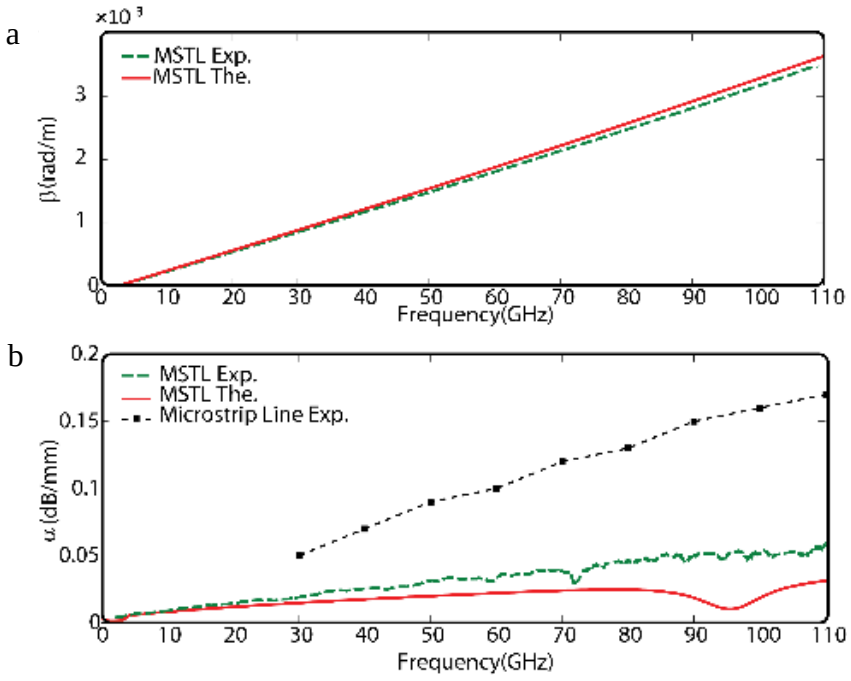

Figure 4.16: a) Comparison of theoretical and experimental propagation phase constant (β) of MSTL prototype fabricated on RT/duroid® 6002 laminates from Rogers Corp. (h=127um, d=20h, s=1.6h, w=2.4h), b) Comparison of theoretical and experimental propagation loss characteristics of MSTL prototype fabricated on RT/duroid® 6002 laminates from Rogers Corp. (h=127um, d=20h, s=1.6h, w=2.4h) and thin film microstrip line from ref [37].

the strip provides the impedance matching. These steps are linearly shaped to vary gradually in geometry, resulting in a smooth field matching.

To test the MSTL, a PNA-X with millimeter-wave modules was used and TRL kits were designed for each 1:8 frequency band. For each millimeter-wave test module, a set of corresponding picoprobes is used. The PNA-X used in this work was limited to 750 GHz, but our available millimeter-wave test modules were limited to 500 GHz, and therefore the measurements are also limited to this frequency. Picoprobes' pitch dimensions decrease with increasing the frequency and above 110 GHz, which is less than the minimum tolerable PCB gap/trace in the processing of our laboratories. Therefore, in the case of the PCB-based MSTL prototype, the maximum frequency that we could measure was up to 110 GHz because of this PCB fabrication accuracy limitation.

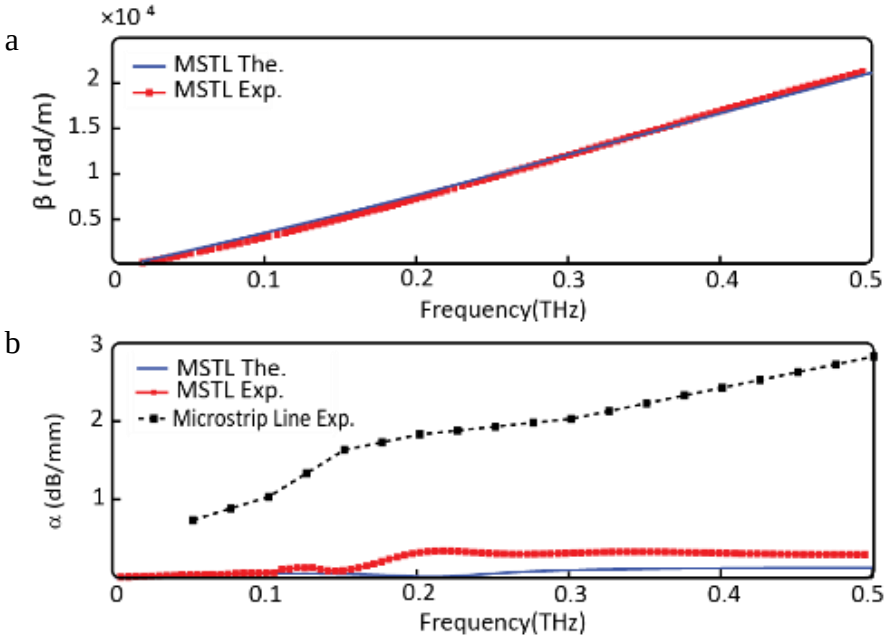

Figure 4.17: a) Comparison of theoretical and experimental propagation phase constant (β) of MSTL prototype fabricated on quartz (h=50um, d=12h, s=0.8h, w=3h); b) Comparison of theoretical and experimental propagation loss characteristic of MSTL prototype fabricated on quartz (h=50um, d=12h, s=0.8h, w=3h) and thin film microstrip line from ref [39].

A launch structure is required to interface between the GSG coplanar probe head and the MSTL. For the PCB prototype, large grounded via-holes were used as reflective sections. As operating frequency increases, its electrical length to the ground plane increases and the via-hole input impedance becomes inductive and prejudicial to the calibration and measurements. For the PCB prototype, oversized rectangular tranches are used to reduce the undesirable inductive effect. However, for the fused-silica prototype, a reflective section in the launch transition was designed with a radial quarter wavelength open sector. The use of such an open stub overcomes the undesirable reactive effects and avoids some fabrication uncertainties at higher frequency.

In the PCB prototype measurements from 10 MHz to 110 GHz, a 1-mm connector together with a 150-μm picoprobe was used, providing broadband and accurate outcomes [43]. For the measurements up to 500 GHz frequency, a set of waveguide modules (WR8, WR5, WR3, and WR2) and their corresponding probes, with a minimum pitch of 40 μm, were used. Our on-wafer measurements using high-frequency probes provide accurate and repeatable results.

Loss and propagation constants are extracted from the S-parameters. Figure 4.17 shows PCB prototype measurement results and their comparison with the related MoL-calculated theoretical results. In Figure 4.17(a), the loss of microstrip line on the same substrate, which has been reported by [43], is also shown. While MSTL shows loss less than 0.04 dB/mm over all the frequency ranges of interest, the loss of microstrip line reaches to 0.17 dB/mm at 110 GHz. Additionally, in the lower frequency range (TEM-mode frequency regime), a much lower loss is obtained for MSTL, which indicates a lower radiation loss compared to its corresponding microstrip line.

The transmission characteristics of the measured MSTL on the fused silica substrate up to 500 GHz are presented in Figure 4.16. Figure 4.16(a) shows the theoretical and experimental propagation phase constant over the entire frequency range of interest. Figure 4.16(b) plots the theoretical and experimental attenuation of MSTL compared to the experimental result of a low dispersive thin-film microstrip line fabricated on low-resistivity Si with polymerized cyclotene as the high quality dielectric substrate from [36]. As expected, MSTL grants a continuous low attenuation characteristic over all the measured frequency range. The measured attenuation exhibits a frequency dependency; close to the TE_{10} cut-off frequency at 120 GHz, the attenuation falls off and goes up again to 200 GHz, from which it continues constantly and roughly flat over the frequency range of interest. However, in case of an optimized well-performing microstrip line, the attenuation easily increases with frequency up to 3dB/mm at 500 GHz.

Except for some fabrication tolerances, other adverse factors may contribute to the discrepancy observed between the theoretical models and experimental measurements. Indeed, MSTL is subject to difficult-to-evaluate copper surface roughness effects in connection with current and field distributions. The field and current move more toward the bottom of the conductor surface, where a roughness lies. The copper surface roughness of substrate affects the conductor losses as well as the propagation constant of the transmission line [48]. Conductor trapezoidal effect or “edge profile,” where the conductors are considered to be rectangular, can increase the influence of copper surface roughness on loss and propagation constants. Morgan correlation [48] is a multiplicative correction factor K to the attenuation constant calculated for a smooth conductor, the RMS value of the conductor roughness, and the skin depth. At low frequencies where the skin depth is large, the value of K is close to one. With higher profile conductors and higher frequencies, the value of K approaches two. This correlation predicts that the maximum effect of the conductor

roughness would be to double the conductor loss and saturate exactly as noticed in Figure 4.15(B) and Figure 4.17(B).

4.8 Conclusions

The proposed mode selective transmission line (MSTL), effectively covering from DC to THz frequency range with the desired operation, is found suitable for full-band electromagnetic propagation and ultra-high-speed pico-pulsed signal transmission. It can be made to support single-mode transmission over a super-wide range of frequency through the process of mode selectivity. MSTL in a fully integrated form that exhibits a disparate modal characteristic of traditional planar microwave transmission lines and non-planar metallic waveguides. Whereas at low frequency MSTL operates under the TEM-mode regime, the operating mode is gradually converted to a low-loss TE_{10} mode for operation at high frequency, such as mmW and THz. In this work, the MoL modeling technique together with two commercial software packages has been used in support of extensive theoretical modeling and numerical analysis dealing with field distributions and parametric studies. Careful experiments have been made with two different sets of experimental prototypes. Calculated, simulated and measured results are in good agreement, validating the proposed MSTL techniques. Physical mechanism and design approaches have been studied in detail. Low-loss and low-dispersion characteristics of MSTL have been well observed and explained with reference to the modal behavior and loss properties.

Through this research, the MSTL is found to allow for the possibility of developing densely integrated interconnects and planar guided-wave structures for DC-THz bandwidth applications. This low-loss, low-dispersion and broadband integrated transmission line is a key-enabling disruptive technology toward the development of the next generation of DC-to-THz integrated electronic circuits and systems. In addition, this concept points out a self-packaging solution that is necessarily required for THz and mmW integrated circuits, as it is anticipated that unavoidable dielectric loss and insufficient patterning accuracy may limit the use of current packaging techniques for mmW and THz-wave applications. Combining the advantages of planar technology of low fabrication cost with the low-loss intrinsic to the operation mode, the MSTL is deemed to be a promising candidate for the future research and development of high-frequency performance-demanding integrated electronic and photonic circuits and systems in which broadband

transmission lines are the most fundamental building elements and techniques, due to its unprecedented attractive features over the entire DC-THz electromagnetic spectrum.

4.9 References

[1] S. Narenda, L. Fujino, K. Smith, “Through the Looking Glass Continued (III): Update to Trends in Solid-State Circuits and Systems from ISSCC 2014 [ISSCC Trends],” IEEE Solid-State Circuits Magazine, vol. 6, no. 1, pp. 49-53, 2014.

[2] K. Feher, Digital Communications. Englewood Cliffs, NJ: Prentice-Hall, 1981.

[3] J. Capmany and D. Novak, “Microwave photonics combines two worlds,” Nature Photon., vol. 1, 319–330, 2007.

[4] F. Fesharaki and K. Wu, “Band-pass non-TEM mode traveling-wave electro-optical polymer modulator for millimeter-wave and terahertz application,” J. Lightwave Technol., vol. 30, no. 23, pp. 3586–3596, 2012.

[5] M. Tonouchi, “Cutting-edge terahertz technology,” Nat. Photon., vol. 1, no. 2, pp. 97–105, 2007.

[6] R. Saleh et al., “System-on-Chip: Reuse and Integration,” Proc. IEEE, vol. 94, no. 6, pp. 1050–1069, 2006.

[7] K. Wu, “Towards system-on-substrate approach for future millimeter-wave and photonic wireless applications,” Proc. Asia-Pacific Microwave Conf., 2006.

[8] H. Casimir and J. Ubbink, “The skin effect. I. Introduction the current distribution for various configurations,” Philips Tech. Rev., vol. 28, pp. 271–283, 1967.

[9] M. Bozzi, A. Georgiadis, and K. Wu, “Review of substrate integrated waveguide (SIW) circuits and antennas,” IET Microw. Antennas Propag., vol. 5, no. 8, pp. 909–920, 2011.

[10] F. Xu and K. Wu, “Guided-wave and leakage characteristics of substrate integrated waveguide,” IEEE Trans. Microw. Theory Tech., vol. 53, no. 1, pp.66–73 2005.

[11] R. Mendis, and D. M. Mittleman, “An investigation of the lowest-order transverse-electric (TE1) mode of the parallel-plate waveguide for THz pulse propagation,” J. Opt. Soc. Am. B, vol. 26, no.9, pp. A6–A13, 2009.

[12] R. Mendis, and D. M. Mittleman, “Comparison of the lowest-order transverse-electric (TE1) and transverse-magnetic (TEM) modes of the parallel-plate waveguide for terahertz pulse applications,” Optics express, vol. 17, no. 17, pp. 14839–14850, 2009.

[13] E. A. J. Marcatili and R.A. Schmeltzer, “Hollow metallic and dielectric waveguides for long distance optical transmission and lasers,” Bell Syst. Tech. J. 43, 1783, 1809, 1964.

[14] G. Gallot, S. P. Jamison, R. W. McGowan, and D. Grischkowsky, “Terahertz waveguides,” J. Opt. Soc. Am. B, vol. 17,no.5, pp. 851–863, 2000.

[15] R. Mendis, and D. Grischkowsky, “THz interconnect with low-loss and low-group velocity dispersion,” IEEE Microwave and Wireless Components Letters, vol. 11, no.11, pp.444–446, 2001.

[16] S. Coleman, and D. Grischkowsky, “A THz transverse electromagnetic mode two-dimensional interconnect layer incorporating quasi-optics,” Applied Physics Letters, vol. 83, no. 18, pp. 3656–3658, 2003.

[17] S. Coleman, and D. Grischkowsky, “Parallel plate THz transmitter,” Applied Physics Letters, vol. 84, pp. 654–656, 2004.

[18] R. Mendis, and D. Grischkowsky, “Undistorted guided-wave propagation of subpicosecond terahertz pulses,” Optics letters, vol. 26, no. 11, pp. 846–848, 2001

[19] J. Liu, R. Mendis, and D. M. Mittleman, “The transition from a TEM-like mode to a plasmonic mode in parallel-plate waveguides,” Applied Physics Letters, vol. 98, no. 23, pp. 231113, 2011.

[20] F. Fesharaki, T. Djerafi, and K. Wu, “Low-Loss and Low-Dispersion Transmission Line over DC-to-THz Spectrum”, IEEE Transaction on Terahertz Science and Technology, vol. 6, no. 4, 2016.

[21] U. Schulz and R. Pregla, “A new technique for the analysis of planar waveguides and its application to microstrips with tuning septums,” Radio Sci., vol. 16, pp. 1173-1178, 1981.

[22] S. B. Worm and R. Pregla, “Hybrid-mode analysis of arbitrarily shaped planar microwave structures by the method of lines,” IEEE Trans. Microw. Theory Tech., vol. 32, no. 2, pp.191–196 1984.

[23] R. Collin, Field Theory of Guided Waves (McGrow-Hill Book Company INC. NY), ch4, 5, 1960.

[24] C. Ch. Tang, Advances in Microwaves, vol. 4, 1969.

[25] J. M. Liu, Photonic devices, Ch. 4, Cambridge University Press, 2009.

[26] C. A. Balanis, Advanced Engineering Electromagnetics, (John Wiley & Sons), Ch. 7, 1989.

[27] K. Yasumoto, “Coupled-mode formulation of multilayered and multi-conductor transmission lines,” IEEE Trans. Microw. Theory Tech., vol. 44, pp. 585–590, 1996.

[28] M. N. Rosenbluth, and R. Z. Sagdeev, Handbook of Plasma Physics, Ch. 24, North-Holland, Amsterdam, 1983.

[29] Z. Ma, E. Yamashita, and S. Xu, “Hybrid-mode analysis of planar transmission lines with arbitrary metallization cross sections,” IEEE Trans. Microw. Theory Tech., vol. 41, pp. 491–497, Mar. 1993.

[30] A. Patrovsky, M. Daigle and K. Wu, “Coupling mechanism in hybrid SIW-CPW forward couplers for millimeter wave substrate integrated circuits,” IEEE Trans. Microw. Theory Tech., vol. 56, no. 11, pp. 2594 –2601, 2008.

[31] C.-C. Tien, C.-K. C. Tzuang, S. T. Peng, and C. C. Chang, “Transmission Characteristics of Finite-Width Conductor-Backed Coplanar Waveguide,” IEEE Trans. Microw. Theory Tech., vol. 41, pp. 1616–1624, 1993.

[32] P. Lampariello, F. Frezza, and A. A. Oliner, “The transition region between bound-wave and leaky-wave ranges for a partially dielectric-loaded open guiding structure,” IEEE Trans. Microwave Theory Tech.., vol. 38, pp.1831–1836, 1990.

[33] B.E. Kretch, and R.E. Collin, “Microstrip dispersion including anisotropic substrates,” IEEE Trans. Microwave Theory Tech., vol. 35, no. 8, pp. 710–718, 1987.

[34] G. Ghione, C. U. Naldi, “Coplanar waveguides for MMIC applications: Effect of upper shielding, conductor backing, finite-extent ground planes, and line-to-line coupling,” IEEE Trans. Microwave Theory Tech., vol. 35, no. 3, pp. 260–267, 1987.

[35] N. Marcuvitz, Waveguide Handbook, vol. 10, 1951 :McGraw-Hill

[36] J. A. Deibel, L. Berndsen, K. Wang, and D. M. Mittleman, “Finite-element method simulations of guided wave phenomena at terahertz frequencies,” Proc. IEEE, vol. 95, no. 8, pp. 1624–1640, 2007.

[37] U. Schulz and R. Pregla, “A new technique for the analysis of the dispersion characteristics of planar waveguides,” 4rch. Elec. Ubertragung., vol. 34, pp. 169–173, 1980.

[38] U. Schulz and R. Pregla, “A new technique for the analysis of the dispersion characteristics of planar waveguides and its application to microstrips with tuning septums,” Radio Sci., vol. 16, pp. 1173–1178, 1981.

[39] S. B. Worm and R. Pregla, “Hybrid mode analysis of arbitrarily shaped planar microwave structures by the method of lines,” IEEE Trans. Microwave Theory Tech., vol. 32, pp. 191–196, 1984.

[40] K. Wu and R. Vahldieck “Field distribution and dispersion characteristics of fundamental and higher-order modes in miniature hybrid MIC (MHMIC) considering finite conductor thickness and conductivity,” IEEE MTT-S Int. Microwave Symp. Dig., pp.995–998 1991.

[41] F. Schm&uuml,ckle and R. Pregla, “The method of the lines for the analysis of lossy planar waveguides,” IEEE Trans. Microw. Theory Tech., vol. 38, no. 10, pp.1473–1479, 1990.

[42] D. Pozar, Microwave Engineering, ch3, Wiley, ed.4, NY, 2009.

[43] K.Howell and K. Wong, “DC to 110 GHz measurements in coax using the 1 mm connector,” Microwave Journal, vol. 42, no. 7, pp. 22–34, 1999.

[44] D. C. Thompson , O. Tantot , H. Jallageas , G. E. Ponchak , M. M. Tentzeris and J. Papapolymerou, “Characterization of liquid crystal polymer (LCP) material and transmission lines on LCP substrates from 30–110 GHz,” IEEE Trans. Microw. Theory Tech., vol. 52, no. 4, pp. 1343–1352, 2004.

[45] H. Heiliger, M. Nagel, H.G. Roskos, H. Kurz, F.Schnieder, W.Heinrich, R.Hey, and K. Ploog, “Low-dispersion thin-film microstrip lines with cyclotene (benzocyclobutene) as dielectric medium,” Appl. Phys. Lett., vol. 70, no. 17, pp. 2233–2235, 1977.

[46] S.P Morgan, “Effect of surface roughness on eddy current losses at microwave frequencies,” Journal of Applied Physics, vol. 20, no. 4, pp. 352–362, 1949.

CHAPTER 5 ARTICLE 4 : MODE-SELECTIVE TRANSMISSION LINE FOR TERABIT-PER-SECOND ON-CHIP INTERCONNECTS

Overview: DC-to-THz on chip interconnects are compulsory for THz electronic and photonics. In this chapter, MSTL is exploited as an alternative transmission line for global and local on chip interconnects.

(IEEE Transactions on Microwave Theory and Techniques, submission date: June 2016)

Mode-Selective Transmission Line for Terabit-Per-Second On-Chip Interconnects

Faezeh Fesharaki[1], Tarek Djerafi[1], Mohamed Chaker[2], and Ke Wu[1]

[1]Poly-Grames Research Center, École Polytechnique de Montréal, QC H3T 1J4, Canada

[2]Centre Énergie Matériaux Télécommunications, Varennes, QC J3X 1S2, Canada

Abstract — The recently developed mode-selective transmission line (MSTL) is proposed and exploited as an alternative approach to accommodate the growing and future ultra-fast interconnects requirements of ultra-large-scale integration (ULSI) for high density, speed, performance, and bandwidth. A parametric study is performed to optimize the MSTL structure for high speed global interconnects and to provide high-performance signal integrity. Picosecond and rectangular pulse propagations on MSTL are examined and pulse distortion, broadening, ringing, and reflection are characterized. Eye diagram is also shown to examine the jitter and noise. Due to our limited low-cost PCB fabrication accuracy, the frequency domain measurement is carried out up to 110 GHz. Our optimal fabricated MSTL structures show an ultra-wide absolute bandwidth covering DC, maintain more than 200% relative bandwidth while transmitting around 90° bends, and achieve a measured crosstalk of better than -45 dB over the entire band. Time domain characterizations imply that the PCB-based MSTL accommodates data rates greater than 200 Gb/s. This technology allows, for the first time, the transmission of ultra-high speed electrical signal and picosecond pulse transmission through global interconnects with much lower dispersion and loss than the today's technologies.

Index Terms — Mode-selective transmission line, high-speed global interconnect, signal integrity, ultra-large-scale integration (ULSI).

5.1 Introduction

The idea of integrated circuits (ICs) was born after the development of the first integrated transistor in 1949. With rise and fall times around 100psec, 3.5 GHz bandwidth (BW) and 7 Gb/s data rate, wire interconnects were transformed to transmission lines and the first operational semiconductor IC was created in 1960s [1]. From there on, the applications of electronics have been expanded phenomenally. ICs are being used in all the electronic equipment today. Computers, smartphones, and other devices that are now inseparable building parts of the structure of modern societies have been rendered possible by low-cost and mass-producible ICs.

The growing cloud computing and big data applications and future wireless systems and mass-deployable Internet of Things (IoT) dictate an ever-increasing demand for signal bandwidth and system capacity. Today, relevant IEEE committees have declared that the bandwidth demand is growing faster than the current capacity to deliver it [2]. More than 44% of the world's population is estimated to be online at this time and this proportion will rapidly grow [3]. More users and more devices generate more demands for transmission bandwidth. In 2010, the booming volume of data transmitted around the globe has rendered the standardization of 100 Gb/s Ethernet and 100G optical transport network, and now much higher rate interfaces are appealed, thus pushing the research community and industry sector toward exploring 400G as well as Terabit Ethernet [4]. On the other hand, increasing data rate in wireless communications necessitates the transformation of radio-frequency (RF) technology toward high millimeter-wave (mmW) and THz region as the highly-publicized fifth generation (5G) wireless communications technology are on the horizon.

With the advances in transistor technology, the maximum oscillation frequency fmax above 1 THz has already been demonstrated, and a single device switching time has been drastically reduced to two picoseconds or less [5], [6]. However, on-board circuit interconnects, in particular on-chip interconnects at such high frequencies are increasingly becoming the major bottleneck issues and greater performance limiters of system-on-a-chip (SoC) and system-on-a-package (SoP) than transistors or clock devices themselves [7]–[9]. Increasing switching speeds of digital systems on one hand and operating frequency of RF applications on the other have merged digital and analog design platforms. In order to develop high-frequency and high performance analog and mixed-signal ICs as well as optical communication systems, signal integrity is amongst the most fundamentally challenging issues that needs to be addressed. In fact, the current circuit and

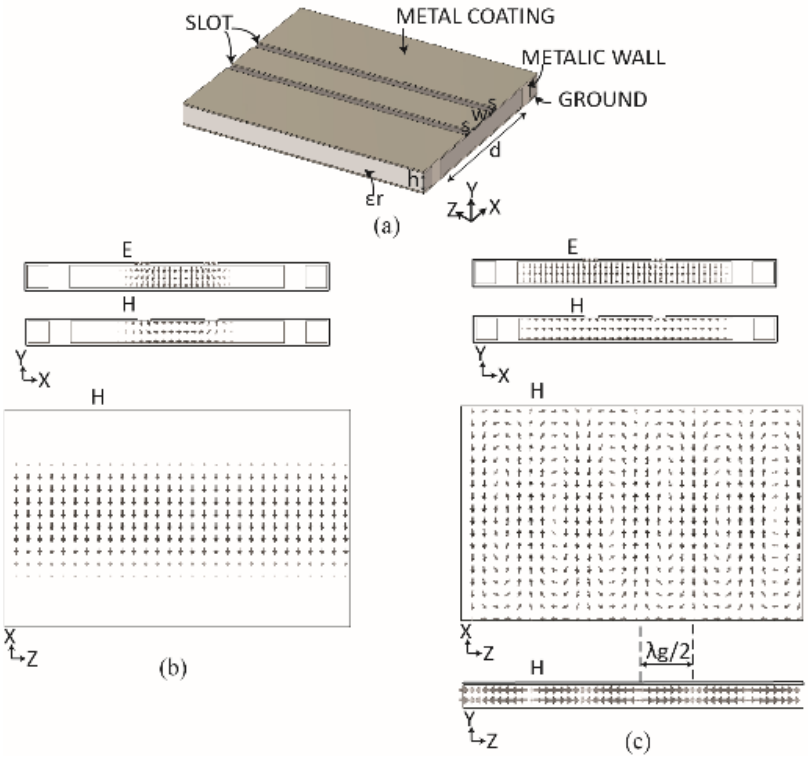

Figure 5.1: a) Mode-selective transmission line (MSTL) on a dielectric substrate. b) MSTL with TEM regime at lower frequency range (d>λg/2): electric and magnetic field distribution over the cross section and top view of magnetic field along the length of MSTL. c) MSTL with TE_{10} regime at higher frequency range (d<λg/2): electric and magnetic field distribution over the cross section and top view of magnetic field along the length of MSTL.

interconnects design approaches result in ineffective packaging and device cascading as well as the probably total failure in realizing the possible potential performance of ultra-high-speed electronic and optoelectronic ICs [10].

The goal of signal integrity in connection with high-speed pulse propagation, through a single chip, a motherboard with embedded transmission line interconnects, or a whole system, is to maximize the probability of delivering a signal without errors. Currently, the interconnection delay time is much longer than the current device switching time, and the performance is limited by power dissipation, signal dispersion, and crosstalk [11]–[13]. As the transistor operating voltage is scaling down, interconnect noise level and crosstalk become more and more critical. Furthermore, delays

because of packaging issues and board-level connections present difficult-to-overcome hurdles. To deliver broadband and/or high-speed signal paths efficiently to other neighboring integrated

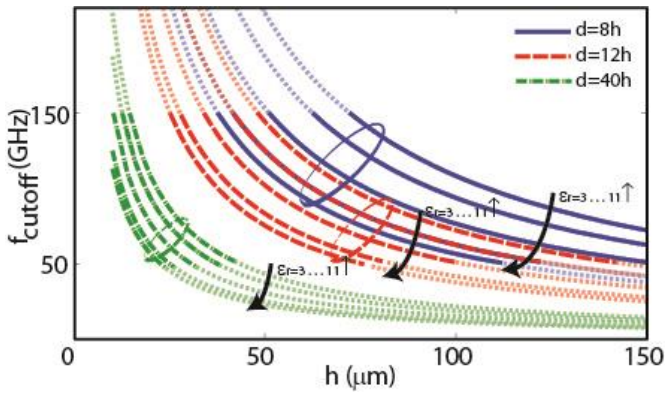

Figure 5.2: MSTL interconnect design curves (the mode-conversion frequency cutoff) for different values of substrate dielectric constants (ε_r =3, 4, 6, 9, 11)

circuits and the outside world through on and off chips, the problem must be addressed by resorting to electromagnetic and radiating systems knowledge. RF interconnect technologies have been the most promising approach for on and off chips, through which wireless communication and high-frequency silicon technologies are compiled [14], [15]. A huge effort has been made over the last twenty years to improve the conventional RF transmission lines by reducing the resistivity of conductors and the dielectric constant of interlayer dielectric materials, but it turns out that revolutionary methods and disruptive techniques are necessary to fulfill the demand of heavily data-centric systems and applications [16]–[19]. The well-known performances of conventional microstrip transmission line and coplanar waveguide (CPW) are not adequate for the development of ultra-fast interconnects when switching speeds are less than 8 ps and this limit would increase to 20 ps when considering the packaging that is essential to reduce radiation and coupling between circuits [20]–[23]. Substrate integrated waveguide (SIW), on the other hand, can be used at higher frequencies but with a limited BW (< 65% relative BW), and it does not support low frequency ranges or DC due to its cut-off frequency nature [24].

To tackle the BW problem and also to overcome the performance limitations of conventional large-scale interconnects, this paper reports our recent study in applying the mode-selective transmission line (MSTL) as a new design technology solution for both intra- and inter-chip high-speed ULSI. MSTL supports a dominant mode very similar to the microstrip line in lower frequency range covering DC whereas it supports the fundamental mode of rectangular waveguide at higher frequency. Therefore, effectively covering the desired operation from DC to THz frequency range,

MSTL is suitable for full DC-THz low-dispersion and low-loss electromagnetic propagation and ultra-high-speed terabit pulsed signal transmission [25], [26].

In this work, design guidelines for MSTL interconnects are established and discussed. MSTL straight lines and 90° bend structures are optimized for the design of high-density integrated circuits. In the consideration of tradeoffs, an optimized design is selected, simulated, and prototyped. The fabricated circuits are then characterized in both frequency domain and time domain. The effects of dispersion and losses on high-speed logic circuits, such as pulses and picosecond pulses, are examined. Eye diagram of the prototyped line is also inspected and the crosstalk of side-by-side lines is measured. Our results indicate that MSTL reduces the crosstalk, noise, power loss, and delay of signal transmission significantly, and the proposed technique provides a huge signal bandwidth. Additionally, the cost would be substantially reduced through reducing an actual number of I/O ports going off-chip.

5.1.1 **Design and optimization**

Figure 5.1 shows the proposed MSTL interconnect on a dielectric substrate and its principle of operation. The dielectric substrate with a permittivity of ε_r, a width denoted by d and a thickness denoted by h, is enclosed by a conductive coating. On the top conductor, two symmetrical slots determined by s are separated by a conductor strip of width w in the middle (Figure 5.1(a)). MSTL supports a dominant mode with propagation wavelength λg, very similar to the microstrip line in lower frequency range ($d< \lambda_g/2$) covering DC, while it is automatically reconfigured to support the fundamental mode of rectangular or substrate integrated waveguide at higher frequency ($d>\lambda_g/2$) (Figure 5.1(b), Figure 5.1(c)). The inclusive design approach of a typical MSTL structure is detailed in [26] and is adopted in this paper.

The frequency at which the mode-conversion phenomenon takes place is $f_{cutoff} = 1/2d\sqrt{\mu_0\varepsilon_0\varepsilon_r}$. To design MSTL for an ultra-broadband interconnect application, the design should be made in such a way that f_{cutoff} resides around the frequency where loss and dispersion of quasi-TEM mode of operation are not negligible and may deteriorate the circuit performance. Figure 5.2 displays a group of characteristic curves, illustrating the relationship of f_{cutoff} with respect to the thickness of substrate h, for different values of substrate permittivity ε_r. Through these curves, it can be seen that the substrate dielectric constant is changed from 3 to 11 to cover all the conventional

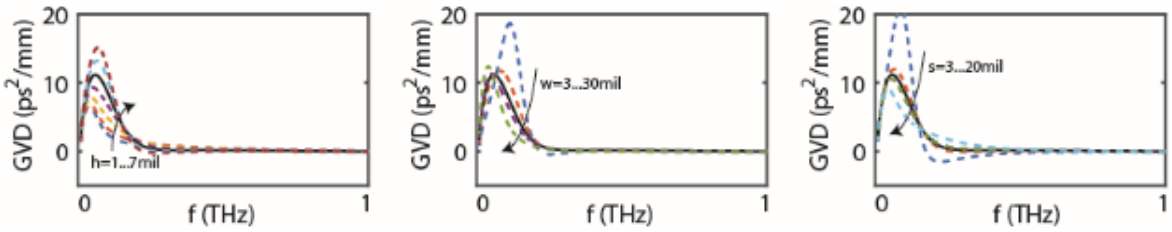

Figure 5.3: Parametric study to optimize GVD over DC to 1 THz: thickness (h), strip width (w), slot width (s).

permittivity value in IC boards. As for the microstrip operation regime d>8h, the curves are obtained with this norm to provide the operation BW, covering very low frequency and DC over which signal energy may be majorly distributed for digital pulses along the interconnect. Once substrate (h, ε_r) is selected, width d can be chosen at its minimum value, provided that the mode conversion takes place at a suitable frequency f_{cutoff}. Selection of this frequency depends also on the package effect and targeted application. For the case of PCB, this frequency can be virtually selected at more than 50 GHz but less than 100 GHz.

As seen from Figure 5.2, in a limiting case, when d=40h, h must be set less than 50μm regardless of the substrate permittivity. Decreasing the value of d/h would result in a more wide-ranged choice of thickness h. Increasing the relative permittivity of substrate ε_r means that a lower value of h must be chosen and the whole circuit size is decreased. In this work, substrate RT/duroid® 6002 laminate with ½ oz. copper thickness from Rogers is used. Its low dielectric constant ε_r=2.94, and low loss tan δ=0.0012 make it a proper choice for higher frequency and higher-speed design. Its thickness h and width d are selected to be 0.127 mm (5 mil) and 1.5 mm, respectively, to achieve a conversion frequency f_{cutoff} around 60 GHz.

To start the optimization, an initial value of s is selected the same as the minimum possible gap realizable in our PCB circuit manufacturing process, and also an initial value is selected for w according to the design criteria [26]. HFSS software is used to optimize loss and group velocity dispersion (GVD) over the whole bandwidth. This step can be limited to an optimization carried out just over a desired frequency range to accommodate desired data rates. GVD is extracted from frequency-dependent propagation constant β as:

Table 5.1: Electric and Magnetic Field Distribution in the Proposed MSTL made on Rogers Substrate at Different Frequency points: Propagating Mode Changes from TEM Mode to TE_{10} Mode

Frequency	Feld Distribution			
	E_y	H_x	H_z	
1 GHz	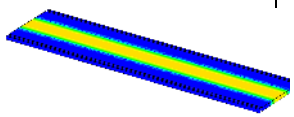	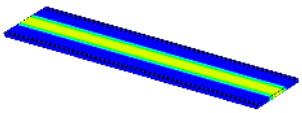	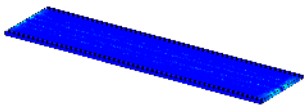	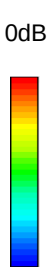
50 GHz	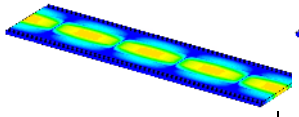	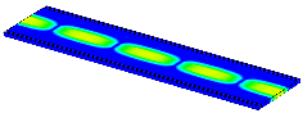	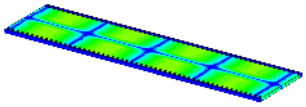	
100 GHz	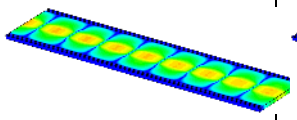	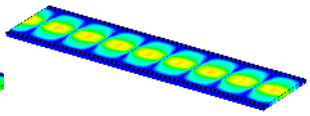	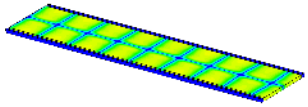	
200 GHz	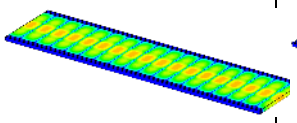	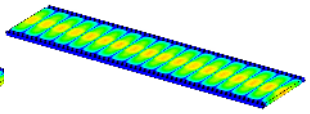	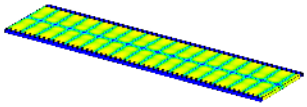	

$$GVD = \frac{\partial^2 \beta}{\partial \omega^2} \tag{1}$$

Figure 5.3 shows a parametric study for our proposed structure in an effort to optimize GVD. The maximum value of GVD is less than 10 ps^2/mm, and takes place around the mode conversion frequency. It must be noticed that this value in the case of SIW is unlimited. A lower value of h provides a lower GVD and radiation, but results in a higher attenuation. On the other hand, increasing the value of w leads to a lower GVD and a more field confinement. Finally, increasing the value of s decreases GVD, but it leads to a more propagation loss. Design parameters are selected as w=2.4h, and s=1.6h. The solid lines in the figure show that our selected parameters in this design provide a good compromise between dispersion and propagation loss over the entire frequency range. Table 5.1 describes the electric and magnetic field propagation and mode conversion phenomena in this MSTL over a number of discrete frequency points, obtained with

CST MWS simulation package. As frequency approaches the cutoff of TE_{10} mode, a remarkable evolution in field distribution is observed, in which the electric field is spread out up to the lateral boundaries of the wave-guiding structure. The longitudinal element of magnetic field Hz appears and power is therefore carried by two bouncing propagating plane waves. In this way, the power is converted from the quasi-TEM mode to a quasi-TE_{10} mode as frequency goes through f_{cutoff}. The magnetic field and surface current distribution are spreading over the whole waveguide section. A 90°-bend MSTL is also designed and optimized using HFSS. To optimize the performance with a maximum possible bandwidth, a curved bend configuration is used. An initial value of 3w was selected for the inner radius, and it was finally selected to be 1.25mm after optimization.

5.2 Fabrication and measurement

Our MSTL prototypes were fabricated on RT/duroid® 6002 Rogers substrate with 0.127 mm thickness (h=5 mil). The dimensions were selected as d=1.5 mm, w=0.3 mm, s=0.2 mm, following a thorough discussion and analysis in the last section. To characterize the circuit with our PNA Network Analyzer over a broadband frequency range, a standard microstrip feed cannot be used because of the frequency cutoff of coaxial connectors. Therefore, a transition section from MSTL to ground-signal-ground (GSG) wafer picoprobes with GCPW head is designed so that on-wafer high frequency picoprobes can be used for the measurements. Figure 5.4 shows the fabricated line and double 90°-bend MSTL with a transition section to GCPW for circuit characterization using the GSG picoprobes. The GSG picoprobes have standard dimensions available in the market, and according to the frequency of operation, they have dimensional limitations that must be respected in the design. Above the frequency of 110 GHz, the GSG pitch dimensions are decreased to less than 100 μm. However, the accuracy of our available PCB fabrication process is limited to ~101μm (4 mil). Therefore, our measurement for the validation of MSTL interconnects is carried out up to 110 GHz even though the proposed techniques can cover a much higher frequency range.

As seen in Figure 5.4(a), for the fabrication of the conductive walls of MSTL straight lines, large rectangular via holes have been made instead of a continuous conductive wall. In this case, the fabrication process is facilitated especially in electroplating and metallization of the conductive walls. The dimension of the rectangular vias are 0.762 mm (30 mil) long and 0.254 mm (10mil) wide, and they are placed with 0.127 mm (5 mil) distance; these dimensions are based on a low-

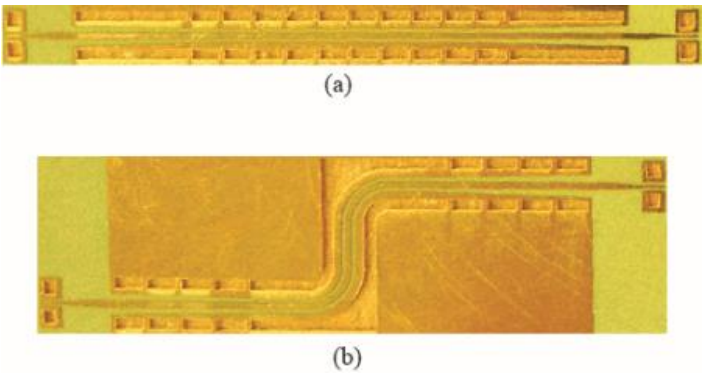

Figure 5.4: a) Fabricated MSTL line; b) Fabricated MSTL bend.

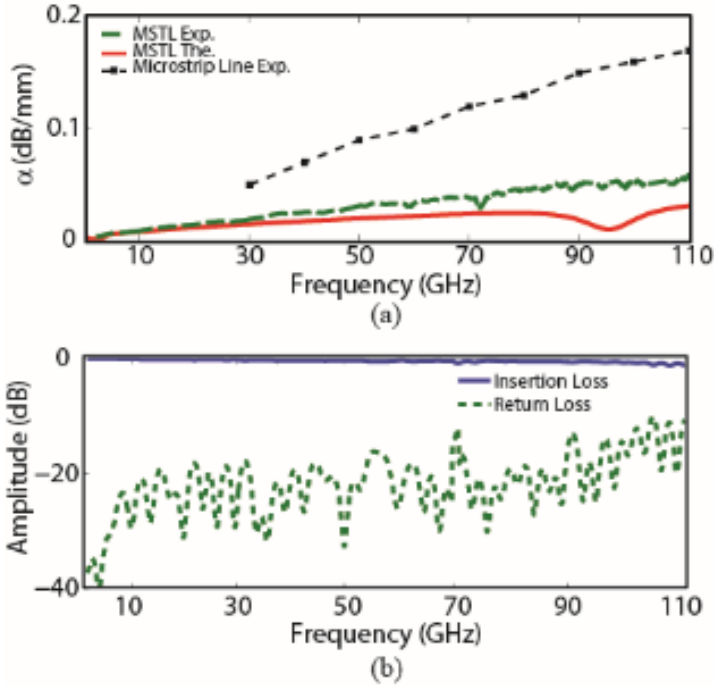

Figure 5.5: a) Comparison of theoretical and experimental propagation loss obtained from frequency domain characteristics of the MSTL prototype fabricated on RT/duroid® 6002 laminates from Rogers (h=127um, d=20h, s=1.6h, w=2.4h) and its corresponding microstrip line from ref [27]. b) Frequency domain characterization of MSTL 90° bend.

cost, commercially available PCB-compatible fabrication process. Along the corner of the MSTL bend, the conductive walls are fabricated continuously (Figure 5.4(b)).

In designing the transition section, slots are tapered out exponentially to the lateral boundaries. The metal strip in the center is tapered to the 50 Ω impedance width. The lateral walls are metalized allowing a smooth field evolution and characteristic impedance transition from MSTL to microstrip line. Large squared via holes (15 mil x 15 mil) are used in the fabrication of lateral probing sections. As operating frequency increases, the via-hole input impedance becomes inductive, because its electrical length to the ground plane increases. The reactance of the grounding via hole becomes noticeable and then prejudicial to calibration and measurements. The large dimensions of the grounding via hole help to stay away from the limitations caused by the via hole inductance and to allow its usage in grounding and building a launch transition for on-wafer measurements. To remove the effects of feeding sections, a through-reflect-line (TRL) calibration was performed with three delay lines, a through, and a short reflect. The measurements were done over a 3-to-110 GHz band using Agilent PNA-X and cascaded picoprobes with 250 μm GSG probe pitch incorporated with 1 mm connector to provide a continuous measurement.

5.3 Characterization

5.3.1 Attenuation

Frequency domain characterizations of the fabricated MSTL circuits are illustrated in Figure 5.5. Figure 5.5(a) shows the signal attenuation of the fabricated MSTL line and a comparison with the theoretical calculation, and the results of the corresponding microstrip transmission line. The theoretical calculation is made with the method of lines (MoL), which is a semi-analytical technique for full-wave analysis [28], [29]. The signal attenuation of the MSTL line is less than 0.07dB/mm up to 110 GHz. The S-parameters of the fabricated MSTL bend is shown in Figure 5.5(b), showing insertion loss less than 0.8 dB over the entire frequency range. A comparison of the loss characteristics of various waveguides and transmission lines is given in Table 5.2. For wideband applications, dispersion is also a performance deteriorating factor for microstrip transmission line and CPW.

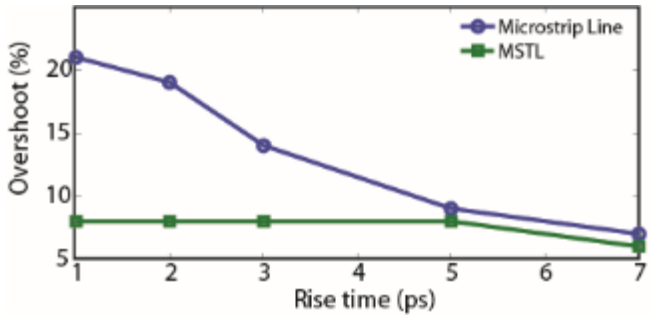

Figure 5.6: Comparison of signal overshoot vs rise time between microstrip line and MSTL.

Table 5.2: TL attenuation summary

Line	Attenuation dB/ mm
Microstrip	0.7 @ 100GHz, 2.2 @500 GHz
CPW	0.1 @ 120 GHz, 2.5 @500 GHz
Circular Waveguide	0.378 @ 120 GHz, 1.084 @500 GHz
SIW	0.04 @100 GHz, 0.3@900 GHz
MSTL	0.07 @100 GHz, 0.3@500 GHz

Signal attenuation of 0.7 dB/mm is obtained at 100 GHz in [32] for microstrip line and 0.1 dB/mm for CPW; these values increase to 2.2 and 2.5 dB/mm at 500 GHz. The hollow metallic waveguides have been traditionally fabricated from metals with rectangular, square, and circular cross sections. TE01 wave mode in circular waveguide yields a transmission loss about 0.4 dB/mm [33] at 120 GHz and 1 dB/mm at 500 GHz. For SIW, attenuation close to 0.04dB/mm was reported in [33] at 94 GHz. Results in [34] show a waveguide loss of about 3 dB/mm. The SIW was designed using a 76-μm-thick quartz substrate with permittivity of 3.8 and loss tangent of 0.003 at 0.9 THz. The proposed MSTL shows not only a lower level of signal attenuation (0.07 dB/mm @100 GHz,

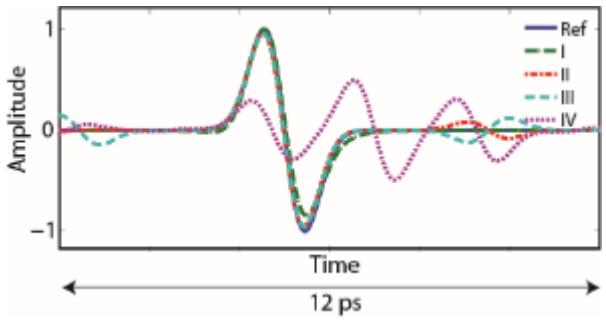

Figure 5.7: Gaussian pulse (Ref: 1ps FWHM) propagation on MSTL line and bend and comparison with microstrip line. I: MSTL line (10mm long) from theoretical calculation, II: MSTL line from experimental result, III: MSTL bend from experimental result, IV: microstrip line (10mm long, the same substrate as MSTL, and 50 ohm characteristic impedance) from ADS simulation.

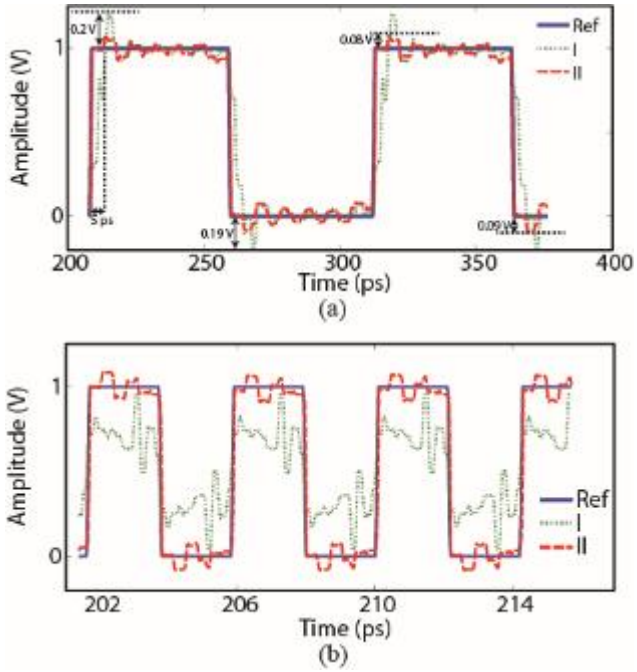

Figure 5.8: a) Rectangular pulse (50 ps width, 1ps rise time) after propagating 10mm through microstrip line and MSTL. I: microstrip line—5 ps rise time and prepulse distortion, 20% overshoot, 18% backswing. II: MSTL, following the same rise time as the reference pulse, 6% overshoot, 8% backswing. b) Time domain characterization of RF/microwave signals: 2ps width, 0.1ps rise time via 1-cm-long MSTL, and comparison with the simulation of conventional 1-cm-long MTL.

Table 5.3: Rectangular Pulse (50 ps width, 1ps rise time) Propagation through Microstrip line and MSTL

	Microstrip Line	MSTL
Prepulse distortion	Yes	No
Rise time (ps)	5.6	1
Overshoot (%)	20	8
Backswing (%)	19	9

0.3dB/mm @500 GHz) but also it is non-dispersive and its loss variation is negligible over all the frequency range covering DC [25].

5.3.2 **Dispersion**

In order to investigate the signal dispersion characteristics of the MSTL illustratively, the evolution of Gaussian-shaped picosecond electrical pulses guided by these structures is examined. Knowing the MSTL's physical characteristics and its finite-size causal passive component, an accurate time domain model is obtained from band-limited S-parameter data with the use of Kramers-Kronig relation, which is provided by ADS Transient Convolution Element [30], [31]. A Gaussian pulse with 1ps full width at half maximum (FWHM) is used as the reference pulse to observe the evolution of Gaussian-shaped picosecond pulse on MSTL. Figure 5.6 displays the time domain characteristics of the fabricated MSTL line and bend. In the same figure, the results are compared with the theoretical calculation; in this case, the propagation characteristics derived from the MoL

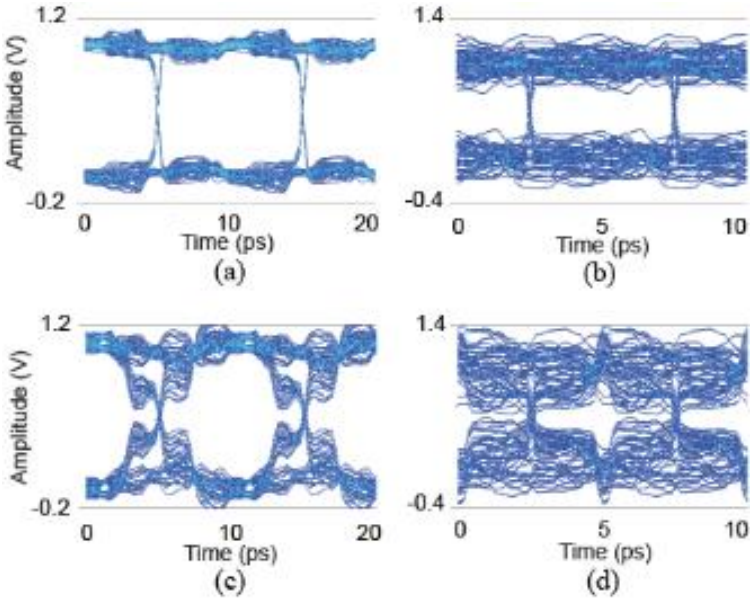

Figure 5.9: Eye diagram fed from a pseudo random bit sequence NRZ signal source generator with a 100-Gb/s data rate and 0.5ps rise time: a) MSTL and b) Microstrip line.

Eye diagram fed from a Pseudo Random Bit Sequence (PRBS) signal source generator with a 200-Gb/s data rate and 0.2ps rise time: c) MSTL and d) Microstrip line.

are used and the propagation of the same reference Gaussian pulse is studied using an inverse Fourier transform. Theoretical and experimental results show an excellent consistency. A 50 ohm microstrip line is also designed on the same substrate and simulated with the Momentum ADS package and the same Gaussian pulse is monitored after passing through this line as well. The signal dispersion characteristics of these transmission lines are clearly observed from the figure.

5.3.3 **Signal reflection and ringing**

A narrow digital pulse with fast rise time contains a broad BW of frequency spectrum. Therefore, similar to a high frequency analog signal, the power of high-speed digital pulses drops and dissipated as the pulse propagates along the traditional transmission lines or interconnects. Because this propagation loss strongly depends on frequency, it distorts the pulse as an oscillatory-tail. These high-frequency effects may include dispersion, attenuation, and also the excitation of a leaky radiating mode or other distortive higher order modes. In this section, the effects of dispersion and losses of MSTL interconnects on high-speed logic-like pulses are examined and compared with the

case of microstrip line. In the first experiment, a rectangular pulse with 50 ps width and 1ps rise time has been used at the input. Figure 5.7(a) shows the reference pulse and the distorted pulse after 1-cm propagation through MSTL and the corresponding microstrip line. It is observed that the MSTL output pulse follows the same rise time as the reference pulse, with 6% overshoot and 8% backswing. The same pulse, after propagating through the analogous microstrip line, shows more than 5 ps rise time and prepulse distortion, 20% overshoot, and 18% backswing. Figure 5.8 compares the overshoot after propagating through the microstrip line and MSTL versus different pulse rise times. With decreasing the rise time to 4ps, the overshoot doubles in case of the microstrip line, while it continues to be constant in the case of MSTL. Table 5.3 is a summary of the pulse characteristics after propagating through these two transmission lines.

In the second experiment, a 2 ps pulse width with 0.1 ps rise time is used at the input. The reference pulse and the distorted pulses after 1-cm propagation through MSTL and microstrip line are presented in Figure 5.7(b). MSTL output pulse follows the same rise time and goes through a faint distortion. On the other hand, the microstrip line output pulse suffers from a severe distortion even though the packaging effect is not included in these results.

5.3.4 **Signal delay and distortion**

To examine the MSTL interconnect for high-speed digital communications, an eye diagram is used and observed to visualize and determine the key parameters of the electrical quality of signals after high-speed digital transmissions through MSTL interconnect and to qualify the signal integrity. Once more, the S-parameters obtained from measurements are used as the circuit component fed from a pseudo random bit sequence NRZ signal source generator in ADS and an eye diagram is thus obtained. This approach represents the real measurement scenario and is specifically advantageous since such a high frequency oscilloscope is hardly available to provide more than 100 Gb/s bit rate measurement. As explained above, a 50 Ω microstrip line is also designed on the same substrate and simulated in momentum ADS and used as a circuit component to compare its simulated eye diagram with the case of a measured MSTL.

Figure 5.9(a) shows the eye diagram that resulted from the feeding MSTL with a pseudo random bit sequence NRZ signal source generator with 100 Gb/s data rate and 0.5ps rise time. Figure 5.9(b) is the same experiment on the corresponding microstrip line. MSTL shows zero jitter and 50%

Figure 5.10:.Fabricated circuit for crosstalk measurement.

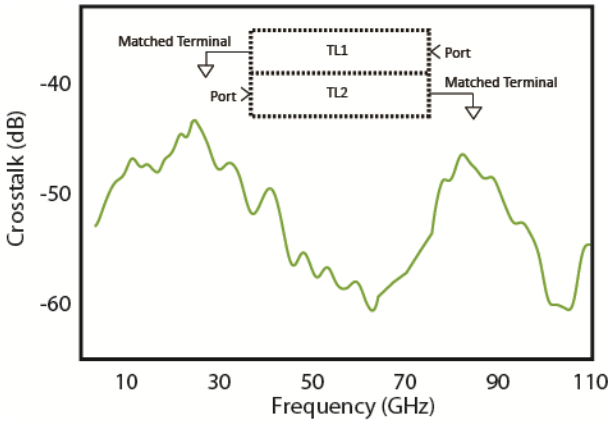

Figure 5.11:.Crosstalk measurement between side by side MSTLs.

better SNR compared to the microstrip line. Figure 5.9(c) is the eye diagram that comes from the feeding MSTL with a pseudo random bit sequence NRZ signal source generator with 200-Gb/s data rate and 0.2 ps rise time. Figure 5.9(d) is the same experiment on the corresponding microstrip line. The result shows an open eye in the case of the MSTL interconnect, while for the microstrip line, noise and delay have resulted in a closed-eye pattern.

5.3.5 **Crosstalk**

Ultra-high-speed and millimeter-wave ICs with unbounded or semi-unbounded multiple line geometries suffer from electromagnetic crosstalk, which has a serious effect on the circuit performance. Cross talk mechanisms may be inductive or capacitive at lower band of frequency and can be controlled by simply spacing the coupled lines. Crosstalk effect becomes radiative when signal leakage occurs; the power from a leaky mode leaks out in the form of a surface wave or a parallel-plate substrate mode, thereby affecting the adjacent line [36].

Our experimental results on the crosstalk between adjacent MSTLs are presented in this section. Two waveguides of the type shown in Figure 5.5 are arranged to share the same row of vias along a common sidewall, as depicted in Figure 5.11. Two transmission lines, namely TL1 and TL2, are placed side-by-side and each of them is terminated with a matched load on the opposite side. To provide the matched load for such a high frequency band, in conjunction with a 50 Ω surface mount resistance, a chromium resistive film is utilized to realize a matched termination. The schematic view of the structure of Figure 5.10 and the measured crosstalk are presented in Fig. 12. Crosstalk is observed less than -45dB over the frequency range of interest. The common row of metalized vias between two adjacent lines, ensures that the cross talk effects are very weak (for both microstrip mode and SIW mode). As a result, MSTL circuits can be made as dense as conventional microstrip circuits. To control the crosstalk of neighboring microstrip transmission lines, pairs should be separated by a minimum of 5w which is of the same dimension as of the proposed MSTL (d=5w). In a case of two adjacent SIW structures sharing a common row of metalized vias, it was proved that the crosstalk depends on the ratio of inter-via distance/via dimension [37]. Therefore, also in the case of demonstrated MSTL, reducing the distance between rectangular vias would reduce the leakage and therefore crosstalk. The results also show that the crosstalk decreases when frequency increases since the waveguide mode become preponderant. This trend is well observed in the design of SIW structures [37], where the lateral radiation and engendered crosstalk are proportional to the inverse of the operation wavelength.

A signal crosstalk is subject to the sidewall capacitance of interconnects. In MSTL with a continuous conductive sidewall [25], a Faraday cage is created because the grounded sidewalls and signals are isolated from external interference. On the other hand, the design is made in such a way that the slots are non-radiating, the fields are confined within the substrate, and the crosstalk from top slots is negligible as confirmed with the measurements.

5.3.6 **Conclusion**

There is a strong virtuous circle encompassing advanced computing tools and better quality networking and information, subject to speed or electrical signal frequency. As frequency increases, signals can carry more information resulting in improved computation speed and communication bandwidth. MSTL is a promising high-speed electronic circuit technology providing design engineers with new building blocks to enable the development of innovative

solutions for next generation computation and communication systems. In this paper, MSTL interconnects have been modeled, designed, fabricated, and characterized. Both frequency domain and time domain results confirm the integrity of transmitted analog and digital signals through MSTL interconnect systems. This has been made possible thanks to the extrame low-loss and low-dispersion behavior of MSTL over an unprecedented frequency range.

5.4 References

[1] J. Kilby, “Invention of the Integrated Circuit,” IEEE Trans. Electron Devices, vol. 23, no. 7, pp. 648–654, 1976.

[2] J. Brodkin, Ars Technica, “Bandwidth explosion: As Internet use soars, can bottlenecks be averted?” http://arstechnica.com/business/2012/05/bandwidth-explosion-as-internet-use-soars-can-bottlenecks-be-averted/).

[3] Manual for measuring ICT access and use by households and individuals, International Telecommunication Union (ITU), Geneva, Switzerland, 2014.

[4] P. J. Winzer, “Beyond 100G ethernet,” IEEE Commun. Mag., vol. 48, no. 7, pp. 26–30, 2010.

[5] R. Lai, X. B. Mei, W. R. Deal, W. Yoshida, Y. M. Kim, P. H. Liu, J. Lee, J. Uyeda, V. Radisic, M. Lange, T. Gaier, L. Samoska, and A. Fung, “Sub 50 nm InP HEMT device with F _max greater than 1 THz,” Int. Electron Devices Meeting Tech., 2007, pp. 609–611.

[6] S. O. Koswatta, A. Valdes-Garcia, M. B. Steiner, Y.-M. Lin and P. Avouris, “Ultimate RF performance potential of carbon electronics,” IEEE Trans. Microw. Theory Techn., vol. 59, no. 10, pp. 2739–2750, 2011.

[7] K. Lim, S. Pinel, M. F. Davis, A. Sutono, C.-H. Lee, D. Heo, A. Obatoynbo, J. Laskar, M. Tentzeris, and R. Tummala, “RF-SOP for wireless communications,” IEEE Microwave Mag., vol. 3, pp. 88–99, Mar. 2002.

[8] K. W. Goossen and R. B. Hammond, “Modeling of picosecond pulse propagation in microstrip interconnections of integrated circuits,” IEEE Trans. Microw. Theory Techn,. vol. 37, no. 3, pp. 469–478, Mar. 1989.

[9] R. H. Havemann and J. A. Hutchby, “High-performance interconnects: An integration overview,” Proc. IEEE, vol. 89, pp. 586–601, 2001.

[10] J. Sinsky and P. Winzer, “100-Gb/s optical communications,” IEEE Microw. Mag., vol. 10, no. 12, pp. 44–57, 2009.

[11] S. Narenda, L. Fujino, and K. Smith, “Through the Looking Glass Continued (III): Update to Trends in Solid-State Circuits and Systems from ISSCC 2014 [ISSCC Trends],” IEEE Solid-State Circuits Mag., vol. 6, no. 1, pp. 49–53, 2014.

[12] A. Tsuchiya, M. Hashimoto, and H. Onodera, “Performance limitation of on-chip global interconnects for high-speed signaling,” IEICE Trans. Fundamentals, vol. E88-A, no. 4, pp. 885–891, 2005.

[13] L. Markov, “Limits on fundamental limits to computation,” Nature, vol. 512, pp. 147–154, 2014.

[14] M. F. Chang , V. P. Roychowdhury, L. Zhang , S. Hyunchol, and Y. X. Qian, “RF/wireless interconnect for inter- and intra-chip communications,” Proc. IEEE, vol. 89, no. 4, pp. 456–466, 2001.

[15] Matsuzawa, “RF-SoC—Expectations and required conditions,” IEEE Trans. Microw. Theory Techn., vol. 50, pp. 245–253, Jan. 2002.

[16] Alduino and M. Paniccia, “Interconnects: Wiring electronics with light,” Nature Photon., vol. 1, no. 3, pp. 153–155, 2007.

[17] R. K. Cavin, P. Lugli, and V. V. Zhirnov, “Science and engineering beyond Moore’s law,” Proc. IEEE, vol. 100, no. Special Centennial Issue, pp. 1720–1749, 2012.

[18] M. Bohr, “Interconnect scaling—The real limiter to high performance ULSI,” Proc. IEDM, pp. 241–244, 1995.

[19] A. Yu, “The Future of Microprocessors,” IEEE Micro, pp. 46–53, Dec. 1996.

[20] R. Achar, “High-Speed Interconnect Modeling,” IEEE Microw. Mag., pp. 61–74, Aug. 2011.

[21] J.-H. Son, H.-H. Wang, J. F. Whitaker, and G. A. Mourou, “Picosecond pulse propagation on coplanar striplines fabricated on lossy semiconductor substrates: Modeling and experiments,” IEEE Trans. Microw. Theory Techn., vol. 41, pp. 1574–1580, 1993.

[22] Bernal, F. Mesa, D. R. Jackson, W. L. Langston and J. T. Williams, “High-frequency pulse distortion on a lossy microstrip line with a top cover,” IEEE Trans. Microw. Theory Techn., vol. 58, no. 7, pp. 1774–1785, 2010.

[23] M. Tsuji and H. Shigesawa, “Packaging of printed circuit lines: A dangerous cause for narrow pulse distortion,” IEEE Trans. Microw. Theory Techn., vol. 42, no. 9, pp. 1784–1790, 1994.

[24] J. Simpson, A. Taflove, J. A. Mix, and H. Heck, “Substrate integrated waveguides optimized for ultrahigh-speed digital interconnects,” IEEE Trans. Microw. Theory Techn., vol. 54, no. 5, pp. 1983–1990, 2006.

[25] F. Fesharaki, T. Djerafi, M. Chaker, and K. Wu, “Low-Loss and Low-Dispersion Transmission Line over DC-to-THz Spectrum,” IEEE Transaction on Terahertz Science and Technology, vol. 6, no. 4, 2016.

[26] F. Fesharaki, T. Djerafi, M. Chaker, and K. Wu, “Guided-Wave Properties of Mode-Selective Transmission Line,” IEEE Transaction on Microwave Theory and Technique, under review.

[27] D. C. Thompson, O. Tantot, H. Jallageas, G. E. Ponchak , M. M. Tentzeris, and J. Papapolymerou, “Characterization of liquid crystal polymer (LCP) material and transmission lines on LCP substrates from 30–110 GHz,” IEEE Trans. Microw. Theory Techn., vol. 52, no. 4, pp. 1343–1352, 2004.

[28] U. Schulz and R. Pregla, “A new technique for the analysis of planar waveguides and its application to microstrips with tuning septums,” Radio Sci., vol. 16, pp. 1173–1178, 1981.

[29] Wu, Ch.Y. E. Tong, and P. Saguet, “Transverse transmission theory for multilayer planar microwave circuits,” International J. of Numerical Modelling: Electronic Networks, Devices and Fields , vol. 7, no. 4, pp. 225–238, 1994.

[30] Warwick, “Understanding the Kramers-Kronig Relation Using A Pictorial Proof,” White paper, Agilent Technologies, http://signal-integrity.blogs.keysight.com/2009/kramers-kronig-in-pictures/

[31] J. S. Toll, “Causality and the Dispersion Relation: Logical Foundations,” Physical Review, vol. 104, issue 6, pp. 1760–1770, 1956.

[32] F. Schneider and W. Heinrich, “Low-dispersive Coplanar Waveguides and Thin-film Microstrip Lines for Sub-mm Wave Monolithic Integration,” International Conference on Terahertz Electronics, Darmstadt, Germany, 2000.

[33] A. Munir, A. Setiawan, “Transmission loss reduction of circular terahertz waveguide using dielectric-lined method,” International Journal on Electrical Engineering and Informatics, vol.5, no.3, pp.377-385, 2013.

[34] Ghassemi, “Millimeter-Wave Substrate Integrated Waveguide Antenna And Front-End Techniques For Gigabyte Point-To-Point Wireless Services,” PhD Dissertation, École Polytechnique De Montréal, Montreal, Canada, 2014.

[35] Kojima, T., Gonzalez, A., & Uzawa, Y. “Design and Loss Measurement of Substrate Integrated Waveguides at Terahertz Frequencies,” Advanced Technology Center, National Astronomical Observatory of Japan.

[36] A. Oliner, “Leakage, Crosstalk and Package Effects in Millimeter-Wave Integrated Circuits,” Microwave Conference, Paris, 2000.

[37] Passian, M. Bozzi, and L. Perregrini, “Crosstalk in substrate integrated waveguides,” IEEE Trans Electromagn Compat, vol. 57, pp.80–86. 2015.

CHAPTER 6 ARTICLE 5 : S-PARAMETER DE-EMBEDDING ALGORITHM AND ITS APPLICATION TO SUBSTRATE INTEGRATED WAVEGUIDE LUMPED CIRCUIT MODEL EXTRACTION

Overview: The work presented in this chapter was inspired by the motivation to extract the characteristic impedance of MSTL or any transmission line regardless of frequency or operating mode. A unified method is introduced and formulated for deriving the equivalent circuit model of a two-port network and also the characteristic impedance of a transmission line or waveguide for any mode. This method is devised through the combination of a multimode calibration and a commercial numerical simulator. It is based on a generalized calibration technique, which is applicable to the case of TEM mode as well as non-TEM and higher-order propagating modes. The method is simple and straightforward without any complication in the calculations or limitation in the operating frequency.

(IEEE Transactions on Microwave Theory and Techniques, submission date: June 2016)

S-Parameter De-Embedding Algorithm and Its Application to Substrate Integrated Waveguide Lumped Circuit Model Extraction

Faezeh Fesharaki[1], Tarek Djerafi[1], Mohamed Chaker[2], and Ke Wu[1]

[1]Poly-Grames Research Center, École Polytechnique de Montréal, QC H3T 1J4, Canada

[2]Centre Énergie Matériaux Télécommunications, Varennes, QC J3X 1S2, Canada

Abstract **—** In this work, a unified method is introduced and formulated for deriving the equivalent circuit model of a guided wave structure as well as its characteristic impedance for any mode. This method is developed through the combination of a generalized multimode calibration and a full-wave simulation, and it is applicable to the fundamental mode as well as higher-order modes. The method is verified for both TEM and non-TEM propagating modes and is applied to extract the characteristic impedance and circuit model of non-TEM guided wave structures. This scheme allows for the effective use of a commercial electromagnetic field simulator in removing inherent numerical simulation noises or errors. Extracting circuit parameters through this technique for establishing equivalent circuit models can overcome the shortcomings encountered in the modeling of guided-wave eigenvalue problems as well as in the design of multimode structures.

Index Terms — Equivalent circuit, TEM mode, non-TEM mode, higher-order mode, numerical modeling, generalized calibration, numerical de-embedding, and characteristic impedance.

6.1 Introduction

6.1.1 Circuit modeling

Microwave and millimeter-wave circuits and embedded or connecting transmission line elements are dimensioned in the range of operating wavelength or its fraction. The analysis and modeling of such structures should be carried out by solving Maxwell's equations in which electric and magnetic fields are formulated as primary unknown quantities. Nevertheless, classical circuit

models, which are composed of lumped elements with well-conditioned input and output voltage/current quantities, are still preferred in the high-frequency circuit design community, since the use of a circuit model can facilitate multi-parameter design procedures and simultaneous optimization tasks, leading to an intuitive and well-established electronic network synthesis. Therefore, a meaningful mapping between field and circuit parameters is of critical importance for high-frequency circuit design and development.

High-frequency effects such as parasitic interactions, packaging effects, and modal dispersions complicate the analysis of such circuits and systems. Due to the distributed nature of fields, modeling complexity in terms of lumped-element extraction and network description accuracy is much more involved. This problem becomes especially pronounced in the design of very-large-scale integrated circuits and antenna feed layouts in which the above-mentioned high-frequency effects as well as hybrid propagating modes, both TEM and non-TEM modes, are involved. In these complex circuits, higher-order modes may appear near discontinuities such as bends, thus accommodating these modes in the circuit representation is also necessary. Moreover, as frequency rises, energy dissipation, because of both dielectric and conductor loss, increases and the consideration of those losses in the equivalent circuit models, is more compelling.

Thus far, no universal method can derive a lumped-element circuit model for a given electromagnetic (EM) structure involving such an intricate mode behavior, though a few ad hoc methods exist. Classical equivalent lumped elements and transmission line network models of microwave circuits generally do not account for those effects. Providing an efficient and accurate design and optimization approach for generating a realistic equivalent circuit model based on an accurate EM full-wave simulation that accounts for all those effects, has always been required [1]. Such a modeling strategy would allow for a complete and quantitative description of the EM fields and physical behavior of the structure.

6.1.2 **Numerical calibration**

A variety of commercial and non-commercial three-dimensional (3D) full-wave EM simulation packages of high-frequency components has been developed with different computational electromagnetic (CEM) techniques. Those simulations provide a quick insight into the EM behavior of a wide range of high-frequency structures. However, they do not yield a highly accurate circuit model of structure-under-simulation (SUS). It has been known that the use of CEM tools

Table 6.1: Comparison among numerical de-embedding techniques

	Reference impedance	Supporting propagating mode	Higher order modes	Commercial software
Double-Delay	port	TEM/ quasi-TEM	no	Sonnet
Short-Open Calibration (SOC)	no need	any	no	Sonnet/AWR
This Method	no need	any	yes	HFSS/CST

generally involves the insertion of ports that act as compressed or artificial electromagnetic sources, and this creates unwanted field discontinuities that are absorbed in simulation results. Therefore, inspired by well-established measurement practices, in which the effects of transitions or connectors between vector network analyzer (VNA) and device-under-test (DUT) are de-embedded by a calibration procedure to obtain the structure's clean modeling results with appropriate reference plane locations, calculated results obtained from simulations should be numerically de-embedded. The goal is to remove the port effects, including numerical noises and higher-order modes, and to obtain the authentic circuit model [2]. The key issue is to formulate an easy-to-use and exact relationship between the SUS characteristic lumped quantities and distributed quantities.

Different EM de-embedding techniques for numerical calibrations have been developed. The double-delay de-embedding [3] and the short-open calibration (SOC) [4] are the two well-known and most common numerical calibration techniques. The double-delay de-embedding is limited to

the TEM/quasi-TEM mode structures. The SOC technique has the advantage of dealing with the other propagating modes, but it cannot be directly applied through commercial software packages. In addition, those techniques cannot include the higher-order mode effects. The TRL calibration technique is another type of numerical de-embedding that was developed to address some of the shortcomings of the SOC method [4], [5]. Nevertheless, implementing TRL or a similar calibration technique, necessitates a prior knowledge of characteristic impedance of the connecting or reference lines. Those factors have limited the applications of those de-embedding procedures.

6.1.3 **Contribution of this work**

To resolve the above-mentioned issues and to extend the de-embedding techniques to a more generalized simulation scenario, this work proposes and presents a unified method, which makes use of the available field simulation software packages to generate a realistic equivalent circuit model of a two-port network involving any guided modes along both TEM and non-TEM transmission structures. The proposed joint field-circuit model is able to include high-frequency parasitic and distributed effects as well as loss, dispersion, and higher-order modes. Thus, it yields accurate results with a minimum computational expenditure, which presents a major benefit when optimization has to be deployed. A summary on the comparison of the present method with the mentioned numerical techniques is presented in Table 6.1.

In this paper, a generalized S-parameter de-embedding algorithm for a two-port network is introduced. This algorithm deploys a theoretical procedure that is developed through signal-flow graph calculations [5]. In this algorithm, an analytical formulation for calculating the parameters of a two-port network model based on two standard simulations is derived. The method is applicable to a general two-port network as well as transmission lines and guided-wave structures. Compared to previously disseminated schemes, the technique described in this paper is not regulated to a special class of port discontinuity [3]. Also, this unified method is not limited to the fundamental mode and it accounts for any higher-order modes as well as non-TEM modes. Another advantage is that, compared to the well-established SOC technique [4], [7], this method is compatible with any full-wave simulator. Depending on the capability of software packages, different sources of loss including metallic, dielectric, radiation, and leakage may be considered in numerical simulations and parameter extractions.

The definition of characteristic impedance has been a long- and hotly-debated issue since the 1970s [8]–[10], when the difference among the basic PI, PV, and VI definitions was observed. These definitions can be viewed as a weighted average of the actual wave impedance. However, the impedance of a wave propagating in a guided-wave structure is a function of location in the cross section of that guided-wave structure, as the proportion of transverse E over transverse H varies throughout the cross section of the waveguide. This debate had been followed by many authors [11], [12] until the 3D impedance definition was proposed and demonstrated [7], [13]. The present method, with its specified advantages, is then used to calculate the 3D impedance of a wider range of EM waveguides and transmission lines. In the section of results presentation, the method is used for both the TEM-mode transmission line and non-TEM mode waveguides and validated with the available results from the literature. The proposed method is also applied to the calculation of the characteristic impedance and circuit model of the substrate integrated waveguide (SIW) for the first time. The effect of loss is also examined and higher-order modes are considered in the calculations. Finally, closed-form equations are derived, representing the 3D characteristic impedance and lumped element model of SIW.

6.2 Description of method

Figure 6.1 is a black-box schematic representation of a typical CEM simulation for any circuit element. Error boxes 1 and 2 are a pair of generalized linear networks standing for numerical errors and/or noises occurring at reference ports in the S-parameter calculation of an SUS.

In this paper, ANSYS HFSS software [14] is used. Lumped ports and wave ports are the two common methods of excitation in this software and other similar commercial simulator. Table 6.2

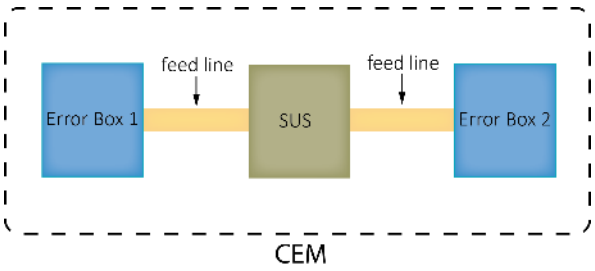

Figure 6.1: A schematic of computational electromagnetic (CEM) simulation involved with numerical calibration techniques.

shows a brief comparison of these two types of ports and more explanations are provided in the appendix A. Wave ports account for higher-order modes; also, when performing a simulation, the reference planes may be relocated and the results are recalculated considering a simple phase shift. Wave ports do not lead to port discontinuity errors, as in the case of lumped ports; however, when

Table 6.2: Comparison between wave ports and lumped ports

	Yields S parameters	Yields Gamma	Reference plane de-embedding	Number of modes	Port discontinuity error
Wave ports	yes	yes	possible	any	no
Lumped / Impressed ports	yes	no	not possible	single mode	yes

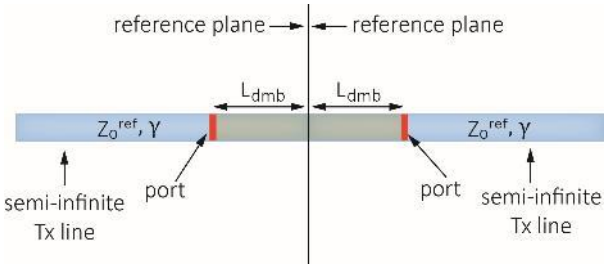

Figure 6.2:. A transmission schematic representing a THRU simulation in a generalized calibration procedure.

applying a wave port excitation, the impressed fields are calculated from a 2D semi-infinite waveguide affected by waveguide walls, and can lead to error due to an incorrect impressed field.

In this work, wave ports are applied in the simulations. The purpose of de-embedding is first to characterize the error boxes and then to remove the influence of these error networks in order to evaluate accurately the S-parameters of the SUS. The highlight is to devise a unique approach that can be used for any structure as any electromagnetic components can be incorporated into a global circuit design platform.

The method is developed based on a generalized TRL algorithm and a signal flow graph calculation [15], [39]. The algorithm applies an incident wave to the SUS through the wave ports, and extracts the vector voltages scattered forward and backward. Three standards are required to characterize the error boxes fully. With the wave port excitation, there are bonus points for obtaining the propagation constant γ of the port and the possibility of phase de-embedding of the reference plane (Appendix A). As such, two simple THRU simulations are enough to characterize the ports completely, and, therefore, it may be called generalized TT calibration method.

Figure 6.2 shows a diagram for realizing the THRU simulation. SUS is connected to the wave ports by a section of several propagating wavelengths of the operating mode in a traveling-wave structure. The THRU simulation consists of feeding traveling-wave sections (Tx) where the reference planes are moved to the middle of that line (see Appendix A for more detail). While performing the whole SUS simulations, two THRU simulations with two Tx lengths are also carried out in order to calibrate the two-port network. These two simulations act as two standards for the general calibration and the results of these two simulations allow for the extraction of port (error boxes) S-parameters. Then from the "port-SUS-port" simulation results and error boxes' characteristics, authentic S-parameters of SUS are derived as a function of the ports' S-parameter and the whole structure simulation S-parameters.

6.3 Derivation of equations

The purpose of this section is to find analytical expressions which relate the S-parameters of an SUS, S_{ij} and error box, S_{ijE}, to the whole simulation results, S_{ijm}. Figure 6.3 describes the network flow graph of a typical and all-inclusive simulations involving SUS, shifted or de-embedded reference planes, and wave ports. According to the wave port characteristics (Appendix A), the de-embedded sections are non-reflecting transmission lines with the following known S-parameter matrix:

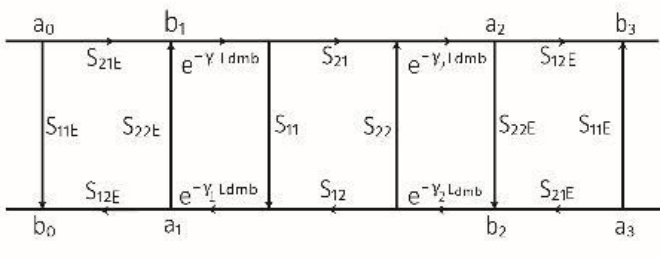

(a)

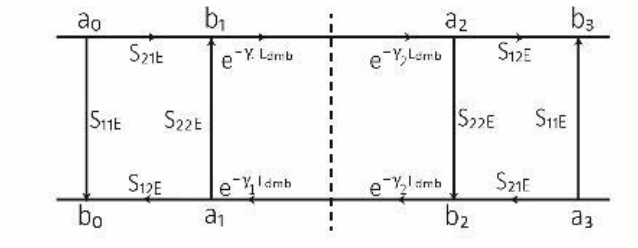

(b)

Figure 6.3:. a) Network flow graph of a generalized TT calibration. b) Network flow graph of a THRU simulation in the proposed TT calibration.

$$S_{L_{dmbd}} = \begin{pmatrix} 0 & e^{-\gamma L_{dmb}} \\ e^{-\gamma L_{dmb}} & 0 \end{pmatrix} \tag{1}$$

in which γ is derived from the 2D calculation of wave port cross section and Ldmb is the distance where reference plane is moved from or de-embedded.

In order to develop the analytical expressions that relate the simulated S-parameters to the S-parameters of SUS, the procedure of [17] is followed. From the network flow graph in Figure 6.3(a):

$$b_0 = S_{11E}a_0 + S_{12E}a_1 \tag{2}$$

$$b_1 = S_{21E}a_0 + S_{22E}a_1 \tag{3}$$

$$a_1 = (e^{-2\gamma L_{dmb}})S_{11}b_1 + (e^{-2\gamma L_{dmb}})S_{12}b_2 \tag{4}$$

$$a_2 = (e^{-2\gamma L_{dmb}})S_{21}b_1 + (e^{-2\gamma L_{dmb}})S_{22}b_2 \tag{5}$$

$$b_2 = S_{22E}a_2 + S_{21E}a_3 \quad (6)$$

$$b_3 = S_{12E}a_2 + S_{11E}a_3 \quad (7)$$

By definition, the modeled S-parameter at the defined ports is expressed by

$$S_{21m} = \frac{b_3}{a_0}|_{a_3=0} \quad (8)$$

$$S_{11m} = \frac{b_0}{a_0}|_{a_3=0} \quad (9)$$

From (6) and (7), for S_{11m} and S_{21m} (a_3=0):

$$b_2 = S_{22E}a_2 \quad (10)$$

$$b_3 = S_{12E}a_2 \quad (11)$$

From (10) and (11), one has

$$b_2 = \frac{S_{22E}}{S_{12E}}b_3 \quad (12)$$

From (2), (3), (4), and (12),

$$b_0(1 - (e^{-2\gamma L_{dmb}})S_{11}S_{22E}) =$$

$$(e^{-2\gamma L_{dmb}})S_{11}S_{21E}a_0S_{12E} + (e^{-2\gamma L_{dmb}})S_{12}S_{22E}b_3 + S_{11E}a_0[1 - (e^{-2\gamma L_{dmb}})S_{11}S_{22E}] \quad (13)$$

With the dividing of (13) by a_0 and use of (8) and (9) mathematical simplifications, the first key equation is derived as follows,

$$(S_{11m} - S_{11E})S_{21E}S_{12E}(e^{-2\gamma L_{dmb}}) = \left(S_{12E}S_{21E}(e^{-2\gamma L_{dmb}}) + S_{22E}S_{11m}(e^{-2\gamma L_{dmb}}) - S_{11E}S_{22E}(e^{-2\gamma L_{dmb}})\right)S_{21E}S_{12E}S_{11}(e^{-2\gamma L_{dmb}}) + S_{12E}S_{21E}S_{22E}S_{21m}S_{12}(e^{-4\gamma L_{dmb}}) \quad (14)$$

From (2) and (3),

$$S_{22E}b_0 = S_{22E}S_{11E}a_0 + S_{22E}S_{12E}a_1 \quad (15)$$

$$S_{12E}b_1 = S_{12E}S_{21E}a_0 + S_{12E}S_{22E}a_1 \quad (16)$$

Therefore,

$$b_1 = \frac{S_{22E}}{S_{12E}}b_0 + (S_{21E} - \frac{S_{11E}S_{22E}}{S_{12E}})a_0 \quad (17)$$

From (5), (10), (11), and dividing (17) by a_0, using (9) and (8), some simplifications can again be made, and the second key equation is derived:

$$S_{21m}S_{12E}S_{21E}(e^{-2\gamma L_{dmb}}) = (S_{12E}S_{21E}(e^{-2\gamma L_{dmb}}) + S_{22E}S_{11m}(e^{-2\gamma L_{dmb}}) - S_{11E}S_{22E}(e^{-2\gamma L_{dmb}}))S_{21E}S_{12E}S_{21}(e^{-2\gamma L_{dmb}}) + S_{21E}S_{12E}S_{22E}S_{12m}S_{11}(e^{-4\gamma L_{dmb}}) \quad (18)$$

At this point, (14) and (18) are used to extract the S- parameters for the error boxes. For this purpose, two THRU simulations, as explained in the above method section, are performed with two different lengths ($L_{\ dmb1}$ and $L_{\ dmb2}$). Figure 6.3(b) shows the network flow graph of a THRU simulation. In this case, equations (14) and (18) are simplified with $S_{11} = S_{22} = 0$ and $S_{12} = S_{21} = 1$, and the analytical expressions for the error box–related S-parameters are derived as functions of the two simulated THRU S-parameters (TT) and S-parameters of the de-embedded part as

expressed in (1). The L_{dmb1} and L_{dmb2} lengths are selected to be as short as possible considering the minimum frequency range (more than the maximum wavelength). Their length difference must be such that their electrical phase shift does not become close to 0° or 180° at the frequency of interest to avoid ill-conditioned solutions. The S-parameters of the error box S_{ijE} may be derived as clear-cut functions of THRU S-parameters S_{ijt1}, S_{ijt2} considering the reciprocity ($S_{12t}=S_{21t}$ and $S_{12E}=S_{21E}$):

$$S_{11E} = ((e^{-2\gamma L_{dmb1}})S_{11t2}S_{12t1} - (e^{-2\gamma L_{dmb2}})S_{11t1}S_{12t2})/((e^{-2\gamma L_{dmb1}})S_{12t1} - (e^{-2\gamma L_{dmb2}})S_{12t2}) \quad (19)$$

$$S_{12E} = -(\sqrt{}((e^{-2\gamma L_{dmb2}})^2 S_{12t1}S_{12t2}^2 + (e^{-2\gamma L_{dmb1}})^2 S_{12t1}(S_{12t1}^2 + (S_{11t1} - S_{11t2})(S_{11t2} - S_{22t1})) - (e^{-2\gamma L_{dmb1}})(e^{-2\gamma L_{dmb2}})S_{12t2}(S_{11t1}^2 + 2S_{12t1}^2 + S_{11t2}S_{22t1} - S_{11t1}(S_{11t2} + S_{22t1}))))/(\sqrt{}((e^{-2\gamma L_{dmb1}})((e^{-2\gamma L_{dmb1}})S_{12t1} - (e^{-2\gamma L_{dmb2}})S_{12t2})^2)) \quad (20)$$

$$S_{22E} = (S_{11t1} - S_{11t2})/((e^{-2\gamma L_{dmb1}})S_{12t1} - (e^{-2\gamma L_{dmb2}})S_{12t2}) \quad (21)$$

Once the error-box is characterized with (19), (20), and (21), the authentic S-parameters of the SUS, S_{ij}, are derived through solving in Mathematica as explicit functions of simulated results of the whole simulation including SUS, S_{ijm}, and error-box S_{ijE}:

$$S_{11} = S_{11E}^2 S_{22E} - S_{12m}S_{21m}S_{22E} + S_{11m}(S_{12E}^2 + S_{22E}S_{22m}) - S_{11E}(S_{12E}{}^2 + S_{22E}(S_{11m} + S_{22m})))/\ (e^{-2\gamma L_{dmb1}}(S_{12E}^4 + S_{12E}^2 S_{22E}(-2S_{11E} + S_{11m} + S_{22m}) + S_{22E}^2(S_{11E}^2 - S_{12m}S_{21m} + S_{11m}S_{22m} - S_{11E}(S_{11m} + S_{22m})))) \quad (22)$$

$$S_{12} = (S_{12E}^2 S_{12m})/(e^{-2\gamma L_{dmb1}}\left(S_{12E}^4 + S_{12E}^2 S_{22E}(-2S_{11E} + S_{11m} + S_{22m}) + S_{22E}^2\left(S_{11E}^2 - S_{12m}S_{21m} + S_{11m}S_{22m} - S_{11E}(S_{11m} + S_{22m})\right)\right))$$

(23)

$$S_{22} = \frac{1}{e^{-2\gamma L_{dmb1}} S_{22E}}(1 + S_{12E}^2(S_{12m} - S_{21m})/S_{21m}(S_{12E}^2 + S_{22E}(-S_{11E} + S_{22m})) - (S_{12E}^2 S_{12m}(S_{12E}^2 + (-S_{11E} + S_{11m})S_{22E}))/(S_{21m}(S_{12E}^4 + S_{12E}^2 S_{22E}(-2S_{11E} + S_{11m} + S_{22m}) + S_{22E}^2(S_{11E}^2 - S_{12m}S_{21m} + S_{11m}S_{22m} - S_{11E}(S_{11m} + S_{22m})))))$$

(24)

Therefore, the S-parameters of SUS, SSUS, are calculated or extracted with the simple analytical equations of (22), (23), and (24).

Procedure for the Equivalent-Circuit Extraction

The proposed approach may be summarized in the following subsequent steps:

Step 1: A full-wave analysis of the whole structure of interest is conducted and the simulated results are recorded (S_{ijm}).

Step 2: Another full-wave analysis is performed for two THRU length (L_{dmb1}, L_{dmb2}), including the reference plane de-embedding, and the simulated results are recorded (γ, S_{ijt1},S_{ijt2}).

Step 3: The S-parameters of the error box are derived from (19), (20), and (21).

Step 4: S-parameters of the SUS are then derived from (22), (23), and (24) and the equivalent two-port network is calculated with (25) and (26), which will be discussed in the following.

Figure 6.4 shows the equivalent Z and Y two-port networks. The relationship between scattering matrix [S] and impedance matrix [Z] for the SUS is given by [18] from which:

$$[Z] = ([S] + [I])([I] - [S])^{-1} \quad (25)$$

And, by definition, the admittance matrix [Y] is given by

$$[Y] = [Z]^{-1} \quad (26)$$

The above equations may include any source of loss such as dielectric, conductor, or radiation whenever possible. Furthermore, such simulations can be done for higher-order modes. In this case, the number of desired modes is selected for each wave port and the corresponding calculated S-parameters are used to extract the network model. For such kind of characterization, propagation

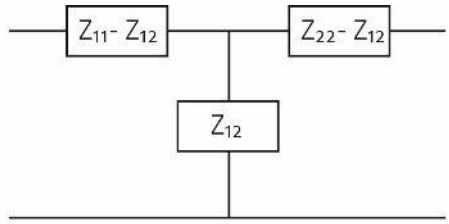

(a)

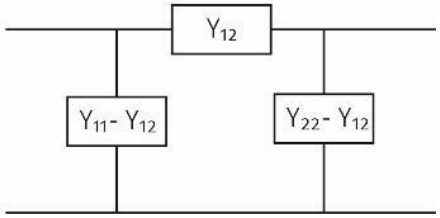

(b)

Figure 6.4: Two-port network equivalence: a) Z-Network and b) Y-Network.

constant and characteristic impedance of each mode is derived separately; to include the coupled mode, a one by one simulation is made for each two modes and therefore corresponding 2x2 matrix is applied. In the case of waveguide, the modes are usually decoupled and the coupling from one to another is very negligible. However, it can be calculated and characterized. Therefore, the calculations and final equations can be customized as desired to include the effect of loss as well as higher-order modes.

6.4 Characteristic impedance calculation from de-embedded s-parameters

The ABCD transmission matrix of SUS (ABCDSUS) is used to obtain the 3D characteristic impedance Z0 and propagation constant γ of the related transmission line:

$$\begin{pmatrix} A & C \\ B & D \end{pmatrix} = \begin{pmatrix} \cosh(\gamma \mathrm{l}) & Z_0 \sinh(\gamma l) \\ \dfrac{\sinh(\gamma l)}{Z_0} & \cosh(\gamma \mathrm{l}) \end{pmatrix} \tag{27}$$

$$Z_0 = \sqrt{\frac{B}{C}} \tag{28}$$

$$\gamma = \frac{\cosh^{-1}(A)}{l} \tag{29}$$

In this method, $ABCD_{SUS}$ is obtained directly from the calculated SSUS. In the previously reported methods for 3D characteristic impedance calculation [7], [13], once the error box is characterized, the total transmission matrix, $ABCD_M$, is pre- and post-multiplied by the inverse of error box transmission matrix, $ABCD_{E1}$, and $ABCD_{SUS}$ is calculated. Therefore, in the present method, the errors caused by the inverted matrix calculation are avoided [21].

When loss is included in the simulations, the same procedure as the non-dissipative transmission is performed, and the "complex" values of Z_0 and γ are derived to characterize the mode propagation behavior. In this case, the calculated Z_0 is related to the global physical effects in which different sources of loss are inevitable. Once characteristic impedance Z_0 and propagation constant γ are calculated, the distributed element model can be obtained [19].

The characteristic impedance definition is extended to explain the behavior of higher-order modes [23]. Subject to the application, the simulations and the calculations may be performed for the fundamental mode as well as higher-order modes. Accordingly, to characterize a guided-wave structure, each of the higher-order modes may be expressed in term of a transmission line [23]; below the cut-off frequency, the associated characteristic impedance may be imaginary, illustrating the reactive nature, and the propagation constant $\gamma=\alpha+i\beta$ may be real, illustrating the attenuating nature. Therefore, the electromagnetic fields in a multimode waveguide or transmission line are explained completely in terms of voltage and current along the symbolized transmission lines. Consequent to including both loss and higher-order modes, the physical guided-wave behavior is described quantitatively by the characteristic impedance and propagation constant of the individual modes.

6.5 Results

In this section, the presented generalized TT calibration technique is used for both TEM transmission lines, and non-TEM waveguides. The effect of loss is also examined and an example of higher-order mode is illustrated.

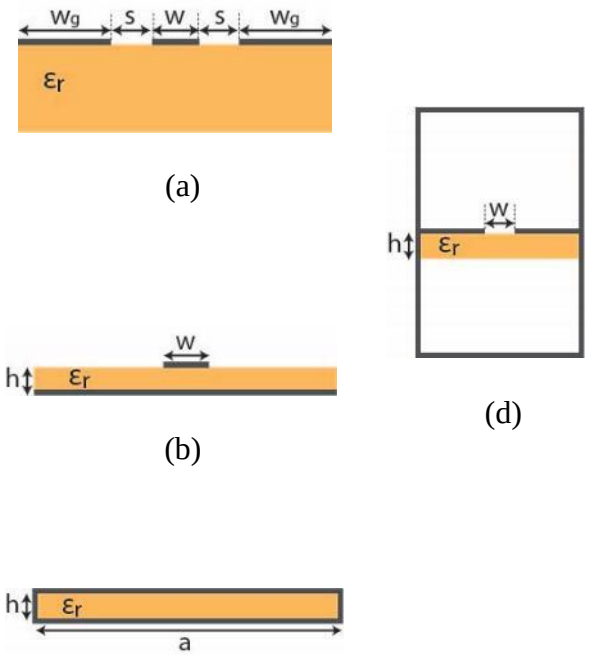

Figure 6.5: TEM/quasi-TEM mode transmission lines: a) CPW, b) Microstrip line; non-TEM mode transmission line, c) SIW, and d) fin-line.

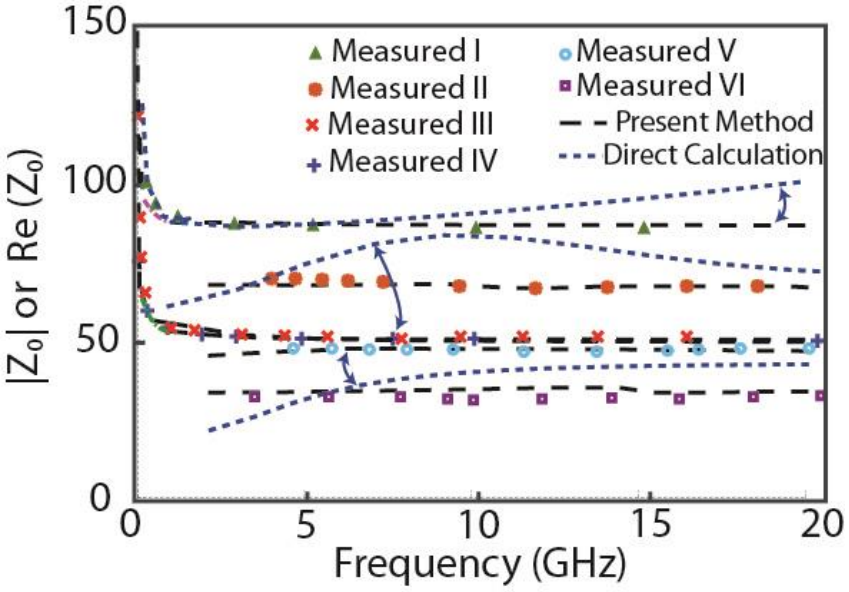

(a)

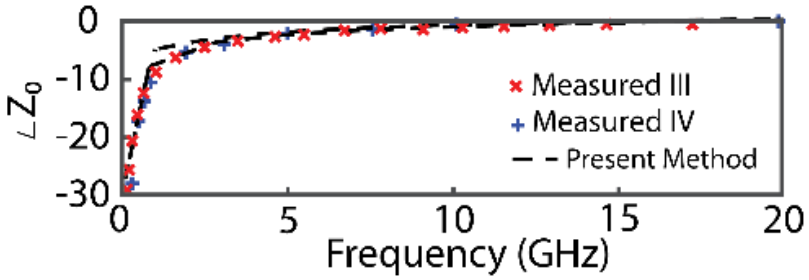

(b)

Figure 6.6: Comparison of the calculated TEM transmission line characteristic impedance using the proposed TT numerical calibration technique, direct calculation from HFSS S-parameter, with experimental results from the literature: a) Amplitude or real part of Z0; b) phase of Z0 - I: CPW transmission line w=73 μm, s= 49 μm, wg= 250 μm on a fused silica substrate [23], II: Microstrip transmission line of 1.3 mil copper, w=0.1-in on an h=0.25-in alumina substrate [13], III: CPW transmission line of 0.5683 μm gold, w=71 μm, s= 49 μm, wg= 250 μm wide ground planes on an h=500 μm gallium-arsenide substrate [24], IV: CPW transmission line of 0.7 μm gold, w=73 μm, s= 49 μm, wg= 350 μm wide ground planes on a 500 μm gallium-arsenide substrate [25], V, VI: Microstrip transmission line of 1.3 mil copper, w=0.25-in, 0.5-in on an h=0.25-in alumina substrate [13].

6.5.1 **Method validation**

Figure 6.5 shows the cross-section view of some common guided-wave EM structures. For TEM/quasi-TEM transmission lines such as coplanar waveguide (CPW) (Figure 6.5(a) and microstrip line (Figure 6.5(b)), the measured characteristic impedances [11], [24], [24], [26] are compared with the calculated characteristic impedance, and the results are displayed in Figure 6.6.

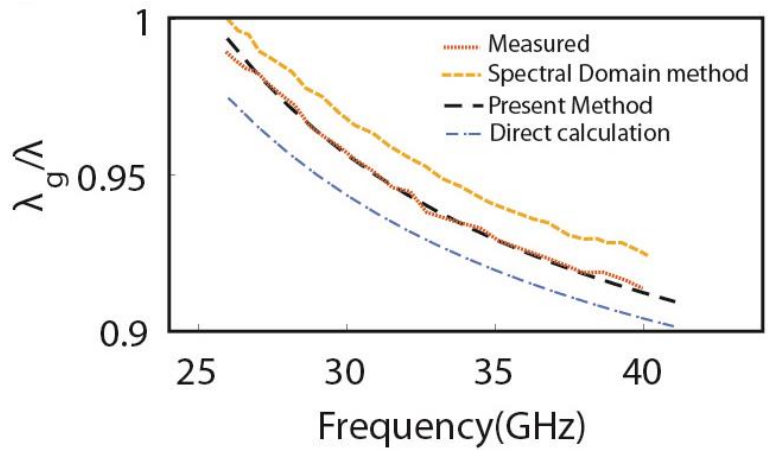

(a)

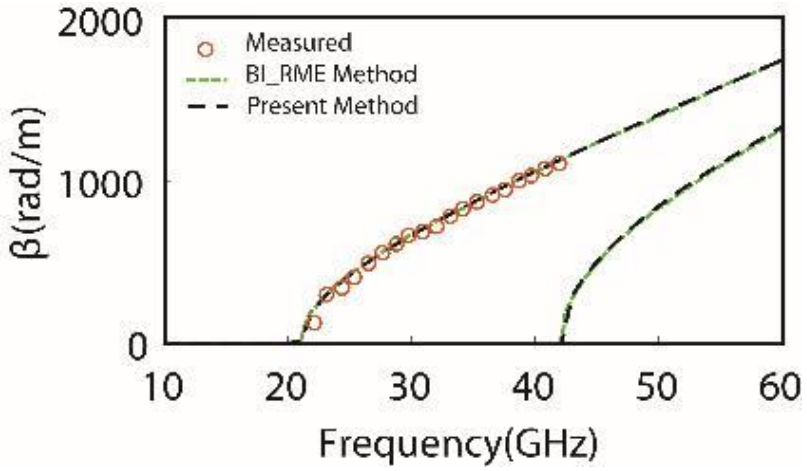

(b)

Figure 6.7: Comparison of the calculated non-TEM transmission line propagation characteristics using the proposed TT numerical calibration technique with direct calculation from HFSS S-parameter, and experimental and numerical results from the literature a) fin-line w=18mil, h=10mil in WR28, b) SIW a=4.8 mm on a h=1.5mm 2.2 permittivity substrate.

Also, the same calculation has been done for the S-parameters directly from HFSS before removing the effect of error boxes and displayed in the same figure. At lower frequency, the amplitude of complex Z_0 of the examined CPW lines increases due to internal inductance caused by the magnetic field penetration into the metal [24]. This shift is drastic in both magnitude and phase, and the agreement between the proposed method and measurements is excellent. To verify the method for non-TEM mode structures, SIW (Figure 6.5(c)) and fin-line (Figure 6.5(d)) are considered. As presented in Figure 6.7, the measured normalized propagation wavelength $\lambda g/\lambda$ of a fin- line is compared with the spectral domain solution [26] and the present method. The proposed method fits better compared to the spectral domain method results and direct calculation from HFSS; the second mode effect is not considered in this example, which explains a small dissimilarity observed around 39 GHz. In addition, the phase constant β of an SIW is compared between results obtained by the boundary integral-resonant mode expansion (BI-RME) method proposed in [28] and the present method. The results of measurements and calculations agree very well. The phase constant β of the second mode using the proposed TT numerical calibration technique agree with the BI-RME method result. It must be noted that since the above comparisons and validations have been made with the measurements, the propagation loss is included in all the mentioned computations.

6.5.2 **Application example: SIW**

Lumped element-based equivalent circuit parameters may be calculated analytically for pure TEM mode structures in connection with a specific circuit model, or they can be extracted directly from

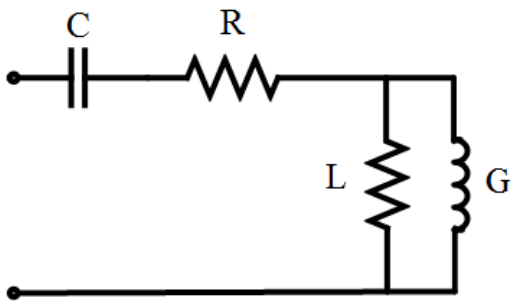

Figure 6.8: The distributed equivalent-circuit model (all elements are defined per length).

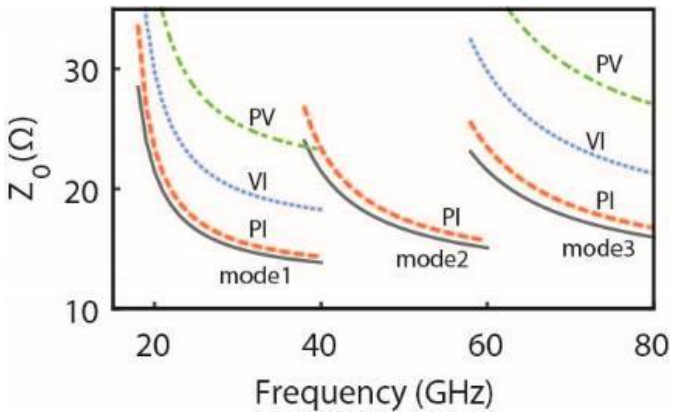

Figure 6.9: Calculated SIW characteristic of the first three modes (substrate ε_r=2.33 and 0.254 mm thickness, width=0.711 mm) using the proposed TT method: a) characteristic impedance, b) effective dielectric constant.

a full-wave simulation. However, for non-TEM mode structures, the longitudinal field elements must be considered in calculations resulting in the same scenario as what was specified for the characteristic impedance. Therefore, by analogy to the 3D characteristic impedance, 3D lumped elements must be calculated for non-TEM mode transmission lines and waveguides. In this part, the proposed method is utilized to extract the propagation characteristic and RLCG circuit model of an SIW. The circuit model of a conventional transmission line is extracted using telegraph equations [19] based on a low-pass configuration. To extract the SIW circuit model, the telegraph equations need to be generalized to comply with high-pass characteristics of such non-TEM structures as rectangular waveguides or SIWs.

Figure 6.8 represents an SIW equivalent circuit model. To extract the SIW circuit parameters, the telegraph equations are adjusted as follows to account for the high-pass characteristics:

$$\gamma / Z_0 = \left(j\omega C + G \right) / \left(1 - \left(f_c / f \right)^2 \right) \tag{30}$$

$$\gamma Z_0 = j\omega L + R \tag{31}$$

Once the values of R, L, C, and G are determined from (28) and (29), a low-pass to high-pass transformation [39] is utilized to calculate the L and C values for the high pass SIW equivalent circuit (Table 6.3). Therefore, considering the high-pass telegraph equations, characteristic impedance is derived from:

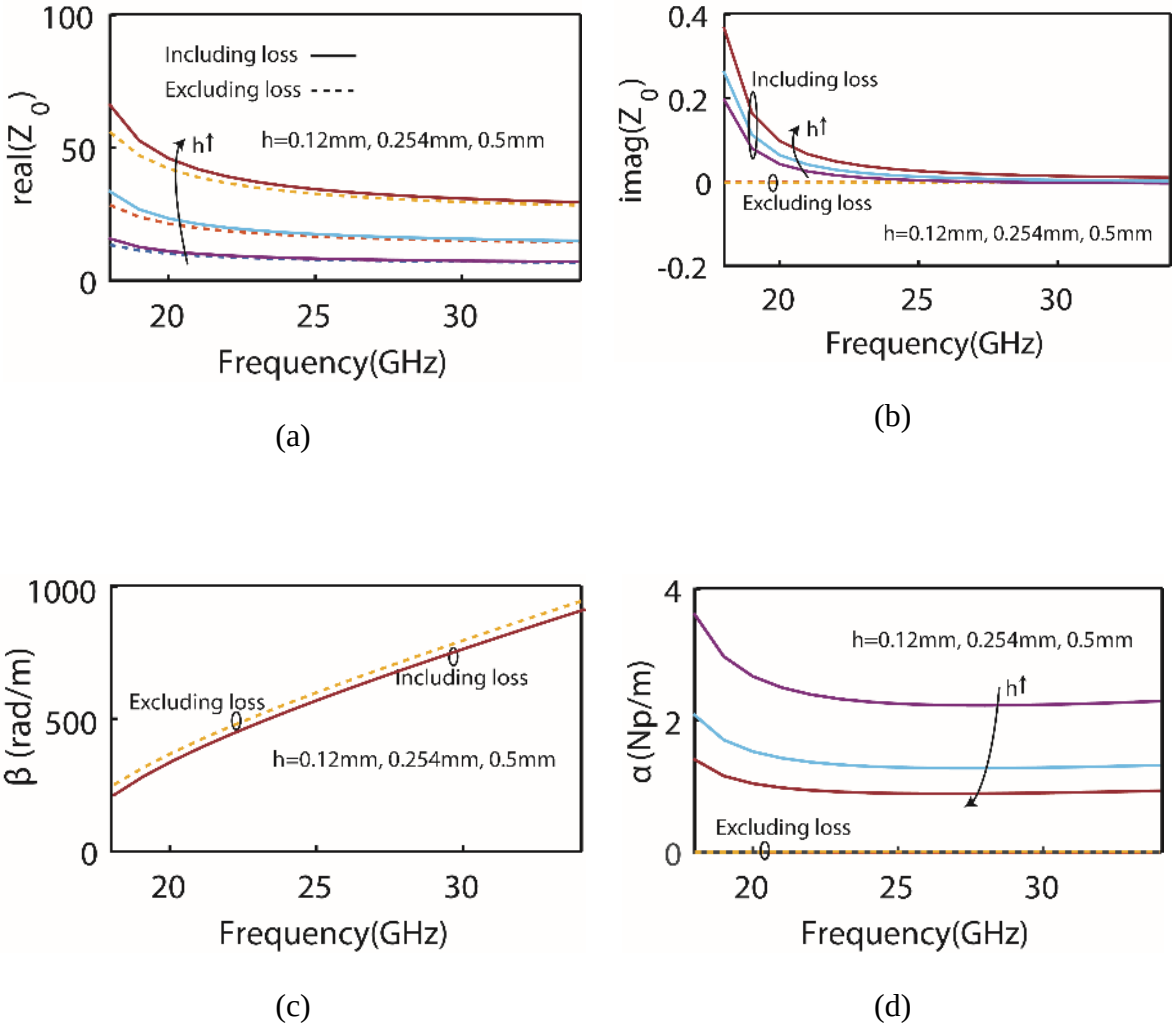

Figure 6.10: Calculated characteristic impedance for SIW of Fig. 5(c) (substrate ε_r=2.33, a = 6.096 mm) for different substrate thicknesses using the proposed TT method including and excluding loss in the calculations a) real part of characteristic impedance b) imaginary part of characteristic impedance, c) The phase constant, d) attenuation constant

$$Z_0 = \sqrt{\frac{L}{C(1-(f_c/f)^2)}} \tag{32}$$

In the same way, taking into account the transformations of Table 6.3, SIW propagation phase constant is calculated from:

$$\beta = \frac{\omega}{\omega_c}\sqrt{\frac{(1-(f_c/f)^2)}{LC}} \tag{33}$$

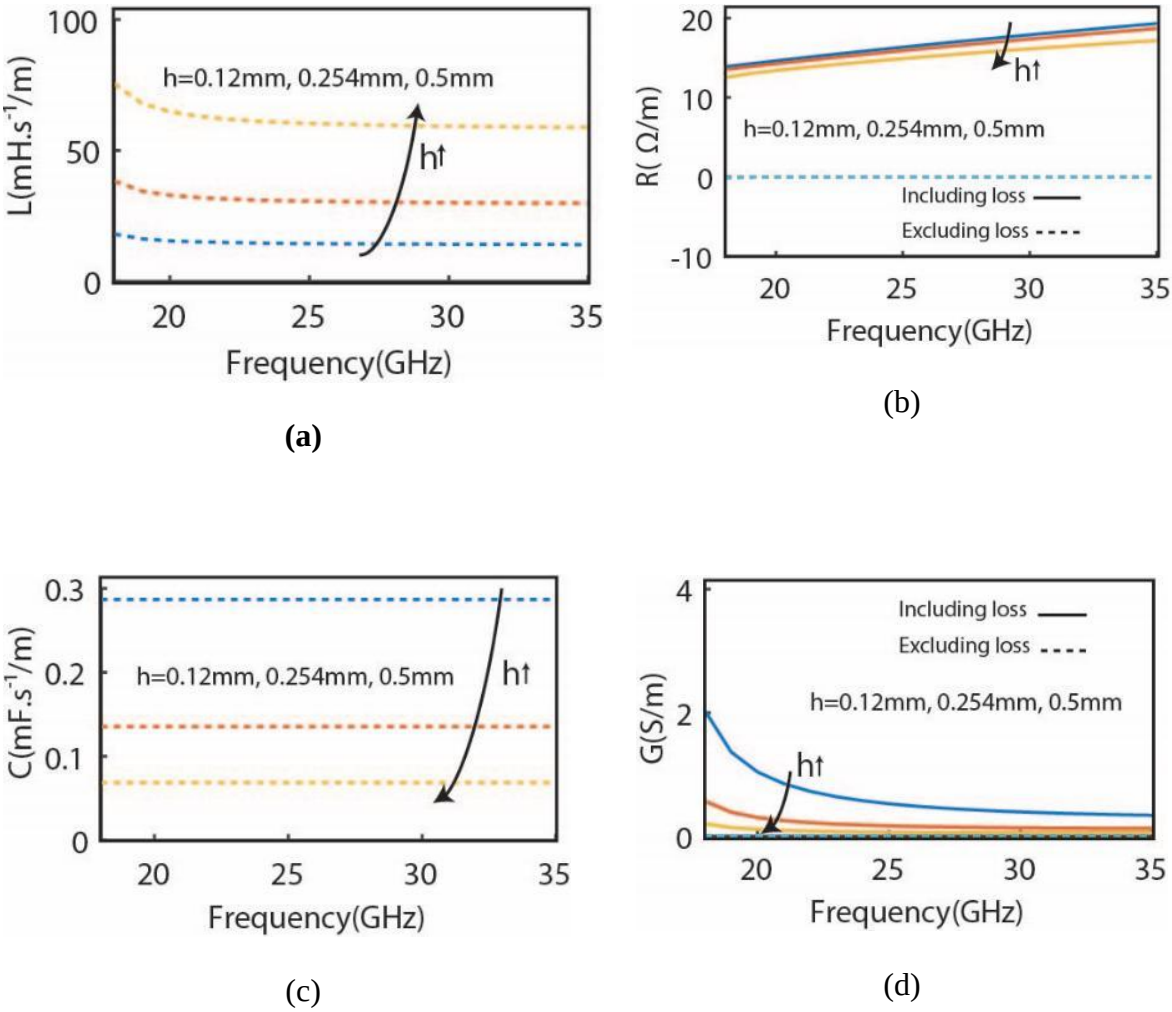

Figure 6.11: Calculated SIW interconnect parameter (substrate ε_r=2.33, width = 6.096 mm) for different substrate thicknesses using the proposed TT method including and excluding loss in the calculations a) L (mH.s^{-1}/m) b) R (Ω) b) C (mF.s^{-1}/m) d) G (S)

First, the characteristic impedance of the dominant mode and two higher-order modes is derived and a comparison is made with the result of the full-wave simulation. The results are shown in Figure 6.9 along with the calculated 2D characteristic impedance through the three definitions of PI, PV, and VI. For all the modes, the PI calculations provide the closest results to the 3D-defined impedance. Close to the cutoff frequency, the impedance value tends to infinity, which indicates the absence of a wave propagation (electromagnetic current I=0). For the second mode, a

Table 6.3: Circuit parameters for SIW circuit model

Parameter	SIW	TEM	TE
L	$\frac{2h\mu_r\eta}{\pi\sqrt{2\varepsilon_r}}[\mathrm{H}.s^{-1}]$	$\frac{h\mu_r\mu_0}{a}$	/
C	$\frac{a^2\sqrt{\varepsilon_r}}{\pi h\eta\sqrt{2}}[F.s^{-1}]$	$\frac{a\varepsilon_r\varepsilon_r}{h}$	/
Z_0/ wave Impedance	$\frac{\sqrt{2}h\eta}{a\sqrt{\varepsilon_r}}\frac{1}{\sqrt{(1-(f_c/f)^2)}}$	$\frac{h\eta}{\mathrm{a}}$	$\frac{\eta}{\sqrt{\varepsilon_r}}\frac{1}{\sqrt{(1-(f_c/f)^2)}}$
β	$\frac{\omega\sqrt{\varepsilon_r}}{c}\sqrt{(1-(f_c/f)^2)}$	$\frac{\omega\sqrt{\varepsilon_r}}{c}$	$\frac{\omega\sqrt{\varepsilon_r}}{c}\sqrt{(1-(f_c/f)^2)}$

symmetric integral line cannot be defined to calculate the voltage and, therefore, VI and PV definitions are not available for this mode (see Appendix B). The characterization of the higher-order modes in terms of their characteristic impedance and propagation constant allows for the quantitative description of a multimode propagation.

Figure 6.10 shows the calculated 3D characteristic impedance Z0 and complex propagation constant γ of the examined SIW. Subsequent to the above calculations, RLCG values are derived and presented in Figure 6.11. The results are presented for different substrate thickness h and also the effect of potential loss (dielectric and conductor loss) is considered in this case. As seen from the figures, when the calculations exclude loss effects, the imaginary part of the characteristic impedance and attenuation constant α are equal to zero. Similarly, in the circuit model representation, resistance R and conductance G are equal to zero, thereby implying a non-dissipative signal transmission. The increase of propagation loss is symbolized by the rising of resistance R (conductor loss). For thicker substrates, the real part of characteristic impedance increases (Figure 6.10(a)); therefore, for a given input power, the electric current, hence the propagation loss, are reduced. The dielectric loss characterized by G decreases when using a thicker

substrate (Figure 6.10(d)). The variation of losses with frequency and thickness are in agreement with general SIW losses analyses [20]. The LC value corresponds to a lossless transmission line case, in which both R and G are zero. As expected, L and C are constants over the entire frequency range. The LC units are divided by sec (s), which is a result of the low-pass/high-pass transformation.

Closed-form equations as functions of SIW dimensions and substrate characteristics are derived for the SIW equivalent circuit model of Figure 6.8. Table 6.4 shows a set of the closed form equations for L, C, Z_0, and β in which η is the impedance of the free space, h is the substrate thickness, a is the equivalent waveguide width, ε_r is the substrate permittivity, and μr is the substrate permeability. It must be noticed that L and C equations are valid for the operating range which starts after 20 % beyond the cutoff frequency point. This is a similar case for the TEM transmission lines as the L and C are not constant in the lower frequency range and the equations corresponds to the higher frequency [30], [31]. This is because the single-element LC model over the transmission line branches for the Telegraph Equations is oversimplified and more reactive element-connected branches should be added, which are not discussed in this work.

Compared to the parallel plate description with TEM mode propagation, SIW TE10-mode capacitance increases with a factor of $\frac{a\,c}{\sqrt{2}\pi\sqrt{\varepsilon_r}}$ and the SIW inductance increases 4 times more. Denormalized by the cutoff frequency, this factor is $2\sqrt{2}\,a^2$. Theses LC values correspond to the 3D definition involving longitudinal field elements. On the other hand, whereas TE10 wave impedance is independent of waveguide thickness, 3D characteristic impedance Z0 is related to the waveguide thickness. SIW characteristic impedance Z_0 matches to the wave impedance reduced by a factor of $\sqrt{2}$h/a. The closed form equation for Z_0 shows an insignificant error of 1% compared to the result from TT method. The calculated propagation constant (38) from L and C through our method is the same as the one from analytical calculation for a rectangular waveguide. As confirmed in [20], the dispersion characteristics of the SIW are the same as those of its equivalent rectangular waveguide.

6.6 Conclusion

Equivalent circuit modeling is a necessary tool for the circuit design in radio-frequency, microwave and millimeter-wave integrated circuits, and it is critically important for engineers to create a

standard design procedure that involves all the circuit and system elements. This work, introducing a universal modeling method for all the circuit elements and transmission lines, formulates a unifying framework to merge different interpretations and paves the way for the analysis and optimization of complex modes-based structures, which present prevalent paradigms in the computer-aided microwave design. The method is simple and straightforward without any complication in the calculations or limitation in the operating frequency. It is independent of the operating mode and type of transmission line. Different comprehensive results, including propagation loss and higher-order modes are presented and the method is verified and validated with the available results in the literature. Calculating the higher-order mode characteristic impedance is greatly important in the applications involving leaky-wave and surface mode structures, which are required to design a proper excitation structure [28]. As one of the most important applications, the characteristic impedance and related circuit model of SIW is studied thoroughly and extensively. RLCG lumped element uniform model is used to characterize the SIW

(a)

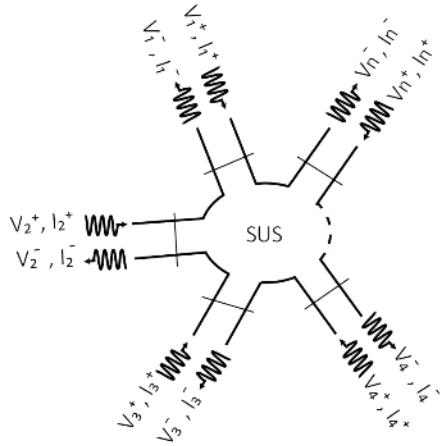

(b)

Figure 6.12: A schematic of two types of ports and their principles of operation a) lumped port and b) wave port.

and to define the characteristic 3D impedance for the first time. These parameters are essential to design transitions between SIW and other transmission lines.

6.7 Appendix A

In a commercial 3D full-wave software package for the simulations of electromagnetic components, ports represent a unique type of boundary condition that allows energy to flow into and out of the structure. The most common types of ports are wave ports and lumped ports. Figure 6.12 shows a schematic of these two types of ports and their underlying principle of operation. When applying the lumped ports (Figure 6.12(a)), the excitation is made by current I and then voltage V is calculated from an electric field integral. This type of calculation is therefore for a single TEM mode operation when an independent integral line exists. The characteristic impedance of the connected line must be known in advance. Lumped port is prone to reflection and evanescent mode propagations. Its application is typically for internal excitations and can be defined only on the edges of a 2D face with contacts to two conductors. The application of this type of port is commonly used in transmission lines. The lumped ports do not provide as much information as the wave ports do.

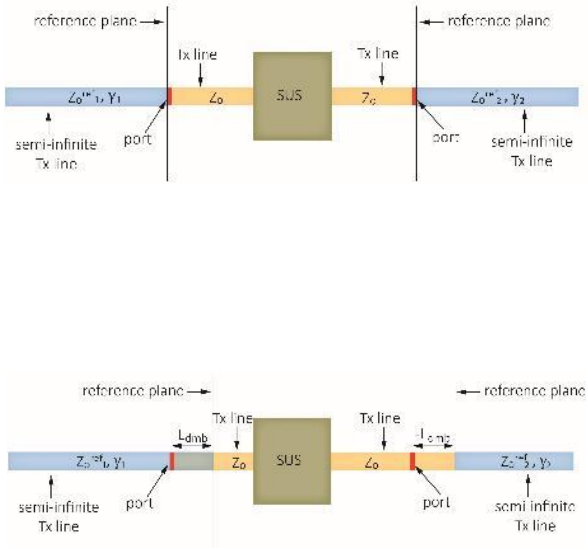

Figure 6.13: Wave port de-embedding in Ansoft HFSS.

The wave port is the most frequently used type of excitation. When applying the wave port, each of the ports is regarded as a semi-infinitely long waveguide with the same cross section and material properties as the port and perfectly matched at every frequency. Knowing the characteristic impedance of the feeding line is not required; the port automatically takes the value of Z_0 of an infinite feeding line connected to the waveport. In simulations, the structure in question must be connected to the wave port by a section of several wavelengths of the propagating mode in the traveling-wave structure. A 2D eigenvalue solver determines the field patterns (modes) of the traveling wave by solving Maxwell's equations:

$$\nabla \times (\frac{1}{\mu_r} \nabla \times \mathrm{E(x, y)}) - k_0^2 \varepsilon_r E(x, y) = 0 \tag{34}$$

where k_0 is free space wave number, μ_r complex relative permeability, and ε_r complex relative permittivity. E(x,y) is a phasor, valid at a single frequency, and therefore the eigenmode pattern of excitation field is computed for each frequency point of interest. In this type of excitation, each port is excited individually, generalized S-parameters are calculated directly, and multiple mode calculation is available as well. When modeling the structure with S-parameters, the 2D field solutions generated for each wave port serve as the boundary conditions at those ports for the 3D problem.

In addition to serving as a boundary condition, the wave port calculation determines the port impedance and propagation constant, which are useful in describing the connected traveling-wave feeding structure. When using the wave ports, since wave port gamma is calculated, the reference plane may be moved, meaning that the length of the connected traveling wave structure may be added or subtracted. In HFSS and CST, this is called port de-embedding. Figure 6.13 is a schematic representing a typical 3D geometry with the wave port calculation and port de-embedding feature in Ansoft HFSS as a 3D simulator. The software package calculates the port properties of propagation constant and reference impedance with 2D calculations and models a wave port as a semi-infinite transmission line Tx, and, therefore, a well-matched wave incidence is provided. While the simulation is underway, the place of the reference plane may be changed with dx (port de-embedding). This built-in de-embedding may add the length of Tx ($dx<0$) or may move the reference plane more inward 3D geometry ($dx>0$).

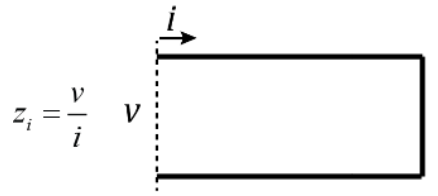

(a)

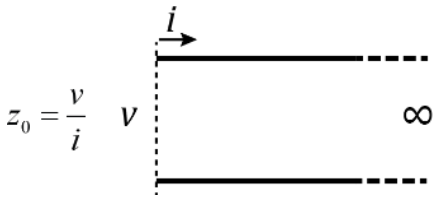

(b)

Figure 6.14: Basic definitions of different impedance in a transmission line: a) input Impedance b) characteristic Impedance

6.8 Appendix B

The term “impedance” is a measure of the opposition to the flow of the alternating electric current in a transmission line. Considering a simple transmission line, Figure 6.14(a) shows the input impedance, that is, the impedance at the origin of the line in which reflected waves are present or the measurements are influenced by wave reflections. Figure 6.14(b) is the characteristic impedance, in which measurements are not influenced by wave reflections and, therefore, it refers to the equivalent impedance of an infinitely long transmission line. Characteristic impedance can be determined by the relationship between propagating power and flowing current when these waves are not influenced by wave reflections; such circumstance is, in fact, impossible in real electrical circuits, and the waves are always altered by wave reflections. Therefore, the characteristic impedance is always measured by counting on an estimation. Input impedance may approximate the characteristic impedance when a long transmission line is used and wave reflection effects are minimized.

To deal with the characteristic impedance definition at high frequency, it is first necessary to recall Maxwell’s curl equations for current and charge free regions:

$$\oint E.dl = -\frac{\partial}{\partial t}\int_s B.ds \tag{35}$$

$$\oint \mathrm{H}.dl = \int_s i.ds + \frac{\partial}{\partial t}\int_s \mathrm{D}.ds \tag{36}$$

At low frequency, and for two conductor transmission lines c1 and c2, equations (35), and (36) are expressed as:

$$V = -\int_{c1}^{c2} E.dl \tag{37}$$

$$I = \oint_c H.dl \tag{38}$$

When 2D or transverse definitions of Z0 (PI, VI, PV) are applied, power is defined by V and I or equivalently by E and H as:

$$P = \frac{1}{2}\mathrm{Re}VI^* \tag{39}$$

$$P = \frac{1}{2}\mathrm{Re}\int_A E \times H^*.dA \tag{40}$$

Therefore, P is the average power and is an absolute physical quantity; however, Z = V/ I or any other V- or I- included definitions, is relative to an arbitrary definition of reference level. The validity of 2D impedance is in the case of TEM, when there is no longitudinal element and when there is no reflection; therefore, these 2D quantities are valid only for low frequency and TEM mode, when they can be defined independent of integral path. The remark is that using the wave formalism, instead of voltage and current quantities, does not help to bypass this problem. For the TEM mode, assuming no longitudinal field element, a uniquely defined voltage, current, and 2D Z0 exists. On the other hand, for TE and TM modes that have longitudinal field components, no unique definition for 2D Z0 is possible [39].

6.9 References

[1] D. G. Swanson and W. J. R. Hoefer, Microwave Circuit Modeling Using Electromagnetic Field Simulation, London: Artech House, 2003.

[2] K. Wu, L. Li, “Numerical calibration and de-embedding techniques for CAD and equivalent circuit models of electromagnetic structures," Microw. Rev., pp. 7–19, 2005.

[3] J. C. Rautio, “A de-embedding algorithm for electromagnetics,” Int. J. Microwave Mill., vol. 1, no. 3, pp. 282–287, 1991.

[4] L. Zhu and K. Wu, “Unified equivalent-circuit model of planar discontinuities suitable for field theory-based CAD and optimization of M(H)MIC's", IEEE Trans. Microw. Theory Tech., vol. 47, pp. 1589-1602, 1999.

[5] L. Li and K. Wu, “Numerical TRL calibration technique for parameter extraction of planar integrated discontinuities in a deterministic MoM algorithm,” IEEE Microw. Compon. Lett., vol. 12 , no. 12 , pp. 485–487, 2002.

[6] C. A. Hoer and G. F. Engen, “Calibrating a dual six-port or four-port for measuring two-ports with any connectors,” Proc. IEEE MTT-S Symp., pp. 665–668, 1986.

[7] L. Zhu and K. Wu, “Revisiting characteristic impedance and its definition of microstrip line with a self-calibration 3-D MoM scheme,” IEEE Microw. Guided Wave Lett., vol. 8, pp. 87–89, 1998.

[8] J. B. Knorr and A. Tufekcioglu, “Spectral-domain calculation of microstrip characteristic impedance," IEEE Trans. Microw. Theory Techn., vol. MTT-23, pp. 725–728, 1975.

[9] R. H. Jansen, “High speed computation of single and coupled microstrip parameters including dispersion, high order modes, loss and finite strip thickness,” IEEE Trans. Microw. Theory Techn., vol. MTT-26, pp. 75–82, eb. 1978.

[10] B. Bianco, L. Panini, M. Parodi, and S. Ridella, “Some considerations about the frequency dependence of the characteristic impedance of uniform microstrips,” IEEE Trans. Microw. Theory Techn., vol. MTT-26, pp. 182–185, 1978.

[11] W. J. Getsinger, “Measurement and modelling of the apparent characteristic impedance of microstrip,” IEEE Trans. Microw. Theory Techn., vol. MTT-31, no. 8, pp. 624–632, 1983.

[12] R. H. Jansen and H. L. Koster, “New aspects concerning the definition of microstrip characteristic impedance as a function of frequency,” IEEE MTT Symp. Dig., pp. 305–307, 1982.

[13] J. C. Rautio, “A new definition of characteristic impedance,” IEEE MTT-S Int. Microw. Symp. Dig., pp. 761–764, 1991.

[14] ANSYS HFSS Simulation Software [online] Available: http://www.ansys.com/

[15] P. Colestock and M. Foley, “A generalized TRL algorithm for S-parameter de-embedding,” Fermi National Accelerator Laboratory, FERMILAB-TM-1781, 1993.

[16] D. M. Pozar, Microwave Engineering, 4th ed., New York: Wiley, 2012.

[17] J. Staudinger and W. Seely, “MMIC tests improved with standards on chip,” Microwaves and RF, pp. 107–114, 1987.

[18] R.E. Collin, Field Theory of Guided Waves, 2nd ed., Piscataway, NJ: IEEE Press, pp. 191–192, 1991.

[19] W. R. Eisenstadt and Y. Eo, “S-parameter-based IC interconnect transmission line characterization,” IEEE Trans. Compon., Packag. Manuf. Technol., vol. 15, no. 4, pp. 483–490, 1992.

[20] M. Bozzi, L. Perregrini, and K. Wu, “Modeling of conductor, dielectric and radiation losses in substrate integrated waveguide by the boundary integral-resonant mode expansion method,” IEEE Trans. Microw. Theory Techn., vol. MTT-56, no. 12, pp. 3153–3161, 2008.

[21] F. Xu and K. Wu, “Guided-wave and leakage characteristics of substrate integrated waveguide,” IEEE Trans. Microw. Theory Techn., vol. 53, no. 1, pp. 66–73, 2005.

[22] L. Li, K. Wu, and P. Russer, “On the thru-reflect-line (TRL) numerical calibration and error analysis for parameter extraction of circuit model,” Int. J. RF Microw. Comput. Aided Eng., vol. 16, no. 5, pp. 470–482, 2006.

[23] N. Marcuvitz, Ed., Waveguide Handbook, 1951, New York: McGraw-Hill Book Co., Inc.

[24] D. F. Williams, B. K. Alpert , U. Arz , D. K. Walker, and H. Grabinski, “Causal characteristic impedance of planar transmission lines,” IEEE Trans. Adv. Packag., vol. 26, no. 2, pp. 165–171, 2003.

[25] R. B. Marks and D. F. Williams, “Characteristic impedance determination using propagation constant measurement,” IEEE Microw. Guided Wave Lett., vol. 1, no. 6, pp. 141–143, 1991.

[26] D. F. Williams, U. Arz, and H. Grabinski, “Accurate characteristic impedance measurement on silicon,” IEEE MTT-S Symp. Dig., pp. 1917–1920, 1998.

[27] J. B. Knorr and P. M. Shayda, “Millimeter-wave fin-line characteristics," IEEE Trans. Microw. Theory Techn., vol. 28, no. 7, pp. 737–743, 1980.

[28] Y. Cassivi, L. Perregrini, P. Arcioni, M. Bressan, K. Wu, and G. Conciauro, “Dispersion characteristics of substrate integrated rectangular waveguide,” IEEE Microw. Compon. Lett., vol. 12, no. 9, pp. 333–335, 2002.

[29] S.-D. Chen and C.-K. C. Tzuang, “Characteristic impedance and propagation of the first higher order microstrip mode in frequency and time domain,” IEEE Trans. Microw. Theory Techn., vol. 50, no. 5, pp. 1370–1379, 2002.

[30] M. J. Degerstrom, B.K. Gilbert, and E.S. Daniel, “Accurate resistance, inductance, capacitance, and conductance (RLCG) from uniform transmission line measurements, IEEE EPEP, 2008.

[31] Keysight Technologies Inc.

[32] http://na.support.keysight.com/plts/help/WebHelp/Analyzing/Analyzing_Transmission_Line_Parameters.html

CHAPTER 7 ARTICLE 6 : THEORETICAL ANALYSIS AND EXPERIMENTAL EVALUATION OF SIO2-CBN-MGO RIB WAVEGUIDE STRUCTURE

Overview: Optical waveguides are the building block structures in all optical devices. On the other hand, EO devices are based on EO effect, which is one of the material properties. Optical waveguides based on a new high-performance EO material are necessary for advancing EO devices and systems. This work focuses on the design, simulation, and characterization of a low loss optical rib waveguide based on an SiO_2-CBN-MgO material system.

(IEEE Photonics Technology Letters, publication date: September 2014)

Theoretical Analysis and Experimental Evaluation of SiO_2-CBN-MgO Rib Waveguide Structure

Faezeh Fesharaki[1], Nadir Hossain[2], Sébastien Vigne[2], Joëlle Margot[3], Ke Wu[1], and Mohamed Chaker[2]

[1]Poly-Grames Research Center, École Polytechnique de Montréal, QC H3T 1J4, Canada

[2]Centre Énergie Matériaux Télécommunications, Varennes, QC J3X 1S2, Canada

[3]Département de physique, Université de Montréal, Montréal, QC, H3C 3J7, Canada

Abstract — This letter reports the design, simulation, optimization, and optical characterization of an electro-optical SiO_2-CBN-MgO rib waveguide structure. To achieve single mode and low loss operation, the proposed rib waveguide structure is simulated and optimized with respect to CBN thin film thickness, etching depth, and rib width. Propagating optical mode profile of the waveguide is simulated using a beam propagation method solver. To verify the design and simulation, CBN thin film is coated on MgO substrate using a pulsed laser deposition technique, and SiO_2-CBN-MgO is fabricated with various CBN thicknesses and rib widths. A smooth and nearly vertical etching of the rib sidewall enables the fabrication of high quality rib waveguides. The waveguides are characterized and measured wave profiles are compared with simulated results. It is found that the guided modes are well confined within the rib and extended through the core. An excellent agreement between simulations and measurements is observed, thereby validating the design method.

Index Terms — CBN, high index contrast optical waveguide, electro-optical devices.

7.1 Introduction

Electro-optical (EO) tetragonal tungsten bronze (TTB) thin films, such as calcium barium niobate (CBN) and strontium barium niobate (SBN), are promising candidates for developing next

generation planar integrated electro-optical devices thanks to their large EO coefficients. Similar to lithium niobate ($LiNbO_3$), CBN and SBN are anisotropic material. However, the availability in thin-film and very large EO coefficient compare to $LiNbO_3$ have made them very desirable for device purposes [1], [2].

SBN has the EO coefficient of 844 pm / V in a thin film 7.6 and CBN thin film has the EO coefficient of 130 pm/V, which is 4 times larger than conventional EO materials such as lithium niobate [2]. However, CBN is more attractive than SBN for very high-speed integrated optics because of its higher thermal stability, shown by a 200 °C higher Curie temperature compared to SBN with an 80 °C Curie temperature [3]. In addition, CBN is an excellent candidate to build high performance integrated optical devices because of its high refractive index (n), low optical loss, and optical transparency at telecommunication wavelengths [4].

Efforts have been made to introduce CBN thin films into the making of optical waveguides as the building block of the CBN-based EO devices [5]–[8]. The previously reported waveguides suffer from a high propagation loss that is likely caused by low mode confinement in strip-loaded CBN waveguide [5], uncontrolled sidewall roughness in CBN ridge waveguide [6], [7], and also multimode propagation because of large waveguide dimensions. This limitation is a real obstacle in achieving a longer length waveguide, which is compulsory for CBN-based EO devices. To address these restraints, a high-index-contrast rib waveguide design in support of single mode propagation [9], [10] is proposed in this work. In this case, the fields are confined between the etched sidewalls of the waveguide and a structure less susceptible to losses induced by the surface roughness is formed. The fabrication of such designed CBN waveguides becomes possible thanks to a precise CBN etching technique reported recently by S. Vigne et al. [11], [12]. The design, optimization, and experimental evaluation of CBN rib waveguides are presented, which effectively solves the specified problems towards the development of CBN-based EO devices.

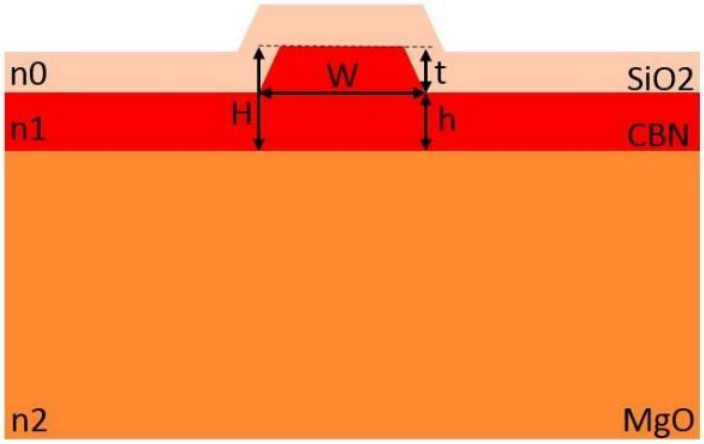

Figure 7.1: Cross-sectional view of CBN rib waveguide

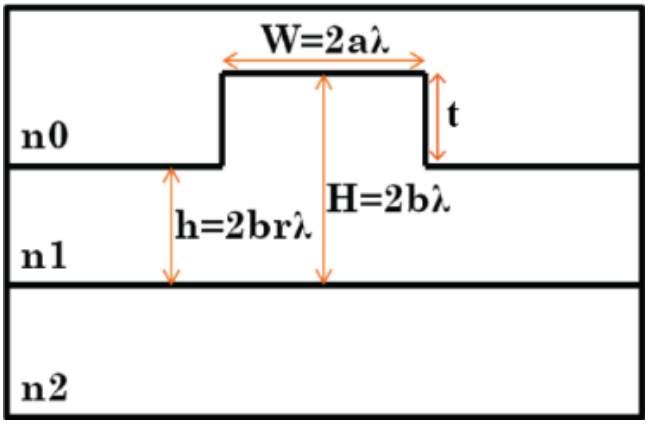

Figure 7.2: Cross section of a rib waveguide

7.2 Design and simulation

The cross section of the proposed CBN rib waveguide structure is shown in Figure 7.1. Electro-optic CBN (n_1=2.24) is bounded by MgO (n_2=1.71) substrate and SiO2 (n_0=1.5) cladding to provide the required optical confinement. The cladding also acts as buffer layer between CBN and conductive electrode in electro-optic devices to avoid plasmonic loss. MgO crystal with (001) orientation is considered because its lattice constant and thermal expansion coefficient allow for the epitaxial growth of CBN thin films [13]. The slanted angle of CBN is 73º because of the etching of the CBN in the fabrication process. The SiO_2 cladding follows the same angle as CBN. For

simulation and optimization purposes, the structure is considered a strip waveguide of width W and thickness t, on top of a slab waveguide of thickness h, as shown in Figure 7.1. Each of the strip waveguides and slab waveguides supports their propagating modes, where the propagation constant depends on the refractive index and the dimensions of the respective waveguide. Modes with the same propagation constant in both strip and slab waveguide are coupled to each other, and finally the only strip waveguide modes with the propagation constant larger than the propagation constant of the slab modes are propagating [14]. Others are leaky modes that are highly attenuated through coupling to the slab modes and therefore radiating to the substrate. Single-mode operation is achieved by adjusting the parameters in such a way that only the propagation constant of the first strip mode is larger than that of the slab modes. As a result, despite the high index contrast, the cross section of a single mode rib-waveguide can be considerably larger than a single mode strip waveguide made from the same material stack [9].

Soref et al. (1999) demonstrated a theory to determine the rib waveguide dimensions that will allow only for the fundamental quasi-TE (HE_{00}) or quasi-TM (EH_{00}) mode to propagate [9]. Accordingly, single mode propagation is feasible even at multimicron dimensions so far as the ratio of rib width (W) to inner rib height (H) is properly chosen for a determined wavelength (λ). For the general structure in Figure 7.2, the following governing equation holds [9]:

$$\frac{W}{H}=\frac{a}{b}\le\left(\frac{q+4\pi b}{4\pi b}\right)\frac{1+0.3\sqrt{\left(\left(\frac{q+4\pi b}{q+4\pi rb}\right)^{2}-1\right)}}{\sqrt{\left(\left(\frac{q+4\pi b}{q+4\pi rb}\right)^{2}-1\right)}} \tag{1}$$

where

$$q=\frac{\gamma_0}{\sqrt{\left(n_1^{\,2}-n_0^{\,2}\right)}}+\frac{\gamma 2}{\sqrt{\left(n_1^{\,2}-n_2^{\,2}\right)}} \tag{2}$$

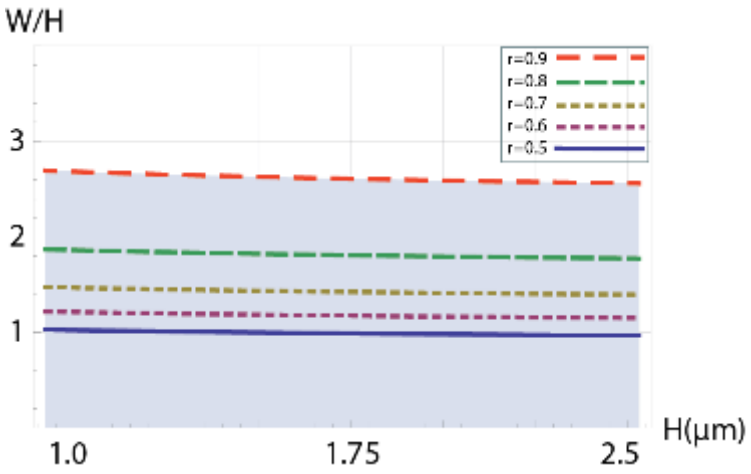

Figure 7.3: Simulated critical W/H ratio as function of the CBN thin film thickness H for various values of r at λ = 1.55 μm in an SiO2-CBN-MgO rib waveguide structure.

r = 1-t/H, $\gamma_{0,2}$ =1 for HE modes, and $\gamma_{0,2}$ =$(n_{0,2}/n_1)^2$ for EH modes. Rib waveguide width W and inner rib height H are selected as 2aλ and 2bλ, respectively, where λ is the optical wavelength in free space. The rib thickness t is the etching-depth of CBN material, H is the thickness of deposited CBN material, and r is the ratio of h/H. As specified by Eq. (1) and (2), Figure 7.3 shows the critical value of ratio W/H as a function of H for various values of r at λ = 1.55 μm. Based on this figure, knowing the thickness of CBN material H, W is chosen so that W/H is below the curve with corresponding r-value; this ensures single mode propagation. A higher etching depth corresponding to a lower value of r may offer a better energy confinement of the propagating mode within the rib; however, it may increase the sidewall roughness and hence optical loss.

Moreover, end-fire coupling is more difficult in the rib waveguide with high etching depth because of the reduced input coupling spot. On the other hand, in the case of a very shallow etching depth, the confinement may be so small that the energy of the propagating modes may leak out laterally along the propagation, resulting in a very high propagation loss. Additionally, due to the complexity of the analysis, the validity of Eq. (1) is restricted to $0.5 < r \leq 1$ [9]. Therefore, a further optimization of r, W, and H based on the experimental feedback is necessary to yield an accurate design.

Propagating mode characteristics of SiO_2-CBN-MgO rib waveguide structure are simulated using a commercially available beam propagation method (BPM) solver [15], and a parametric study is performed for various CBN thicknesses H, r, and widths W. Given H=2μm deposited CBN, and r=0.9 (10% etching depth to avoid surface roughness), simulation results predict that the rib waveguides with width W≤ 4 μm guide single mode at 1550 nm. With regard to previous explanations, it implies that the first mode of the strip is confined in the waveguide and the higher order modes are coupled to the slab. In the following, the proposed SiO_2-CBN-MgO rib waveguide structures are fabricated based on this design, and simulated results are experimentally verified.

7.3 Fabrication

For this work, 2 μm thick epitaxial CBN thin films were deposited on 500 μm thick (001) MgO substrate at 800 °C by a pulsed laser deposition (PLD) technique using a KrF laser (248 nm, 16 ns pulse) focused on a stoichiometric CBN-28 target. Epitaxial quality of the thin films was verified using X-ray diffraction. A nickel (Ni) hard mask was deposited on the top of the CBN layer using a nickel sulfamate solution from Transene (Transene Co., Inc., Danvers, MA, US) by electroplating through a patterned photoresist. In order to etch the CBN, the Ni patterned samples were placed in a PlasmaLab ICP 380 System 100 from Oxford Instruments (Tubney Woods, Abingdon, UK) operated at 1000W power and at 1 mTorr pressure. The samples were etched using Cl2 gas with a DC Bias of 200V. Finally, a 1μm layer of SiO2 was deposited using plasma enhanced chemical vapor deposition (PECVD) from a mix of SiH4, N2, and N2O. High resolution images were taken on a Jeol JSM-7401F Scanning Electron Microscope (SEM) (Jeol USA, Inc., Peabody, MA, US) with acceleration voltage and current set at 5 kV and 10 μA, respectively, to measure the thicknesses of the etched and deposited material as well as to characterize the sidewalls, and quality of the cleaved facets. Further details of the deposition, structural characterization, and fabrication of this material stack can be found in [10]–[12]. Figure 7.4 shows the SEM cross-section image of the input side of a 10% etched (r = 0.9) CBN epitaxial thin film with a subsequent deposition of 1 μm SiO_2 layer. The high quality of deposited CBN material, with its smooth and nearly vertical etching capability of the rib sidewall, has enabled us to fabricate the simulated SiO_2-CBN-MgO rib waveguide structures. In order to verify the design and simulation comprehensively, waveguides with widths of 4, 5, 7, and 10 μm are fabricated.

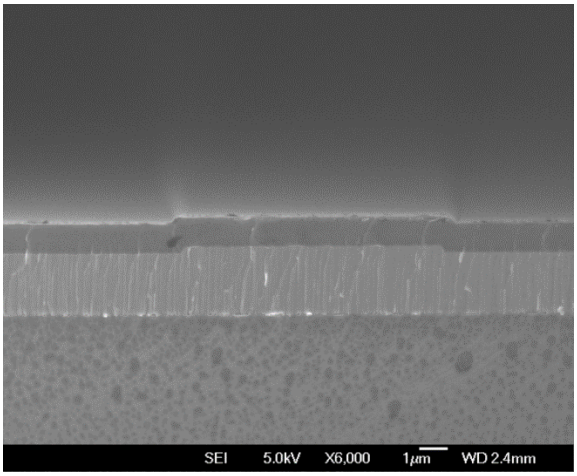

Figure 7.4: SEM image of a 10% etched 2um epitaxial CBN thin film with 1μm SiO2 deposited by PECVD.

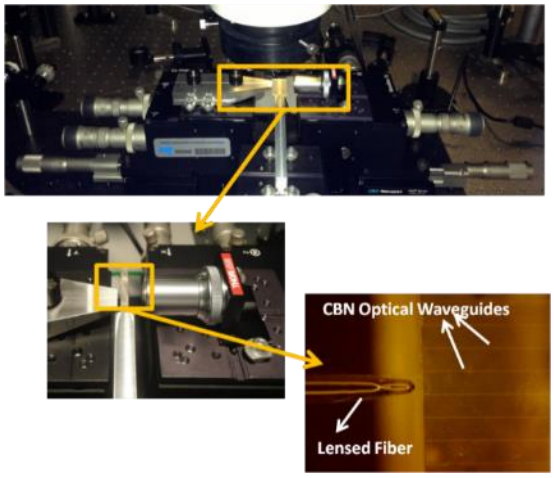

Figure 7.5: Characterization setup with lensed fiber input (~2um spot size and ~50um working distance), 10x objective output (5.6mm working distance).

7.4 Characterization and experimental evaluation

Figure 7.5 shows the characterization setup. Waveguides have been characterized by end-fire coupling from an optical fiber to the sample end using the beam generated by a CW laser diode at 1550nm. The guided light from the waveguide end-facet is extracted using a long working distance (LWD) 10x microscope objective lens.

The input-output facets of the waveguides are prepared by cleavage, and the quality of the cleaved facets is verified by SEM. In order to efficiently inject light within the thin waveguide (~2 μm thick CBN core), a lensed fiber (LaseOptics Corp. SMF-28 Conical 1 μm SS, Williamsville, NY, US) with ~2 μm spot diameter have been installed at the output of the laser source to focus the laser light at the waveguide facet. The input fiber, output objective, and the waveguide sample are separately mounted on high precision micro-positioners and stages (Thorlabs NanoMax-TS, Newton, NJ, US) to achieve accurate and stable alignment, where both top and front views are controlled to achieve the efficient coupling. Top-view observation is performed using an optical microscope attached to a camera mounted on top of the measuring system. This camera is computer-controlled by image processing software [16]. The front view is captured by focalizing the light coming from the objective to a high performance computer-controlled charge coupled device (CCD) camera (Model C2741, Hamamatsu Photonic Systems, Bridgewater, NJ, US). The image of the propagating optical modes from the output facet of SiO2-CBN-MgO rib waveguide structures is captured by an in-house developed LabVIEW program, and optical mode profiles are further analyzed by MATLAB.

Figure 7.6 shows the measured (in grey) optical mode profiles of an SiO2-CBN-MgO (1 μm, 2 μm, 500 μm thick) rib waveguide structure with various rib widths and 10% etching depth corresponding to r=0.9. We found that modes are well confined within the rib and extended through the core. Figure 7.6 also compares the simulated (using BPM solver) and experimentally measured mode profile using the same rib waveguide design parameters. As predicted by simulation, 4 μm width rib waveguide shows a monomode characteristic; 5 μm and 7 μm width rib waveguides allow the propagation of the second mode, where 10 μm width supports the third mode as well. The agreement between the simulation and experiment is remarkably good, therefore validating our design method.

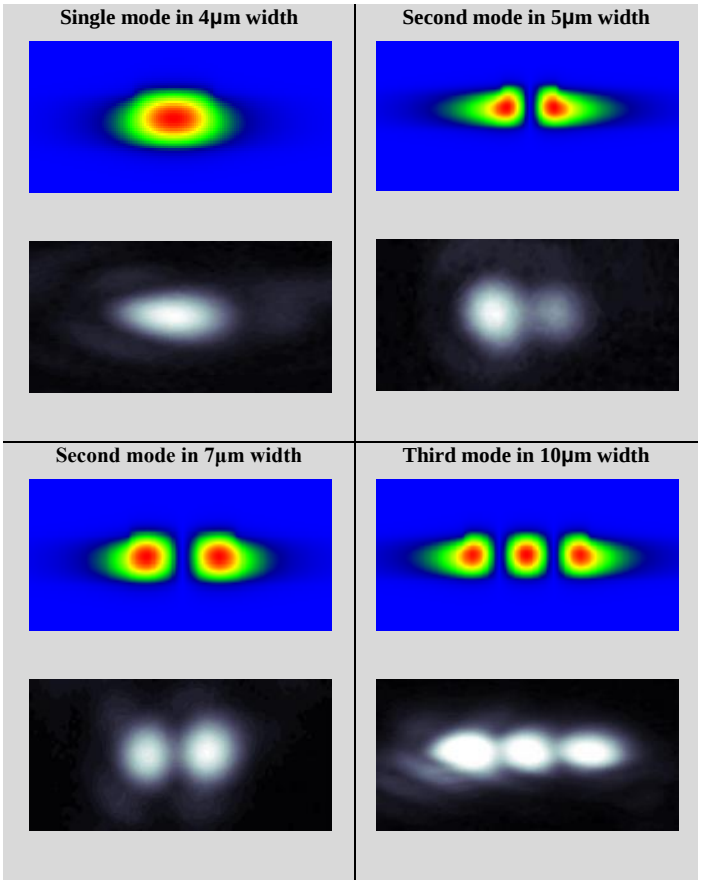

Figure 7.6: Simulated (in color) and experimentally (in grey) measured mode profiles of SiO2-CBN-MgO rib waveguide structure with 2 μm CBN thickness, etch depth ~10% of CBN thickness and various rib widths.

7.5 Conclusions

To solve the problem of the previously reported CBN waveguide, the SiO_2-CBN-MgO rib waveguide structure is designed and simulated, in an effort of enabling the single mode and low loss operation. For a given value of H =2 μm CBN thickness, and a chosen value of 10% etching depth to minimize surface roughness, the simulation result shows that the rib waveguides with width W ≤ 4 μm present single mode propagation at 1550 nm. CBN is epitaxially deposited on (001) MgO substrate using a PLD technique. Smooth etching capability with near vertical sidewalls enabled the fabrication of high quality SiO2-CBN-MgO rib waveguide structures. Experimentally measured propagation modes of the designed waveguide structure present an excellent agreement with the simulated results, which is a key step towards the design and fabrication of high-performance EO devices.

7.6 References

[1] R. Helsten, L. Razzari, M. Ferrera, P. F. Ndione, M. Gaidi, C. Durand, M. Chaker, and R. Morandotti, “Pockels response in calcium barium niobate thin films,” Appl. Phys. Lett., vol. 91, no. 26, pp. 1106–1108, 2007.

[2] P. Tayebati, D. Trivedi, and M. Tabat, “Pulsed laser deposition of SBN: 75 thin films with electro-optic coefficient of 844 pm/V,” Appl. Phys. Lett., vol. 69, no. 8, pp. 1023–1025, 1996.

[3] S. David, T. Granzow, A. Tunyagi, M. Wöhlecke, T. Woike, K. Betzler, M. Ulex, M. Imlau, and R. Pankrath, “Composition dependence of the phase transition temperature in SrxBa1−xNb2O6,” Phys. Stat. Sol. (a), vol. 201, pp. R49–R52, 2004.

[4] M. Eßer, M. Burianek, P. Held, J. Stade, S. Bulut, C. Wickleder, and Mühlberg, “Optical characterization and crystal structure of the novel bronzetype CaxBa1-xNb2O6 (x = 0.28; CBN-28),” Cryst. Res. Technol., vol. 38, no. 6, pp. 457–464, 2003.

[5] P. F. Ndione, M. Ferrera, D. Duchesne, L. Razzari, M. Gaidi, M. Chaker, and R. Morandotti, “Hybrid integration of Ca0.28Ba0.72Nb2O6 thin film electro-optic waveguides with silica/silicon substrates,” Opt. Express, vol. 17, no. 17, pp. 15128–15133, 2009.

[6] I. Stateikina, E. Mortazy, S. Delprat, K. Wu, and M. Chaker, “Fabrication of a silicon-based CaxBa1−xNb2O6 ridge waveguide for electro-optical phase modulation,” Semicond. Science and Technology, vol. 25, no. 11, pp. 115005–115009, 2010.

[7] E. Mortazy, I. Stateikina, A. Tehranchi, S. Delprat, M. Chaker, and K. Wu, “Calcium barium niobate ridge waveguide on silicon substrate,” Opt. Eng., vol. 49, no. 7, pp. 074601–074601-3, 2010.

[8] G. Fu, K.-M. Wang, X.-L.Wang, H.-J. Zhang, X.-G. Xu, H.-L. Song, and H.-J. Ma, “Planar waveguides in calcium barium niobate fabricated by MeV He ion implantation,” Appl. Phys. B, vol. 87, no. 2, pp. 289–292, 2007.

[9] R. A. Soref, J. Schmidtchen, and K. Petermann, “Large single-mode rib waveguides in GeSi-Si and Si-on-SiO2,” IEEE J. Quantum Electron., vol. 27, no. 8, pp. 1971–1974, 1991.

[10] R. G. DeCorby et al., “High index contrast waveguides in chalcogenide glass and polymer,” IEEE J. Sel. Top. Quant., vol. 11, no. 2, pp. 539–546, 2005.

[11] S. Vigne, J. Munõz, S. Delprat, J. Margot, and M. Chaker, “Plasma etching dynamics of CaxBa1–xNb2O6 (CBN) material,” Microelectron. Eng. Vol. 110, pp. 265–269, 2013.

[12] S. Vigne, S. Delprat, M. Chaker, and J. Margot, “Investigation of nickel as hard mask for patterning multicomponent oxide materials in chlorine plasmas,” J. Appl. Phys., vol. 114, no. 10, pp. 103303, 2013.

[13] P. F. Ndione, M. Gaidi, C. Durand, M. Chaker, R. Morandotti, and G. Rioux, “Structural and optical properties of epitaxial CaxBa1-xNb2O6 thin films grown on MgO by pulsed laser deposition,” J. Appl. Phys., vol. 103, no. 3, pp. 033510, 2008.

[14] E. A. J. Marcatili, “Slab-coupled waveguides,” Bell Syst. Tech. J., vol. 53, pp. 645–672, 1973.

[15] OptiBPM© ver. 11.0, by OptiWave Systems, Inc., Nepean, ON, Canada.

[16] ScopeImage ver 9.0, by Bioimager, Inc., Maple, ON, Canada.

CHAPTER 8 ARTICLE 7 : ACCURATE THEORETICAL AND EXPERIMENTAL CHARACTERIZATION OF OPTICAL GRATING COUPLER

Overview: Optical grating couplers are used to couple light to optical waveguides. The work in this chapter was motivated by the problems to couple light to CBN waveguide (chapter 7). A generalized method for the design and optimization of grating coupler was necessary that can be used for any material system.

(Optics Express, publication date: September 2016)

Accurate Theoretical and Experimental Characterization of Optical Grating Coupler

Faezeh Fesharaki[1], Nadir Hossain[2], Sebastien Vigne[2], Mohamed Chaker[2], and Ke Wu[1]

[1]Poly-Grames Research Center, École Polytechnique de Montréal, QC H3T 1J4, Canada

[2]Centre Énergie Matériaux Télécommunications, Varennes, QC J3X 1S2, Canada

Abstract — Periodic structures, acting as reflectors, filters, and couplers, are a fundamental building block section in many optical devices. In this paper, a three-dimensional simulation of a grating coupler, a well-known periodic structure, is conducted. Guided waves and leakage characteristics of an out-of-plane grating coupler are studied in detail, and its coupling efficiency is examined. Furthermore, a numerical calibration analysis is applied through a commercial software package on the basis of a full-wave finite-element method to calculate the complex propagation constant of the structure and also evaluate the radiation pattern. For experimental evaluation, an optimized grating coupler is fabricated using electron-beam lithography technique and plasma etching. An excellent agreement between simulations and measurements is observed, thereby validating the demonstrated method.

OCIS Codes — (050.0050) Diffraction and gratings; (220.0220) Optical design and fabrication; (230.0230) Optical devices

8.1 Introduction

Grating coupler, a region on top of or below a waveguide where there is a grating, is a structure in which guided-mode resonance takes place. Once designed accurately, resonance happens for specific combinations of incident angles and light frequencies and allows the grating to couple light into a guided mode of the waveguide. They have prominent applications in integrated optics to efficient butt-coupling of light from a single mode fiber (~125μm diameter) to a thin-film planar

waveguide (dimensions around ~1μm or less). The power distribution diffracted by a grating depends on the properties of electromagnetic fields guided by the structure [1], which necessitates a rigorous electromagnetic method in order to simulate, understand and design the grating coupler.

Numerous theoretical studies of grating couplers have been conducted based on both exact and approximate formulations [1]-[5]. However, the precedent methods based on an exact treatment of the pertinent boundary-value problem are complex and cumbersome to use [1]-[4]. On the other hand, traditional perturbation method, although simplifying the problem, has limitations and complications for treating general geometry cases, and is not accurate for grating with a small number of periods [6]. In the eigenmode expansion [2] and coupled-wave [4]-[5], [7]-[8] approaches, the system of coupled differential equations may be large and difficult to solve [2]. In addition, some of the solution algorithms are unstable for thick gratings and may become inefficient for computation, as mentioned in references [2], [5], [8]. Two-dimensional (2D) modeling of the grating is quite common and widely used; although faster than 3D simulation, because of the simplifications in considering the whole radiated beam in a horizontal plane and also neglecting the radiation side lobes, it leads to an inaccurate result. Therefore, the real coupling efficiency, obtained with a three-dimensional (3D) configuration, will be lower than that of 2D model-based simulations [9]. Moreover, with the conventional design and simulation technique, it is difficult to transfer easily the existing well-known design of Silicon-on-Insulator (SOI) grating coupler to another material system such as III-V [10], which is essential for integration with active optoelectronic components [11].

In this paper, a 3D simulation of the grating coupler is performed. This approach enables a rigorous and general investigation of this periodic structure. Using the vector formulation of Maxwell's electromagnetic equations with a commercial software package on the basis of a full-wave finite-element method (FEM), the power distribution diffracted by a grating is resolved and the grating efficiency is examined. A parametric study is performed to determine the dependence of the wave leakage on structural geometry, operating wavelength, and polarization as well as incident angle of the light. In addition, since the complex propagation constant ($\gamma=\alpha+j\beta$) cannot be obtained directly from the simulation, we have used a numerical calibration method to extract this critical parameter. The numerical calibration method is a well-established technique for the study of any guided or leaky wave structures [12]. This method allows the analysis of optical periodic structures with a very large number of periods with minimal numerical problems. Such devices are of

considerable technical importance [13]. The grating coupler is fabricated using electron-beam lithography (EBL), followed by plasma etching and measured for the validation of our simulation results.

8.2 Method of Analysis

The grating coupler is an open guided-wave structure in which the gradual wave leakage along the propagation is used advantageously to couple the light to the fiber optic. The wave leakage is related to the wave guidance and is fundamentally characterized by the complex propagation constant, which depends on many parameters, including the structural geometry, polarization, the incident angle of light, material, groove spacing, operating frequency, and the guided mode.

The physical structure of the grating coupler is considered a leaky waveguide with a length *L* along which the leakage occurs. The propagation characteristic of the leaky mode in the longitudinal (z) direction is determined by phase constant β and leakage constant α, where α is a measure of the power leaked (radiated) per unit length. The theoretical determination of β and α, although difficult, is essential to any systematic design procedure. Once β and α are known for the considered wavelength, the required principal features such as coupling angle and coupling efficiency will follow in sequence.

In a grating coupler the fundamental mode is slow compared to the free space: the phase constant of the fundamental mode is larger than the free space wavenumber or $b > k_0 = 2p / l$ [8] where λ is the wavelength in the free space. According to Floquet's theorem [13], the grating periodicity introduces an infinite number of space harmonics, which are characterized by phase constant β_n:

$$\beta_n = \beta_0 + \frac{2n\pi}{d} \tag{1}$$

where *d* is the period of the grating, and β_0 is the phase constant of the fundamental mode of the waveguide without grating. The grating is designed in such a way that the first space harmonic ($n = -1$) with phase constant $\beta_{-1} = \beta_0 - 2\pi/d$ becomes fast ($\beta_{-1} < k_0$). The beam can be created in either the forward or backward direction; however, the range in the forward quadrant is usually limited by the appearance of the $n = -2$ beam [14]. Design is carried out based on the criteria introduced by [6] which are:

$$n_{eff} - \frac{\lambda}{d} < n_{air} \tag{2}$$

and

$$\frac{2\lambda}{d} - n_{eff} < n_{substrate} \tag{3}$$

in which n_{eff} is the refractive index of the optical waveguide, n_{air} is the air refractive index, and $n_{substrate}$ is the substrate refractive index. Through three-dimensional simulations and using near and far field calculations, the field distribution and radiation patterns are monitored. A radiation boundary is used to simulate the grating coupler, which is an open problem. Radiation boundary allows waves to radiate infinitely far into space. Model exterior has been selected as HFSS-IE domain; in this case, conformal radiation volumes are used advantageously and the overall finite element solution domain is reduced, resulting in more efficient simulation for electrically large open boundary problems. The solution frequency is selected according to the operating wavelength.

To obtain the complex propagation constant $\gamma=\alpha+j\beta$, the numerical calibration technique [15] is used to extract the phase and attenuation constants. To perform the numerical calibration, the periodic structure of the grating coupler structure is simulated as a two-port waveguide with different lengths or different period numbers. The number of periods is optional; to speed up the simulation, a few periods are used. In this case, the whole structure consists of an input tapered section, grating section, and an output tapered section. The transmission matrix T can be written as a cascade matrix in the form of:

$$T = T_{in} T_{grating} T_{out} \tag{4}$$

Where $T_{grating}$ is a diagonal matrix

$$T_{grating} = \begin{bmatrix} e^{-\gamma L} & 0 \\ 0 & e^{\gamma L} \end{bmatrix} \tag{5}$$

in which L is the grating length. Once two different lengths (i and j) are simulated, T_i and T_j are obtained and the equations can be combined as:

$$T^{ij}T_{in} = T_{in}T^{ij}_{grating} \tag{6}$$

where $T^{ij} = T^i(T^j)^{(-1)}$ and $T_{grating}{}^{ij} = T_{grating}{}^{i}(T_{grating}{}^{j})^{-1}$. Since $T_{grating}{}^{ij}$ is a diagonal matrix, the eigenvalues of T^{ij} are the diagonal elements of $T_{grating}{}^{ij}$ matrix. This feature is used to derive the unknown propagation constant of grating coupler:

$$e^{\gamma_i \Delta L} = \lambda_i \tag{7}$$

where λ_i is the eigenvalue of T^{ij}, and ΔL is the difference of two simulated gratings of differing lengths. Accurate complex propagation constants are therefore obtained from the parameters generated in two simulations. The extraction of propagation constant and attenuation from HFSS simulation and eigenvalues of the transmission matrix have been detailed in [12]. Since the proposed grating structure is uniform, the beam direction can be obtained from:

$$\sin\theta_m \approx \beta \Big/ k_0 \tag{8}$$

in which θ_m is the angle of the maximum of the beam. The larger value of α involves a larger leakage rate and results in a greater beamwidth; on the contrary, the lower value of attenuation constant α causes a narrower beam. When the length of the grating is finite and the attenuation constant is small, the beamwidth is determined primarily by the grating length and the value of α mainly affects the grating efficiency. The beamwidth can be calculated by

$$\Delta\theta \approx \frac{1}{(L/\lambda)\cos\theta_m} \tag{9}$$

Knowing the complex propagation constant γ, the radiation or power pattern $R(\theta)$ is approximated by [14]:

$$R(\theta) = \frac{cos^2\theta}{\left(\frac{\alpha}{k_0}\right)^2 + \left(\frac{\beta}{k0} - sin\theta\right)^2} \tag{10}$$

This equation is obtained from the Fourier transform of the grating filed distribution considering that the grating length is infinite and the grating field distribution is exponentially decaying. According to this equation, a grating coupler with an infinite length is ideally free of any side lobe radiation. However, in reality, the length of the grating is finite and therefore the efficiency is less and possesses side lobes. To improve the performance and efficiency in relation with side lobes, the structure must be designed in such a way that the value of α decreases slowly along the geometrical length of the grating, while the value of β remains constant so that the radiation from all parts of the grating direct to the same direction. As an example, a kind of tapered grating structure can be designed in which the width of the grating decreases along its length. The advantage of using numerical calibration and Eq. (10) is that for any structure and any length, the radiation pattern may be obtained systematically with a quick simulation. This allows the analysis of optical periodic structures with a very large number of periods with minimal numerical problems.

8.3 Simulations and Calculations

A grating design based on SOI wafer was optimized for operation at λ = 1550nm wavelength. According to last section, once the material system is selected, the design procedure is as follows:

1. The refractive index of silicon (n_{Si} = 3.48) and silicon oxide (n_{SiO2} = 1.46) are verified experimentally on the commercial wafer.
2. Using the finite difference beam propagation method of Optiwave [17], the width of the SOI strip waveguide is chosen to provide single mode propagation.
3. The cross-section of the waveguide is simulated using 2D finite element method solver of HFSS [15] and the effective refractive index of the fundamental mode (n_{eff}) is extracted.

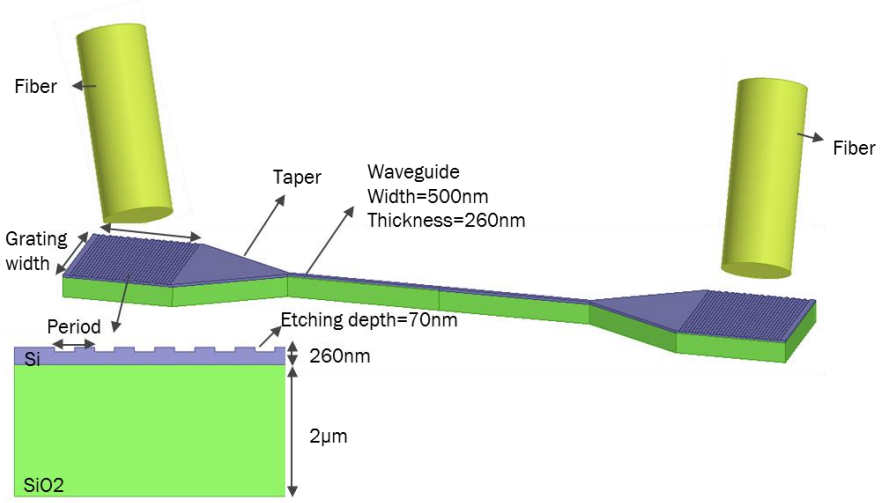

Figure 8.1: Complete three-dimensional model of the SOI grating-waveguide device is considered in this paper in both simulation and fabrication. In the simulation, half of the structure with shorter taper and waveguide length is simulated.

4. From Eqs. (2) and (3), an estimated value for the grating period *d* is derived, which is used as an initial value in the 3D simulations.
5. The initial value of etching depth h is chosen around 0.1*d* to have a flat efficiency over the spectrum [18].
6. Starting from these initial values, a parametric setup sweep analysis is used to find the optimized value for grating period d and etching depth *h*.

For the commercially available SOI wafer with a 260nm silicon layer and 2 μm buried oxide, the waveguide width is selected equal to 500nm confirmed by Optiwave simulation to assure the single mode propagation. The fiber mode is approximately a Gaussian profile with a beam diameter of 10.5μm, and to maximize the overlap, the grating width is chosen 25 times larger than the width of the waveguide (12.5μm), and a total number of 16 to 18 repetitions is used. Figure 8.1 shows the complete 3D model of the SOI grating-waveguide devices that are used in this paper. In the simulations, we use half of this symmetrical structure to calculate the coupling efficiency from the

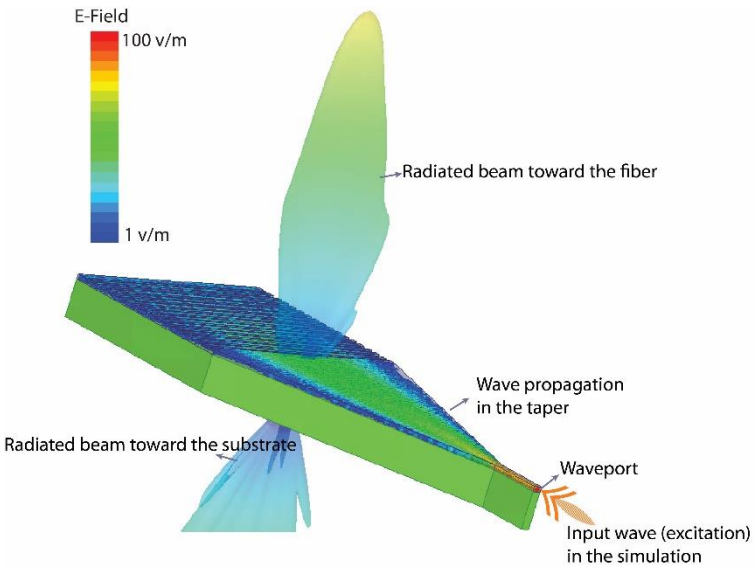

Figure 8.2: 3D Simulated structure. Half of the device is simulated using the wave port excitation of the waveguide and the radiated beam is monitored.

waveguide to fiber, which is the same as the coupling from fiber to waveguide [9]. As illustrated in Figure 8.2, the optical waveguide is excited using wave port excitation and the wave is propagating through the waveguide and taper. Field distributions and radiation patterns are monitored to achieve the desired coupling of the grating coupler.

The length of the taper is optimized to 650μm using beam propagation method to minimize the radiation loss. However, in the 3D simulation, a much shorter length is used to speed up the simulation. To avoid any error in the analysis because of this estimation, the return loss of the wave port is observed; provided the matching condition is preserved, return loss is close to zero and trimming the taper length does not affect the normalized simulation result.

Figure 8.3 shows the 2D radiation pattern of the grating coupler with 70nm etching depth and three different periods. Part of the wave is radiated toward the substrate and part is a coupling beam radiating toward the fiber. The coupling angle varies with changing the grating period. The 530nm period provides the negative coupling angle around 7º; by increasing the period to 580nm and 600nm, the coupling angle is changed to positive angles around 7º and 13º. The ratio of the desired coupling beam to the whole radiated stream determines the coupling efficiency.

Figure 8.4 also shows the calculated radiation pattern for the proposed grating coupler with 580nm grating period using the numerical calibration (NC) method. For that, the simulation result of two different lengths (2 periods and 4 periods) is used to extract the complex propagation constant. The real and imaginary parts of the S-parameters are derived from HFSS simulation for two different lengths (ΔL). These data are used to calculate the transmission matrix (T), whose eigenvalues are used to extract the propagation constant and attenuation. For the proposed structure, phase constant β = 6.1074*10^5rad/m, and attenuation constant α = -1.0810*10^5 np/m is derived, from which the radiation pattern is calculated. The slight difference in the radiation patterns of the simulation and theoretical model is observed. The reason is that in the calculation, the radiation pattern is obtained

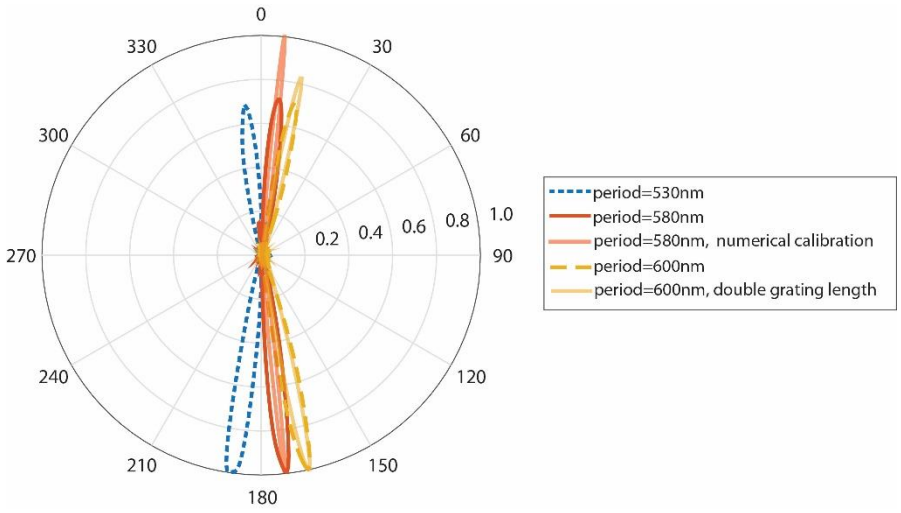

Figure 8.3**:** The simulated radiation pattern of the proposed SOI grating coupler optimized to work at 1550nm wavelength for the different grating periods. SOI wafer (260nm silicon layer and 2µm buried oxide), waveguide width 500nm, grating width 12.5µm, etching depth 70nm, and taper length 650µm. Coupling angle is changed with the grating period.

by taking the Fourier transform of the aperture field distribution, assuming infinite aperture length.

However, in the simulation, the actual limited length of the grating structure is simulated. The Fourier transform relationship between field distribution and radiation is exact; however, since the electric field is not exact, radiation always involves an approximation. This formula is based on an infinite length and the result does not have side lobe radiation. In general, for a larger dimension, the beamwidth or angular bandwidth is smaller [19]. Figure 8.3 shows that it has been also confirmed with simulation. The grating coupler with 600nm grating period has been simulated using a total of 35 periods. As shown in the figure, the beamwidth is narrower compare to the original one with 18 periods.

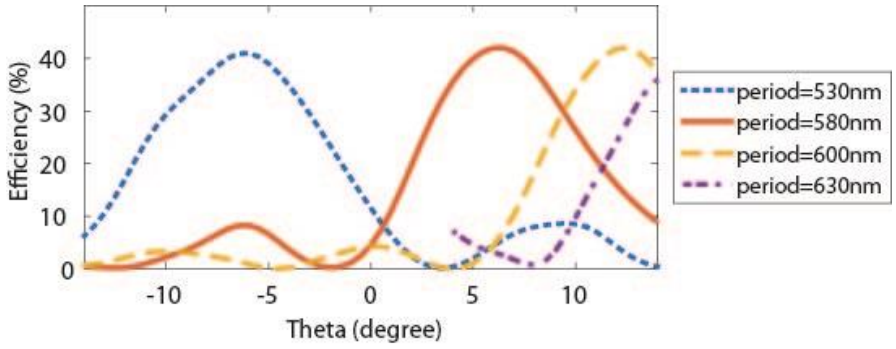

Figure 8.4**:** Simulated efficiency versus incident angles for the proposed SOI grating coupler at 1550nm wavelength for the different grating period. SOI wafer (260nm silicon layer and 2μm buried oxide), waveguide width 500nm, grating width 12.5μm, taper length 650μm, and etching depth 70nm.

From the radiation patterns, the radiated power to the substrate is identified and the efficiency of the grating coupler is estimated. Figure 8.4 shows the coupling efficiency versus incident angle for the proposed SOI grating coupler with different coupling angle. With a slight increase in the period, coupling angle is increased, keeping roughly the same efficiency, around 41%. The dimensions are optimized to obtain a compromise between angular bandwidth and efficiency. Deeper etch-depth can increase the efficiency, but in the same time period must be optimized to couple light toward the desired angle. Beamwidth is determined through Eq. (9). Considering that 90% of the power is radiated through the length, then:

$$\frac{L}{\lambda_0} \approx \frac{0.18}{\alpha / K_0} \tag{11}$$

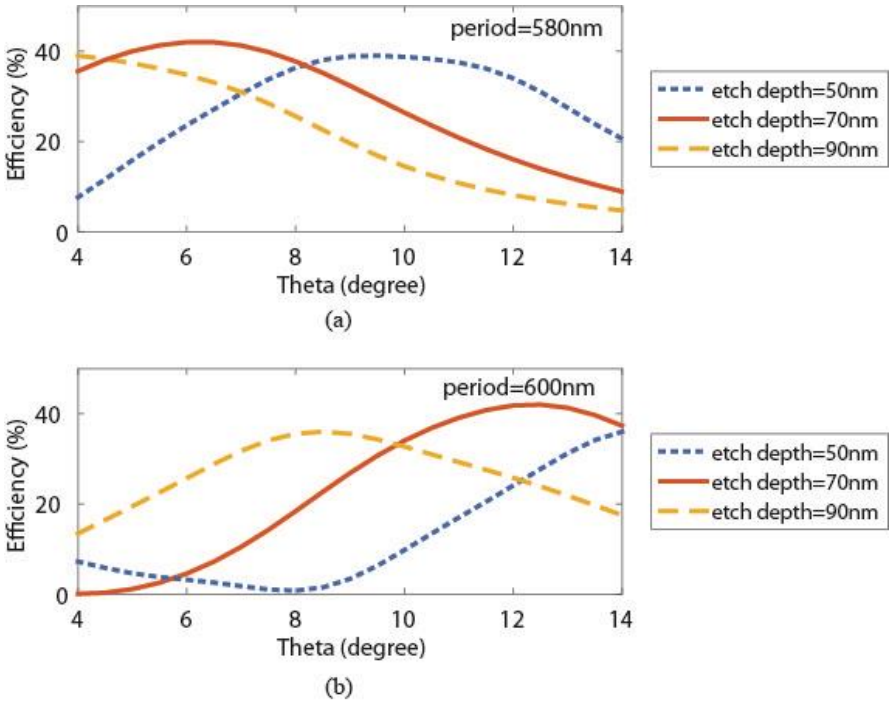

Figure 8.5**:** Simulated efficiency versus incident angle for the proposed SOI grating coupler at 1550nm wavelength for different grating etching depth. SOI wafer (260nm silicon layer and 2 μm buried oxide), waveguide width 500nm, grating width 12.5μm, taper length 650μm. a) grating period = 580nm, b) grating period = 600nm.

Therefore, $\Delta\theta \propto \alpha / K_0$. As a result, decreasing loss would result in decreasing beamwidth ($\alpha\downarrow \Rightarrow \Delta\theta\downarrow$). It suggests that narrower beam can be created by smaller α value. On the other hand, side lobes are inevitable because the structure is finite along z. When we change the etch-depth to change the α, β would also be modified slightly. However, because we do not want β to change because it affects the angle of coupling, the period must be altered in the same time. In this work, using a specified material system, we have two parameters to play with: period and etch-depth. Therefore, it will include a two-step process: slightly increasing etch-depth while playing with period, to maintaining β constant to keep the angle of maximum radiation the same. In this work, the optimization of the structure is accomplished by simulating different periods and etching depths with an aim to obtain maximum efficiency over coupling angle from 4° to 14°.

Figure 8.5 shows the simulated efficiency versus incident angle for the proposed SOI grating coupler at 1550nm wavelength with periods of 580nm and 600nm. For 70nm etching depth, more

than 40% coupling efficiency is expected over the desired coupling angle. Figure 8.6 shows the variation of the simulated efficiency with wavelength for the proposed SOI grating coupler with a 580nm grating period and 70nm etching depth. According to Eq. (4), because the phase constant β changes with wavelength, the maximum coupling angle is also changed with wavelength. In this structure, by increasing the wavelength, coupling angle is decreasing and the maximum efficiency is expected at 1550nm wavelength.

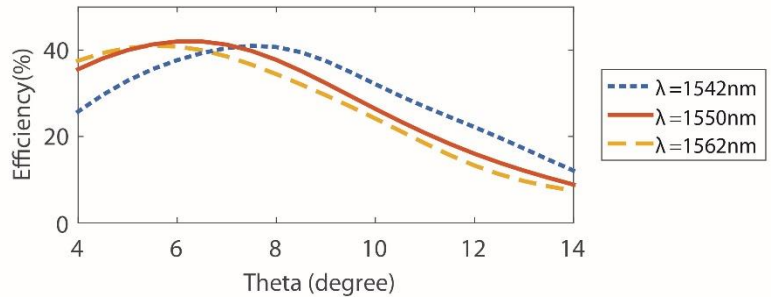

Figure 8.6**:** Simulated efficiency versus incident angle for the proposed SOI grating coupler for different wavelengths. SOI wafer (260nm silicon layer and 2 µm buried oxide), waveguide width 500nm, grating width 12.5 µm, taper length 650 µm, grating period 580nm, etching depth 70nm.

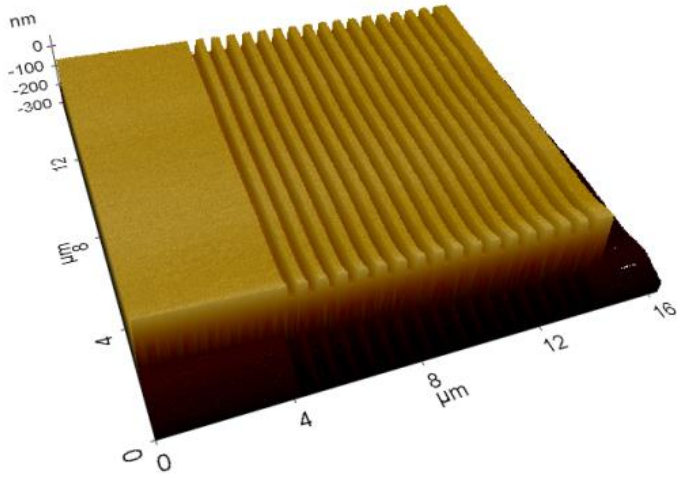

Figure 8.7: AFM scan of a grating coupler.

8.4 Fabrication and Measurement

Electron Beam Lithography (EBL) (Vistec VB6 UHR-EWF) and Inductively Coupled Plasma – Reactive Ion Etching (ICP-RIE) (Oxford PlasmaLab System100) were used for the fabrication of our device based on SOI substrate with a 260nm silicon device layer and a 2µm buried oxide (BOX) layer. Because the fiber couplers require a different etch depth than the other optical structures, they have to be fabricated in a separate process step. Two sets of alignment marks for these two-level microfabrication steps were first patterned by EBL in positive electron beam resist ZEP520a and then transferred into the top Si layer using an SF6/C4F8 ICP etch chemistry. The optical end-point detection system stops the etching process when the BOX is reached, to maximize the contrast during subsequent EBL exposures.

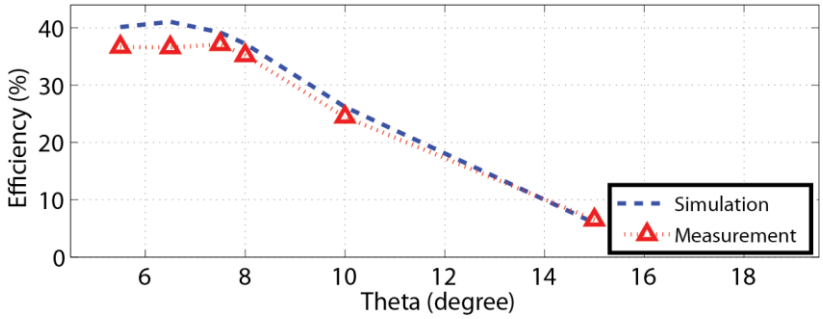

Figure 8.8**:** Measured efficiency of SOI grating coupler (260nm silicon layer and 2 µm buried oxide, 580nm grating period and 70nm etching depth) at 1550nm wavelength and comparison with the simulation

The sample was then cleaned, the same positive resist was spin coated, and the grating couplers were patterned by EBL using the first set of alignment marks. Grating couplers with 70nm etch depth were then obtained using the same ICP etching recipe described above. The sample was then cleaned again, and the same positive resist was spin coated. For the definition of the waveguide, the second set of alignment marks was used to obtain exposure by EBL 3 µm–wide trenches along the side of the waveguides, which were then transferred to the underlying top Si device layer (260nm), all the way down to the BOX layer, using the same SF6/C4F8 ICP-RIE process. The fabrication process was completed after removing the resist using oxygen plasma. Figure 8.7 above shows the atomic-force microscopy (AFM) scan of a grating coupler on one of our devices.

A grating design involving SOI wafer—with a 260nm silicon layer and 2μm buried oxide—was optimized for operation at 1550nm wavelength. The design is also able efficiently to couple the light over a broad range of wavelengths. Two different periods were studied, resulting in two slightly different coupling angles. Test structures with grating couplers and tapered strip waveguides were fabricated. They are characterized by various coupling angles over 100nm wavelength spectrum. The fabricated grating couplers show a coupling efficiency higher than 35% over 50nm wavelength bandwidth. The selection of period and etch depth of the proposed SOI grating coupler is done with consideration to achieving the maximum bandwidth. According to the theory, to attain wider bandwidth, a material system with larger refractive index must be used, as this value is the dominant factor in determining the maximum bandwidth. For lower value of n_{eff}, n= -2 beam begins propagating in a closer operating wavelength [20]. The optimized coupling angles are 7.5° and 12° for the 580nm and 600nm grating periods, respectively, in agreement with the full-wave simulation values of 7° and 13°. The corresponding coupling efficiencies were 42% and 38%. Figure 8.8 shows the measurement result for the 580nm grating period versus different coupling angle and the comparison with simulation. The discrepancy with simulation is less than 12% and also the curve trends are exactly the same. The discrepancy, using 2D eigenmode expansion method with perfectly matched layer boundary conditions, has been reported more than 34% and also 54% [21] and more than 20% in case of 2D finite-difference time-domain [22]. This deviation can be due to an aberration of the fabricated structure from the targeted structure. This excellent agreement among theory, simulation, and experiment fully validates the design method.

8.5 Conclusion

Three-dimensional full-wave analysis of an out-of-plane grating coupler is conducted and guided wave and leakage characteristics are studied in detail. The radiation pattern is obtained from the simulations, also using numerical calibration method. Coupling efficiency is derived from the radiation pattern. SOI grating coupler design is optimized to obtain a maximum coupling efficiency at operating 1550nm wavelength and over 4° to 14° degree coupling angle. The optimized grating couplers are fabricated using electron-beam lithography technique and plasma etching, and characterized. An excellent agreement between simulations and measurements is perceived, thereby validating the demonstrated method.

8.6 References

[1] S. T. Peng, T. Tamir, and H. L. Bertoni, "Theory of periodic dielectric waveguides," *IEEE Trans. Microwave Theory Tech.*, no. 23, pp. 123-133, 1975.

[2] D. P. Pai and K. A. Awada, "Analysis of dielectric gratings of arbitrary profiles and thicknesses," *J. Opt. Soc. Amer. A, Opt. Image Sci*., no.8, pp.755-762, 1991.

[3] C. C. Ghizoni, B-U. Chen, and C. L. Tang, "Theory and experiments on grating couplers for thin-film waveguides," *IEEE J. Quan- tum Electron*., no.12, pp.69-73, 1976.

[4] N. Neviere, R. Petit, and M. Cadilhac, "About the theory of optical grating coupler-waveguide systems," *Opt. Commun*., no.8, pp.113-117, 1973.

[5] D. E. Tremain and K. K. Mei, "Application of the unimoment method to scattering from periodic dielectric structures," *J. Opt. Soc. Am*., no.68, pp.775-783, 1978.

[6] T. Tamir and S. T. Peng, "Analysis and Design of Grating Couplers," *Appl. Phys*., no.14, pp.235-254, 1977.

[7] K. C. Chang, V. Shah, and T. Tamir, "Scattering and guiding of waves by dielectric gratings with arbitrary profiles," *J. Opt. Soc. Am*., no.70, pp.804-813, 1980.

[8] R. Magnusson and T. K. Gaylord, "Equivalence of multiwave coupled-wave theory and modal theory of periodic-media diffraction," *J. Opt. Soc. Am*., no.68, pp.1777-1779, 1978.

[9] D. Taillaert, W. Bogaerts, P. Bienstman, T. F. Krauss, P. Van Daele, I. Moerman, S. Verstuyft, K. De Mesel, and R. Baets, "An out-of-plane grating coupler for efficient butt-coupling between compact planar waveguides and single-mode fibers," *IEEE J. Quantum Electron.*, no.38, pp. 949-955, 2002.

[10] Moerman, P. P. Van Daele, and P. M. Demeester, "A review on fabrication technologies for the monolithic integration of tapers with III-V semiconductor devices," *IEEE J. Select. Topics Quantum Electron.*, no.3, pp.1308-1320, 1998.

[11] F. Van Laere, G. Roelkens, M. Ayre, J. Schrauwen, D. Taillaert, D. Van Thourhout, T. E. Krauss, and R. Baets, " Compact and highly efficient grating couplers between optical fiber and nanophotonic waveguides," *J. Lightwave Technol*., no.25, pp.151-156, 2007.

[12] F. Xu and K. Wu, “Numerical multimode calibration technique for extraction of complex propagation constants of substrate integrated waveguide,” *IEEE MTT-S Int. Microwave Symp. Dig*., pp.1227-1230, 2004.

[13] S. F. Helfert and R. Pregla, “Efficient analysis of periodic structures,” *J. Lightwave Technol.*, no.16, pp.1694-1702, 1998.

[14] A. Oliner, and D. R. Jackson, *Antenna Engineering Handbook* (New York: McGraw-Hill, 1993).

[15] R. Collin, *Field Theory of Guided Waves* (McGraw-Hill Book Company INC. NY, 1960).

[16] ANSYS Academic Research, Release 15.0.

[17] Optiwave, Release 11.0.

[18] Palmer and E. Loewen, *Diffraction Grating Handbook* (Newport Corporation, 2005).

[19] E. V. Jull, *Aperture antennas and diffraction theory* (IET, 1981).

[20] M. Guglielmi and D. R. Jackson, “Broadside radiation from periodic leaky-wave antennas,” *IEEE Trans. Antennas Propagat*., no.41, pp.31-37, 1993.

[21] Taillaert, F. Van Laere, M. Ayre, W. Bogaerts, D. Van Thourhout, P. Bienstman, and R. Baets, “Grating couplers for coupling between optical fibers and nanophotonic waveguides,” *Jpn. J. Appl. Phys*., no.45, pp.6071–6077, 2006.

[22] Z. Cheng , X. Chen , C. Y. Wong , K. Xu , C. K. Y. Fung , Y. M. Chen and H. K. Tsang, “Mid-infrared grating couplers for silicon-on-sapphire waveguides”, *J. IEEE Photon*., no.4, pp.104-113, 2012.

CHAPTER 9 GENERAL DISCUSSION

In order to keep up with rising global demand for bandwidth, future generations of both wireless and wireline technology will need to exploit the spectral range over 100 GHz - 1 terahertz (THz) and beyond. However, the integrated building blocks that will well define such an ultra-high frequency system technology architecture and protocol are unclear and mostly unavailable. This dissertation sets the stage in responding to this emerging challenge by exploring new guided wave structures, concepts and techniques for the development of millimeter-wave (mmW) and THz electronic and photonic integrated circuits and systems. Three research orientations are considered in this PhD thesis: electro-optic, microwave, and optics.

After introduction and literature review in the first chapter, in second chapter a new type of electro-optic modulator is introduced. A complete theoretical study is done in using the concept of substrate integrated circuits technology in order to realize low-cost, low-voltage, and ultra-high-speed electro-optical modulators with more than hundreds of GHz speed of modulation. SIW (substrate integrated waveguide) is used as an alternative traveling-wave structure of a polymer EO modulator and therefore the carrier frequency is determined by the SIW frequency of operation. The design in this work is completed for an EO modulator with the center frequency of 160 GHz achieving more than 22% optical bandwidth. This work was presented at European Microwave Conference 2012 and the whole work was published in the IEEE/OSA Journal of Lightwave Technology.

Second orientation is addressed through chapter three to six. Chapter three includes devise and demonstration of a class of transformative transmission lines and waveguides that can be used in the making of performance-demanding integrated electronic and photonic circuits and systems. Transmission lines and waveguides are the building blocks of all electronic and photonics integrated circuits and systems and in spite of a substantial expansion of electronic and photonic applications towards terahertz (THz), the basic structure of traditional transmission lines, developed in the 1950s, have not changed. There are two categories of waveguiding structure, namely, transverse electromagnetic (TEM)-mode type such as microstrip line and transverse electric/magnetic (TE/TM)-mode type such as substrate integrated waveguide. TEM structures support the transmission of signal from zero frequency (DC) but they experience increasing signal attenuation and dispersion at millimeter-waves (mmW) and terahertz (THz) frequencies. TE/TM structures, on the other hand, support the transmission of those high frequency signals but cannot

cover DC and low frequency signals, and they are dispersive because of cut-off frequency. In this work, a DC-to-THz waveguide structure is introduced. The strength of this work is that the design is done in such a way that with increasing frequency, a mode conversion phenomenon takes place and the operating mode is reconfigured intentionally to ensure a desired low-loss and low-dispersion performance. This is therefore a mode-selective transmission line (MSTL) that operates with TEM mode over low frequency range and TE/TM mode over high frequency range. This work would have a significant impact on the future research and development of high-frequency and high-speed electronics and photonics and will be of significant interest to a wide range of readers including researchers, engineers and technologists who are concerned with integrated circuits, optoelectronics, microwave photonics, interconnects, and THz. This work was presented at Photonic west 2016 and the whole work was published in IEEE Transaction on Terahertz Science and Technology.

In chapter 4, complete theoretical study, full-wave three-dimensional simulations, and experimental measurements of the fabricated prototypes are presented. MSTL is fabricated in two different platforms of quartz substrate and PCB and characterized from DC to 500 GHz. This work was presented at Internarial Microwave Symposium 2016 and the whole work is under review in IEEE Transaction on Microwave Theory and Technique. As one of the fundamental applications, MSTL interconnects, including lines and bends, are studied and designed (chapter five). The structure characterization is carried out in both frequency domain and time domain to examine and verify the propagation behaviors of picosecond pulses, high frequency digital rectangular pulses, and to obtain the eye-diagram. The crosstalk of the side-by-side placed lines is also measured to confirm the performance for high-density interconnects. Both fabrication of MSTL and its experimental measurement (up to 500GHz) have been done at the École Polytechnique de Montréal. This technology allows, for the first time, the transmission of fast pulses along the transmission lines with much lower dispersion and loss than the today's technologies. This work was presented at Internarial Microwave Symposium 2016 and the whole work is under review in IEEE Transaction on Microwave Theory and Technique. In chapter six, a unified method for extracting the circuit model and calculating the characteristic impedance of arbitrary transmission line and waveguide in connection with any type of mode is also introduced, and may be applied to obtain the MSTL characteristic impedance over all frequencies of interest. This work is under review in IEEE Transaction on Microwave Theory and Technique.

Chapter seven and eight are allocated to the last orientation. In chapter 7, a new optical rib waveguide based on calcium barium niobate (CBN) Thin-Film is designed and demonstrated. CBN is a high performance novel electro-optic material and is available in thin-film as well as bulk form. The fabrication and experimental measurement of this work is done at INRS and the result was presented at Conference on Lasers and Electro-Optics 2014 and also published in IEEE Photonics Technology Letters. Also, because of the challenge that we faced in coupling light to the very thin CBN-based waveguides, a CBN-based grating coupler was required. For this reason, a new way of design and analysis of optical grating coupler was required. A three-dimensional simulation of the grating coupler was performed for the first time, which enables a rigorous and general investigation of this periodic structure and a full-wave three dimensional analysis of optical grating coupler is demonstrated for the first time. The optimum designed grating coupler is fabricated using an electron-beam lithography. Simulation results are verified through experimental characterization. Three-dimensional (3D) full-wave analysis of an out-of-plane grating coupler is achieved for the first time, and the radiation pattern and characteristics are derived. The design and optimizations of both structures have been validated through fabrication and characterization. The fabrication of this work is done in INRS-LMN and the experimental part of this work is done at University of Laval and it has been presented in Photonic North 2014 and the extended version was published in Optics Express. Finally, the last chapter provides the conclusions of the thesis and outlines some of the future works planned in the field of mmW/THz electronics and photonics.

CHAPTER 10 CONCLUSIONS AND FUTURE WORK

10.1 Conclusions

This PhD thesis focuses on devising and developing original concepts toward a technological breakthrough in mmW/THz photonics and electronics. This multidisciplinary project necessitated a combination of microwave, optical, and electro-optical design, analysis, simulation, and characterization. After a complete literature review, unconventional approaches have been explored, through determining the root of problems, to overcome the involved restrictions in increasing the operating frequency and bandwidth. The key accomplishments of this work have been in introducing and realizing a class of high-performance building-block transmission lines and waveguide structures, formulating alternative modeling and simulation approaches, and utilising new high-performance materials. Accordingly, the principle scientific contributions of this thesis can be summarized as follows:

1)Electro-optics:

With regard to the state of the art in microwave and mmW photonics, a new prototype for EO MZ modulator has been introduced. The traveling-wave structure was altered to improve the RF performance and increase the carrier frequency in an EO modulator. A band-pass non-TEM mode EO push-pull MZ modulator was designed and demonstrated based on substrate integrated waveguide (SIW) and nonlinear optical polymer [17], [18].

2)RF and Microwaves:

a. As one of the main areas of emphasis in this dissertation, a new type of transmission line, called MSTL, was theoretically designed and experimentally demonstrated. MSTL is a low-loss and low-dispersion transmission line over the DC-to-THz frequency spectrum. Such transmission lines present widely applicable building blocks for all electronic and photonic circuits and systems [34], [35], [37], [38].

b. In support of one of the main MSTL applications, DC-to-THz MSTL on-chip interconnects were designed and characterized in both frequency domain and time domain [36], [39].

c. A new type of modelling approach was developed to deal with different guided wave structures regardless of propagating modes. This model accounts for high-frequency effects and can be used for higher-order modes. Such a generalized modelling approach is applicable to different types of two-port networks, including all the transmission lines and waveguide structures [40].

3)Optics:

a. Optical rib waveguides based on CBN, a high performance thin-film EO material, were designed, fabricated, and characterized. The demonstrated CBN optical waveguide offers low-loss propagation characteristics and is the building block for all CBN electro-optical devices [46]–[48].

b. Since CBN optical waveguides presented some difficulties in terms of waveguide characterization due to the thinness of the waveguides, a new method for design and 3D full-wave analysis of out-of-plane grating coupler has been developed. This method has been verified for SOI waveguides and grating couplers [49], [50].

10.2 **Future work**

The research contributions presented in this thesis deal with a wide range of analog and digital applications. With reference to the specified categorization in the last section, the research may be extended as follows:

1)Electro-optics and opto-electronics:

a. In this research, although a great effort has been made for the fabrication of the proposed SIW EO modulator, it was unsuccessful. The process to deposit EO polymer material presented some challenges that were not possible to be addressed with our available processing techniques. Therefore, this structure should be fabricated in the next research efforts. Some collaboration has been initiated and would be continued to finalize this work.

b. The structure of band-pass SIW EO modulator can be modified by using MSTL instead of SIW as the traveling-wave structure. In this case, a truly broadband DC to THz EO modulator would be realized.

c. MSTL can be utilised in place of the traveling-wave structure in building optoelectronic devices. A specific example is the application of MSTL as the transmission line in an optoelectronic photoconductive switch. Photoconductive switching has been the most common method for producing THz bandwidth electrical signals for data transmission in integrated circuits and devices. However, ultrafast DC-to-THz electrical pulses necessitate transmission lines with low dispersion and loss, which can be readily interconnected with other devices. Currently, dispersion is a major problem in transmission lines for ultrafast electrical pulses since it causes loss of speed due to pulse broadening [50]–[54]. As illustrated in Figure 10.1, MSTL can be utilised as an alternative supporting traveling-wave structure in a photoconductive switch. The picosecond pulses are created by driving THz switches with femtosecond laser pulses. Using a material such as LT-GaAs, free carriers are generated and accelerated in an applied bias field producing an electromagnetic transient.

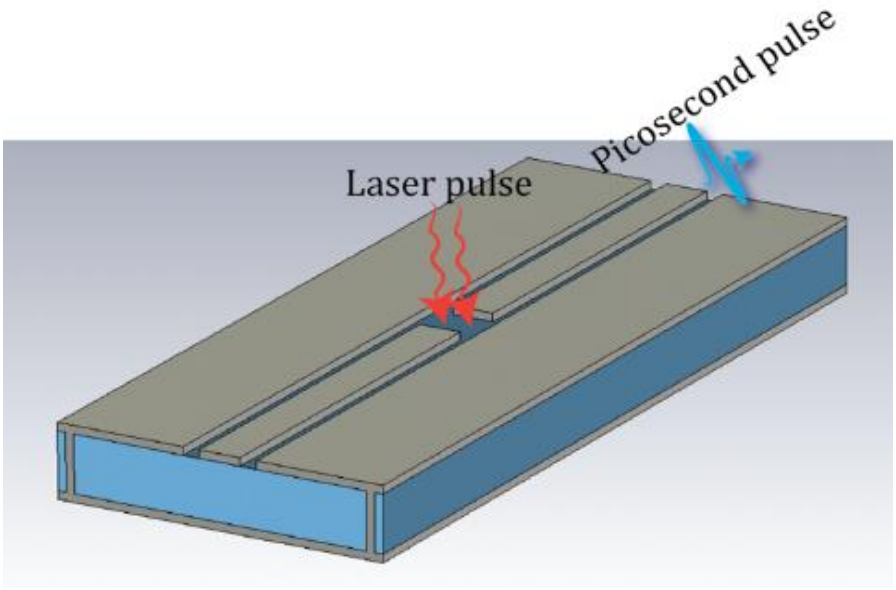

Figure 10.1: A schematic of the proposed MSTL photoconductive switch.

2)Microwaves, mmW, and THz:

a. Different types of MSTL junctions and discontinuities must be studied and designed. Since in MSTL the propagating mode is altered by increasing the frequency, a rigorous analysis is required to realize different types of MSTL discontinuities with the same performance as an MSTL straight line.

b. Different ultra-broadband electrical circuits and devices, such as hybrid circuits, mixed ICs, filters, directional couplers, power dividers, and antennas, can be designed based on MSTL.

c. MSTL can be used as low-loss interconnect waveguides in photonic and electronic integrated circuits. In the case of photonic integrated circuits, MSTL structure can be customized for a variety of material systems.

d. MSTL can be employed to increase the speed in both wireline and wireless applications. Broadband wireless applications also need wireline that can support broadband data offloading.

e. Generalized circuit modelling should be applied to extract an MSTL circuit model. Additionally, circuit models of truly broadband structures and non-TEM mode waveguides can be derived through this method.

3)Optics:

a. CBN optical rib waveguides can be used as the building block to design and fabricate different CBN electro-optical devices such as EO ring resonators and MZM.

b. Optical grating coupler design approach can be applied to design grating couplers for different kinds of photonic material systems such as group III and IV.

BIBLIOGRAPHY

[1] W. B. Shockley, J. Bardeen, and W. H. Brattain, “Nobel prize in physics 1956: Presentation speech,” Nobel Lectures, Physics 1942–1962, Elsevier Publishing Company, Amsterdam, 1964.

[2] Miniaturized Electronic Circuits, by Jack S. Kilby. 1964, June 23. United States Patent Office, US Patent 3,138,743. Available: http://ieeexplore.ieee.org/stamp/stamp.jsp?arnumber=4785580.

[3] J. Orton, Semiconductors and the information revolution: Magic crystals that made IT happen. Amsterdam, Boston: Academic Press/Elsevier, 2009, pp. 35–36.

[4] J. Brodkin, Ars Technica – “Bandwidth explosion: As Internet use soars, can bottlenecks be averted?” http://arstechnica.com/business/2012/05/bandwidth-explosion-as-internet-use-soars-can-bottlenecks-be-averted/).

[5] International Telecommunication Union (ITU), 2014. Manual for measuring ICT access and use by households and individuals, Geneva, Switzerland.

[6] R. W. McMillan, “Terahertz imaging, millimeter-wave radar,” Advances in Sensing with Security Applications Digest, NATO Advanced Study Institute, Il Cioceo, Italy, pp. 1–26, 2005 July.

[7] M. J. Fitch and R. Osiander, “Terahertz waves for communications and sensing,” Johns Hopkins APL Tech. Dig., vol. 25, no. 4, pp. 348–355, Oct./Dec. 2004.

[8] J. Federici and L. Moeller, “Review of terahertz and subterahertz wireless communications,” J. Appl. Phys., vol. 107, pp. 111101–111122, 2010. http://dx.doi.org/10.1063/1.3386413.

[9] M. Tonouchi, “Cutting-edge terahertz technology,” Nat. Photon., vol. 1, no. 2, pp. 97–105, 2007. http://dx.doi.org/10.1038/nphoton.2007.3.

[10] P. J. Winzer, “Beyond 100G ethernet,” IEEE Commun. Mag., vol. 48, no. 7, pp. 26–30, 2010. http://dx.doi.org/10.1109/MCOM.2010.5496875.

[11] J. Sutherland “As edge speeds increase, wires become transmission lines,” EDN, pp. 75–85, Oct. 1999.

[12] R. Kirchain and L. Kimerling, “A roadmap for nanophotonics,” Nat. Photon., vol. 1, pp. 303–305, 2007. http://dx.doi.org/10.1038/nphoton.2007.84.

[13] M. Bohr, “Interconnect scaling: The real limiter to high performance ULSI.” Proc. IEDM, pp. 241–244, 1995.

[14] D. Loke, J. Skelton, W.-J. Wang, T.-H. Lee, R. Zhao, T.-C. Chong, and S. R. Elliott. “Ultrafast phase-change logic device driven by melting processes,” Proc. Natl. Acad. Sci. USA, vol. 111, no. 37, pp. 13272–13277, 2014. http://dx.doi.org.10.1073/pnas.1407633111

[15] S. Narenda, L. Fujino, and K. Smith, “Through the looking glass continued (III): Update to trends in solid-state circuits and systems from ISSCC 2014 [ISSCC Trends],” IEEE Solid-State Circuits Magazine, vol. 6, no. 1, pp. 49–53, 2014. http://dx.doi.org/10.1109/MSSC.2013.2289636

[16] J. Capmany and D. Novak, “Microwave photonics combines two worlds,” Nature Photon. 1, 319–330, 2007. http://dx.doi.org.doi:10.1038/nphoton.2007.89

[17] F. Fesharaki and K. Wu, “Band-pass non-TEM mode traveling-wave electro-optical polymer modulator,” European Microwave Conference Proceeding, pp. 991–994, 2012.

[18] F. Fesharaki and K. Wu, “Band-pass non-TEM mode traveling-wave electro-optical polymer modulator for millimeter-wave and terahertz application,” J. Lightwave Technol., vol. 30, no. 23, pp. 3586–3596, 2012.

[19] S. E. Thompson and S. Parthasarathy, “Moore’s law: the future of Si microelectronics,” Materials Today, vol. 9, no. 6, pp. 20–25, 2006.

[20] L. R. Dalton, P. A. Sullivan, and D. H. Bale, “Electric field poled organic electro-optic materials: state of the art and future prospects,” J. Chem. Rev., vol. 110, no. 1, pp. 25–55, 2009. http://dx.doi.org.10.1021/cr9000429.

[21] J. Capmany and D. Novak, “Microwave photonics combines two worlds,” Nature Photon., vol. 1, pp. 319–330, 2007. http://dx.doi.org.doi:10.1038/nphoton.2007.89.

[22] J. P. Yao, “Microwave photonics,” J. Lightwave Technol., vol. 27, no. 3, pp. 314–335, Feb. 2009. http://dx.doi.org.10.1109/JLT.2008.2009551.

[23] D. H. Auston. (1993, June 28), Ultrashort laser pulses: Generation and applications. (2nd ed.).

[24] R. Lai, X. B. Mei, W. R. Deal, W. Yoshida, Y. M. Kim, P. H. Liu, J. Lee, J. Uyeda, V. Radisic, M. Lange, T. Gaier, L. Samoska, and A. Fung, "Sub 50 nm InP HEMT device with fmax greater than 1 THz," in Int. Electron Devices Meeting Tech. Dig., pp. 609–611, 2007.

[25] D.-H. Kim, J. A. del Alamo, P. Chen, W. Ha, M. Urteaga, and B. Brar, "50-nm E-mode In0.7Ga0.3As PHEMTs on 100-mm InP substrate with fmax > 1 THz," Int. Electron Devices Meeting Tech. Dig., pp. 692–695, 2010.

[26] B. Heinemann, R. Barth, D. Bolze, J. Drews, G. G. Fischer, A. Fox, O. Fursenko, T. Grabolla, U. Haak, D. Knoll, R. Kurps, M. Lisker, S. Marschmeyer, H. Rucker, D. Schmidt, J. Schmidt, M. A. Schubert, B. Tillack, C. Wipf, D. Wolansky, and Y. Yamamoto, "SiGe HBT technology with f T/f max of 300 GHz/500 GHz and 2.0 ps CML gate delay," IEEE Int. Electron Devices Meeting, pp. 688–691, Dec. 2010.

[27] M. Bohr, "Interconnect scaling: The real limiter to high performance ULSI," Proc. IEDM, pp. 241–244, 1995.

[28] A. Matsuzawa, "RF-SoC: Expectations and required conditions," IEEE Trans. Microwave Theory Tech., vol. 50, pp. 245–253, Jan. 2002.

[29] K. Lim, S. Pinel, M. F. Davis, A. Sutono, C.-H. Lee, D. Heo, A. Obatoynbo, J. Laskar, M. Tentzeris, and R. Tummala, "RF-SOP for wireless communications," IEEE Microwave Mag., vol. 3, pp. 88–99, Mar. 2002.

[30] S. O. Koswatta, A. Valdes-Garcia, M. B. Steiner, Y. M. Lin, and P. Avouris, "Ultimate RF performance potential of carbon electronics," IEEE Trans. Microw. Theory Tech., vol. 59, no. 10, pp. 2739–2750, 2011.

[31] R. H. Havemann and J. A. Hutchby, "High-performance interconnects: an integration overview," Proc. IEEE, vol. 89, no. 5, pp. 586–601, May 2001.

[32] T. Spencer, T. Osborn, P. A. Kohl, "High-frequency chip connections," Science, vol. 320, pp. 756–757, 2008.

[33] "GigOptix," retrieved http://www.gigoptix.com/.

[34] F. Fesharaki, T. Djerafi, M. Chaker, and K. Wu, “Mode-selective transmission line for DC-to-THz super-broadband operation,” IMS 2016, San Francisco.

[35] F. Fesharaki, T. Djerafi, M. Chaker, and K. Wu, “Low-Loss and Low-Dispersion Transmission Line over DC-to-THz Spectrum,” IEEE Transaction on Terahertz Science and Technology, vol. 6, no. 4, 2016.

[36] F. Fesharaki, T. Djerafi, M. Chaker, and K. Wu, “High-Integrity Terabit-per-Second Signal Interconnects with Mode-Selective Transmission Line”, IMS 2016, San Francisco.

[37] F. Fesharaki, T. Djerafi, M. Chaker, and K. Wu, “Guided-wave properties of mode-selective transmission line,” IEEE Transaction on Microwave Theory and Technique, under review (TMTT-2015-09-1155).

[38] F. Fesharaki, T. Djerafi, M. Chaker, and K. Wu, “Low-loss and low-dispersion transmission line over DC-to-THz spectrum,” SPIE Photonic West 2016, San Francisco.

[39] F. Fesharaki, T. Djerafi, M. Chaker, and K. Wu, “Mode-selective transmission line for terabit-per-second on-chip interconnects,” IEEE Transaction on Microwave Theory and Technique, under review (TMTT-2016-06-0645.).

[40] F. Fesharaki, T. Djerafi, M. Chaker, and K. Wu, “Generalized S-parameter de-embedding algorithm and equivalent circuit model extraction of electromagnetic networks,” IEEE Transaction on Microwave Theory and Technique, accepted.

[41] R. Helsten, L. Razzari, M. Ferrera, P. F. Ndione, M. Gaidi, C. Durand, M. Chaker, and R. Morandotti, “Pockels response in calcium barium niobate thin films,” Appl. Phys. Lett., 91, 261101, 2007.

[42] P.F. Ndione, M. Gaidi, C. Durand, M. Chaker, R. Morandotti, and G. Rioux, “Structural and optical properties of epitaxial CaxBa1−xNb2O6 thin films grown on MgO by pulsed laser deposition,” J. Appl. Phys., vol. 103, pp. 033510–15, 2008.

[43] R. G. DeCorby, N. Ponnampalam, M. M. Pai, H. T. Nguyen, P. K. Dwivedi, T.J. Clement, C. J. Haugen, J. N. McMullin, S. O. Kasap, “IEEE Journal of high index contrast waveguides in chalcogenide glass and polymer,” IEEE Journal of Selected Topics in Quantum Electronics, vol. 11, no. 2, pp. 539–546, 2005.

[44] S. Vigne, J. Munõz, S. Delprat, J. Margot, and M. Chaker, “Plasma etching dynamics of CaxBa1−xNb2O6 (CBN) material,” Microelectron. Eng. 110, 265–269, Oct. 2013. http://dx.doi.org.10.1016/j.mee.2013.01.052.

[45] S. Vigne, S. Delprat, M. Chaker, and M. Margot, “Investigation of nickel as hard mask for patterning multicomponent oxide materials in chlorine plasmas, J. Appl. Phys., vol. 114, no. 10, 103303, Sept. 2013. http://dx.doi.org/10.1063/1.4820934.

[46] F. Fesharaki, N. Hossain, S. Vigne, J. Margot, K. Wu, and M. Chaker (2014). “Electro-Optic CaxBa1−xNb2O6 (CBN) thin-film based rib waveguide structure” IONS-NA 2014, Montreal.

[47] F. Fesharaki, N. Hossain, S. Vigne, J. Margot, K. Wu, and M. Chaker, “Demonstration and fabrication of electro-optic CaxBa1−xNb2O6 (CBN) thin-film based rib waveguide structure,” CLEO 2014,San Jose, http://dx.doi.org/10.1364/CLEO_AT.2014.JTh2A.42.

[48] F. Fesharaki, N. Hossain, S. Vigne, J. Margot, K. Wu, and M. Chaker, “Theoretical analysis and experimental evaluation of SiO2-CBN-MgO rib waveguide structure,” IEEE Photonic Technology Letters, vol. 26, no. 18, pp. 1821–1824, July 2014. http://dx.doi.org/10.1109/LPT.2014.2336731.

[49] F. Fesharaki, N. Hossain, S. Vigne, K. Bédard, B. Le Drogoff, S. Larochelle, M. Chaker, and K. Wu. (2014). “Full-wave analysis of optical grating coupler,” May 28-30, 2014, Photonics North 2014, Montreal, QC, Canada.

[50] F. Fesharaki, N. Hossain, S. Vigne, M. Chaker, and K. Wu, “Accurate Theoretical and Experimental Characterization of Optical Grating Coupler,” J Optics Express, vol. 24, no. 18, pp. 21027-21037, 2016.

[51] D. H. Auston, “Picosecond optoelectronic switching and gating in silicon,” Appl. Phys. Lett., vol. 26, pp. 101–103, 1975. http://dx.doi.org/10.1063/1.88079.

[52] D. H. Auston, “Ultrafast Optoelectronics,” in Ultrashort Laser Pulses and Applications, 2nd ed., vol. 60 in Topics in Applied Physics, W. Kaiser, Ed., Berlin, Springer-Verlag, 1988.

[53] M. B. Ketchen, D. Grischkowsky, T. C. Chen, C.-C. Chi, I. N. Duling III, N. J. Halas, J.-M. Halbout, J. A. Kash, and G. P. Li, “Generation of subpicosecond electrical pulses on

coplanar transmission lines," Appl. Phys. Lett., vol. 48, pp. 751–753, 1986. http://dx.doi.org/10.1063/1.96709.

[54] K. Jürgen, "Contact-Free Characterization of Electronic and Optoelectronic Devices With Ultrashort Laser Pulses," in Ultrashort Processes in Condensed Matter, W. E. Bron, Ed., 1993, New York: Springer US, ch. 3, pp. 143–195. https://dx.doi.org/10.1007/978-1-4615-2954-5.